8-2018

Investigation of the Effects of Oxidizer Temperature on the Stability of a Gas-Centered Swirl Coaxial Injector

William Zach Hallum
Purdue University

INVESTIGATION OF THE EFFECTS OF OXIDIZER TEMPERATURE ON THE STABILITY OF A GAS-CENTERED SWIRL COAXIAL INJECTOR

A Dissertation

Submitted to the Faculty

of

Purdue University

by

William Zach Hallum

In Partial Fulfillment of the

Requirements for the Degree

of

Doctor of Philosophy

August 2018

Purdue University

West Lafayette, Indiana

THE PURDUE UNIVERSITY GRADUATE SCHOOL
STATEMENT OF DISSERTATION APPROVAL

Dr. William Anderson, Chair

Purdue University, School of Aeronautics and Astronautics

Dr. Stephen Heister

Purdue University, School of Aeronautics and Astronautics

Dr. Timothee Pourpoint

Purdue University, School of Aeronautics and Astronautics

Dr. Li Qiao

Purdue University, School of Aeronautics and Astronautics

Approved by:

Dr. Wayne Chen

Head of the School of Aeronautics and Astronautics Graduate Program

This work is dedicated to my family. Thank you, in all possible ways.

ACKNOWLEDGMENTS

I would like to thank Professor William Anderson for his continued support and guidance during my time at Purdue University. I greatly appreciate the opportunity to be part of his research group and all the invaluable experiences I have shared as a result.

Thank you to the members of my committee, Professors Stephen Heister, Timothee Pourpoint, and Li Qiao, for their involvement and advice not only through this work but during my academic career.

Many thanks to the students and colleagues that have often provided assistance, guidance and support. To those who were there before me - Dr. Chris Fugger, Dr. Matthew Wierman, Dr. Rohan Gejji, Dr. Cheng Huang - those who were there alongside me - Dr. Mike Bedard, Tristan Fuller - and those who followed - Thomas Liu, Cory Back, Michael Orth. Thank you as well to Dr. Swanand Sardeshmukh for always serving as fountain of knowledge.

Thanks to B.J. Austin of IN Space, LLC, for all of his efforts ranging from hardware design, experimental support, to practical lab skills.

Many thanks to Venkateswaran Sankaran and the ALREST and VISP combustion stability programs at AFRL for their financial and technical support. This work would not exist without their involvement.

Thanks also to Scott Meyer and Rob McGuire. Without them, there would not be a Zucrow Laboratory. Their constant vigilance is what keeps the experiments and students from falling apart. Thank you for pushing us to do our very best.

TABLE OF CONTENTS

Page

LIST OF TABLES

Table Page

LIST OF FIGURES

Figure Page

Figure Page

Figure Page

Figure Page

Figure Page

Figure Page

SYMBOLS

A	geometric constant, area
α	spray angle
β	compressibility
c	sound speed, $[m/s]$
$c*$	characteristic velocity, $[m/s]$
C_d	discharge coefficient
δ_f	flame edge thickness
d	diameter
f	frequency, $[Hz]$
γ	specific heat ratio
h_s	lip thickness
J	momentum flux ratio
L	length, $[m$, cm, or μm$]$
λ	effective resonator length
μ	viscosity, $[Pa \cdot s]$
M	Mach number
$\dot{m}$	mass flow rate, $[kg/s]$
MW	molecular weight
∇	nabla, differential operator
ϕ	coefficient of filling
P	pressure, $[kPa]$
q	heat release
ρ	density, $[kg/m^3]$
r	radius, $[cm]$
R	universal gas constant

$\mathbb{R}$	reflection coefficient
Re	Reynolds Number
RI	Rayleigh Index
RR	recess ratio
σ	surface tension
S	gas core to injection recess diameter ratio
t	time, $[s, ms]$
T	period
τ	thickness
$\mathbb{T}$	transmission coefficient
v	velocity, $[m/s]$
ξ	spray angle contraction
x	spatial location
Z	acoustic impedance, $[\frac{Pa \cdot s}{m^3}]$

ABBREVIATIONS

CEA	Chemical Equilibrium with Applications
CFD	Computational Fluid Dynamics
CVRC	Continuously Variable Resonance Combustor
CWT	Continuous Wavelet Transform
DVRC	Discretely Variable Resonance Combustor
DES	Discrete Event Simulation
GCSC	Gas-Centered Swirling Coaxial
LEE	Linearized Euler Equations
LES	Large Eddy Simulation
MFR	Momentum Flux Ratio
O/F	Oxidizer-to-Fuel ratio
ORSC	Oxidizer Rich Staged Combustion
PSD	Power Spectral Density
RMS	Root Mean Square
SMD	Sauter Mean Diameter
TBC	Thermal Barrier Coating
UEC	Uni-Element Combustor

ABSTRACT

Hallum, William Zach PhD, Purdue University, August 2018. Investigation of the Effects of Oxidizer Temperature on the Stability of a Gas-Centered Swirl Coaxial Injector . Major Professor: William E. Anderson.

Rocket engines achieve extraordinary high energy densities within the chamber in the form of high pressure turbulent combustion. Successful design of these engines requires sustained, stable operation of a combustor exposed to extreme thermal loads. Slight deviations in operating conditions can then incur consequences ranging from reduced performance up to catastrophic failure in the face of excess heat loading. Sustained periodic oscillations, termed combustion instabilities, are often encountered during development, as fluctuations produced by combustion noise couple with heat release modes by way of modulation of the feed system, injector hydrodynamics, chemical kinetics, and mixing and atomization process. Successful development of reliable, high performance rocket engines can be achieved either through a thorough understanding of both injector and combustor dynamics to mitigate these instabilities or through the laborious design/test iteration process.

This document describes a two-fold work by the author. The first objective considers the acquisition of high-fidelity data sets of a single gas-centered swirl coaxial injector for use in the validation of computational models. Secondly, the stability of this injector was studied at two oxidizer inlet temperatures. Combustion stability was assessed through variation of the combustor geometry. Previous research shows that varying this geometry can either drive or dampen pressure oscillations. Testing was conducted on an experimental test bed equipped with modular sections to accommodate changing oxidizer post and chamber lengths. A single gas-centered swirl coaxial injector was used, with operating parameters based on the RD-180 injector element, such as equivalence and momentum flux ratios. Two oxidizer inlet temper-

atures were chosen. The first was oxygen combusted with gaseous hydrogen at lean conditions in a preburner to produce hot oxidizer near 700 K. The second was pure oxygen delivered at room temperature.

Results from the test campaign revealed the system to be classically stable across all configurations and inlet conditions tested, with pressure perturbations less than 10% of the mean chamber pressure. Discriminating behavior was observed between the two oxidizer inlet temperatures. At elevated temperatures, peak-to-peak pressure oscillations observed throughout the system were small at less than 4% of the mean chamber pressure. There was no observed dependency of the amplitude on geometry. At ambient temperatures, the pressure oscillations ranged from 4% up to 7%. The increase in amplitudes were similar to that of the acoustic reflection coefficient between the oxidizer and chamber gas, based on their acoustic specific impedance. An increase in the acoustic transmission coefficient was also observed, going from hot to ambient oxidizer. The increase in these two values would not necessarily lead to enhanced coupling between the chamber and resonance behavior in the post, but is expected to amplify pressure oscillations.

At the ambient condition, clear variation in amplitudes were generated through manipulation of the geometry. The general trend matched previous experiments but was not followed by all tested configurations. It was determined that a methodology solely based on the effective resonator wavelength was not sufficient to predict the amplitude of pressure oscillations. Instead, a better predictor of amplitude was found based on the alignment of the system with postulated vortex generation from the injector face and impingement on the chamber walls. The time between local pressure oscillations and final impingement of the resulting vortices fell between one and two cycles of the fundamental longitudinal chamber mode, increasing linearly in strength as phase lag increased.

1. INTRODUCTION

Modern technological advances and the innate pioneering spirit have brought humanity to the edge of space. Over the past half century, mankind has gone from its first forays into lofty reaches of space with beeping metal canisters, to a blistering number of achievements: contact with the majority of celestial bodies within the solar system, a sustained human presence in an orbiting station, a burgeoning space tourism industry, and plans to establish a permanent base on Mars. Increased access to earth orbit and beyond requires the transportation of thousands of kilograms of cargo from the surface to space. To support this initiative, a new generation of rocket engines are being developed to boost payloads up and out of the gravity well of Earth. These engines are designed towards the goal of higher performance, reduced cost, and an extremely high degree of reliability.

The Atlas family of rockets, starting with Atlas III, have relied on the Russian designed and built RD-180 engine as part of the first stage. The current geopolitical climate has led to a cooling of relations between the United States and Russia. As a result, there has been concern over the reliance of American military resources on the manufacturing and provision of technology that cannot currently be replicated or replaced domestically. This places at risk the strategic and tactical advantages of space access, jeopardizing national defense. To counter this, the United States is working towards creating an RD-180 replacement.

Private corporations appear to be migrating towards liquid methane as a fuel for the sake of reusability, as kerosene leads to coking. Such methane-based options include the BE-4 engine from Blue Origin [1], and the Raptor engine from SpaceX [2]. Each of these engines relies on staged combustion to achieve the higher chamber pressures to reach increased power levels. The AR1 engine, in development by Aero-

jet Rocketdyne [3], continues to use liquid kerosene for its proven track record in reliability and performance.

No matter the choice of propellant or injector design, the development of a first stage engine is very difficult. Rocket engines operate at extreme operating conditions, managing high thermal loads and pressures for up to several minutes. Stable operation is imperative, as deviations from design conditions can have consequences that run the gamut from decreased operating efficiency up to catastrophic destruction of hardware. Confined reacting flow is subject to the acoustic modes that are a natural product of the geometry of the containment device. As combustion noise is generated, it can resonate with the acoustic modes to drive periodic fluctuations. These pressure oscillations can result in variations in system parameters, such as propellant mass flow rate, and can influence or alter the mixing schemes of the injector. At sufficient levels or in the right conditions the response to pressure perturbations can cause oscillations in the heat release rate, which in turn can cause a pressure response. Coupling between the acoustic and heat release field can initiate a positive feedback loop, where synchronization between the two drives strong oscillations. This phenomenon of thermoacoustic coupling is referred to as combustion instability.

The requirement for unstable behavior was postulated simply by Lord Rayleigh in 1878, stating that "If heat be given to the air at the moment of greatest condensation, or be taken from it at the moment of greatest rarefaction, the vibration is encouraged. On the other hand, if heat be given at the moment of greatest rarefaction, or abstracted at the moment of greatest condensation, the vibration is discouraged [4]."

This statement was rewritten into mathematical notation by Putnam and Dennis in 1953, then later refined by Zinn [5] who added spatial dependency. This mathematical form permits calculation of Rayleigh indices for a defined integration volume, based on the mean and fluctuation components of pressure, p, and heat release, $\dot{q}$, as shown in Equation (1.1). This equation is integrated over a given volume, $d\bar{x}$, and the initial and final times, t_0 and t_f.

$$RI = \frac{1}{t_f - t_0} \int_{t_0}^{t_f} \left(\frac{\int_V (p(\mathbf{x},t) - \bar{p}(\mathbf{x}))d\bar{x}}{\int_V \bar{p}(\mathbf{x}))d\bar{x}} \right) \left(\frac{\int_V (\dot{q}(\mathbf{x},t) - \bar{\dot{q}}(\mathbf{x}))d\bar{x}}{\int_V \bar{\dot{q}}(\mathbf{x}))d\bar{x}} \right) \left(\right. \tag{1.1}$$

The sign of the indices reflects whether instabilities are expected to be driven or damped. A positive value occurs when the pressure and heat release are in phase, the two are considered to be coupled and actively drive instabilities. Conversely, the values is negative when the pressure and heat release are out of phase. This would lead to a damping of instabilities.

While it is simple enough to summarize the requirements for driving a thermoacoustic instability, prediction of which conditions satisfy the requirements is much more challenging. The injection process is highly complex; perturbations in a single flow property can easily affect a wide range of injection parameters. An understanding of the complete process and possible interactions is not fully realized. This can lead to the generation of spontaneous instabilities late in an engine development cycle, where modification to mitigate or eradicate the instability could require significant resources.

Achieving an *a priori* understanding of the intricacies of rocket combustion is currently being pursued through a parallel effort relying on experimental testing and computational modeling. Experimental testing provides reliable, realistic data but requires the cost and effort of designing, fabricating, assembly and testing of the hardware. Testing of subsystem or subscale models alleviates the costs by reducing the problem size. However, the physics do not all scale proportionally, so the subscale model might not adequately represent the final product.

The types of data that can be collected may also be limited. Quantitative measurements of some parameters, such as temperature or heat release within the combustion field, may be possible but can be prohibitively difficult to capture.

Non-intrusive measurement techniques are required in order to obtain representative data. This often leads to reliance on simple but highly localized measurements, such as pressure measurements. Spatially resolved diagnostics are also possi-

ble, often using transparent windows for optical accessibility with high speed imaging. At its simplest, line-of-sight measurements, such as chemiluminescence [6–11] or schlieren [12–17], are captured. While these measurements suffer from information loss by reducing a three-dimensional field into two dimensions, they continue to serve as useful data sets for characterizing combustion. More complex diagnostics techniques can better preserve the data, either by capturing tomographic data [18], or along a plane via a laser sheet, such as planar laser induced fluorescence and particle image velocimetry [19–21]. However, at the high pressure and temperature conditions found within a rocket combustor, these techniques begin to falter [22].

Computational fluid dynamics (CFD) complements the experimental approach. Whereas experiments yield accurate but limited data, CFD models provide spatially and temporally resolved solutions to a set of governing physical rules. These predictions are only as good as the underlying physical models. Assuming a solid physical foundation, CFD simulations can be used to predict a number of parameters, from velocity components to heat release rate to vorticity, throughout the full domain of the model.

Determining whether a model is accurate or suitable requires validation. This typically involves designing a benchmark test case for measurement and simulation. The results are then compared to determine whether the model realistically captures the specific physics. But comparing the two data sets is itself an exercise. Determining useful and viable comparative approaches is an ongoing research topic [23]. The effort laid out in this document aims to assist in this endeavor by acquiring valuable experimental data sets that can be used to test and improve the capability of existing computational models. This is achieved through the development and subsequent testing of a model rocket engine with a single injector element at realistic conditions.

The injector in this study is a gas-centered swirl coaxial (GCSC) injector which has a demonstrated history of providing efficient mixing and atomization of a liquid/gas propellant combination. This element design surrounds a central gaseous propellant

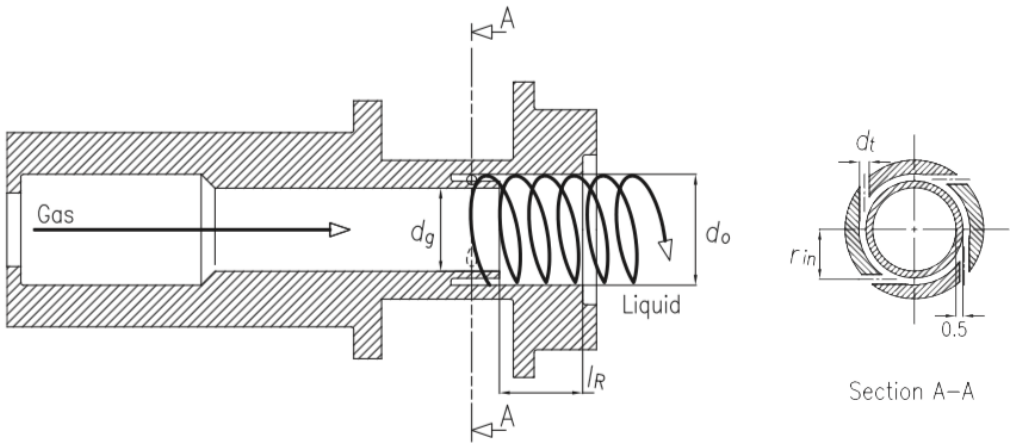

Figure 1.1.: An example of a GCSC injector. Gaseous propellant is injected along central post. Liquid propellant is injected tangentially into shielded annulus before entering injection cup where mixing and atomization begins [24].

with a liquid propellant given circumferential momentum through tangential injection. The two fluids mix at the shear layer before entering the combustion chamber.

The GCSC injector was invented by the Russians [25], who successfully integrated it into a number of their engines, such as the Kuznetzov NK-33 and the NPO Energomash RD-170 family [26]. The RD-170 and its derivatives - the single axis RD-171, the dual-chamber RD-180, and the single chamber RD-191 - were not only capable of producing great power but were quite stable [27–29]. The impressive results caught American interest, who then began to study the injector for the past few decades [25, 30–32].

The staged combustion cycle has the highest performance of any single-mode rocket engine cycle [33], where the use of preburners allows for higher main chamber pressures and further expansion of the exhaust. This engine cycle is typically split into three subgroups: fuel-rich, oxidizer-rich, and full-flow staged combustion. The GCSC supports oxidizer rich staged-combustion engine cycles (ORSC), where the oxidizer is combusted and serves as the central fluid in the injector, surrounded by a liquid hydrocarbon fuel. This injector complements the staged combustion cycle as

it suffers low atomization efficiency at lower operating pressures, but its performance scales with increased pressure [34].

Research into the physics of GCSC injectors on ORSC engines is ongoing as a means of extracting its proven performance capabilities and apply it to high-output domestic engines. Achieving this goal requires a systematic approach to studying the problem from a number of vantage points, ranging from full-scale engines near mission operating conditions, down to benchmark tests of a single injector at reduced scales.

The work presented in this document has two main objectives. The primary objective is to acquire direct and quantitative data of ORSC main chamber stability for use in the validation of computational models. To achieve this, an experiment was designed to be easily modelable with well-established boundary conditions and heavily instrumented to accurately collect quantitative data at a high resolution. The experiment was also designed to be modular to allow for the generation of a diverse suite of validation data. Both standard and high frequency pressure transducers were installed throughout the chamber and manifolds to reconstruct the system acoustic fields, while thermocouples embedded within the walls of the combustor allowed for the calculation of heat lost to the environment as a means of estimating the deviation of the experiment from an adiabatic assumption.

Validation data was acquired for a number of configurations. These configurations varied based on changes made to independent variables, such as the geometry in the form of oxidizer post or chamber length or changes to oxidizer post inlet type.

The second objective is to examine the impact of oxidizer temperature on the stability of a GCSC injector. The GCSC injector is considered to be one of the more inherently stable injector designs. It is theorized that by changing the inlet oxidizer temperature, the stability of the combustion field can be changed. This is based on an increase in energy requirement to achieve combustion with a cooler oxidizer, along with any other potential slowing of chemical kinetics that would lead to an increased time required to achieve ignition.

Two oxidizer temperatures were studied. The cooler temperature was chosen to be room temperature, while the elevated temperature of 685 K was achieved through lean combustion in a preburner. Assessment of the combustion field was conducted by varying the geometry of the oxidizer post and chamber, in particular the lengths. Based on previous work, the effective length of the post varies the resonant behavior of the system, allowing for effective tuning and de-tuning of the post.

Choice of oxidizer temperature had a clear impact on the amplitude of pressure oscillations exhibited system wide. At the hot oxidizer configuration, very low amplitude oscillations were achieved throughout the post and chamber, with few organizing structures observed either temporally and in the frequency domain of the acoustic field. The reduced oxidizer inlet temperature promoted stronger amplitudes throughout the post and chamber. These stronger amplitudes were further modulated depending on geometry. A general trend appeared that mostly agreed with previous results, suggesting a 3/8-wave resonator configuration for the post generated the strongest fluctuations. However, this was not consistent as tests with differing geometries but with the same acoustic profile of the system exhibited dissimilar amplitudes. It is postulated that specific timing is required to drive stronger oscillations. While the same acoustic mode shapes can be found in different geometries with the identical acoustic profiles, heat release events may shift timing in a way that is not accounted for with a purely acoustic approach. It is also theorized that acoustic impedance of the propellants and combustion gases drive the capability of the system to preserve acoustic energy, as higher reflection and transmission coefficients coincided with higher pressure fluctuations.

A break down of the elements of this report is provided. First, a relevant background information is presented in Chapter 2. This chapter starts with a quick primer on combustion instability. A description of the gas-centered swirl coaxial injector is then discussed, focusing on the critical aspects and parameters of the design. This is followed by summaries of trans- and supercritical effects, relevant work and instability

mechanisms. Finally, diagnostics and analysis techniques that are used in this work are presented.

The experimental approach is presented in Chapter 3. Here, a description of the chamber and its various components is provided, along with a discussion on the merits and impacts of the design parameters. The linearized Euler equations are also presented alongside their use in determining the acoustic mode shapes of the system. Next are the design and testing requirements for the initial validation data collection campaign, along with configurations and conditions where these data sets were collected. This is followed by a description of the instrumentation and facility.

The results are presented in Chapter 4. This section examines the impact that the oxidizer temperature has on the acoustic field and how it is further augmented by the geometry of the system. The findings of this work are then summarized in Chapter 5, presented along with recommendations for future work.

2. BACKGROUND

This chapter is broken down into several sections. The first section provides a brief description of combustion instability. The second section provides background on the gas-centered swirl coaxial (GCSC) injector. A description of the injector components and a break-down of the controlling geometries and physics of the injector are discussed, along with a discussion on trans- and supercritical fluids. This is followed by a description of related work. Two previous combustion stability experiments are presented and discussed in the context of the work described in this document. Following this is a description of mechanisms that initiate and sustain unstable combustion that have been identified in the discussed works. Diagnostics and instrumentation used in this work are then discussed. Finally, the various analysis techniques employed in understanding the dynamics of combustion are presented, providing background to assist in interpreting the results presented in Chapter 4.

2.1 Combustion Instability

As Culick writes, the term 'combustion instability' "is usefully descriptive but slightly misleading" [35]. He states that uncontrolled explosions or other intrinsic instabilities are not the source for what is commonly considered and defined as a combustion instability. Instead, these instabilities are due to coupling between perturbations in the acoustic or velocity fields and energy released through combustion - all of which alone can be stable processes. Of primary concern is the coupling between the release of thermal energy and fluctuations in the acoustic field. When oscillations in the two fields are in phase, coupling can take place that leads to a feedback loop promoting stronger oscillations, further strengthening the coupling. This would result in operation at off-nominal conditions. This oscillatory behavior can become periodic,

leading to a limit cycle that drives unsteady motions in a positive feedback loop that can increase thermal loading, force flame blow out, or create uncontrolled pulsations that at high amplitudes can cause hardware fatigue and degradation and even sudden catastrophic failure. Such consequences can greatly prolong engine development, requiring large amounts of both time and money to eradicate instabilities.

This work sets out to provide insight into the GCSC injector by examining the impact of oxidizer inlet temperature on the stability of the system. This work aims to build upon the legacy and knowledge gained from previous similar experiments to study this injector design in a setting more representative of ox-rich staged combustion through use of a preburner. By gaining further understanding of the dynamics and coupling between the injector and heat release modes, more accurate predictions can be made to inform future development.

2.2 Injector Description

The injector element controls the performance of a rocket engine as it essentially governs the mixing and combustion process. The mixing and subsequent combustion of propellants should maintain steady, even burning that is best distributed across a wide range of temporal and spatial scales to reduce the risk of organization and forcing. Detailed knowledge of the processes and physical mechanisms present in the injector is required to achieve efficient, stable combustion across a range of operating conditions. Often, that understanding comes from relying on sub-scale single-element experiments or simulations. In this work, a gas-centered swirl coaxial injector design is studied at two different oxidizer temperature conditions to examine its impact on combustion stability. The various components and features that drive injector dynamics are discussed here.

2.2.1 Gas-Centered Swirl Coaxial Injector

The GCSC injector has demonstrated excellent capabilities of atomizing liquid fuels to achieve high levels of performance [27, 32, 36–38], especially at conditions typical of oxidizer rich staged combustion [39]. This is made possible through a number of mechanisms that contribute to the break down of the injected liquid sheet and subsequent mixing of fuel droplets with the central gas core [40–42]. It has also been shown to have improved engine performance over shear coaxial injectors [43–45].

Impinging jets are highly susceptible to manufacturing defects, which can have a deleterious effect on the mixing trajectories of the jets, resulting in reduced efficiency. The jets are also susceptible to high frequency pressure oscillations, according to Takahashi et al. [46], which would impact feed rate and subsequently the spray and atomization properties of the injectors. Swirl injectors, which do not rely on precise placement of jets, are much less sensitive to manufacturing defects [38]. The fuel injectors are also fairly insensitive to chamber pressure pulsations by stabilization of the liquid on the wall due to the imposed swirling motion. The injector is also further insensitive to any pulsations occurring in the liquid flow due to the simultaneous atomization of liquid portions that were injected at different times and having different flow rates [30, 47–49]. The central gas flow benefits from the large injection area in the form of a reduced pressure drop, but with the cost of increased sensitivity to chamber pressure fluctuations, leading to variation in the O/F ratio [34]. However, this non-uniformity in composition is ultimately spread spatiotemporally, ultimately decreasing the effect of the variation. Thus, the GCSC injector is considered to have a linear dampening and surpressing effect on liquid flow pulsations, but also serve as a non-linear servo-stabilizer of the injection process [50].

The injector design found within the RD-170 and RD-180 is lauded for its reliability while remaining stable across a wide range of operating conditions, including the ability to throttle down to 47% of nominal thrust levels [51]. As a result, much attention has been focused on the intricate physics within this particular injector in

order to understand, replicate and improve it. A diagram of the main and baffle GCSC RD-170 injectors are shown in Figure 2.1. The main injector, featured on the left, consists of a post that feeds hot oxidizer from the preburner to the chamber, a fuel manifold that injects heated liquid fuel into a shielded annulus with a swirling motion, and an injection recess where the two propellants interact before delivery to the chamber. A bevel sits as an intermediary geometry between the injector and the chamber, allowing for the fuel film to spread and interact with adjacent elements. The baffled injector, on the right, differs in the downstream end. Instead of direct injection into a discrete mixing section, the fuel is kept in a manifold that has been extended and swirled. This section protrudes into the chamber and the fuel acts to cool the injector. The extended injector acts as a physical barrier to transverse modes. The fuel is then dumped directly into the oxidizer jet at the far end of the post.

The injector in the DVRC holds similar to the design of the main RD-170 injector. A cutaway of the injector is shown in Figure 2.2 with components labeled. An oxidizer post, marked in blue, connects the chamber to the oxidizer manifold. The fuel manifold, in red, injects the fuel tangentially into the annulus. The fuel swirls around, filling the annulus as it flows into the injector cup, highlighted in yellow. Atomization of the fuel, primarily through shearing between the fast traveling oxidizer jet and the liquid fuel, takes place within region and continues into the chamber. Unlike the RD-170, the DVRC does not have a bevel, instead having a backwards facing step that opens up into the chamber.

The oxidizer post serves as a tube that conditions the incoming oxidizer jet. At the upstream end sits an inlet that sets the pressure drop driving the flow. The inlet strives to achieve a balance to provide a small pressure drop to serve the overall pressure budget, but large enough to prevent oscillations within the post from reaching and initiating fluctuations within the manifold. The inlet will also act as an acoustic boundary condition, where depending on inlet type, and the associated the pressure drop, the inlet can behave akin to an open or closed acoustic boundary, or something

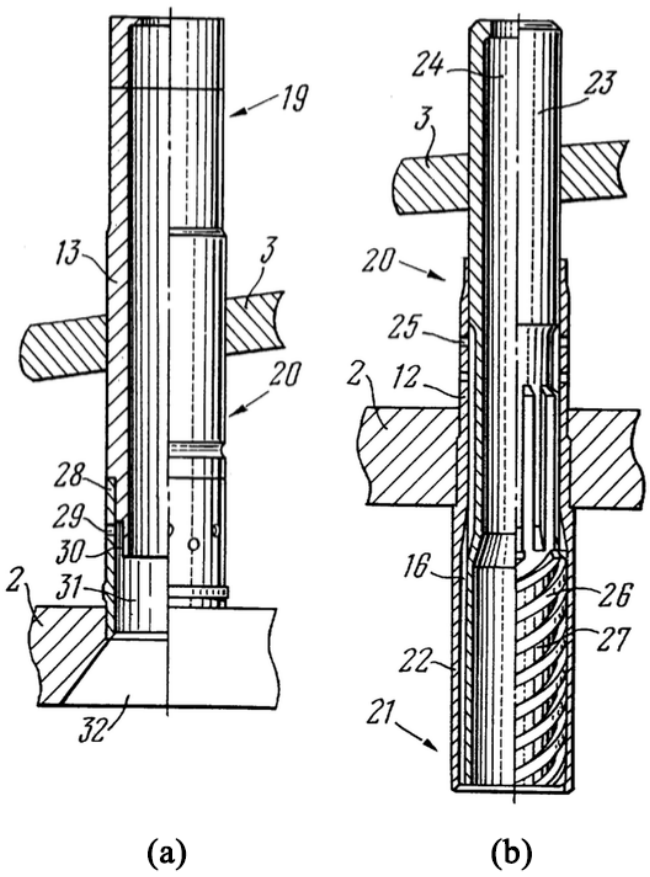

Figure 2.1.: Diagram of the (a) main and (b) baffle injectors for the RD-170. The main injector supposedly uses a baffle to promote cooling and surpasses longitudinal pressure waves while the baffle injector breaks up transverse pressure waves [26].

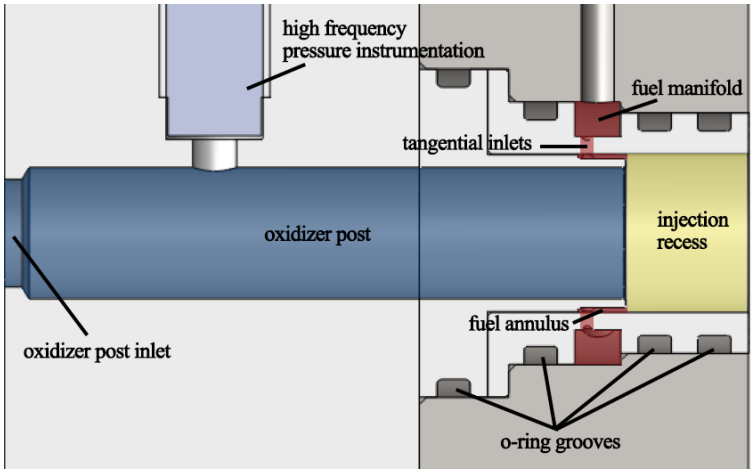

Figure 2.2.: Diagram of the DVRC GCSC injector with labeled components. Blue highlights the oxidizer post, red highlights the fuel injector, and yellow the injection recess.

in between. The post also acts as a resonator to the chamber. Depending on its length and conditions of the oxidizer flow, the post can drive or dampen acoustic fluctuations generated within the combustor.

The fuel injector comprises the fuel manifold, several tangential fuel inlets and the fuel annulus. A pressure drop across the fuel inlets drives the supply of fuel into the fuel annulus. The tangential design of the inlets provides circumferential momentum, giving the fuel within the annulus its swirl. A collar sits between the oxidizer post and the fuel annulus, shielding the fuel and giving it time to develop.

At the termination of the collar is the injection recess, where the fuel film is exposed to the oxidizer jet. Shearing and atomization of the fuel by the jet takes place, while still leaving enough fuel for cooling purposes. The volume within the recess also acts as a shelter for combustion to be initiated and sustained away from the chamber, protecting the heat release rate from chamber acoustic perturbations [52].

2.2.2 Swirler Design

An important parameter in designing a swirl injector is the geometrical characteristic constant, A. It can be thought of as an indicator of the swirl intensity of the flow [53]. This constant is a ratio of the product of the tangential velocity and normalized momentum arm, and the axial velocity. Equation (2.1) mathematically defines the ratio, further reducing it into geometric parameters [54].

$$A = \frac{(Q/n\pi R_{f,in}^2)(R_{in}/R_{sw})}{(Q/\pi R_{sw}^2)} = \frac{R_{in}R_{sw}}{nR_{f,in}^2} \tag{2.1}$$

The volumetric flow rate of the injector is represented by Q. The radius of the swirl cup is represented by R_{sw}, while the radius to the center of the fuel inlets is represented by R_{in}. The number and radius of the fuel inlets are defined as n, and $R_{f,in}$, respectively.

Figure 2.3 demonstrates the effect the geometrical constant has on the spray characteristics for a constant pressure drop. As the geometric constant increases, the spray

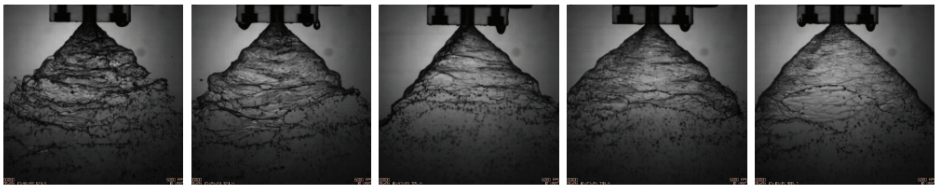

Figure 2.3.: Representative images of spray features at a pressure drop of 0.3 MPa (43.5 psi) for geometrical characteristic constants of (a) 5.8, (b) 9.6, (c) 12.3, (d) 13.5 and (e) 20 [55].

becomes smoother and more well-developed. This is expected, as an increase in A can be viewed as an increase in centripetal acceleration, which acts as a stabilizing force [39].

The geometric constant is also defined as a function of the coefficient of filling, ϕ. This coefficient is a ratio of the cross-sectional area of the flow to that of the nozzle. Calculation of ϕ from the geometric constant follows Equation (2.2).

$$A = \frac{(1-\phi)\sqrt{2}}{\phi\sqrt{\phi}} \tag{2.2}$$

Once the coefficient of filling is known, it is possible to calculate the discharge coefficient. Flow through the injector suffers from low discharge coefficients, due to the development of the gas core along the axis, reducing the effective cross-sectional flow area. The discharge coefficient can be expressed in terms of the coefficient of filling via Equation (2.3).

$$\mu = \phi\sqrt{\phi}/\sqrt{2-\phi} \tag{2.3}$$

The combination of discharge coefficient and geometric constant can then be used to determine the ratio of the inner gas core diameter to the diameter of the exit orifice, S, following Bayvel and Orzechowski [54].

$$\mu = \sqrt{1-\mu^2A^2} - S\sqrt{S^2-\mu^2A^2} - \mu^2A^2 \ln \left(\frac{1+\sqrt{1-\mu^2A^2}}{S+\sqrt{S^2-\mu^2A^2}} \right) \tag{2.4}$$

At this point, estimates of the flow area for both the inner gas core and the outer liquid film have been made. Velocities for the fluids can be calculated. The velocity of the gas core is considered to be purely axial. Any radial or tangential component is neglected. The gas velocity is then based on conservation of mass, where $\dot{m}_g$ is the mass flow rate of the gas, ρ_g is the density of the gas, and A_g the cross-sectional area of the gas flow.

$$V_{g,ax} = \frac{\dot{m}_g}{\rho_g A_g} \tag{2.5}$$

The axial and tangential velocities of the liquid are based on the total velocity of the fluid, which can be derived from Equation (2.6) using the density of the liquid, ρ_l, and the change in pressure across the fuel inlets, ΔP_l.

$$V_{l,tot} = \sqrt{\frac{2}{\rho_l}\Delta P_l} \tag{2.6}$$

Then, axial and tangential liquid velocities are derived using the already obtained geometric parameters.

$$V_{l,ax} = \sqrt{1 - \frac{4\mu^2A^2}{(1+S)^2}} \tag{2.7}$$

$$V_{l,tan} = \frac{2\mu A}{1+S} V_{l,tot} \tag{2.8}$$

In the absence of other influencing factors, the spray angle can then be defined as the inverse tangent of the ratio tangential and axial velocities, as shown in Equation (2.9).

$$\frac{\alpha}{2} = tan^{-1}\left(\frac{V_{tan}}{V_{ax}}\right) \tag{2.9}$$

The spray angle, α, is the full cone angle. Often, it is easier to use the spreading angle, $\alpha/2$, to discuss the spray of the liquid from the centerline.

2.2.3 Film Profile

The film of liquid fuel plays multiple roles in the GCSC injector. First, it acts as a coolant, preventing excess heat loads on the injector walls. Reduced hardware temperatures decreases the complexity of the engine design, allowing for thinner geometries or alternate material [56]. This can also lead to improved performance, as potentially higher chamber temperatures can be reached. Second, it is a driver in the atomization and mixing process as it interacts with the central high-velocity gaseous oxidizer core. Generally, a thinner film better promotes atomization. Conversely, complete or even near-complete burning of the film exposes the recess to the full brunt of the combustion, jeopardizing the hardware. An ideal GCSC injector promotes steady, uniform atomization of the liquid fuel, while preserving enough to achieve proper cooling.

As was made evident in the previous subsection, the film is highly dependent on the geometric parameters of the injector. Changes in the film, such as velocity profile or thickness, will augment the mixing process. For example, Lefebvre [57] writes that the Sauter mean diameter (SMD) is proportional to film thickness. An increase in swirl number would lead to a thinner film and therefore smaller, finer droplets.

Rizk and Lefebvre [58] used experimental data to derive an empirical formula for calculating film thickness based on geometry, properties of the fuel and the pressure drop,

$$h = 3.66\sqrt[4]{2r_p\dot{m}_l\mu_l/\rho_w\Delta P}, \tag{2.10}$$

where r_p is the radius of the swirl chamber, $\dot{m}_l$ the mass flow rate, μ_l and ρ_w the viscosity and density of the liquid, respectively, and ΔP the pressure drop across the injector.

Suyari and Lefebvre update the correlation based on measurements made using the conductance method [59], as shown in Equation (2.12).

$$h = 2.7\sqrt[4]{2r_p\dot{m}_l\mu_l/\rho_w\Delta P} \tag{2.11}$$

Recent work has begun using a similar correlation proposed by Fu et al. [31], also relying on the same parameters but with a different scaling factor,

$$h = 3.1\sqrt[4]{2r_p\dot{m}_l\mu_l/\rho_w\Delta P} \tag{2.12}$$

Since its proposal, much work conducted on open-end swirl injectors have opted to use this method of estimating film thickness [24, 60–62].

The influence of chamber backpressure on film thickness was the focus of work conducted by Kenny et al. [63]. Chamber backpressure was varied between atmospheric conditions and 4.81 MPa for a fixed mass flow rate of 0.09 kg/s. Average film thickness increased alongside chamber pressure. The increase in film thickness led to higher discharge coefficients and lower spray angles. It was also noted that while the average film thickness increased with chamber backpressure, the thickness at the exit of the injection recess nearly converged at all pressures to a single value close to what was predicted by Bazarov [64].

Fu et al. [31] studied the effect of unsteady pressure profiles on film thickness. A pulsing flow generator upstream of an injector was used to provided a controlled means of driving unsteady behavior. As demonstrated in Figure 2.4, at low frequencies, such as 20 Hz and 100 Hz, both the pressure fluctuations and film thickness share similar modulations, albeit with some phase shift dependent on the frequency. At higher frequencies, the film thickness continues to vary, but the trends begin to diverge. This is due to the fact that the liquid film cannot respond fast enough to more frequent oscillations. By the time the film starts to respond to a given perturbation, it has already begun to recede. This is most evident in Figure 2.4d, where although the film thickness continues to modulate, it is unable to do so as consistently as it has at lower frequencies.

Generally, the properties of the film, such as thickness and distribution of velocity across the axial and tangential components, are driven by the injector geometry and

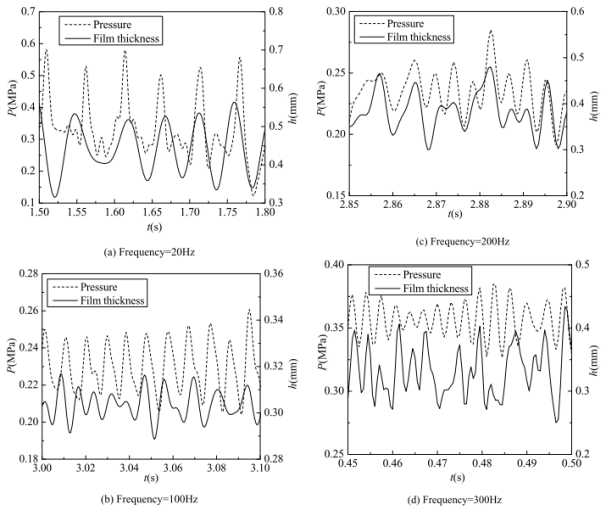

Figure 2.4.: The effect of unsteady pressure oscillations on the film thickness for forcing frequencies of (a) 20 Hz, (b) 100 Hz, (c) 200 Hz, and (d) 300 Hz [31].

inlet conditions. Atomization and mixing are then a function of characteristic injector parameters, such as the momentum flux ratio.

2.2.4 Atomization

While mixing and atomization considers a multitude of physics and interactions, it is predicated on two well-understood cornerstones: geometry and thermophysical properties of the fluids [57]. In the context of liquid rocket engines, the term atomization refers to the physical mechanisms that break down a continuous liquid stream and produces droplets fit for mixing and combustion. However, while the involved mechanisms eventually produce droplets, they are often preceded by disturbances in the liquid film which are an equally important part of the process. Summaries of various disturbance breakdown can be found in Reference [65]. Three mechanisms considered to be dominant in GCSC injectors will be described here: liquid turbulence, wave stripping, and gas-phase vortex shearing. These three mechanisms have been observed independently, and operate at different temporal and spatial scales. There is no indication they are exclusive, however, and it is expected that multiple mechanisms can be at play at a given time [41]. The liquid turbulence and wave stripping mechanisms have long been documented [66–68], while the gas-phase vortex mechanism has only recently been identified [42].

Injection at high Reynolds numbers creates turbulent eddies as the liquid interacts with the wall. The eddies roughen the liquid surface, producing ligaments then subsequently forming droplets via Plateau-Rayleigh breakup. The mechanism was observed in both planar [68] and annular jets [49] into a quiscent environment. Dia et al. [68] provided several non-dimensional parameters that can be used to estimate length to atomization onset.

In the absence of dominating aerodynamic forces, the instability of the liquid surface becomes dependent on flow turbulence, assuming the film satisfies the criteria to allow for turbulent boundary layer growth. As aerodynamic forces come into play,

Figure 2.5.: Time steps from axisymmetric simulation showing effects of liquid turbulence mechanism. Turbulent eddies roughen the film, creating undulations that eventually grow large enough to break into droplets [41].

the environment becomes more resistive. Fewer ligaments are formed, with fewer droplets breaking off those ligaments.

Azimuthal pulsations in the liquid film are expected to occur, caused by pulsations in the tangential inlets. A consequence of the film thickness being on the same order as the diameter of the holes [64].

Work performed by Sarpkaya and Merrill [66] also demonstrated the inherent relationship of ligament and droplet production on the wall surface condition.

Application of aerodynamic forces to the liquid film prompts hydrodynamic instabilities. Instabilities due to differences in physical properties, such as Rayleigh-Taylor or Kelvin-Helmholtz, deform the gas/liquid interface. The resulting waves along the interface can isolate pockets of the liquid. Work conducted by Woodmansee and Hanratty [67] investigated the process of parallel air flow amplifying these waves and separating the mass at the peak. They determined a critical Weber number, for a given film thickness, that prompted onset of atomization, as well as governing parameters of the process. Figure 2.6 provides an example of wave stripping in action from an axisymmetric simulation.

The third and final atomization mechanism described here considers the space behind the backwards facing step, such as the region behind the collar in the GCSC injector. In this case, a vortex is shed from the high velocity oxidizer and falls behind

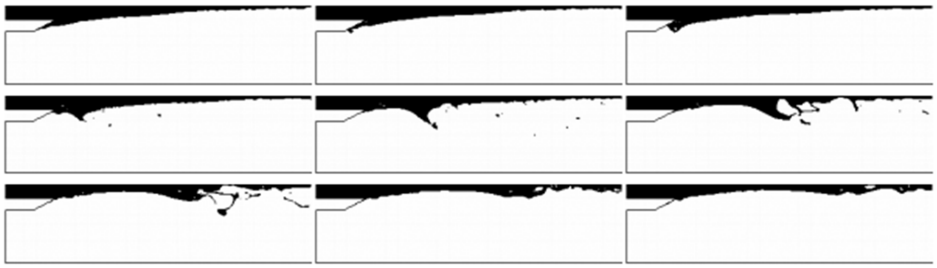

Figure 2.6.: Time steps from axisymmetric simulation showing effects of wave stripping mechanism. Differences in physical properties at the gas-liquid interface generate waves that can ultimately be stripped by the aerodynamic stresses imposed by the oxidizer jet [41].

Figure 2.7.: Time steps from axisymmetric simulation showing effects of proposed vortex shearing mechanism. A gas-phase vortex behind the collar shears the liquid film, pulling a portion of it into the oxidizer jet and separating it [41].

the collar. As the liquid passes by this rotating vortex, it experiences shearing and tearing. This leads to a distorted film appearance. It is not until the vortex pushes some of the film past the collar where it protrudes directly into the oxidizer does the liquid break into droples. Figure 2.7 demonstrates this phenomenon in action. The first step in this sequence follows a gas vortex that moves behind the collar. The vortex approaches the liquid film, shearing it and pushing it back up against the collar. The kicked-up sliver of film is then caught up in the expanding oxidizer jet, where aerodynamic forces break it apart. This mechanism requires a sufficiently high kinetic energy ratio (or momentum flux ratio), lest the vortex be displaced by the liquid fuel.

The discussed atomization mechanisms are believed to be controlled predominantly by the Reynolds numbers of the two fluids, Weber number, and also the momentum flux ratio. It is believed that liquid turbulence first occurs when there is minimal aerodynamic forces. This is replaced or augmented by wave stripping as the velocity of the oxidizer jet increases. Increasing the aerodynamic forces further transitions the atomization process into gas-phase structure dominance.

2.2.5 Spray Angle

The spray angle of the propellant at the dump plane is a qualitative measure of mixedness of the propellants.

In the absence of the central oxidizer jet, the spray angle would simply be a ratio of the tangential and axial velocities, *a la* Equation (2.9). In this case, spray angle in only a function of tangential to axial momentum, a product of geometry and fuel mass flow rate.

With the inclusion of the oxidizer jet, the spray angle is influenced by momentum transfer at the gas-phase liquid interface and the pressure differentials in the space between jet and liquid stream. The former is a product of the recess ratio, while the momentum flux ratio controls the latter. For this reason, the recess and momentum flux ratios are considered to be key parameters in defining the mixing and spray characteristics of a GCSC injector, with further implications both ignition and steady-state operation, and chamber wall heat load [32, 69]. These two parameters are discussed further below.

2.2.6 Recess Ratio

The recess ratio is defined as the ratio between the length of the injection recess and the diameter of the oxidizer post before entering the recess. Following the nomenclature of Figure 2.3, it can be defined as shown in Equation (2.13).

$$RR = \frac{L_{sw}}{2R_{sw}} \tag{2.13}$$

As the injection recess serves as a primary location for mixing, it follows that a longer recess would lead to increased exposure time between the oxidizer jet and the liquid fuel, and therefore enhanced mixing. However, this also serves to reduce the spray angle, limiting the distribution of fuel in the chamber. The optimal injector must then balance these two factors.

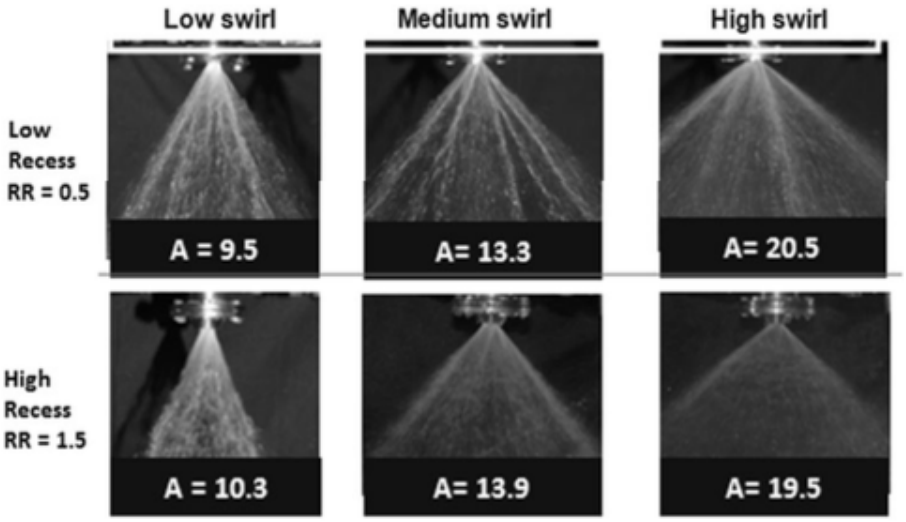

Figure 2.8.: Dependency of recess ratio on spray quality at various injector swirl numbers. Increasing recess ratio leads to the removal of streaks in the spray. No central gas jet is present [62].

Spray uniformity increases with longer recess ratio [62]. Figure 2.8 compares the effect of recess ratio on the spray profile for two recess ratios, 0.5 and 1.5, at low, medium and high swirl constants. Streaks are evident for all swirl levels at the shorter recess ratio, and vanish at the longer ratio.

Without the presence of the recess, minimal mixing occurs, having detrimental effects on the mixing efficiency and flame stability, as noted by Mayer et al. [70] in shear coaxial LOX/GH2 injector.

There is also a connection between combustion performance and recess ratio, specifically concerning the ratio between film residence time and break-up time of the fuel film. Strakey et al. [71] reworked a correlation first proposed by Mayer [72] to optimize the film residence time, shown in Equation (2.14).

$$\frac{t_r}{t_b} = \frac{C_1 L}{\tau_f} \left[\frac{A_l^3}{A_g^4} \frac{\mu_l \rho_l}{\sigma_l} \frac{1}{\rho_l^2} \frac{\dot{m}_g^4}{\dot{m}_l^3} \right]^{1/3} \tag{2.14}$$

Here, t_r and t_b are the residence and break-up times, respectively. C_1 is an arbitrary constant designed to set $t_r/t_b = 1$ when c* efficiency is 100%. L is the length of

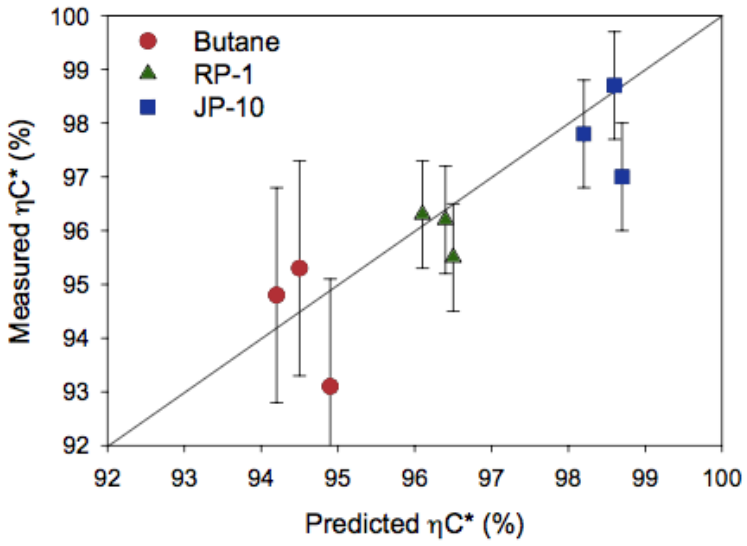

Figure 2.9.: Prediction of c* efficiency for butane, RP-1 and JP-10 versus measured c* efficiency [71].

the injection recess, τ_f the thickness of the film, μ_l the liquid viscosity, σ_l the liquid surface tension, and ρ_g and ρ_l the densities of the gas and liquid, respectively.

The hypothesis behind this correlation is that maximum efficiency is achieved when the residence time of the fuel is equal to or greater than the break-up time. Decreasing residence time such that the left hand side of Equation (2.14) falls below unity leads to decreased c* performance.

The correlation was tested for a trio of fuels: butane, RP-1 and JP-10. Based on the fluid properties (viscosity, density, surface tension), and fixed geometry and inlet conditions, c* efficiency predictions were calculated. Predictions for these propellants, and the measured efficiencies are shown in Figure 2.9.

As mentioned previously, a larger recess reduces spray angle as increased mixing time further lowers tangential momentum. In a study of both recess and momentum flux ratio effects, Kim et al. [69] provides visual evidence in the form of backlit images of the reduction of spray angle in a cold flow test of a GCSC injector.

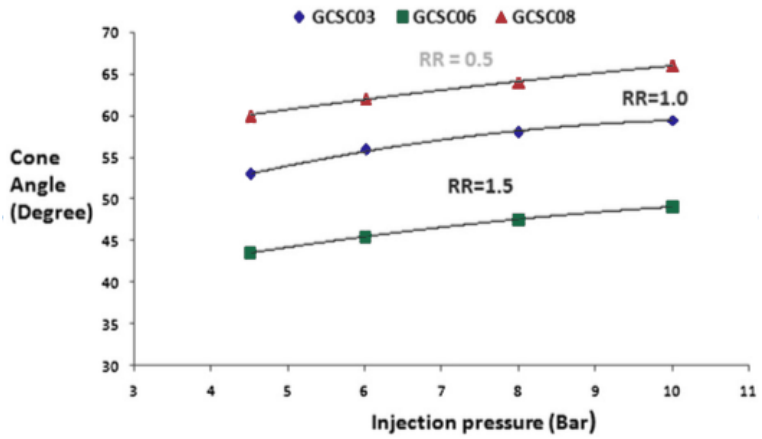

Figure 2.10.: Dependency of spray angle on recess ratio for a range of injection pressures [62].

The reduction in spray angle with an increase in recess ratio was also shown by Anand et al. [62]. Recess ratio, along with injection pressure, were varied for a given injector and resulting spray angle was measured. Results are shown in Figure 2.10. Spray angle increased slightly with raised injection pressure, but dropped drastically as the recess ratio grew. The empirical correlation they derived, shown in Equation (2.15), relates the half spray angle to the geometrical constant, A, and the recess ratio, RR. This correlation is consistent with correlations reported elsewhere in literature [31, 32, 42, 57]. Influence of the central oxidizer jet, and resulting interaction, is not considered in this correlation.

$$tan(\alpha/2) = 0.01A^{1.64}RR^{-0.242} \tag{2.15}$$

Given more time to mix, injectors with longer recess ratios tend to produce finer droplets. Radial profiles of the Sauter Mean Diameter (SMD) were obtained for a variety of recess ratios [32]. At lower ratios, inner most region of the liquid-dominant zone produced droplets 40% larger than at higher recess ratios, an indication of more effective atomization.

Park et al. [60] observed that measured film thickness decreased as a function of recess ratio. This was more significant at low Reynolds numbers. Sarpkaya and Merrill [66] showed that increased loss of momentum to the wall increased the film thickness, and this effect increased as the surface of the wall become rougher.

2.2.7 Momentum Flux Ratio

The momentum flux ratio is a simple ratio between the momentum of the central oxidizer jet and the outer liquid fuel. Wrapped up in this parameter is a measure of aerodynamic force applied onto the fuel by the oxidizer. At low values, the liquid fuel is more resistive to the gas jet, resulting in a wider spray angle. At high values, the oxidizer overpowers the liquid fuel and better strips the film, resulting in smaller droplets and better atomization.

There have been conflicting definitions for momentum flux ratio in GCSC injectors found in the literature, differing in the inclusion of the tangential component of the fuel. Recent work from AFRL suggests that the total velocity of the fuel provides the best fit in defining the relationship between momentum flux ratio and normalized liquid film thickness [39]. In a number of injectors studied, variables such as number of fuel inlets, swirl levels, geometry and flow conditions. Average liquid film thickness, normalized by initial film thickness, collapsed to a single fit for the tested variations of each injector. However, the range of ratios tested in this work greatly exceed the typical range of momentum flux ratios commonly used in industry.

Most typically, it is the axial velocities used to define the momentum flux ratio. The reasons for relying solely on axial velocity, and not a combination of tangential and axial velocities, are rarely provided. However, Jeon et al. [24] do provide one explanation, in that an empirical relationship between the ratio of breakup length and thickness of the liquid and momentum flux ratio implies that it is the axial energy that competes with the central gas jet during the atomization process. It is also likely that the reliance on axial velocity is due to ease of calculating and accurate

value for axial velocity for the liquid fuel based solely on continuity, compared to deriving an estimate of the tangential velocity imparted by the swirl while taking into account the equations discussed in earlier in Section 2.2.2.

For this work, the axial velocity of the fuel will be used when discussing the momentum flux ratio due to its prevalence in literature and to allow for comparison to published work.

As touched upon earlier, the central oxidizer jet will interact with the liquid film, altering the spray angle. The deviation of spray angle due to the high velocity gas has been studied, with empirical fits for the spray contraction determined.

Im et al. [32] revealed that two regimes exist in the relationship between momentum flux ratio and spray angle in GCSC injectors. At low ratios, an increase in momentum flux ratio led to a decrease in spray angle for a variety of liquid Reynolds numbers and recess ratios. At some critical value the trend reversed, where increasing the ratio beyond a certain value led to a widening of the spray. Where one regime ended and transitioned to the other appeared to be dependent on recess ratio, and independent of liquid Reynolds number. The correlations for spray angle contraction are shown in Equations (2.16) and (2.17) for the low and high momentum flux ratio range, respectively.

$$\alpha/\alpha_0 = 0.61 Re^{0.08} e^{-0.0657J} \tag{2.16}$$

$$\alpha/\alpha_0 = 0.33 Re^{0.08} e^{0.02518J} RR^{0.33} \tag{2.17}$$

The results are non-dimensionalized by dividing by the spray angle in the absence of the central oxidizer jet. The former equation has a weak dependency on liquid Reynolds number and a stronger, although inverse dependency on momentum flux ratio. The latter equation has the same dependency on liquid Reynolds number, and a positive dependency on momentum flux ratio, along with a moderate dependency on recess ratio added.

The authors suggest that two physical processes sensitive to momentum flux ratio are present. At lower momentum flux ratios, the space between the liquid fuel sheet

and the oxidizer jet becomes entrained into the jet, resulting in a lower pressure in the space. The higher pressure outside the fuel then pushes the spray inwards. Beyond a certain point, the increased momentum of the oxidizer jet leads to an increase in the interspace. A possible explanation for this is that the momentum flux ratio is typically raised through an increase in the gaseous mass flow rate, which would cause a higher interspace pressure, redirecting the spray outwards.

Kim et al. [69] also studied the relationship between momentum flux ratio and spray angle contraction at four different recess ratios. Here, the spray angle contraction was reduced to a single parameter, ξ, defined in Equation (2.18).

$$\xi = \frac{\alpha_{nogas} - \alpha_{gas}}{\alpha_{nogas}} \tag{2.18}$$

The α variable refers to the full spray angle, with the subscript denoting whether the spray angle represents liquid only flow ("no gas"), or liquid and central gas jet ("gas"). Similar trends were captured at the four different recess ratios. In each case, increasing momentum flux ratio directly led to an increase in ξ until it reached an asymptote at around $\xi = 0.9$. The value at which the spray angle no longer changes (or reverses trends, according to Reference [62]) is defined as the critical momentum flux ratio. This ratio is often considered to be the value at which optimum mixing occurs. The authors of Reference [62] suggest that operating at or above the critical momentum flux ratio carries with it good gas-liquid interaction and increased combustion efficiency and stability. The critical ratio tends to decrease with recess ratio. The findings of Park et al. [60] agree with this trend, with larger recess ratios more strongly influenced by momentum flux ratio.

Anand et al. [62] studied a selection of 11 injectors, investigating effect of momentum flux ratio, swirl level (through the geometrical constant), and recess ratio. Like References [31, 32, 69], spray angle was also found to decrease with increased momentum flux ratio until the critical value is reached. This critical value is also subject to the swirl number, where higher swirl number injectors had lower critical ratios.

Likewise, generally increasing the recess ratio also lowered the critical momentum flux ratio, similar to Reference [69].

The authors of Reference [62] further explored the effect of momentum flux ratio on SMD at atmospheric pressures. For all injectors tested, increasing momentum flux ratio led to an increase in percentage of smaller particle diameters. Recorded momentum flux ratios where SMD is 90 microns or less were slightly higher than critical values determined by spray angle for the same injector. Injectors with swirl numbers below 10 required momentum flux ratios above 5 to achieve proper atomization. This number drops the suggested ratio for good atomization down to 3.5 At high swirl numbers, such as $A > 19$, good atomization does occur, with the production of very fine droplets near the core of the jet at critical ratios between 2.5 and 3. At the outer periphery, the atomization becomes quite poor and subject to unstable mixing and combustion. Based on the results of their study, the authors advise to avoid too low or too high of a swirl number. In the case of the former, the fuel film thickness becomes larger, inherently leading to droplets with larger SMD and poorer atomization. In the latter, discharge coefficients become very low, and the region in which high atomization occurs shrinks. An injector with a swirl number between 13 and 15 is thought to find the right balance between flow capability and atomization.

2.2.8 Collar

The collar is a small piece of hardware that can have a major impact in the injection process. First, it serves as a means of redirecting the injected fuel, providing the axial momentum driving the liquid forward, Second, it shelters the fuel within the annulus as it develops. During this time, the fuel, which was injected at discrete locations, begins to spread out circumferentially. Third, the termination of the collar at the start of the injection recess forms a recirculation zone. The central gas expands into the shadow of the collar, stripping some of the fuel and entraining it in the

recirculation. Having a stationary, pre-mixed zone allows for the flame to anchor itself behind the collar.

Flame is stabilized by recirculation flow downstream of LOX post for shear coaxial injector with cryogenic propellants [73, 74]. It has been shown that the recirculating flow provides an energy pool to ignite the incoming propellants [75, 76].

Singla et al. [77] studied high pressure cryogenic flames with LOx and both gaseous hydrogen and methane. Flame boundary was visualized through planar laser induced fluorescence of OH. It was shown that the flame was stabilized behind the injector lip for both fuels. The anchor point was found to be closer to the lip for the hydrogen case compared to the methane. Also, variation of the anchor location was higher in the methane case. This was attributed to a dimensionless parameter which is the ratio of the lip thickness to flame edge thickness, $\Phi = h_s/\delta_f$. Flame stabilization is expected when the flame edge is thinner than the lip, or when Φ is equal or greater than unity. This was the case with the hydrogen. The methane case produced a value of Φ less than one, resulting in a flame edge thickness that protruded out of the shielded region provided by the lip, making it more sensitive to the high speed methane stream. Nevertheless, the flame remains anchored, resulting in global stabilization but the shear layer is subject to pressure fluctuations. The flame is considered anchored, and stabilization achieved, when the anchoring distance is on the order of the lip thickness, or $O(h_s/L_c)$ 1, where h_s is the lip thickness and L_c the anchoring distance.

This follows similar work by Nicoli et al. [78] which showed that an increase in lip thickness favored flame stabilization. They found the lip thickness to have a stronger effect on the flame stability compared to the velocity of the gas jet in a coaxial injector. While this work considered a gas/gas injector, the role of the lip thickness in stabilizing the flame in a liquid/gas injector was demonstrated by Juniper and Candel [79].

Yang et al. [80] investigated cryogenic combustion to discern whether shear coaxial injector design methods with gaseous hydrogen were scaleable to gaseous methane. The two propellant combinations exhibited different behaviors when operated across

the same range of momentum flux ratios and Weber numbers. Their work described the extreme propensity for LOX/H2 flames to anchor to the injector rim across the operating range. The LOX/CH4 flame was easily lifted in the vicinity of the conditions tested. While the difference in fuel lead to altered mixing and atomization levels, the slower chemical kinetics of the methane compared to the hydrogen are considered the driving factor in lifting the flame.

In the study of a LOX/LH2 engine, Nunome et al. [81] observed transitions between stable and unstable behavior they attributed to flame anchoring. During experimental testing of a single coaxial injector, moderately sized pressure amplitudes were observed for the first half of the test. Near the halfway point, the oscillations disappeared and the combustion became stable. High-frequency pressure measurements also show a sharp decrease in frequency content at the same time. The authors believe that the at start up, the flame is lifted away from the oxidizer post lip. When the combustion becomes stable, they reason, the flame has anchored itself to the lip and remains fixed.

Kang et al. [82] used Large Eddy Simulation (LES) in conjunction with a flamelet progress variable method to study the mixing layer of a kerosene surrogate, JP-10, and heated oxidizer. The mechanism of flame anchoring found in this study is shown in Figure 2.11. Four instantaneous snapshots are shown, each corresponding to a different part of the mechanism cycle. First, a vortex on the oxygen side provides fresh oxidizer to flame kernel. Simultaneously, a portion of the incoming fuel stream is separated by a small clockwise vortex which is directed towards the kernel. At the next time step, in Figure 2.11b, the kernel has moved downstream. Fuel continues to be supplied by a small vortex. By Figure 2.11c, a new vortex is created on the oxidizer side. The fuel side vortex has moved downstream and the kernel is no longer receiving a constant stream of fuel. Instead it begins to pool in a small region. In the last time step, the original kernel is extinguished, but gives rise to a newly generated flame on the oxidizer side, which restarts the cycle. Meanwhile, the pooled fuel continues to translate downstream and ignites.

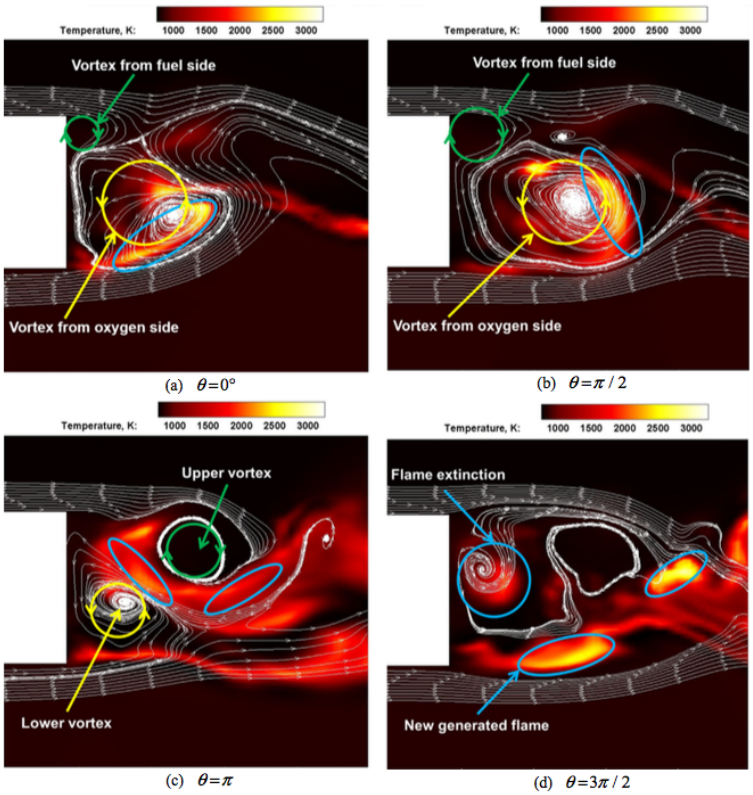

Figure 2.11.: Instantaneous snapshots from a cycle of the flame anchoring mechanism in a kerosene/GOX injector [82].

The collar can also be a source of oscillations in the distribution of propellants. Canino et al. [25] simulated gas flow over a splitter plate and determined that shedding due to the collar step could create vortices that can impinge on the chamber walls, presenting a possible mechanism for unsteady heat release and combustion instability. These vortices were also identified in work performed by Bedard [83] in a configuration similar to that of the DVRC. In a configuration where the injectors opens into the chamber with a bevel, a high frequency mode attributed to this behavior was identified and appeared to propagate downstream while weakening and reducing in frequency. It was postulated that this was due to vortex pairing and breakup. This behavior was not observed in a flat-faced configuration, tying it to a hydrodynamic event.

2.3 Transcritical and Supercritical Effects

Liquid rocket engines can easily operate at conditions where propellants are either injected at or into supercritical conditions. At these elevated temperatures and pressures, thermophysical properties are easily affected by small changes in operating conditions, greatly altering diffusivity, mixing, atomization and even chemical kinetics, all of which have a profound connection to the overall stability of the combustion dynamics.

The critical points of various working fluids are presented in Table 2.1. Many of the gaseous fuels, such as hydrogen and methane, have critical temperatures well below atmospheric conditions. The alkane group exhibits an increase in critical temperature but a decrease in critical pressure as the number of atoms increases, starting with the critical pressure and temperature of methane (CH4) 4.60 MPa and 190 K, respectively, while for dodecane (C12H26) the critical values are 1.80 MPa and 658 K.

An illustration of the effects of trans- and supercriticality on density, specific heat, viscosity and thermal conductivity of aviation kerosene are presented in Figure 2.12 [86]. Discontinuities can be found in density, viscosity and thermal conductivity within the transcritical region, where small changes to a single thermophysical

Table 2.1.: Critical properties of various propellants and simulants [84, 85].

	N2	He	O2	H2	CH4	C12H26	RP-1
Critical Pressure [MPa]	3.40	0.23	5.04	1.28	4.60	1.80	2.17
Critical Temperature [K]	126	5	154	32	190	658	662

property can have large swings in others. At the right conditions, this could lead to two-phase flow where the thermophysical properties of the fluid can change by an order of magnitude across a very small distance. Beyond the critical point, the gradient of the properties becomes much more smooth where the fluid is considered to exhibit both liquid- and gas-like behavior.

A substantial amount of work on transcritical and supercritical effects has been published Chehroudi [87], covering a variety of fluids and injector types. His investigations examine easily modelable fluids such as gaseous and liquid nitrogen and liquid oxygen into supercritical conditions in non-reactive flows. Parameters such as jet spreading angle, core length, and break up were studied for single, coaxial and impinging injectors, as well as the effect of momentum flux and velocity ratios in coaxial injectors. The effects of acoustic excitation were also discussed, with the theory put forward that the interactive surface area between a supercritical fluid and an adjacent fluid is reduced, leading to reduced intrinsic sensitivity of the injector as well as promoting mixing. Davis and Chehroudi [88] examined the behavior of an LN2 jet shrouded within a coaxial GN2 jet, with the LN2 jet injected at sub-, near-, and supercritical conditions. The effects of acoustic forcing on the jets were compared. The results are shown in Figure 2.13. At subcritical conditions, the liquid nitrogen jet extends deep into the chamber. When a transverse acoustic wave is directed into flowfield, the jet quickly changes shape with the dark liquid core being sharply reduced in length. As the pressure is brought near to the critical point of nitrogen, the dark core length has been greatly reduced and the jet takes on a fuzzy appearance consistent with the diffusive properties of a supercritical fluid. Forcing effects are still

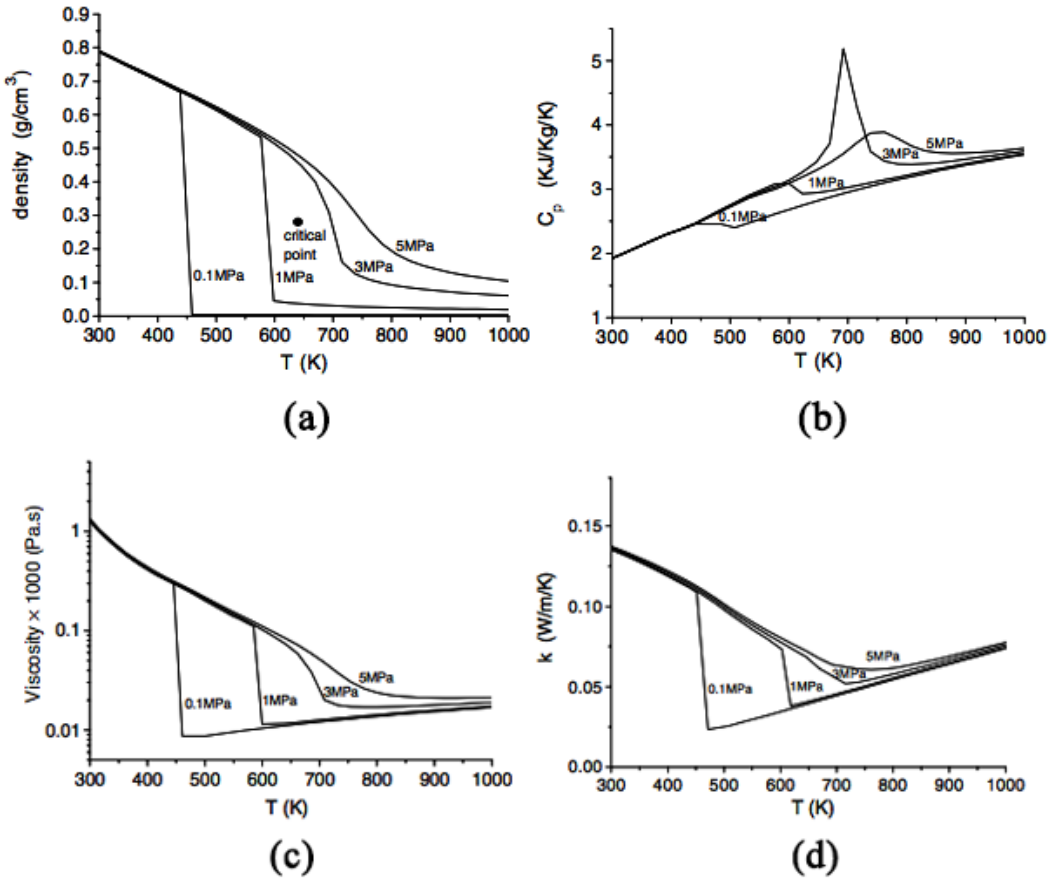

Figure 2.12.: The effects of transcriticality and supercriticality on (a) density, (b) specific heat, (c) viscosity, and (d) thermal conductivity of aviation kerosene for several isobars [86].

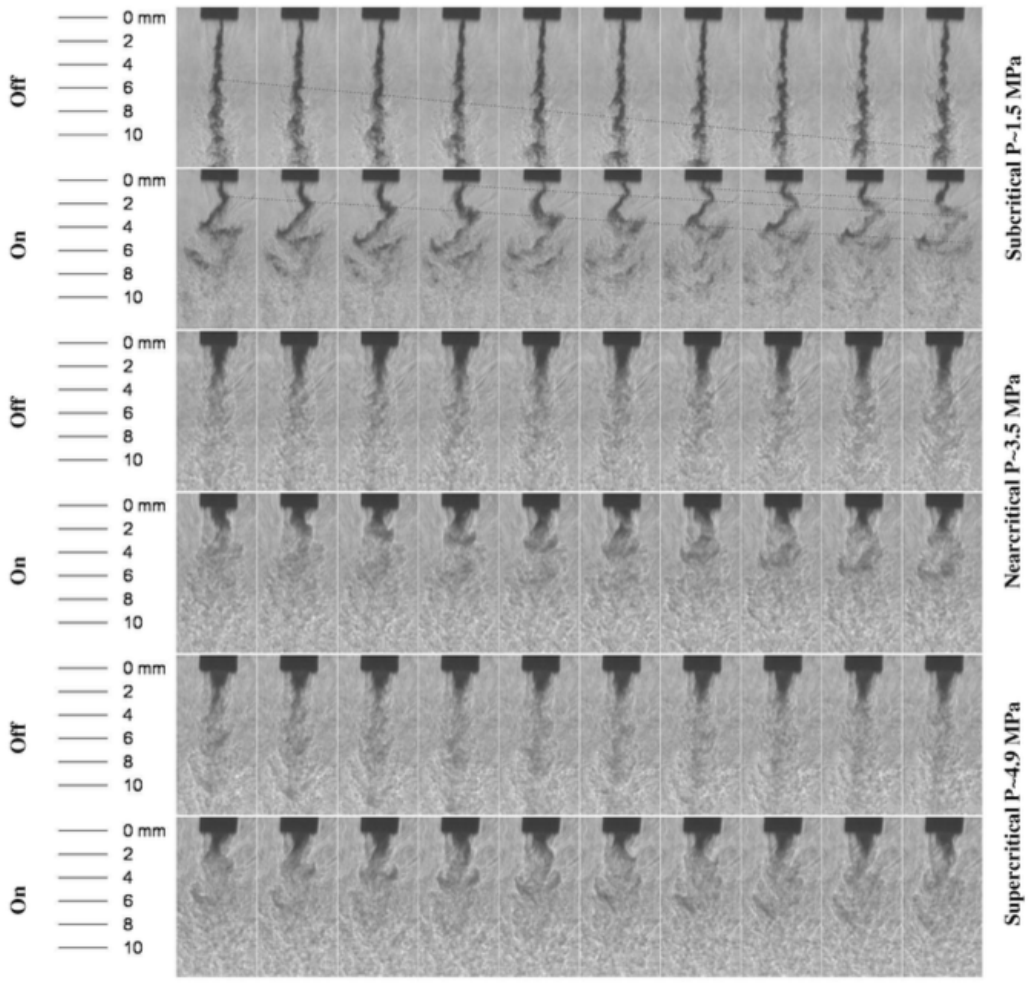

Figure 2.13.: Acoustic forcing effects on a sub-, near-, and supercritical nitrogen jet. Effects of acoustic forcing are most pronounced for at subcritical conditions, weakening as reduced pressure increases [88].

visible when an external modulator is engaged. There are few changes between the near- and supercritical conditions. The dark core length has been reduced yet further, and weak sinusoidal modulation appears when external forcing is applied. In the context of combustion instability, the authors hypothesize that the reduced variations observed in the dark core length in the near- and supercritical cases compared to the subcritical case could weaken a key feedback mechanism in self-excited combustion instability.

Locke et al. [89] conducted tests of reacting hot fires and cold flows at both sub- and supercritical conditions. In the hot fire tests, liquid oxygen was injected into gaseous hydrogen, while the non-reacting tests injected liquid oxygen into gaseous oxygen. High speed imaging using shadowgraphy was collected to visualize supercritical injection parameters such as core length and break up in both hot fire and cold flow cases, demonstrating that the classical atomization and break up model is not adequate for supercritical fluids.

Across the studies reviewed, all of them focused on a singular or central jet that was injected at or into supercritical conditions. In coaxial injectors, this results in a denser fluid core within a gaseous sheath. The effective length and spread angle of this denser core was a primary indicator for the effective mixing rate and level of injector sensitivity. However, measurements of these parameters, along with their interpretations, would drastically change for an injector where the supercritical fluid is the outer propellant, such as kerosene in the RD-170.

Aviation kerosene has been studied at supercritical conditions, both numerically and experimentally, and the thermophysical properties are published. However there is limited published work on the effects of supercritical kerosene, primarily RP-2, in reactive flows. Kim et al. [90] performed cold flows and hot fires of liquid oxygen and kerosene in a bi-swirl coaxial injector at transcritical injection conditions for the fuel. They found the oxidizer post recess length had a significant impact on mixing, indicated by distributions from a mechanical patternator for cold flows and an increase in chamber pressure and characteristic velocity in hot fire tests.

Recent work by Wang [91] studied a bi-swirl liquid oxygen/kerosene injector at supercritical pressures and subcritical temperatures through large-eddy simulation combined with a unified treatment of real-fluid thermodynamics. They found the flame to be stabilized by the counter-rotating vortex injection design. The flame became relatively unstable once the flame thickness became larger than the liquid oxygen post thickness.

There is a lack of both knowledge and understanding of how kerosene in the transcritical and supercritical states impacts combustion stability, in terms of injector hydrodynamics as well as acoustically. The work presented in this document provides benchmark data of transcritical kerosene in a GCSC injector at a variety of configurations for use in the validation of computational models.

2.4 Related Work

A review of relevant work is provided here. Experiments similar to the DVRC are first discussed. These experiments examined the effect of geometry on behavior of confined high-pressure combustion. In particular, the oxidizer post can behave as a resonator for chamber, such that particular combinations of lengths can drive or dampen unstable behavior. Background on these two experiments is provided, detailing operating conditions, configurations and results.

2.4.1 Uni-Element Combustor

Previous research into combustion stability at Purdue University focused on a single element experiment with variable chamber length. This combustor, referred to in this document as the Uni-Element Combustor (UEC), exhibited discriminating behavior based on the length of the chamber. This effort spawned further research into combustion instability at Purdue, including the new research presented in this document.

The theory driving the UEC was rooted in the coupling of acoustic pressure modes and heat release. Considering the oxidizer post a resonator for the chamber, the geometry of the post could be tuned to promote acoustic reflections that raise the local pressure in time with a heat release event. Likewise, de-tuning the post desynchronizes the timing between local pressure and heat release oscillations. This dependency on the phase relationship follows Rayleigh's Criterion, which states that in-phase

fluctuations in acoustic and heat release modes will drive instabilities, while out-of-phase fluctuations will instead dampen any instabilities.

With this framework in mind, the UEC was designed to promote unstable combustion through geometrical means by maximizing constructive interference of pressure waves in the chamber along with their reflections in the oxidizer post [92]. First order acoustic analysis was used to determine frequencies for a given geometries, based on an assumption of a homogeneous mixture distributed through the oxidizer post or chamber. By matching (or avoiding matching) the frequencies in the chamber and the oxidizer post, it was presumed that the system was primed to go unstable (or remain stable).

Experiment Description

The Uni-Element Combustor studied a single injector in a simulated oxidizer rich staged combustion cycle. A diagram of the test article is shown in Figure 2.14. A photograph of the installed test article at a chamber length of 88.9 cm in shown in Figure 2.15. A catalyst bed decomposed 90% hydrogen peroxide (by weight), which then entered an oxidizer manifold. The oxidizer was introduced radially to the midpoint of the post through ten inlet holes. The injection point was chosen because the midpoint sits at a pressure node for the odd numbered acoustic modes. The full length of the oxidizer post was 17.1 cm, with a diameter of 2.1 cm. Liquid JP-8 was injected into the fuel annulus from the fuel manifold through either four or eight tangential holes, depending on the fuel injector used. Mixing then begins in the swirl cup, where the fuel is first exposed to the oxidizer jet. A backwards facing step opened into the combustor chamber, which had a diameter of 4.7 cm. The chamber comprised several section to allow for discrete changes to the overall chamber length. Several chamber lengths were possible: 25.4, 38.1, 50.8, 63.5 and 88.9 cm. The first chamber section is made of copper to serve as a thermal heat sink, pulling heat away from the high frequency instrumentation installed at the head end. This also has the

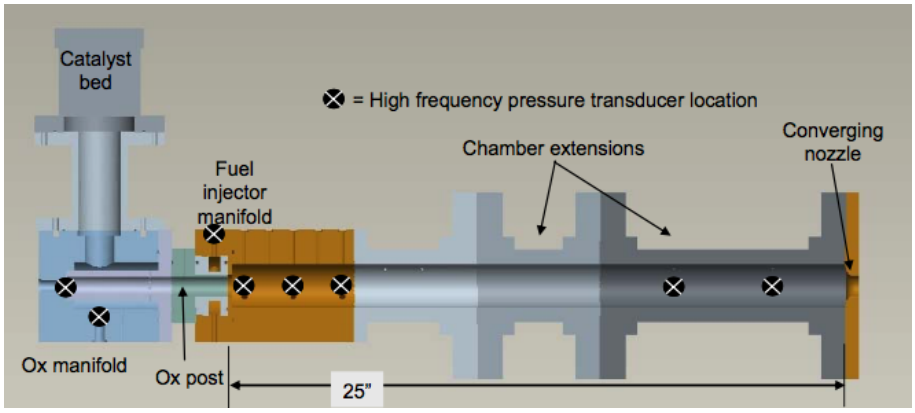

Figure 2.14.: Cut-away diagram of the Uni-Element Combustor, with high frequency pressure transducer locations marked. Baseline configuration with a chamber length of 63.5 cm is shown, although chamber lengths of 25.4, 38.1, 50.8, and 88.9 cm were also tested [92].

unfortunate side effect of drawing heat out from the combustion gas, lowering the combustion efficiency. A short nozzle terminates the chamber, choking the exiting combustion gases and encouraging reflection of acoustic waves [93].

Acoustic analysis was used to define *a priori* conditions that would drive or dampen instabilities, based on a method outlined by Kinsler et al. [94]. In the view that the oxidizer post acts as a resonator for the chamber, it can be sized for destructive interference as a means of system stabilization, or tuned to time pressure oscillations to synchronize it with heat release. To achieve maximum damping of a specific chamber mode, the oxidizer post required a length, L, that was one quarter of the equivalent post wavelength, λ. In this configuration, a pressure wave generated at the dump plane will travel both upstream along the post and downstream through the chamber. The maximally damping configuration acts as a quarter-wave resonator, see Equation (2.19), such that a pressure pulse traverses upstream through the post, reflects off the far upstream boundary and returns to the dump plane, does so when the chamber pressure pulse reaches the throat. In this scenario, the oxidizer post achieves maximum pressure oscillations at the dump plane while the chamber is

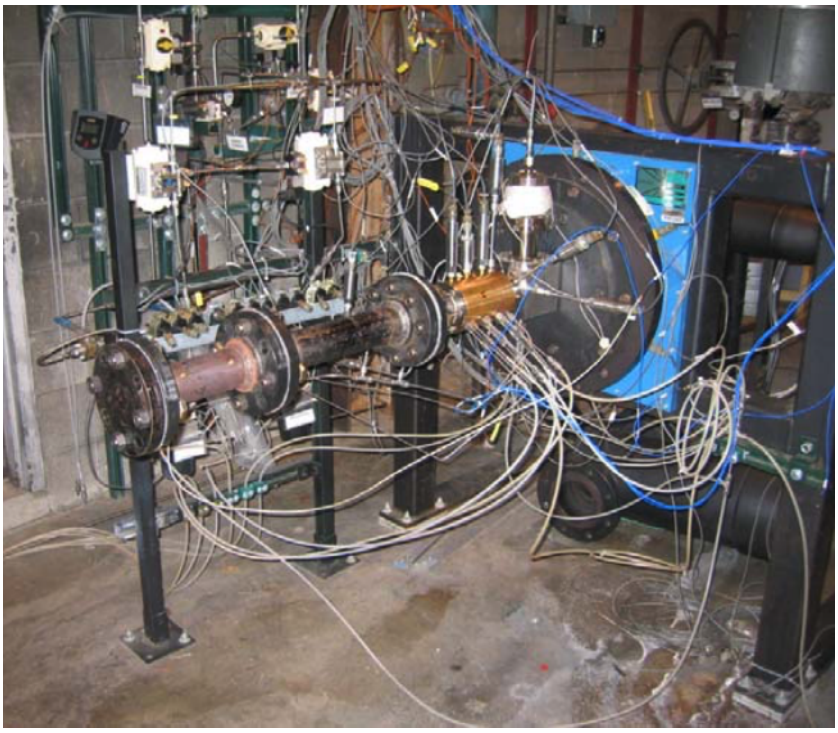

Figure 2.15.: Photograph of UEC located in the Rocket Cell of the High Pressure Lab of Zucrow Laboratories at Purdue University [92].

at a pressure minimum, leading to destructive interference of the acoustic waves as a stabilizing effect.

$$\frac{L}{\lambda} = \frac{1}{4} \tag{2.19}$$

The post wavelength is defined by the sound speed in the post, $\bar{c}$, and the frequency of interest in the chamber, f_n, as shown in Equation (2.20).

$$\lambda = \frac{\bar{c}}{f_n} \tag{2.20}$$

Conversely, constructive interference is expected when the post length is half the equivalent post wavelength, or when the post is a half-wave resonator, as shown in Equation (2.21).

$$\frac{L}{\lambda} = \frac{1}{2} \tag{2.21}$$

In this configuration, a pulse generated at the dump plane will travel the length of both the oxidizer post and the chamber at the same time, with both pressure waves returning to the dump plane at the same time.

For the UEC, the post is considered to be filled with a uniform distribution of decomposed 90% peroxide, or 42% oxygen and 58% water vapor. The decomposition process can cause the products to reach up to 1000 K, with sound speeds around 670 m/s. The oxidizer post had a fixed length of 0.171 m. From this information it is possible to estimate the natural frequency of the post.

Assuming an acoustically closed/closed system (pressure anti-nodes at the upstream and downstream ends of the oxidizer post), and also a homogenous mixture of combustion gases in the chamber and decomposed peroxide in the post, estimation of the natural longitudinal frequency and its harmonics for a domain is produced by Equation (2.22).

$$f = \frac{nc}{2L} \tag{2.22}$$

Here, c is the sound speed, and L is the length of the post, where n is an integer to denote the harmonic. Using the upper bounds based on adiabatic conditions, a predicted 1L frequency of the oxidizer post is around 1960 Hz.

This same method is applied to the chamber. Using results calculated from CEA, combustion of the propellants at the nominal flow rate yields chamber temperatures of 2534 K, with sound speeds of 1084 m/s.

Based on the acoustic theory described above, configurations with equivalent wavelengths around 1/2 are expected to minimally dampen pressure oscillations, permitting instabilities. Likewise, equivalent wavelengths around 1/4 are expected to stabilize oscillations. The baseline configuration of the UEC with a chamber length of 63.5 cm is designed to dampen the first longitudinal chamber mode, where the post has an equivalent wavelength of 0.24, and drive the second longitudinal chamber mode, where the post has an equivalent wavelength of 0.49. Of the five chamber lengths tested, all save the 25.4 cm length were unstable.

The frequencies for the first three longitudinal modes in the chamber for the lengths tested are provided in Table 2.2. Also provided in the table are equivalent wavelengths, based on a 25% reduction in oxidizer temperature.

Sisco [95] describes the proposed mechanism in detail, which is discussed later in Section 2.5. Briefly, velocity gradients at the dump plane induce vortices, which entrain unburnt fuel products and oxidizer. The vortices, which do not initially combust due to lack of ignition source right at the location of inception, are essentially premixed pockets of propellant. The location and timing of vortex impingement on the wall is determined by the height of the back step. By reducing the step height, impingement can occur sooner and in a location closer to the dump plane. A version of the UEC where the most upstream section of the chamber was made narrower was used to study this phenomenon. Initially the 25.4 cm chamber section was selected for study, as it was the only chamber length that demonstrated stable behavior with the baseline chamber diameter. The chamber diameter was reduced from 2.25 cm to 1.91 cm, with a resulting reduction of the step height from 1.10 to 0.76 cm. This

Table 2.2.: Uni-Element Combustor Acoustic Mode Frequencies

Chamber Length	Acoustic Mode	Frequency [Hz]	L/λ
25.4 cm	1L	2134	0.55
	2L	4268	1.09
	3L	6402	1.64
38.1 cm	1L	1423	0.36
	2L	2845	0.73
	3L	4268	1.09
50.8 cm	1L	1067	0.27
	2L	2134	0.55
	3L	3201	0.82
63.5 cm	1L	854	0.22
	2L	1707	0.44
	3L	2561	0.65
88.9 cm	1L	610	0.16
	2L	1219	0.31
	3L	1829	0.47

change theoretically would change impingement time of shed vortices without altering operating conditions. Unstable operation was achieved through this modification, with amplitudes increasing from around 2% of the mean chamber pressure to between 29% and 49%.

Tests were also conducted at the 50.8 cm configuration. As this chamber was twice the length of the 25.4 cm chamber, and the 2L and 4L modes of the former matched the 1L and 2L modes of the latter, similar results were expected. Both nominal and narrow chamber configurations were unstable, with an increase from mid-to-high 20s%, up to low-to-mid 30s%. This increase is much less than the one observed for the shorter chamber.

Results

For a set of given oxidizer post and chamber conditions, along with a fixed post length, it is possible to predict the acoustic modes of both the chamber, post, and system modes using linearized acoustic analysis. A map can then be created based on the results of this analysis, where chamber and system modes are predicted as a function of chamber length. One such map is presented in Figure 2.16. It can also be seen that this figure incorporates the predicted chamber modes listed above in Table 2.2. Chamber modes (dashed lines) are calculated simply from the chamber domain. System modes (solid lines) consider both the oxidizer post and chamber. The chamber length often dominates system modes, illustrated by the ranges where a system and chamber mode overlap. The oxidizer post 1L frequency is presented as a green region. Later experiments showed that extensive heat loss to the oxidizer injection system was possible, with temperatures measured in the post 30% lower than the expected temperature. The solid black horizontal line in the figure represents the oxidizer post 1L frequency.

Superimposed on Figure 2.16 are the frequencies of strongest amplitudes for each chamber length, denoted by the red circles. Magnitude of amplitudes are repre-

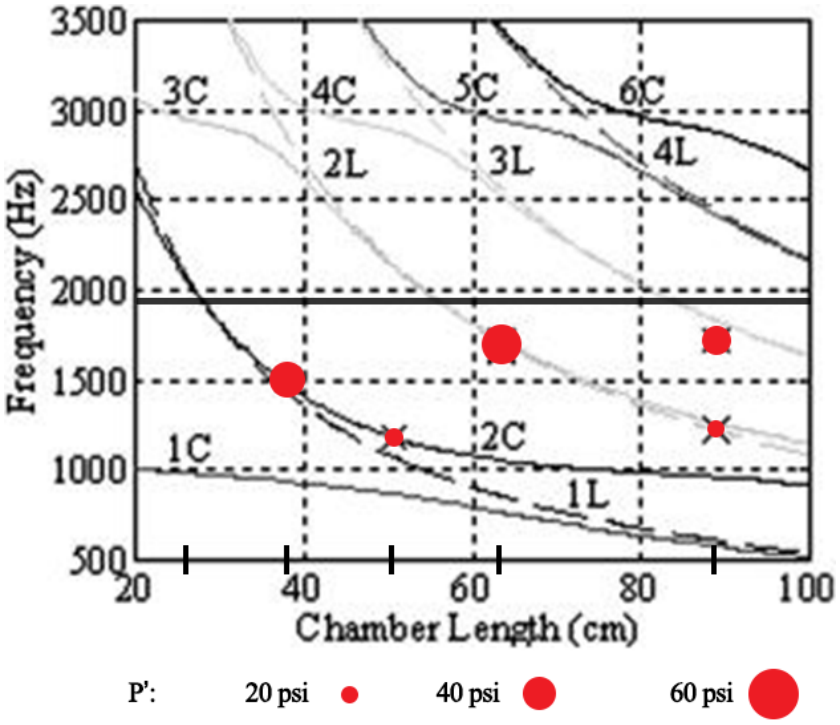

Figure 2.16.: Frequency map for chamber (dashed lines) and system modes (solid lines). Chamber and oxidizer conditions, as well as oxidizer post length, are fixed. Red circles indicate frequency of strongest amplitude, with size of circle a marker of pressure oscillation level. Solid horizontal black line represents the oxidizer post 1L mode. Chamber lengths tested are indicated by tick marks on the x-axis. Adapted from [92]

sented by the size of the circle, with increased amplitudes having larger markers. Through solely varying the chamber length, different levels of pressure oscillations were achieved during hot fire. The strongest oscillations were observed for a chamber length of 63.5 cm, reaching peak-to-peak amplitudes at 1709 Hz around 15% of the mean chamber pressure. This is followed by the 38.1 cm chamber, with amplitudes 13% of mean chamber pressure at 1502 Hz. The 88.9 cm chamber demonstrates two stability levels during a single test, with pressure amplitudes of 11% at 1721 Hz before shifting to 7% at a lower frequency of 1233 Hz. Tests conducted at a chamber length of 50.8 cm exhibited oscillations around 7% of mean chamber pressure. At the shortest chamber length of 25.4 cm, combustion was stable with no discernible frequency content.

The strongest amplitudes appear to be at frequencies closest to the predicted oxidizer post 1L frequency. This is expected, as the post acts as a resonator for the chamber. Tests conducted at 38.1, 63.5, and 88.9 cm exhibited the strongest pressure amplitudes at frequencies within approximately 300 Hz of the oxidizer post frequency. Moderately unstable oscillation were observed for a chamber length of 50.8 cm, where there is approximately a 500 Hz difference between the oxidizer post 1L and the closest chamber and system acoustic modes. Likewise, the test conducted at 88.9 cm shifted to a lower dominant frequency. This frequency shift led to a larger gap between oxidizer post 1L frequency and most excited frequency, along with a drop in pressure oscillation amplitudes. There was no dominant frequency content in the test conducted with a chamber length of 25.4 cm. According the the frequency map, the oxidizer post 1L frequency should either match or be somewhat lower than the chamber 1L or system 2C mode. However, the results from testing at other chamber lengths suggests a preference of choosing lower modes to excite as opposed to higher ones, such as in the example of the 50.8 cm chamber. It is possible that the chamber and system frequencies for the 25.4 cm chamber are too far from the oxidizer post frequency to successfully couple, resulting in stable operation.

Computational work performed by Smith et al. [96] simulated this combustor at the tested configurations. It was shown that the the full nonlinear Euler equation framework used to model the experiment correctly captured the instability characteristics of the experiment. Experimental data taken from the dominant modes for the unstable tests were compared to mode shapes produced by the computational model. This is shown in Figure 2.17. The simulation was also able to reproduce the steepening of the pressure signal due to the non-linear forcing at high amplitudes.

Work by Xia et al. [98] continued to study the UEC computationally, upgrading the model to use multistep reduced chemical kinetics as opposed to the single step method of the previous work, as well as doubled grid spacing for finer spatial resolution. The improvement to grid spacing appeared to better match the acoustic mode frequencies of the computation to that of the experiment. This was countered by the change in frequency associated with the multistep reduced chemical kinetics, since the reaction region covers a larger volume and extends further downstream than the single step reaction.

One thing of interest to the work presented in this document is a shift in flame anchor positioning between the single step and the multiple step reactions. As shown in Figure 2.18, the temperature distribution at the injector is modified by the reaction model used. The single step reaction temperature distribution suggests that the flame is anchored to the collar, as temperatures of 1400 and 1600 K are reached in that location. In the multiple step reaction, the temperature near the collar has been reduced to 1000 K, matching the temperature of the incoming oxidizer jet and indicating combustion is no longer fixed to this point.

Also demonstrated is stratification of the temperature distribution. The hot oxidizer core extends along the central axis throughout the visible region. There is no evidence of combustion occurring at the center line in either case. Moving radially from the center line the temperatures increases with steeper gradients at further axial locations, indicating an expanding reaction zone.

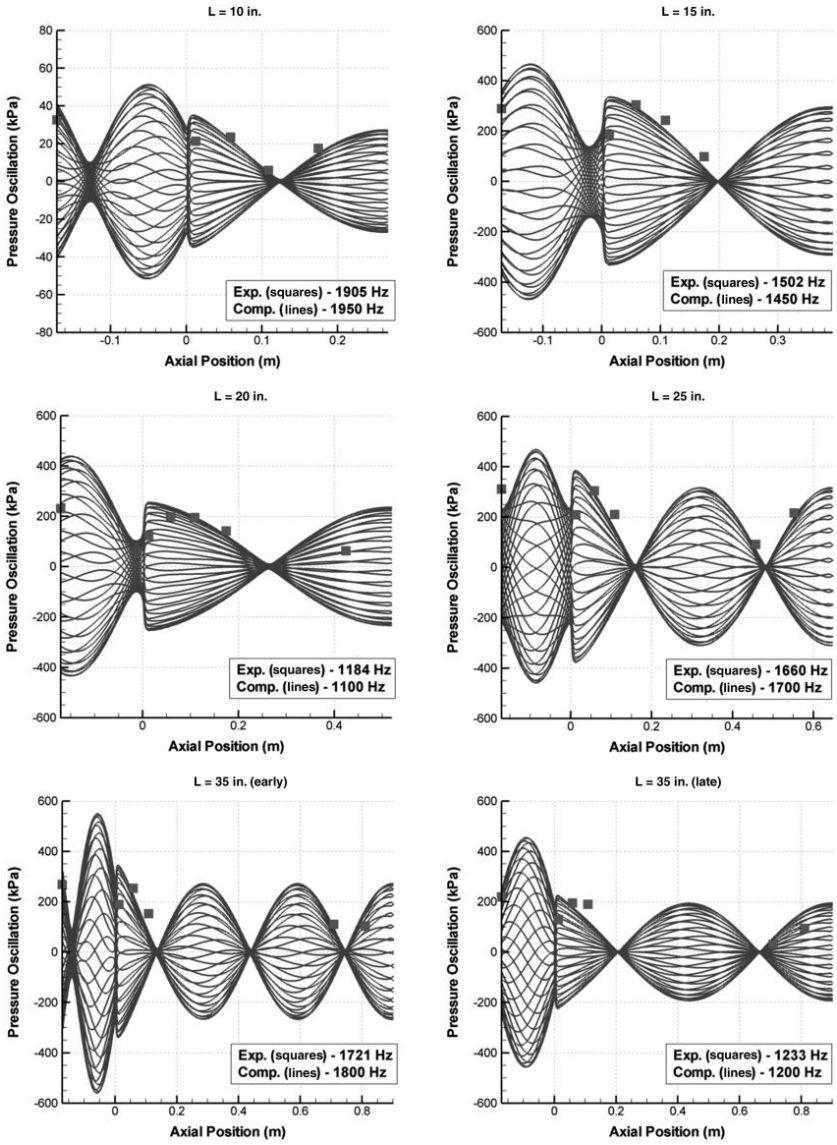

Figure 2.17.: Comparisons of computationally acquired mode shapes and experimental data of the dominant modes from various configurations of the UEC [97].

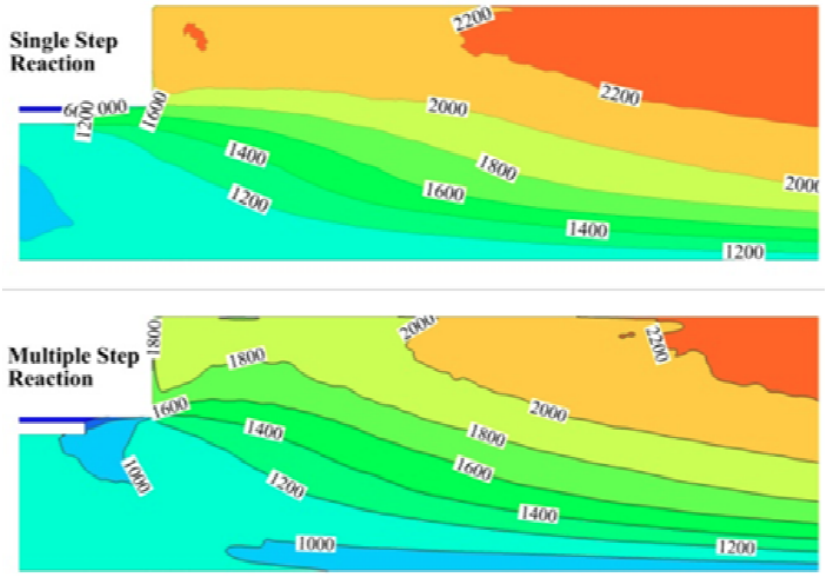

Figure 2.18.: Comparisons of the temperature field predicted for the UEC when using single step reaction (top) and multiple step reaction (bottom). Shift in temperature distribution near the injector collar indicates flame anchoring has moved away from the collar in the multiple step reaction [98].

In the single step reaction case, combustion occurs immediately near the introduction of the fuel behind the collar. This flame anchoring has been shown to have a stabilizing effect, as discussed in Section 2.2.8. This is not seen in the multistep case, as the injection recess remains cool throughout. Instead, the combustion zone has migrated downstream to the head end of the combustor at a pressure anti-node. The combined impact of the unanchored flame and positioning of the reaction zone to a region of increased pressure fluctuations would explain the stronger pressure amplitudes observed in the mutlistep case.

In the narrow chamber experiment designed to study the impact of vortex shedding and impingement, a clear difference in behavior was observed. The short chamber configuration was chosen, as it was initially stable with amplitudes at the dominant frequency roughly 27 kPa, or around 1% of the total mean chamber pressure. The pressure oscillations increased in amplitude dramatically with the narrow face, with

Table 2.3.: Dynamic pressure summary comparing effect of step height of the 25.4 cm UEC experiment. Results from Reference [95] unless otherwise noted.

Test Designation	Dominant Frequency/Amplitude (Peak-to-Peak/Pc)
10D1 [92]	26.3 kPa @ 1905 Hz (1.11%)
10HI01	29.0 kPa @ 2070 Hz (1.21%)
10HI02	27.2 kPa @ 1930 Hz (1.11%)
10NF01	343 kPa @ 2060 Hz (14.36%)
10NF02	562 kPa @ 2045 Hz (24.30%)
10NF03	662 kPa @ 2015 Hz (28.56%)

levels between 14% and 29% of the mean chamber pressure. The dominant mode appears to be the 2L chamber mode, where the oxidizer post is a half-wave resonator of the chamber.

The results from tests conducted at the short chamber length are presented in Table 2.3. The first two numbers in test designation are chamber length in inches. The following letters indicate whether the configuration was the original design, 'D', conducted with a highly instrumented head end section, 'HI', or used the narrow face configuration, 'NF'. Numbers following the configuration designation indicate test number in series.

A comparison of the spectrograms and PSDs from the highly instrumented and narrow face tests are shown in Figure 2.19. The PSDs are taken from a 200 ms time slice in the middle of hot fire. Ignition begins around 4.7 seconds and shut down occurs around 5.5 seconds. The 1L mode, which coincides with the oxidizer post 1L, is visibly excited in the narrow face configuration, along with the second and third harmonics. The nominal chamber diameter configuration is clearly stable, with no distinctive peaks. Note that this oxidizer post frequency is also excited early on in

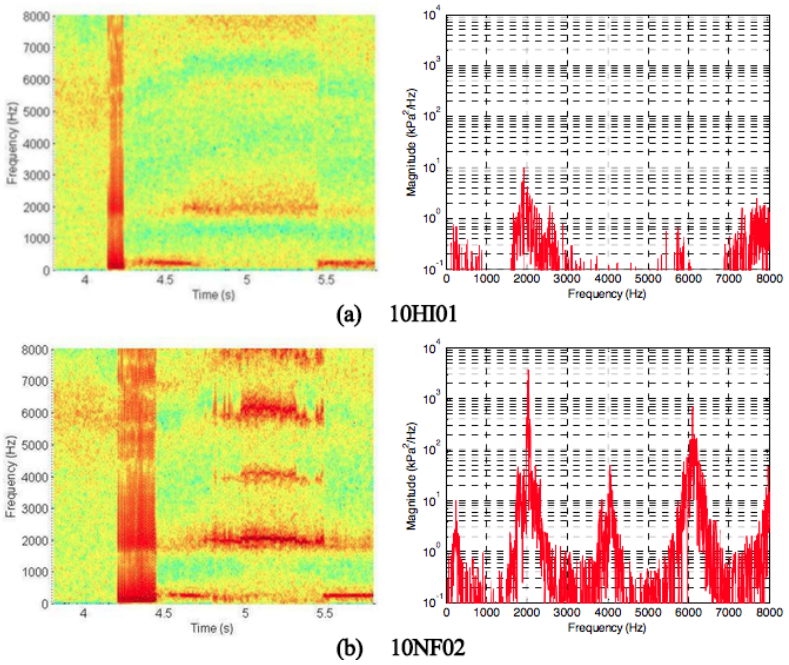

Figure 2.19.: Spectrogram and PSD taken from a 200 ms during hot fire tests with the 25.4 cm (10 in) chamber for the (a) highly instrumented baseline diameter case, 10HI02, and (b) the narrow face chamber, 10NF02. Ignition begins around 4.75 seconds and hot fire ends at 5.5 seconds. Adapted from [95].

the test, as early as the monoprop portion of the test, indicating it is tied to the oxidizer injection system.

The tests were repeated at a longer chamber length of 50.8 cm. Since this chamber length is twice that of the 25.4 cm chamber, the 2L and 4L modes match the 1L and 2L modes of the latter. Because the oxidizer post exists as a resonator for the chamber at a comparable wavelength, results similar to the shorter chamber were expected. At the baseline diameter, the 1L mode was excited around a frequency of 1175 Hz, with amplitudes approximately 19% of the mean chamber pressure. At the narrow face, the frequency shifted upwards to 1230 Hz, with increased amplitudes around 25-28%. The second harmonic, however, did not change nearly as drastically.

Table 2.4.: Dynamic pressure summary comparing effect of step height of the 50.8 cm UEC experiment. Results from Reference [95] unless otherwise noted.

Test Designation	Dominant Frequency/Amplitude
20D1r [92]	448 kPa @ 1180 Hz (19.59%)
20HI01	452 kPa @ 1165 Hz (18.90%)
20NF01	655 kPa @ 1230 Hz (28.05%)
20NF02	593 kPa @ 1235 Hz (25.35%)

Test Designation	Secondary Frequency/Amplitude
20D1r [92]	27 kPa @ 2035 Hz (1.19%)
20HI01	15 kPa @ 2105 Hz (0.61%)
20NF01	46 kPa @ 1975 Hz (1.98%)
20NF02	69 kPa @ 1965 Hz (2.94%)

There was also an increase in the strength at the oxidizer post 1L frequency. The baseline configuration resulted in amplitudes around 1%, which increased to 2-3% at the narrow face chamber. While this pales in comparison to the 1L frequency, it is a clear change, as seen in Figure 2.20.

The UEC experiment is important to the DVRC for two reasons. First, the UEC showed it was possible to trigger self-excited instabilities in a single-element combustor simulating oxidizer-rich staged combustion with a liquid fuel by modifying only the geometry while keeping flow conditions constant. However, it will be shown that achieving high amplitude, self-excited instabilities requires more than proper tuning of the geometry. This is demonstrated on the experiment that is the subject of this thesis, where the main difference between the DVRC and the UEC is the use of heated oxygen in the former instead of decomposed hydrogen peroxide. Second, the experiment demonstrated an interaction between oxidizer post and chamber. The

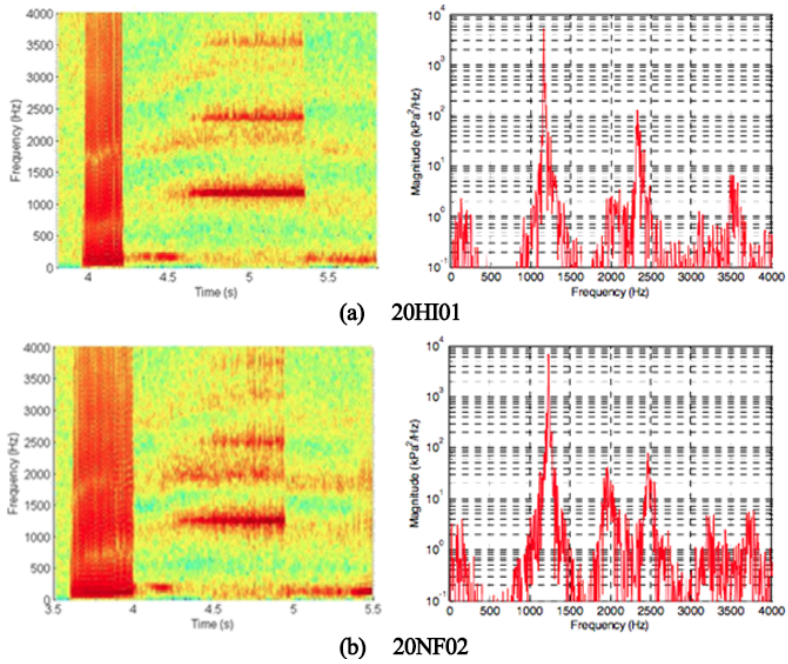

Figure 2.20.: Spectrogram and PSD taken from a 200 ms during hot fire tests with the 50.8 cm (20 in) chamber for the (a) highly instrumented baseline diameter case, 20HI02, and (b) the narrow face chamber, 20NF02. Ignition begins around 4.75 seconds and hot fire ends at 5.5 seconds. Adapted from [95].

oxidizer post acts as a resonator, amplifying acoustic perturbations and leading to modulation of the combustion field. It appears that there is a window of frequencies the acoustic frequencies need to be within, such that tuning the system can allow for the post and chamber to couple. Tuning the system, such that the oxidizer post and chamber frequencies more closely match, also appeared to increase the amplitude of the pressure oscillations. Further discussion on the mechanisms that initiate and maintain instabilities is presented later in Section 2.5.

2.4.2 Continuously Variable Resonance Combustor

The Continuously Variable Resonance Combustor (CVRC) was a follow up to the UEC experiment. The CVRC exchanged the idea of varying the chamber length for modifying oxidizer post length instead. This change permitted a design of a continuously varying oxidizer post through the use of an adjustable upstream boundary condition. Similar to the UEC, this configuration allowed for study of chamber resonance in the oxidizer post, with much improved frequency resolution compared to the original experiment.

The CVRC was also designed as a test bed for collecting validation data for simulations. To assist in this endeavor, other changes were made to simplify the experiment for modeling.

Experiment Description

While the UEC featured a single gas-centered swirl coaxial injector for combusting 90% decomposed hydrogen peroxide and liquid JP-8, the CVRC relies on a shear coaxial injector for combusting decomposed peroxide with gaseous methane. A cross-section of the experiment is shown in Figure 2.21. The chamber remains a dump combustor with a fixed length of 38.1 cm. A short nozzle terminates the downstream end of the chamber, promoting acoustic reflections.

Instead of radially injecting decomposed peroxide into the midpoint of the oxidizer post akin to the UEC, a more traditional axial injection method was chosen. Decomposed peroxide exhaust exits the catalyst bed and fills the oxidizer manifold. A choking orifice sits inside the oxidizer post, both metering the flow and providing an acoustically closed boundary to reflect pressure waves. The choking orifice is attached to the arm of a translating shaft. The translating shaft is connected to a programmable actuator. Both forward and backwards translation is possible, with translating speeds between 1.27 to 5.08 cm/s tested. The system is designed to handle testing between 8.89 and 19.05 cm.

The fuel injector is similar to that of the UEC, save for the removal of swirl velocity and the replacement of a liquid with a more modelable gas propellant, methane. The fuel manifold is supplied by a pair of inlets, injecting the fuel through 36 radial holes. A collar shields the fuel in the fuel annulus, redirecting the flow from radial motion to axial. An injection recess provides time for the fuel and oxidizer to mix before it enters the combustor.

Following the method laid out in References [29, 92, 99], the oxidizer post was designed to be operated at lengths that would serve to maximize acoustic damping at one length, and minimally dampen at another. A selection of achievable oxidizer post lengths and their respective equivalent wavelengths are listed in Table 2.5. Equivalent wavelengths are based on expected combustor sound speeds of 980 m/s determined by CEA, and expected oxidizer post sound speeds of 581 m/s determined by REFPROP [100] and experimental temperature measurements.

Figure 2.22 is included to illustrate the effect of equivalent wavelength in terms of acoustic timing. For a given cycle, based on the first longitudinal chamber acoustic mode, six time steps are shown noting where a pressure pulse emitted at the dump plane at time $t = 0$ would be. The 8.9 cm oxidizer post configuration most closely models a 1/4-wave resonator. As such, the pulse is able to travel upstream through the oxidizer post and back down to the dump plane in the time the pulse in the chamber reaches the throat.

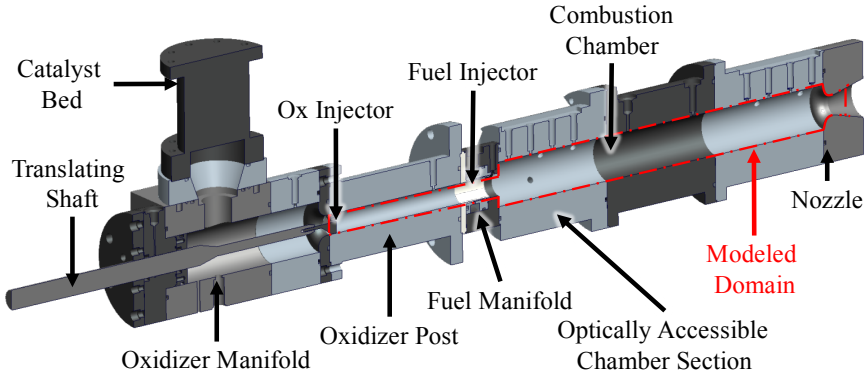

Figure 2.21.: Cross-section of the Continuously Variable Resonance Combustor (CVRC).

Table 2.5.: CVRC Oxidizer Post Equivalent Wavelengths

Oxidizer Post Length [cm]	Equivalent Wavelength
8.9	0.20
11.4	0.26
14.0	0.31
16.5	0.37
19.1	0.43

Likewise, the 19.1 cm oxidizer post configuration most closely resembles the 1/2-wave resonator. The pulses travel the length of the post and the chamber in approximately the same time, reaching the dump plane almost simultaneously. The 14.0 cm post length sits in the middle of the other two, such that the pulse in the oxidizer makes it back to the dump plane and begins a second trip towards the upstream choked boundary when the chamber pulse arrives at the dump plane.

Similar to the map for the UEC presented in Figure 2.16, a frequency map of the CVRC is presented in Figure 2.23. Acoustic frequencies determined by the linearized Euler equation are presented for varying oxidizer post length, as opposed to chamber length. Dashed lines represent chamber modes, while solid lines are system modes, including both oxidizer post and chamber. On top of this map are markers indicating the amplitude of frequencies measured in a translating test. Weak fluctuations, less than 1 psi (6.89 kPa), are denoted by the black asterisks, while fluctuations between 1 and 10 psi (6.89 to 68.95 kPa) are marked with blue squares. Green circles are reserved for amplitudes greater than 10 psi (68.95 kPa) and are limited to the first longitudinal chamber mode. Measurements are similar to predictions, although it appears that predictions for the fundamental mode are slightly higher than the actual frequency, causing the separation between experimental and LEE results at higher harmonics to drift further apart. Nonetheless, it is clear that the strongest oscillations are tied to the chamber modes.

Results

Testing was conducted at selected fixed oxidizer lengths, as well as tests where the oxidizer length was increased (or decreased), demonstrating changes in stability midtest [102–104].

Figure 2.24 provides a look at the effect of the oxidizer post on stability. This figure presents a visual representation of the amplitude of the frequency spectrum between 0 and 8000 Hz (background, left y-axis) as a function of the current oxidizer

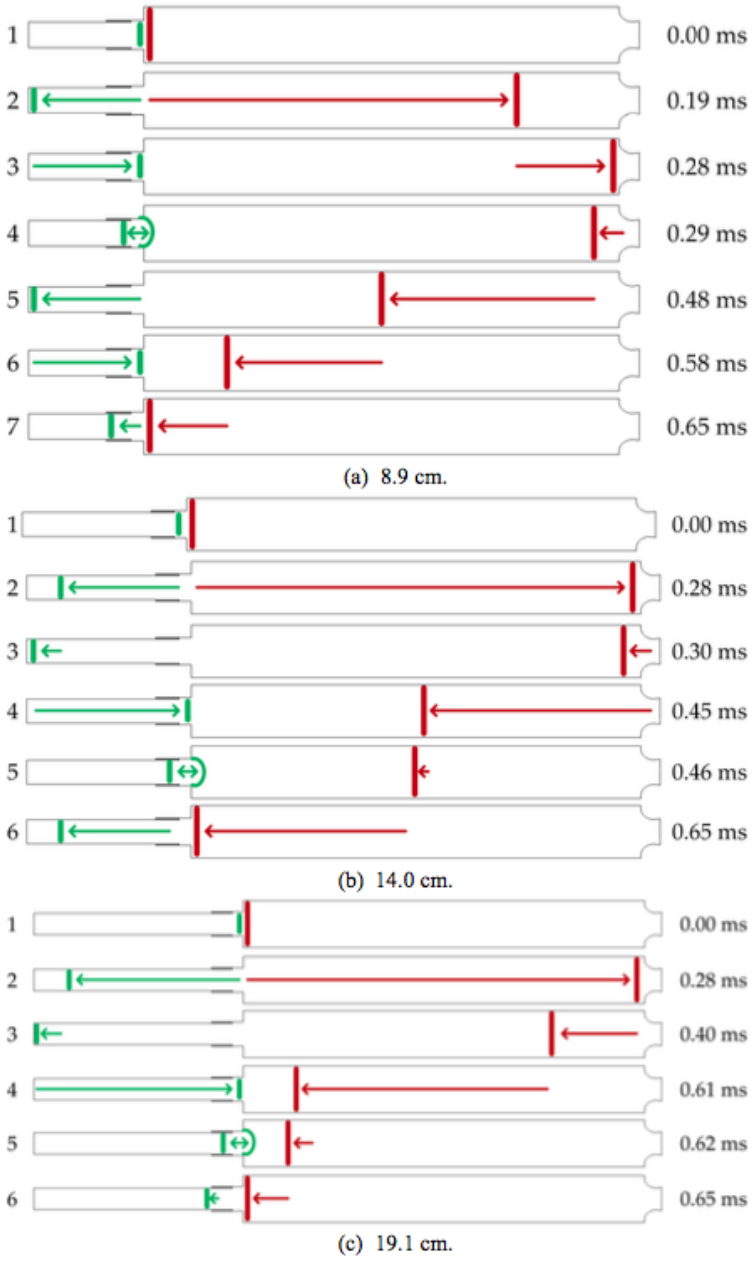

Figure 2.22.: Visualization of the traversal of pressure pulses for the (a) 8.9, (b) 14.0 and (c) 19.1 cm posts. Six time steps from a single cycle are shown, based off the first longitudinal mode of the chamber. Vertical bar indicates the location of a pressure pulse after a given amount of time since being generated at the dump plane, with green indicating within the oxidizer post and red in the chamber [101].

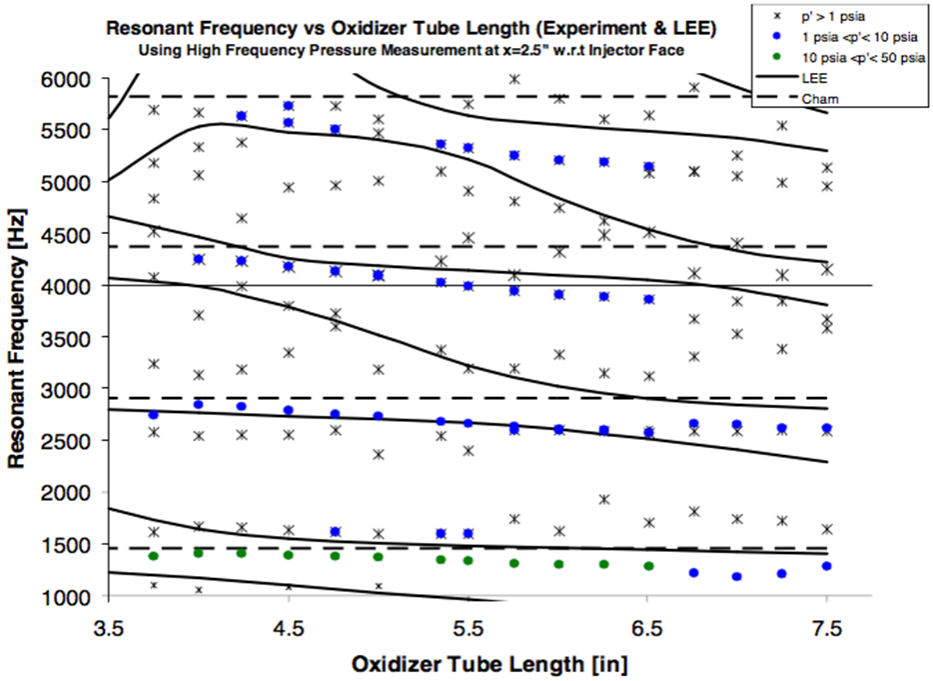

Figure 2.23.: Frequency map for the CVRC with acoustic frequencies of both the chamber (dashed lines) and system modes (solid lines). Overlaid on top of this map are frequencies measured from experiments during a translating test at a location 6.4 cm downstream of the dump plane. Black asterisks indicate recorded pressures fluctuations of less than 1 psi (6.89 kPa), blue squares represent pressure fluctuations between 1 psi and 10 psi (6.89 to 68.95 kPa), while fluctuations greater than 10 psi (68.95 kPa) are marked by green circles and are limited to the first chamber mode [102].

post length (blue line, right y-axis). A discontinuity appears in the oxidizer post line midtest. This is due to a voltage spike in the signal that reads the position of the actuator arm, and not an actual jump in oxidizer post length. Amplitudes are based on color, with red meaning high amplitudes, blue meaning low amplitudes, with greens and yellow in the middle. At the start of the test, there is visible, albeit weak, excitation of the first two longitudinal modes around 1300 and 2600 Hz. At around 9.5 seconds, the oxidizer post begins to translate forwards, reducing oxidizer post length. There is a noticeable increase in amplitude for the first two acoustics modes. At 10 seconds, with the oxidizer post length around 16.26 cm, the amplitude increases again, becoming very well defined. Multiple harmonics are present, with up to the 6L and beyond present. Unstable operation continues until around 11.35 seconds when the oxidizer tube length reaches the minimum value of 8.89 cm. Only the fundamental mode and the first harmonic are present, and at a diminished amplitude compared to the intermediate post lengths.

Another view of the resonance effect of the oxidizer post length is shown in Figure 2.25. This figure captures the stability window of the combustor. For the forward translating tests, there is a clear, repeatable sudden increase in pressure amplitude between 10 and 11.5 cm. The amplitudes continue to increase slightly up to 13.8 cm, where afterwards they decrease until 15.3 cm. At this point the amplitude plateaus until about 16.6 cm, except for test FWD1, which drops off sooner around 15.8 cm. The amplitude immediately drops for all longer post lengths.

The backwards translating tests follow the same general trend, but suffer hysteresis effects. The rise in amplitude at short post lengths happens at even shorter lengths, compared to the forward translating tests. Then the amplitude plateaus until 15.3 cm, where the values dip, identical to the forward tests. A secondary plateau continues to exist for the backwards cases, starting at the same post length. However, the raised amplitudes persist until 18 cm, where the amplitudes quickly fall at longer lengths.

The existence of two different unstable regions is interesting, prompting the question on whether the two distinct regions are evidence for a shift in the instability

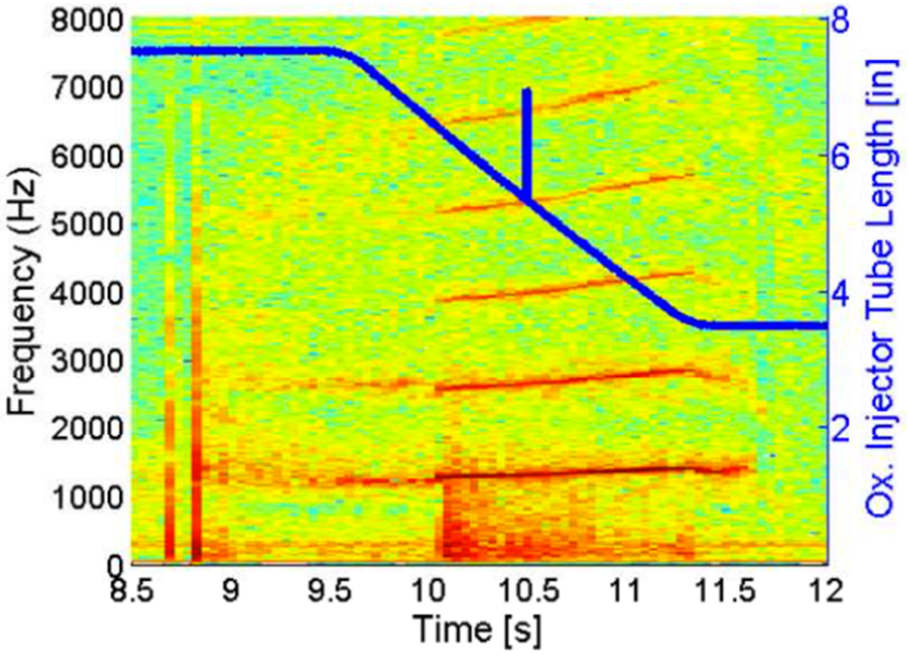

Figure 2.24.: An overlay of the oxidizer post length (blue line) atop the spectrogram taken from a measurement of the pressure at the dump plane for a translating post test. There is a clear transition between stability modes throughout the test, starting in a stable mode until translation begins, where the first two modes increase in amplitude. Stronger, more defined appear, with multiple harmonics, at intermediate oxidizer post lengths, then drop off near the end of translation when the combustor returns to a stable operation mode. Discontinuity in oxidizer post length attributed to noise in the voltage signal used to determine actuator arm position [102].

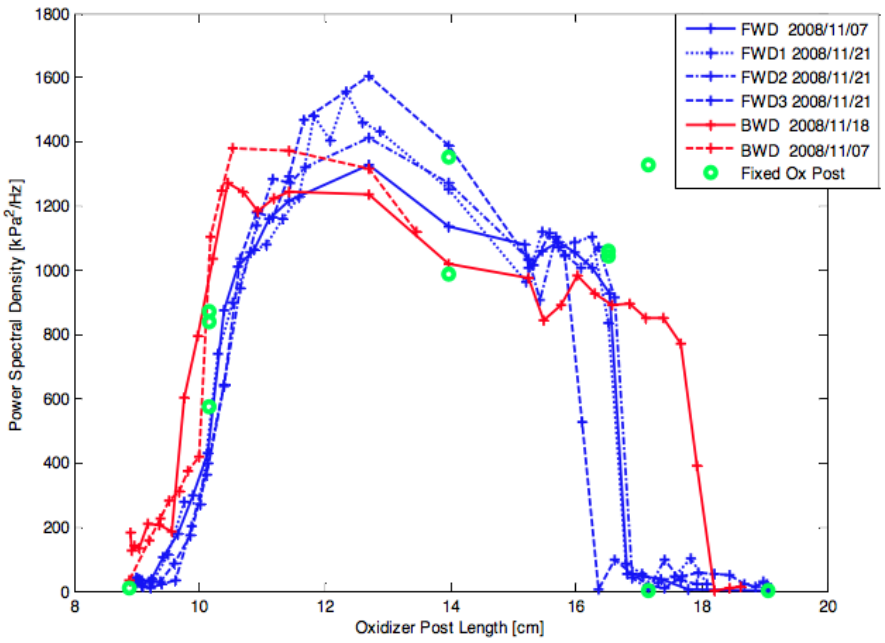

Figure 2.25.: Power spectral density of the dominant acoustic mode against the oxidizer post length from a collection of translating tests. Blue lines indicate tests that translated forward from 19.05 to 8.89 cm, while red lines ranged across the same lengths but in reverse. Green circles indicate amplitudes measured from tests where the post length remained fixed.

mechanism at work, or a transition from one mechanism to another. Subsequent computational investigation of this combustor determined that two unique instability mechanisms can be activated in the CVRC [101]. At short to intermediate post lengths, pulses in the oxidizer post became strong enough to modulate fuel flow. This modulation led to coupling of bursts of heat release at the dump plane due to the modulated fuel flow, to returning pressure pulses in the chamber. At higher post lengths, a vortex shedding/impingement based mechanism, similar to the one observed in the UEC, sustains unstable behavior. Further discussion of these instability mechanisms is presented in Section 2.5

To gain better insight into spatio-temporal evolution of the combustion field and the interaction between heat release and presure, the CVRC was modeled and simulated at three oxidizer post lengths: 8.89, 13.97 and 19.05 cm. Harvazinski et al. [101] implemented hybrid RANS/LES to study the CVRC, which correctly captured the stable behavior at the 8.89 cm post length, and the unstable behavior at the 13.97 cm post length. At the 19.05 cm post length, the simulation captured unstable behavior, whereas the experiment observed bifurcated stability behavior.

At the shortest and longest post lengths, the simulation predicted the flame to be anchored at the back step, instead of the fuel collar. And at the most unstable post length of 13.97 cm, pressure oscillation reached amplitudes that prevent any sort of anchoring, containing the combustion field in the chamber.

This agrees with research performed by Garby et al [105]. In simulation of the CVRC at the 12 cm post length, it was noted that the chemical kinetics for this propellant mixture are too slow, preventing it from combusting fast enough to anchor to the collar. Instead, the flame is anchored to the back step by hot burnt gases in the recirculation region.

Simulations reported by Srinivasan et al. [106] showed similar results. They noted that the CVRC was unique among 3D LES and Discrete Event Simulation (DES) studies in that a high strain-rate in the mixing layer prevented the diffusion flame from being sustained at the injector post tip. The combustion mode became more

complex in that anchoring of the flame at the injector face led to mixing of unburnt products and incoming oxidizer. Further complexity in the flame holding occurred due to the premixing induced by the collar, causing the flame to occasionally lift off from the injector face and propagate upstream.

The effects of chemical kinetics were studied in computational models of the CVRC through varying the reaction mechanisms used during combustion [107]. Four chemical kinetics mechanisms were implemented and are listed in order of increased complexity. The first is a single-step mechanism where fuel and oxidizer react to form water and carbon dioxide. The second mechanism, a two-step mechanisms, builds off of the first and adds carbon monoxide as an intermediate step in the hydrocarbon oxidation. The third mechanism is based off work from the Gas Research Institute and is referred to as GRI-1.2. This mechanism comprises 177 reactions, involving 32 species. The final mechanism, GRI-3.0, accounts for nitrogen compounds, increasing the number of involved species to 53 and reactions to 325. Ignition delay, maximum temperature, and heat release rate were compared between the different mechanisms at three different oxidizer post lengths.

Of the three parameters studied, the ignition delay is most pertinent to this work. The ignition delay for the mechanisms at different equivalence ratios are provided in Figure 2.26 as a function of local equivalence ratio. These comparisons are presented at two different oxidizer inlet temperatures, 1000 K and 1400 K. The one-step and two-step mechanisms have very short ignition delays regardless of inlet temperature or equivalent ratio. As the pathways become more complicated, the ignition delay increases. For an inlet temperature of 1000 K, more time is required for the GRI-1.2 pathway, and still further more for GRI-3.0. At an elevated inlet temperature, the clear discrepancy between global and GRI-based mechanisms is still present. Notably, the GRI-3.0 mechanism has a shorter ignition delay than the less complicated mechanism at this temperature. More importantly, though, is the overall change in ignition delay between the two oxidizer temperatures. The two GRI mechanisms range between 30 and 50 microseconds at 1000 K. This delay drops to between 1 and

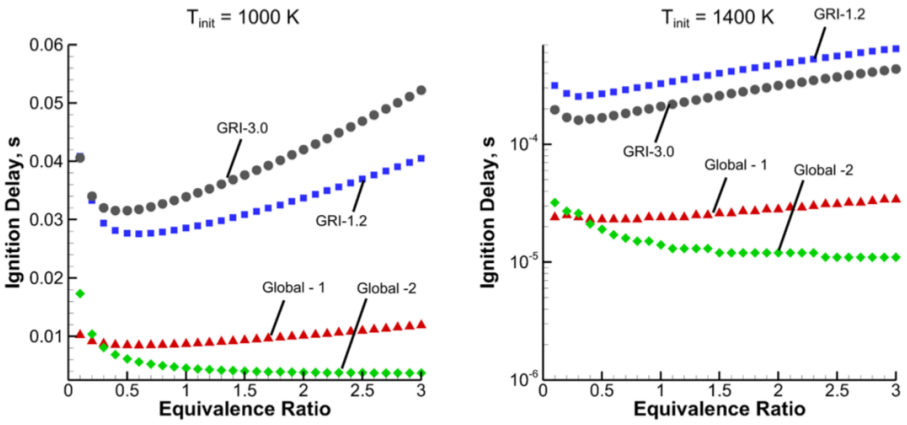

Figure 2.26.: Comparison of ignition delay for varying chemical kinetic mechanisms for a range of equivalence ratios for two oxidizier inlet temperatures [107].

6 microseconds at 1400 K, roughly an order of magnitude faster. Clearly, temperature has a significant effect on chemical kinetics.

2.5 Instability Mechanisms

Instabilities arise from the coupling of fluctuations in flowfield: pressure, hydrodynamics, and heat release. Often a trigger is present, such as a pressure pulse that may occur at random or due to a disturbance in the flow. This initial fluctuation can then be amplified by an acoustic mode, the product of the combustor and feed system geometry.

High-energy production in a constrained environment naturally generates small fluctuations, such as combustion noise in a rocket engine. Acoustic modes, defined by the geometry and operating conditions, allow pressure oscillations to settle into a natural frequency and resonate. This periodic behavior is capable of amplifying natural hydrodynamics and modulating the heat release modes of the system. The temporal and spatial relationship between these oscillations then determines whether the feedback loop serves to amplify or dampen the instability. This relationship is

described in the Rayleigh Criterion, where instabilities are predicted to be driven when the oscillations are in phase, and damped when they are out of phase [4].

Oscillations in the flow lead to localized changes in burning rate and therefore heat release, that alone is typically not enough to capture the two in a positive feedback loop. Instead, the oscillating parameters are but steps in a chain of events that lead to sustained and amplified instabilities, involving a large array of fluid dynamic interactions. The processes that connect pressure and heat release fluctuations, generating positive feedback loops, are considered instability mechanisms. Identification of these mechanisms that instigate and sustain combustion instabilities is crucial to minimizing the risk of having instabilities manifest in late-phase engine testing. *A priori* knowledge of these mechanisms would allow for the development of injectors that reduce and perhaps even dampen pressure fluctuations, as well as define operating conditions envelopes that avoid unstable regimes.

High frequency instabilities, with frequencies in the kilohertz range and higher, are generally considered to be the most destructive. Instabilities in this range can be classified into two categories as defined by Crocco [108], injection-coupled and intrinsic. Injection-coupled instabilities occur when the feed supply is modulated by downstream events. For example, a sudden excess of fuel burning near the dump plane can create a local increase in pressure. The pressure drop across the fuel injector decreases, as does the injection rate. The chamber pressure relaxes to mean values, and continues to decrease due to reduction in fuel flow rate. This in turn can lead back to a surplus of fuel, restarting the cycle. However, if the variation in fuel couples with a chamber acoustic mode, the feedback loop is strengthened and the instability can grow. This class of instabilities maintains a temporal relationship between feed oscillations and chamber pressure oscillations, but not a spatial one.

Intrinsic instabilities do not rely on modulation of incoming propellants. Instead, this class of instabilities features coupling between chamber acoustic modes and the mixing and combustion processes. These processes are diverse, including mixing (atomization and droplet breakup, vaporization) and hydrodynamics (vortex roll up,

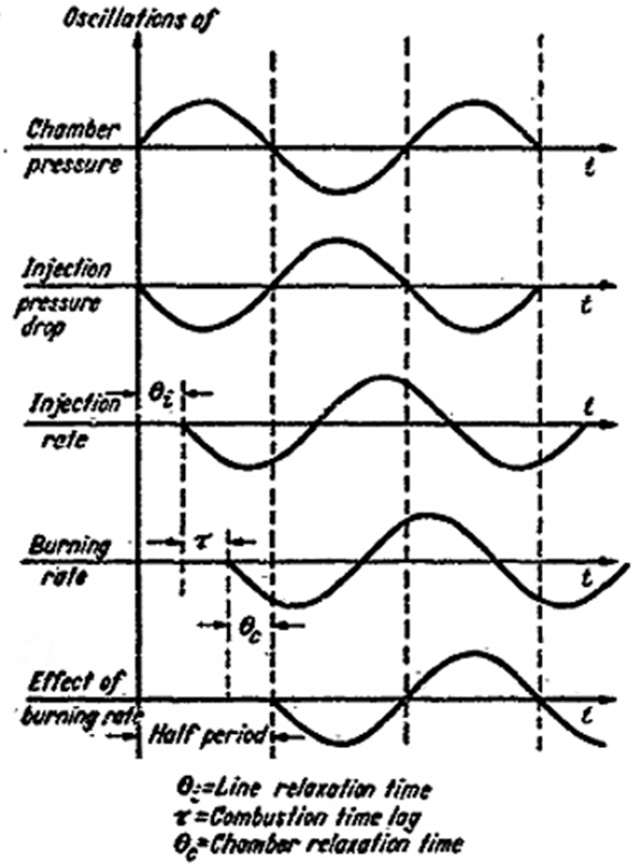

Figure 2.27.: Schematic diagram of various oscillating quantities versus time with constant time lag [108].

shedding, flapping, recirculation, baroclinic torque), as well as chemical reaction (kinetics, burn rate, ignition delay [80, 107, 109]). These processes are complex and are not yet understood enough to make predictions of how they interact, either with other processes or with the natural acoustic modes of the combustor. To supplement our current understanding, experimental and computational studies generate data sets that are then used to identify the instability mechanisms.

Three instability mechanisms are presented here, each being relevant to the work discussed in this document. The first two rely on vorticity to entrain fuel (or unburnt fuel products) and oxidizer, creating partially-mixed pockets of propellants primed for ignition. The second considers high pressure pulses that are capable of cutting off the fuel supply, modulating the heat release profile. These mechanisms are described in greater detail below.

This first mechanism considers the shedding of vortices off the back step. The oxidizer post can be tuned to provide an acoustic mode shape that places pressure or velocity nodes (or anti-nodes) in specific locations. A vortex is shed at the step in the presence of a velocity gradient [110–112]. A large velocity gradient at the dump plane can then be produced to generate strong vortices. The shed vortex enhances mixing of the fuel and oxidizer as it convects downstream. The expansion into the chamber directs the vortex away from the chamber axis and towards the wall. If the vortex remains coherent at the time of impingement on the wall, it can ignite and generate sudden and localized heat release. As the vortex breaks down, the heat release is spread out both spatially and temporally [96].

This mechanism is considered to be responsible for the instigating of instabilities at the short chamber length of 25.4 cm of the UEC. As described briefly in Section 2.4.1, changing the step height of the injector face resulted in a previously stable configuration becoming highly unstable, with the modification made based on the theory of vortex shedding and wall impingement. Simulation of the baseline and narrow injector face by Smith et al. [96] captured the mechanism in action. The underlying theory predicts that a vortex is shed when the velocity gradient is at its

greatest. According to acoustic theory, and the work of Poinsot et al. [111], this coincides when the pressure fluctuation is zero, or 90° after maximum pressure in the cycle. The vortex rolls out beyond the injector face towards the chamber wall. Literature disagrees where the ultimate impinging point of a vortex should be, varying between 2.5 [111] and around 5 step heights [113]. The value obtained from simulation of the UEC is around 4.5 step heights [96] and agrees with the work of Smith and Zukoski [110]. Entrapment of the fuel occurs as the shear layer is folded over, mixing fuel and oxidizer. As the vortex moves outwards, it begins to break apart. This is seen in Figure 2.28. At the first time step in the baseline case, the vortex remains intact shortly after it is shed. In the following two time steps, the outermost braid is severed. The downstream portion is convected further downstream, while the upstream portion is stretched. By the time it impinges on the wall, it is no longer coherent. Compare this to the narrow diameter configuration, where after the vortex is shed in time step one, it impinges on the wall within 0.1 ms. At this early in its life, the vortex is intact, such that the majority of it ignites, triggering sudden heat release. Alongside the heat release is a pressure pulse. This pressure pulse travels upstream through the post, where shortly after the pressure is at a maximum near the dump plane, another vortex is shed, closing the cycle.

The vortex-based mechanism which causes the CVRC to have bifurcated stability at the long oxidizer post length relies on pressure-induced baroclinic torque in the injection recess. This mechanism was studied through simulation by Harvazinski et al. [101], and a breakdown of the pressure and heat release for a cycle is shown in Figure 2.29. Compression at the head end generates pressure pulses that travels away from the dump plane in both directions. The axial gradient in pressure, coupled with the radial gradient in density at within the injection recess, generates vortices. These vortices roll up incoming fuel along with oxidizer, seen in Figure 2.29c. This creates premixed pockets that are convected downstream, Figure 2.29c and e. At this point the returning pressure pulse in the chamber has nearly reached the dump plane. By Time 5, the pressure pulse has reached the furthest downstream pockets,

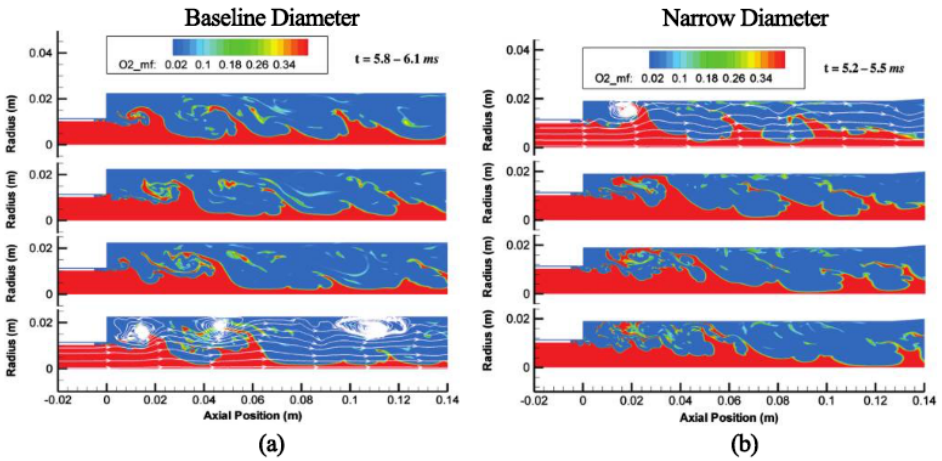

Figure 2.28.: Comparison of vortex shedding in the (a) baseline and (b) narrow diameter configurations of the UEC at a chamber length of 25.4 cm with a subsonic oxidizer post inlet. Snapshots are taken 0.1 ms intervals. One time step for each diameter includes instantaneous streamlines [96].

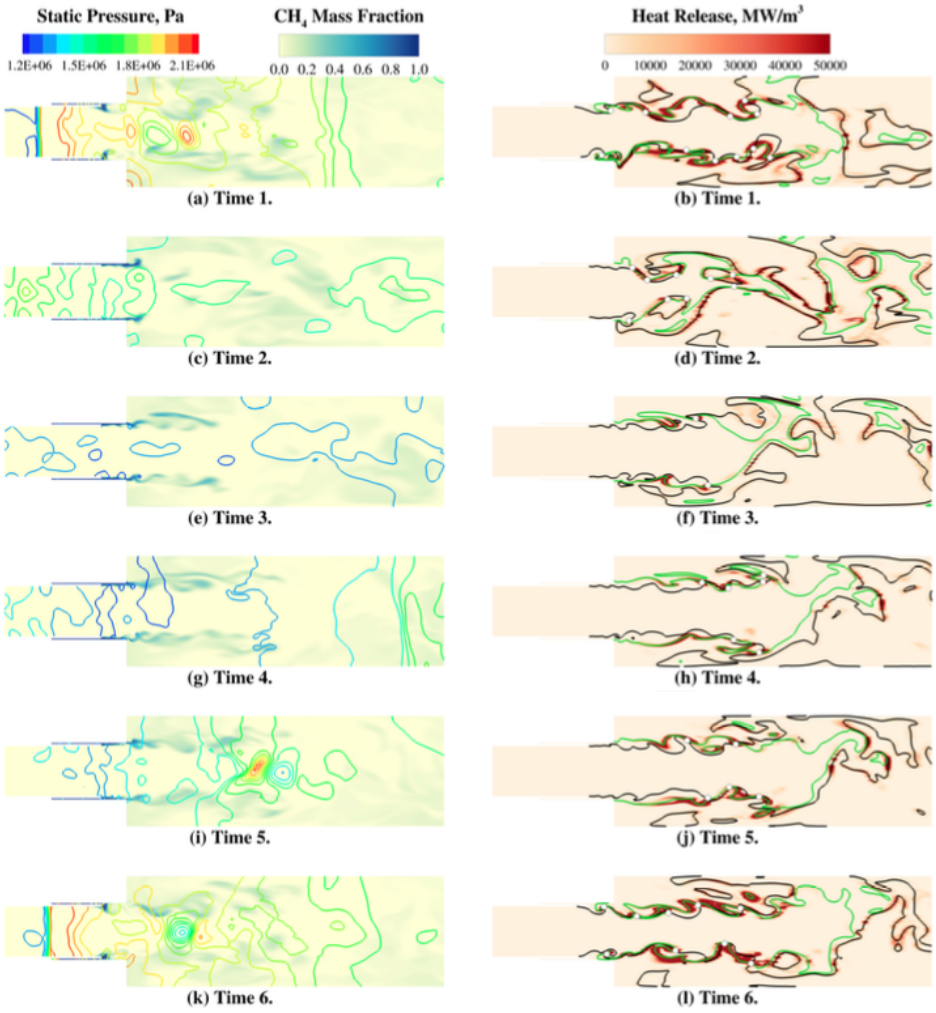

Figure 2.29.: Static press, methane mass fraction and heat release taken from six time steps within a single limit cycle from the CVRC at the 19.05 cm oxidizer post length [101]

igniting them, as made evident in Figure 2.29i and j. The majority of the fuel rapidly consumed, leading to another pressure pulse at the head end to close the loop.

At the middle oxidizer post length for the CVRC at 14 cm, a different mechanism drives the instability. This configuration generates pressure oscillations that are high enough to temporarily cut off fuel flow into the injection recess. While the initial mechanism that generated the pressure pulses strong enough to suppress fuel flow are still unknown, the transition to high amplitude, nonlinear oscillations are observed.

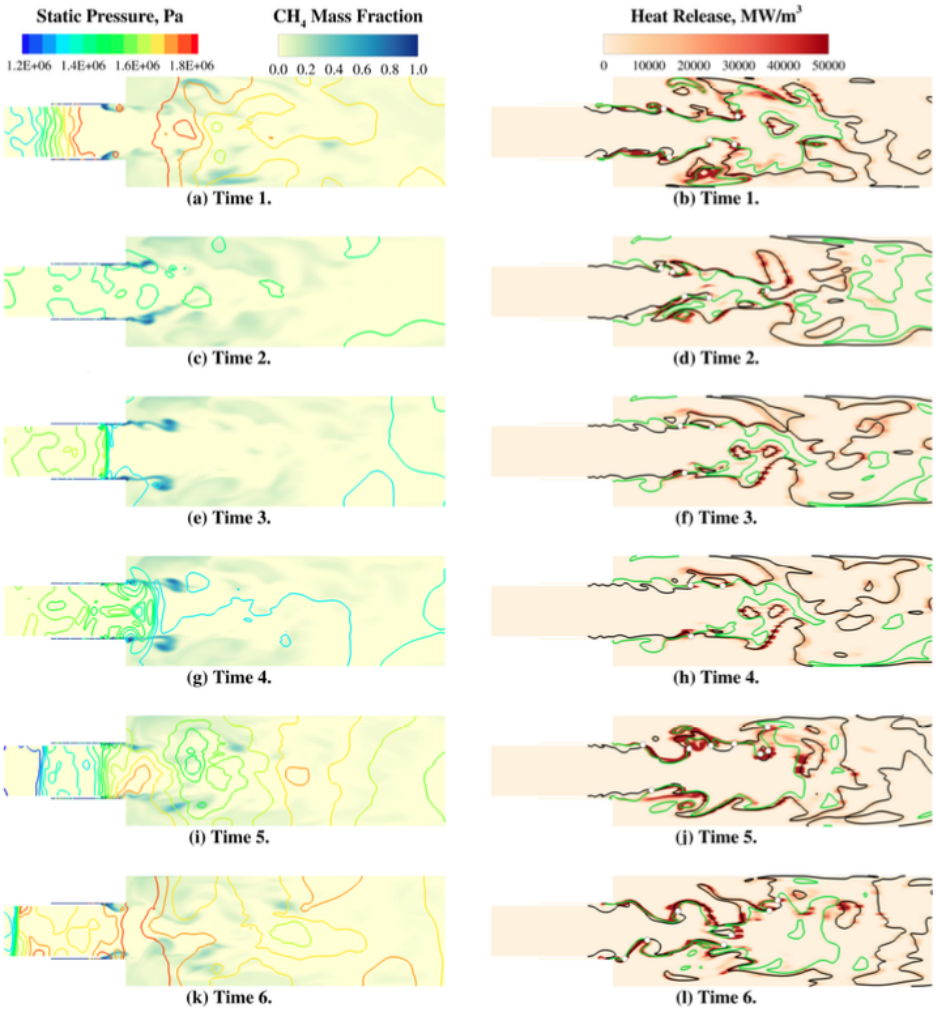

Figure 2.30.: Static press, methane mass fraction and heat release taken from six time steps within a single limit cycle from the CVRC at the 13.97 cm oxidizer post length [101]

A cycle of this mechanism in action is shown in Figure 2.30, comparing pressure and heat release.

The first step in the cycle shows a pressure pulse at the head end that travels upstream along the oxidizer post and downstream through the chamber. As it travels through the injection recess, it disrupts the fuel flow, seen in Figure 2.30a. At Time 2, expansion occurs at the head end and the blocked fuel now openly flows into

the chamber and begins to pool. At this time, the amount of heat release at the head end has dropped due to the temporary starvation of the fuel. At Time 3, the pressure pulse in the oxidizer post has returned to the injection recess. As it moves downstream, it pushes the fuel ahead of it, into the chamber, where, at Time 5, it ignites as it is hit by the returning chamber wave. The sudden increase in pressure and heat release drives another pressure pulse to restart the cycle. It is interesting to note that this condition results in one-dimensional pressure pulses at the dump plane. The pressure wave is distributed across the entire radius at a given axial location, unlike the mechanism driving the instability at the longest post length, where the pressure pulses are concentrated at the centerline.

These mechanisms are presented as instability drivers present in model combustors that led up to the DVRC experiment. As such, they were kept in mind during design and testing proven methods of achieving unstable combustion. Despite testing at similar acoustic timing profiles and geometries, the DVRC was unable to rely on these mechanisms to operate in an unstable mode. However, there are several differences between this combustor and the experiment that that can contribute to the difficulty in reaching self-excited instabilities in the DVRC. This includes the higher operating pressures of the DVRC by nearly a factor of three, the use of liquid fuel injected at transcritical conditions, and reliance on heated oxidizer instead of decomposed hydrogen peroxide.

2.6 Diagnostics

2.6.1 Low Frequency Pressure Measurements

Instrumentation is included in order to assess the conditions of the incoming fluids, the state of the testing hardware, as well as determining mean and fluctuating pressure levels. Installed measuring devices are split into two categories by their sampling rates. Low-frequency instrumentation, sampled at rates around 1000 Hz and lower, include thermocouples and static pressure transducers. System monitoring, as well as

mean or steady state conditions are determined through this class of instrumentation. The high-frequency instrumentation classification is reserved for sampling rates in the tens and hundreds of kHz and above. This class includes high-frequency pressure transducers

System pressures, such as manifold and chamber pressures, are used to monitor system health and ensure expected performance is met. Likewise, temperatures in these same locations can aid in identifying unexpected behaviors, such as unexpected vaporization in a liquid oxygen feed line.

Determining flow rates through venturis requires fluid measurements just upstream of the venturi. Under the assumption the venturi is choked, mass flow rate, $\dot{m}$ can be determined using the continuity equation, along with isentropic relations. Considerations for discharge coefficients, C_D, and in the case of gases, compressibility, β, are also included. This is expressed in terms of a sonic venturi in Equation (2.23), and cavitating venturi in Equation (2.24).

$$\dot{m} = C_d A \frac{P\sqrt{\gamma}}{\beta\sqrt{\frac{RT}{MW}}}\left(\frac{\gamma+1}{2}\right)^{-\left(\frac{\gamma+1}{2(\gamma-1)}\right)} \tag{2.23}$$

$$\dot{m} = C_d A\sqrt{2\Delta P\rho} \tag{2.24}$$

2.6.2 Thermocouples

Another low sampling speed instrumentation set, thermocouples monitor the temperature at metering locations, as well as measuring flow temperature at inlets and manifolds. Thermocouples embedded in the hardware can be used to measure heat loss to the environment, with multiple locations allowing for calculation of heat flux, such as into the chamber walls. The response time for a thermocouple increases as the size decreases, as the amount of probe volume needed to be heated is reduced. Likewise, junctions that are exposed directly to the probe field respond faster than those that are shielded.

2.6.3 High Frequency Pressure Measurements

High frequency instrumentation samples at speeds capable of resolving the rapidly evolving physics involved in turbulent combustion. There are a variety of instruments and measurement techniques available at this high sampling rate, from accelerometers, to thrust and force sensors, to ion probes that detect local ionization amounts. Two sensors are often used in the measurement and response of combustion fields. The first is the high frequency pressure transducers as they can directly measure the local dynamic acoustic pressure. The other are photomultiplier tubes, can capture variations and amplitudes of the light emitted from the combustion field. In this work, high frequency pressure transducers are installed throughout the chamber and oxidizer post to back out acoustic mode shapes. Related work on a similar injector utilized an array of photomultiplier tubes to study the combustion field near the injector [83].

2.7 Analysis Techniques

Acoustic measurements taken from confined, turbulent combustion contains pressure fluctuations that can be attributed to a number of sources. Various analysis techniques are applied to these signals to extract characteristic combustion behavior in order to study and understand it. The techniques used in this work are presented here, providing background information along with examples to illustrate usage of the techniques.

Prior to applying the techniques, the signal is conditioned by passing it through a high pass filter. This is done in order to remove the static, or DC component, of the signal. This reduces the signal to the dynamic component.

Filtering of the signal is conducted through Matlab. A high-pass Butterworth filter is created with a cut-off frequency of 75 Hz. This frequency was chosen to block out any noise associated with facility electrical interference and effects around 60 Hz, yet leave the signal otherwise intact. The high-pass filtered is then applied to signal

twice, first in the forward then the reverse direction to prevent phase distortion. The resulting signal can then be treated as quais-stationary with a mean of zero. The signal is then ready for processing through the various techniques described below.

2.7.1 Statistics

Direct interpretation of the raw, or even high-pass filtered, data remains difficult; multiple frequencies of constantly varying magnitudes overlaid on turbulent combustion noise. A statistics-based analytical approach provides quantitative means of not only understanding the data, but also metrics for comparison to other sets of data. This could be for data obtained from the same combustor at different conditions, or even simulated compared to experimentally acquired data. In this work, a handful of metrics are used to characterize the stability of the combustor. Comparisons between the results of different oxidizer temperatures, as well as acoustic profiles, are studied.

The range of dynamic pressure measured during combustion is useful for assessing the roughness of combustion, especially when normalized by the mean chamber pressure. The extreme 1% of the highest and lowest values are filtered out to remove outliers. Then, for a stationary signal, a wider range corresponds to stronger amplitude fluctuations occurring within the time trace. Likewise, a narrow range of fluctuations is indicative of steady, stable combustion.

The second statistical measurement derived from the pressure signals is the root mean square (RMS). The RMS provides a simple metric to compare signals between tests and locations. This is especially useful in the context of rapidly fluctuating signals with minimal forcing. A signal with a high RMS presents values with large deviations from the mean. This would likely represent an unstable behavior through large oscillations. A reduction in RMS would generally be considered a trend towards more stable and consistent condition.

2.7.2 Power Spectral Density

Identification of modal behavior in pressure signals is paramount in this work. This task is not always simple, as the presence of multiple frequencies can lead to complex waveforms. Estimation of the power across the frequency spectrum can be accomplished through the power spectral density (PSD). By knowing which frequencies are present in a signal, along with their magnitude, characterization of thermoacoustic instabilities is possible.

This analytical method first requires conversion of the signal into the frequency domain via Fourier transformation,

$$\hat{f}(\omega) = \int_{-\infty}^{\infty} f(t) e^{-2\pi i t \omega} dt \tag{2.25}$$

Equation (2.25) is only applicable to continuous data. For discrete data, the discrete Fourier transform is use instead, shown in Equation (2.26) for a general array of equally spaced measurements.

$$F_n = \sum_{k=0}^{N-1} f_k e^{-2\pi i n k/N} \tag{2.26}$$

The discrete power spectral density is then estimated in similar fashion.

$$P(\omega) = \frac{(\Delta t)^2}{T} \left| \sum_{k=0}^{N-1} f_k e^{-2\pi i n k/N} \right|^2 \tag{2.27}$$

The time between samples is represented by Δt, while the measurement time, $T = n\Delta t$, where n is the total number of samples. This estimate is referred to as a periodogram, and approaches the statistical true answer as the measurement time, T, approaches infinity.

The built in Matlab function, *periodogram*, was used to estimate the PSDs in this work. Proper use of the function requires the inclusion of a window to view the data. This suggests that the PSD estimate yielded through the periodogram can be biased, or is at least subject to external modification. That is, a good PSD estimate

is dependent on the proper usage of the applied window. A comprehensive look at the effects of windowing in the discrete Fourier transform can be found in Reference [114].

2.7.3 Cross-Correlation

The cross-correlation is a useful mathematical technique that describes the similarity of two signals. In the time domain, the cross-correlation is akin to the convolution. Conceptually, the cross-correlation essentially places one signal on top of the other. The first signal is then shifted through time, where the shared area under the curve is calculated. Generally, the higher the result of cross-correlation, the more similar the signals at a given moment in time.

In this work, cross-correlation is used to identify shared structures in acoustic signals. Unstable behavior in the form of acoustic forcing would present as coherent, periodic behavior throughout the chamber and into the injector at stronger amplitudes. This large scale behavior can be identified through cross-correlation. Phase information is also collected by the inherent time lag calculation.

The mathematical formulation for cross-correlation is written in Equation (2.28).

$$(f \star g)(\tau) = \int_{-\infty}^{\infty} \hat{f}(t) g(t+\tau) dt \tag{2.28}$$

The cross-correlation of two signals, f and g, is the convolution of the complex conjugate of f, $\hat{f}$, with g. This approach only applies to continuous functions, and for discretized data, a similarly discrete form of cross-correlation is required, in the form found in Equation (2.29).

$$(f \star g)(\tau) = \sum_{m=-\infty}^{\infty} \hat{f}[m] g[m+n] \tag{2.29}$$

In the case of stationary signals of stochastic processes, the cross-correlation can be represented as a normalized measure of the cross-covariance. The covariance between two random variables, X and Y, is considered the expected product of the deviations of those variables from their respective expected values,

$$\mathrm{cov}(X,Y) = \langle (X - \mu_X)(Y - \mu_Y) \rangle = \langle XY \rangle - \mu_X \mu_Y, \tag{2.30}$$

where μ_X and μ_Y are the mean values of X and Y, respectively. Equation (2.30) can then be written out as

$$\mathrm{cov}(X,Y) = \sigma_{XY} = \sum_{i=1}^{N} \frac{(x_i - \mu_X)(y_i - \mu_Y)}{N} \tag{2.31}$$

Correlation then requires a nonzero covariance. A positive convariance implies that variables X and Y tend to increase together. Negative covariance implies that as once increases, the other tends to decrease.

In the special case where $Y = X$, the covariance reduces to the variance of X, or $\mathrm{cov}(X,Y) = \sigma_X^2$, or the square of the standard deviation of X, σ_X.

The cross-correlation can be written out based on the standard deviation,

$$\mathrm{cor}(X,Y) = \frac{\mathrm{cov}(X,Y)}{\sigma_X \sigma_Y} = \frac{\sigma_{XY}}{\sqrt{\sigma_{XX}\sigma_{YY}}} \tag{2.32}$$

This correlation is normalized, as can be seen through the autocorrelation. Taking again the special case of where $Y = X$, the autocorrelation is written out as below.

$$\mathrm{cor}(X_i, X_i) = \frac{\mathrm{cov}(X_i, X_i)}{\sigma_i^2} = 1 \tag{2.33}$$

The cross-correlation can then be used to analyze the similarity of structures between two signals, or to itself at different times.

Coherence is a similar metric, representing the correlation of two signals, but on a frequency basis. For stationary signals, it can be taken as an estimate of the causality between the input and output at some frequency. Values are normalized between 0 and 1. A coherence of zero indicates the two signals are completely unrelated, while a coherence of unity indicates a linear dependency between input and output.

The coherence between two signals is written out below,

$$C_{xy}(\omega) = \frac{|P_{xy}(\omega)^2|}{P_{xx}(\omega)P_{yy}(\omega)}. \tag{2.34}$$

The coherence is also referred to as the magnitude-squared coherence due to the squared term in the numerator. It can be seen that the coherence is simply the ratio of the square of the cross power spectral density to the product of the power

spectra of the two signals. The results of coherence can then inform interpretation of the cross-correlation results, providing a measure of confidence as a function of frequency.

2.7.4 Continuous Wavelet Transform

Many of the above analysis methods rely on the assumption that the pressure signals are stationary, with stable statistical properties. This assumption does not always hold in high pressure turbulent combustion, prompting the use of alternative methods of analysis. Wavelet analysis is one such method [115]. The continuous wavelet transform (CWT) is used in this work.

The CWT of a signal $x(t) \in L^2\mathbb{R}$ the projection of the signal onto a map of scaled and translated wavelet functions, $\psi(t)$,

$$W(\tau, s) = \int_{-\infty}^{\infty} \frac{1}{s}\psi^{\star}\left(\frac{t-\tau}{s}\right)x(t)dt \tag{2.35}$$

Or, more in line with Fourier transformation, the CWT is presented as,

$$W(\tau, s) = \int_{-\infty}^{\infty} \mathbf{\Psi}^{\star}(s\omega)X(\omega)e^{i\omega t}d\omega. \tag{2.36}$$

Here, $\mathbf{\Psi}$ is the Fourier transform of the wavelet, $\int_{-\infty}^{\infty}\psi(t)e^{-i\omega t}dt$, and $X(\omega)$ the Fourier transform of the signal, $x(t)$. The coefficient $1/s$ is a normalization factor, often substituted by $1/\sqrt{s}$. The format presented is more convenient when working with oscillatory signals [116].

The wavelet function family is the result of scaling and translating the mother wavelet, ψ. The mother wavelet can be chosen from a number of functions that satisfy the following conditions. First, it must have a mean of zero. Second, it must satisfy the admissibility condition [117],

$$C_{\psi} \equiv \int_{-\infty}^{\infty} \frac{|\Psi(\omega)|^2}{|\omega|}d\omega < \infty. \tag{2.37}$$

This, however, is considered to be only a weak requirement. Third, to be considered analytic, $\Psi(\omega) = 0$ for $\omega < 0$.

Having analyticity is an important trait for a wavelet. It has been shown by Olhede and Walden [118] that when a wavelet is not precisely analytic, it can demonstrate leakage to negative frequencies, resulting in spurious variation of the transform phase. This issue can scale with time resolution, having little to no effect at one scale, but causing drastic, erroneous changes at another scale.

The properties of the transform are dictated by the wavelet family choice. The estimate of instantaneous amplitude, phase and frequency of the transformation is modulated by the choice of wavelet function. The built-in continuous wavelet transformation Matlab function, *cwt*, provides three family options. A primer on those three, *Morlet*, *Morse* and *Bump* is provided here.

The first option is the Morlet wavelet [117],

$$\psi_\omega(t) = a_\omega \mathrm{e}^{-\frac{1}{2}t^2}\left[\mathrm{e}^{i\omega t} - \mathrm{e}^{-\frac{1}{2}\omega^2}\right] \tag{2.38}$$

The normalization coefficient, a_{ω_0}, is often defined as,

$$a_{\omega_0} \equiv 2\frac{\omega_{0_P}}{\omega_0}\mathrm{e}^{\frac{1}{2}(\omega_{0_P}-\omega_0)^2}. \tag{2.39}$$

Here ω_{0_P} is the peak frequency where the first derivative of the wavelet vanishes. This wavelet has four interesting properties that have launched it into being the most used wavelet [115]. First, this wavelet is analytic. Second, the peak frequency, $\omega^P_{\psi_{\omega_0}}$, the energy frequency, $\omega^E_{\psi_{\omega_0}}$, and central instantaneous frequency, $\omega^I_{\psi_{\omega_0}}$, are equal, which streamlines the conversion from scales to frequencies. Third, the wavelet optimizes the joint time-frequency localization operator. The CWT requires a trade-off of time and frequency resolution, akin to the Heisenberg uncertainty principle, demonstrated in Figure 2.31. At Time 1, the time is well resolved but with a wide frequency window, and vice versa at Time 2. Transformation via this wavelet minimizes the uncertainty, $\sigma_{t;\psi_{\omega_0}} = \sigma_{\omega;\psi_{\omega_0}} = 1/2$. And fourth, the time radius and frequency radius are equal, representing the best compromise between time and frequency resolution.

The form presented in Equation (2.38) is not precisely analytic. The wavelet becomes unsuitable for use when ω_0 becomes sufficiently large [119]. In these situations, another wavelet should be selected.

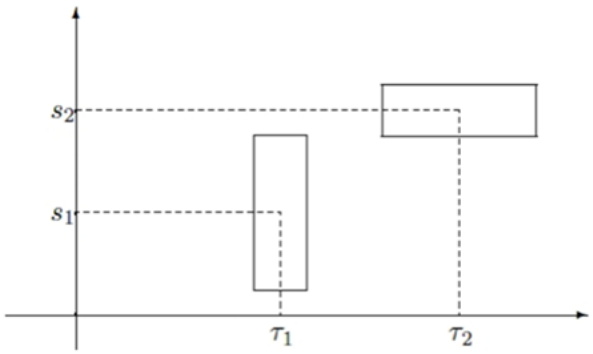

Figure 2.31.: Demonstration of the trade-off relationship between temporal and frequency resolution for the CWT, similar to the Heisenberg uncertainty principle. At Time 1, the time is well-resolved, but spread across a wide frequency range, and vice versa for Time 2 [115].

The generalized Morse wavelet fulfills the requirement of being precisely analytic for all frequencies. This wavelet is defined, in the frequency domain, as,

$$\Psi_{\beta,\gamma}(\omega) = K_{\beta,\gamma} H(\omega) \omega^{\beta} \mathrm{e}^{-\omega^{\gamma}}, \tag{2.40}$$

where $K_{\beta,\gamma}$ is the normalizing coefficient and $H(\omega)$ the Heaviside unit step function. The parameters β and γ must be both real and positive for the Morse wavelet to be analytic. The wide acceptable range of values permits the wavelet to be versatile. However, it is not possible to directly convert scales to frequencies like it is for the Morlet wavelet.

The final wavelet family mentioned here is the bump wavelet. This wavelet places an emphasis on frequency resolution, as illustrated below,

$$\Psi(\omega) = \mathrm{e}^{1-\frac{1}{1-(\frac{\omega-\mu}{\sigma})^2}} \chi_{[\mu-\sigma,\mu+\sigma]}, \tag{2.41}$$

where χ_I is the indicator function of the set I. This wavelet permits the peak frequency, $\omega_\Psi = \mu$, greatly increasing frequency resolution.

The CWT analysis presented in this work uses the bump wavelet. All three wavelets discussed here have sufficient temporal resolution, so the increased frequency resolution afforded by the bump wavelet makes it a more attractive option. When the oxidizer post length is near that of a half-wave resonator, the natural frequencies of the post and chamber converge. A wavelet that prioritizes frequency resolution would better enable identification of near-by acoustic modes.

3. EXPERIMENTAL APPROACH

There were two objectives set for this work. The first was to build a suite of validation data at a variety of configurations in the use of testing computational models. The second was to further understand the dynamics of a gas-centered swirl coaxial (GCSC) injector as it relates to the condition of the oxidizer as it enters the injector. Assessment of the stability of the combustor relies on previously utilized methods of varying geometry to augment the acoustic field.

To achieve these goals, experiments were conducted on a model rocket combustor known as the Discretely Variable Resonance Combustor (DVRC) at the Zucrow Laboratories at Purdue University. This combustor served as a test bed to study an RD-170 injector design, emulating oxidizer-rich staged combustion on a single GCSC injector with liquid hydrocarbon fuel. A modular design allowed for a parametric investigation of the response of the injector to various acoustic profiles, as well as different oxidizer and fuel inlet conditions. Furthermore, easily modelable boundary conditions were implemented to collect data for validation of simulations.

In this document, the term acoustic profile is coined to represent the equivalent wavelength of the oxidizer post in relation to the fundamental chamber longitudinal mode. For a set chamber length, increasing the oxidizer post length will increase the acoustic profile. The same acoustic profile can be produced through different oxidizer post and combustor lengths, as well as changing conditions of domains. For example, a reduction in oxidizer temperature lowers the local sound speed. This in turn reduces the acoustic profile, as the natural resonant frequency decreases, effectively shortening the post. A shared acoustic profile between two configurations means that although the fundamental frequencies are different, the spatial distribution of the mode shapes are the same between the two. A post acting as a 1/2-wave resonator for the chamber

will always have an anti-node at the inlet and dump plane for the first chamber mode, and by definition share the same frequency.

This chapter outlines the design methodology of the DVRC through descriptions and discussions of the integral components and their effects. A discussion on acoustics, specifically acoustic impedance and the linearized Euler equation, is presented. The former is used to define the expected level of reflection and transmission of acoustic energy between media at an interface, as this value is expected to influence post/chamber coupling. The latter assists in determining the acoustic profile of the system and was employed to select particular geometry configurations. Following this is a discussion of the design and testing requirements of the initial validation effort and conditions/configurations of the collected data sets, and a description of the test facility, including descriptions and usage of installed instrumentation and an outline of the test procedure.

3.1 Chamber Design

3.1.1 Overview

The DVRC is a single-element liquid fueled model rocket engine designed to test the capability and accuracy of high-fidelity simulations at predicting self-excited instabilities. To that order, the combustor is designed to allow for changing of independent test variables, such as oxidizer post length or inlet type. The experiment is highly instrumented so that statistically meaningful data representing different stability behavior can be obtained. A cutaway of the experiment is shown in Figure 3.1, and a cutaway of the injector element in Figure 3.2.

Oxygen is combusted with hydrogen in a preburner at high O/F ratios to generate warm oxidizer, simulating the oxidizer-rich staged combustion cycle relied upon in many high-power first stage engines, such as the proven RD family of Russian made engines, or currently in development domestic designs like the AR1 by Aerojet Rocketdyne or the BE-4 from Blue Origin.The warm oxygen from the preburner enters the

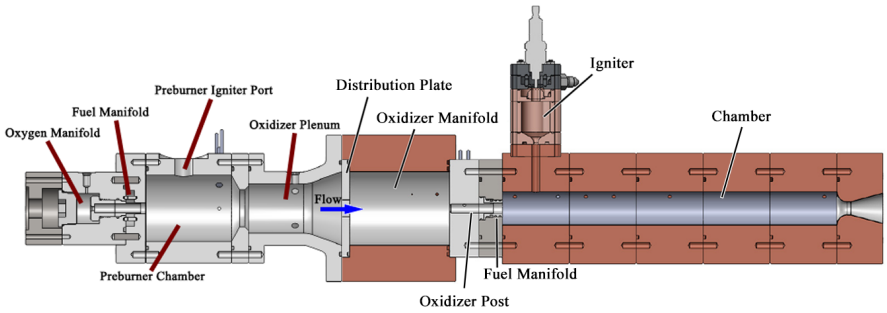

Figure 3.1.: Cutaway diagram of the baseline configuration of the DVRC, featuring original preburner design, subsonic oxidizer inlet, 3/8-wave resonator post configuration (5.27 cm long), and 34.10 cm chamber length.

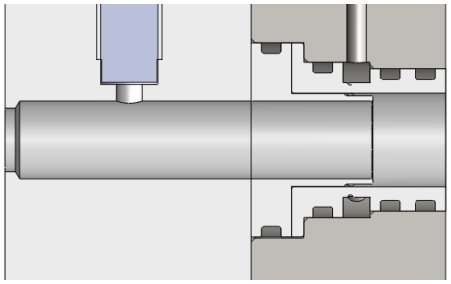

Figure 3.2.: Cutaway diagram of the baseline injector of the DVRC at 5.27 cm long with a subsonic inlet.

plenum, where a distribution plate chokes the flow as it enters the oxidizer manifold. The oxidizer then enters the oxidizer post, through either a subsonic or a choked inlet. A coaxial fuel annulus surrounds the downstream end of the oxidizer post. Liquid fuel is injected from the manifold into the annulus tangentially, providing circumferential velocity to stabilize the liquid. A collar separates the fuel annulus and oxidizer post. Mixing begins in the swirl cup, where the collar terminates, exposing the liquid fuel to the high-velocity oxidizer gas. At the end of the swirl cup is a backwards facing step that opens up to the chamber. The main chamber igniter is installed near the head end of the chamber. The chamber is a cylinder with a constant diameter, terminated at the downstream end by a shortened nozzle with a sharp contraction profile that promotes reflection of acoustic waves. Expansion of the throat in a small nozzle reduces the exit pressure. Dimensions of various sections of the experiment are contained in Table 3.1. Ranges for the oxidizer post length and chamber length are also provided.

3.1.2 Boundary Conditions

Matching of boundary conditions is required to best reach parity between experimental and simulation results. Two boundary conditions were considered critical: 1) oxidizer inflow conditions, and 2) heat transfer in combustion chamber. These, and other boundary conditions are discussed here.

As discussed earlier in this document, the Continuously Variable Resonance Combustor (CVRC) was a test bed for capturing validation data of a shear coaxial injector featuring decomposed hydrogen peroxide and gaseous methane. Comparison of the experiment and simulation results showed a discrepancy between the frequencies of the acoustics modes, consistent in both stable and unstable operation [23, 120]. This can be seen in the frequency spectrum of the pressure signal taken from the chamber, shown in Figure 3.3. In both cases, the experiment shows the 1L acoustic mode to be

Table 3.1.: Nominal dimensions for various DVRC geometries.

Geometry	Dimension
Oxidizer Plenum Diameter	7.62 cm
Oxidizer Plenum Length	5.08 cm
Oxidizer Manifold Diameter	7.62 cm
Oxidizer Manifold Length	10.16 cm
Oxidizer Post Diameter	0.95 cm
Oxidizer Post Length	5.27 - 14.36 cm
Swirl Cup Diameter	1.15 cm
Swirl Cup Length	0.89 cm
Collar Thickness	0.06 cm
Chamber Diameter	3.39 cm
Chamber Length	20.46 - 38.47 cm
Throat Diameter	1.33 cm

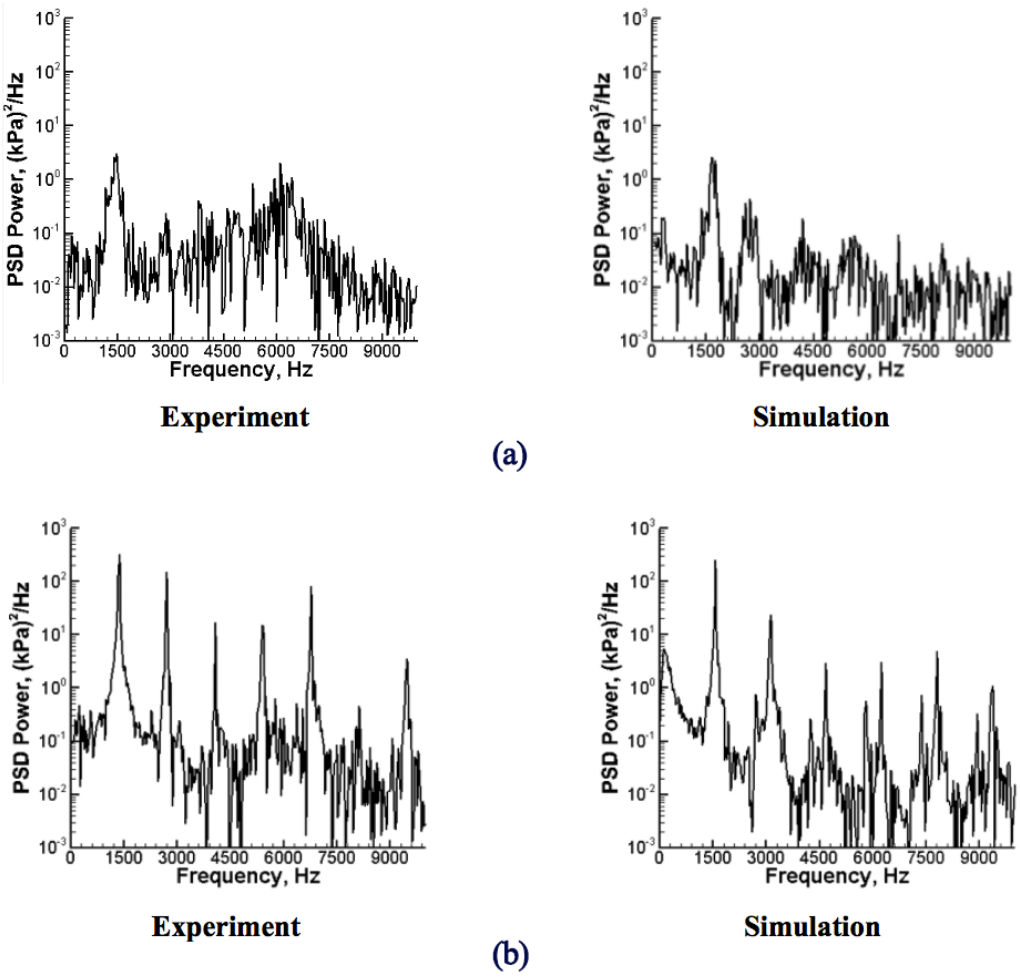

Figure 3.3.: Comparison of frequency spectrum of pressure signals taken from aft end of chamber during (a) stable operation and (b) unstable operation between experiment and simulation results [23].

around 1375 Hz, while the simulation predicts it to be around 1567 Hz. That shift is amplified in the harmonics.

Garby, et al studied the effects of chamber wall heat loss on an LES of the CVRC experiment [121]. In this work, it was shown that heat loss through the walls had a stabilizing effect by cooling the burnt gases trapped in the recirculation zone. While the experiment cannot perfectly match a simulated adiabatic boundary condition,

heat loss can be minimized through the use of material with a low heat transfer coefficient lining the inside diameter of the chamber.

Harvazinski et al. [122] also studied the impact of chamber wall temperature. Two-dimensional axisymmetric simulations of the CVRC with fixed wall temperatures representing heat loss were conducted at the most unstable geometric configuration with an oxidizer post length of 13.97 cm. Different levels of pressure fluctuations as well as mean conditions were exhibited. The baseline configuration, utilizing an adiabatic boundary condition at the walls, reached pressure oscillations of 135.19 kPa, or 9% of the mean chamber pressure. When the wall temperature was fixed at a reduced temperature of 1200 K, the oscillations dropped to a peak-to-peak level of 40.04 kPa, or 3%. Further reduction of wall temperature to 900 K resulted in oscillations at 27.34 kPa, 2%.

Yttria-stabilized zirconia is the current industry standard thermal barrier coating (TBC), with a proven experience and thermal conductivity values between 2 and 4 $\frac{W}{mK}$ (0.35 and 0.70$\frac{Btu}{ft^2/^\circ F/hr}$), as shown in Figure 3.5. A 0.38 mm thick layer of TBC was applied to the inner diameter of the chamber, as well as oxidizer manifold and plenum. The sections with TBC application were made of oxygen-free copper alloy C11000, which served as a heat sink for what heat was lost through the walls. Remaining components were made of Inconel 600, which is oxygen compatible and has a relatively low thermal conductivity value around 2.78 15.8$\frac{W}{mK}$ ($\frac{Btu}{ft^2/^\circ F/hr}$).

To estimate heat loss through the walls, several pairs of thermocouples were installed at various axial locations along the chamber. The thermocouple pairings were embedded at different depths, with one 0.32 cm and the other 0.73 cm away from the inner diameter (including TBC). Together, temperature readings from each pairing, alongside knowledge of the gases in combustion chamber and properties of the materials, would provide estimates of the wall heat flux and temperature at the wall. Examples of embedded wall temperatures throughout a test sequence are shown in Figure 3.6, comparing results from shallow and deep embedded thermocouples through the test, as well as an axial distribution at the end of hotfire.

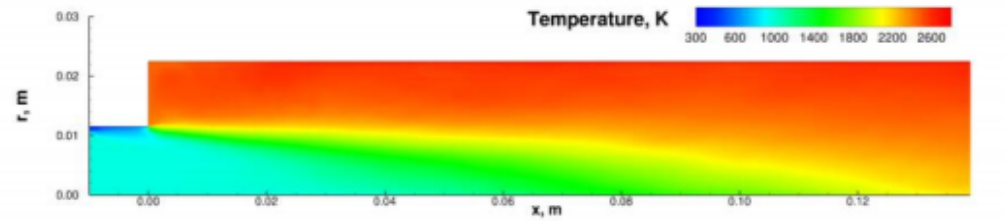

(a) Case BL.

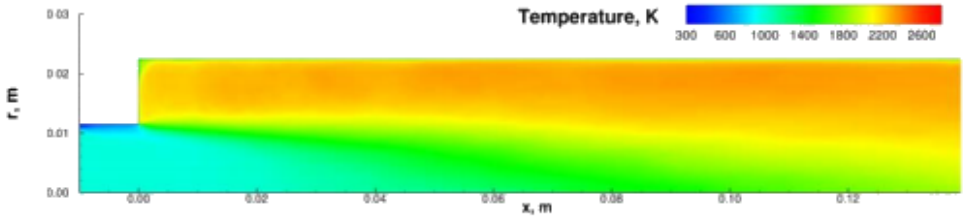

(d) Case TW-3.

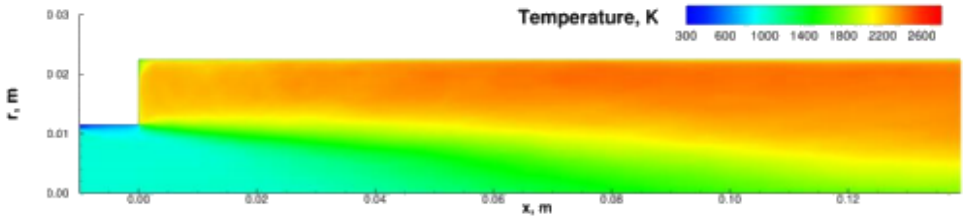

(e) Case TW-4.

Figure 3.4.: Time-averaged temperature in a combustor four simulation cases where defined wall temperature was varied: (a) adiabatic, (b) T = 300 K, (c) T = 600 K, (d) T = 900 K, (e) T = 1200 K [122].

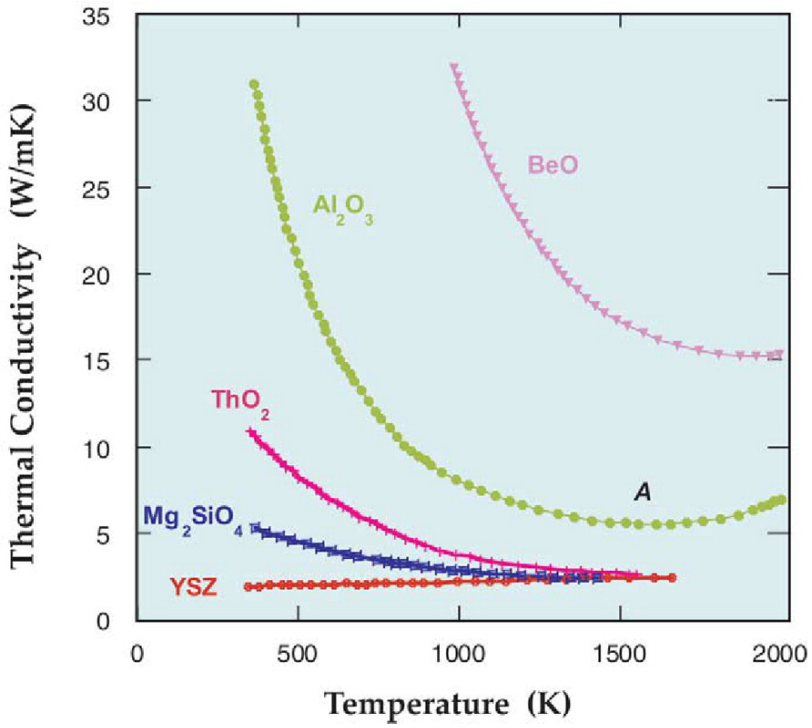

Figure 3.5.: Comparison of thermal conductivity of various thermal barrier coatings across a range of temperatures [123].

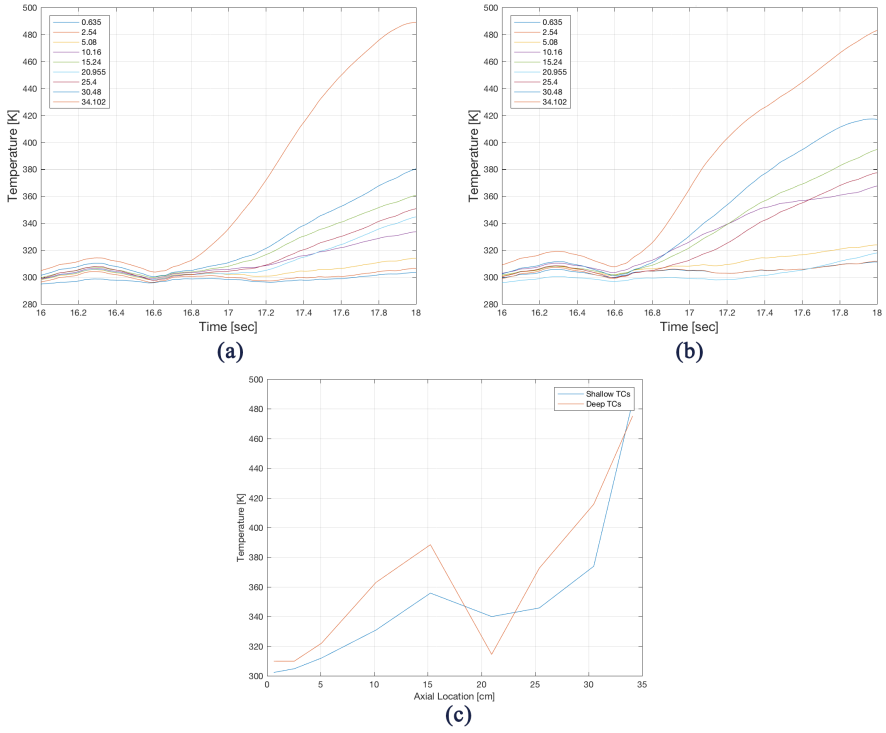

Figure 3.6.: Temperature measurements taken along the chamber in the DVRC for (a) shallow and (b) deep embedded thermocouples during hotfire operation, and (c) axial distribution for shallow and deep thermocouples at end of hotfire.

Modeling of discrete injection points requires more computational resources than a uniform inlet. However, achieving such a uniform distribution of flow in an experimental setting is unlikely, especially at a large cross-sectional area like the oxidizer manifold. A suitable compromise is to use a distribution plate in the experiment. Numerous small holes inject the oxidizer at various radial and azimuthal locations, where a large pressure drop ensures even flow distribution across those holes. This replicates the uniform inflow boundary condition of the simulation, while also acoustically closing the oxidizer manifold. In configurations where the oxidizer post inlet is choked, the oxidizer manifold is fully decoupled from the downstream components with the choking orifice playing the role of the inflow in the simulation.

Modeling of the fuel inlets differs from the experiment. In the experiment, the fuel manifold feeds the fuel annulus via several discrete tangential holes. The tangential orientation provides the azimuthal momentum needed to swirl the liquid fuel. In a three-dimensional simulation, it is possible to capture this geometry, but not directly in two-dimensions. In 2D simulations, the fuel manifold and tangential inlets are not modeled. Instead, the fuel is introduced directly into the fuel annulus, where the bulk mass flow rate and geometry of the annulus define the axial velocity, while an independent azimuthal velocity component is superimposed [124].

A short nozzle is used to converge from the chamber diameter to the throat. This is done to better approximate an acoustically closed boundary used in linear models. It was shown that mean flow effects causes the short nozzle to deviate from a fully-reflecting boundary [93, 103]. Instrumentation located near the nozzle should be included to assess the applicability of treating the nozzle as a boundary with zero admittance.

3.1.3 Preburner

To best simulate the ORSC cycle used in next generation engines, heated oxidizer was generated through lean combustion of gaseous oxygen and hydrogen in a pre-

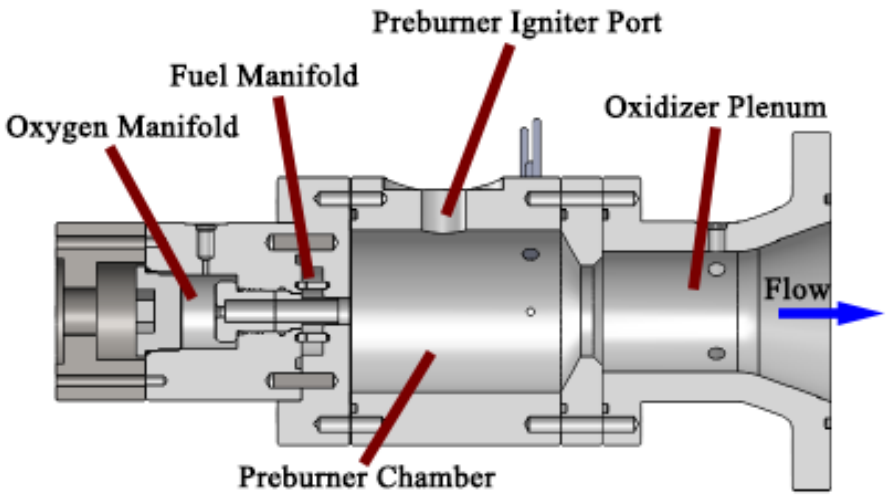

Figure 3.7.: A cutaway of the preburner for the DVRC. Labels of the various components are provided.

burner. Varying the O/F ratio by adjusting the mass flow of the hydrogen allows for control across a wide range of oxidizer temperatures. The preburner design permitted operation of O/F ratios from 120 to 340 for a preburner chamber temperature range from 650 to 1200 K.

A cutaway of the preburner is shown in Figure 3.7, with labels of the various components. Oxygen is injected into a manifold before entering axially into a post. Gaseous hydrogen is then introduced radially through four inlets directly into the oxygen jet. An igniter is installed within the preburner chamber, serving as the source of ignition. From the chamber, the hot oxidizer enters the oxidizer plenum, which then expands to meet the distribution plate that conditions the flow as it enters the oxidizer manifold of the main chamber.

3.1.4 Oxidizer

The oxidizer temperature is a central parameter in this work, as varying it had a direct impact on the amplitude of pressure fluctuations in the system. This small

adjustment has a drastic impact on a number of injection parameters. First, changing the temperature inherently changes other thermophysical properties, such as density and sound speed. This then affects injection parameters, such as the velocity and Mach number in the oxidizer post, and subsequently the momentum flux ratio.

Two oxidizer temperatures are targeted in this work. The higher temperature, reached through combustion of oxygen and hydrogen at high O/F ratios in the pre-burner, is around 690 K. The lower temperature is the temperature of the gaseous oxygen as it is stored in the gas cylinders, kept at ambient conditions.

The temperature effects on the thermophysical properties and injection parameters is illustrated in Figures 3.8 and 3.9. The change in density is quite dramatic, jumping from 22.2 kg/m^3 at hot oxidizer conditions up to 55.6 kg/m^3 with the ambient oxidizer. This is a 250% increase. The rise in specific heat ratio is also considerable, increasing from 1.347 at 686 K to 1.485 at 285 K, corresponding to a 10% increase. The sound speed, post velocity and Mach number for the oxidizer trends in the other direction, increasing with temperature. The sound speed shifts from 495 to 322 m/s between the hot and ambient oxidizer conditions, resulting in a mean flow velocity of 159 and 63 m/s, respectively. The Mach number is then found to change from 0.32 and 0.20 at these two conditions.

Thee effects of these parameters on the injection process is discussed below in Section 3.1.6. It is more difficult to quantify the effect the change in temperature will have on the ignition process, such as ignition delay. A reduction in temperature will leader to a lower reaction rate for a given volume of fuel. A heated pre-mixed packet of propellants would be expected to ignite before the same packet initially at a cooler temperature. It is not only initial temperature that will affect the reaction rate. Physical state of the propellant, local mixture ratio, and vaporization/atomization rates are among the factors that can influence the process of converting non-premixed propellants into combustion.

The effect of water vapor addition on chemical kinetics and ignition delay was studied by Le Cong and Dagaut [125]. A methane/oxygen/argon mixture, along

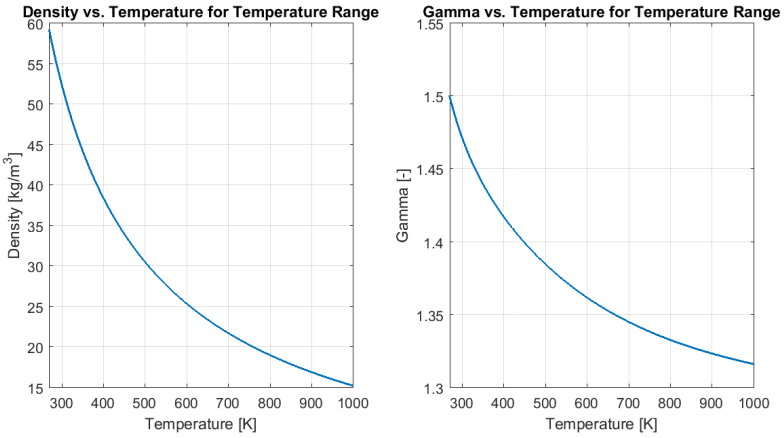

Figure 3.8.: Variation in density (left) and specific heat ratio (right) for oxidizer with temperature variation.

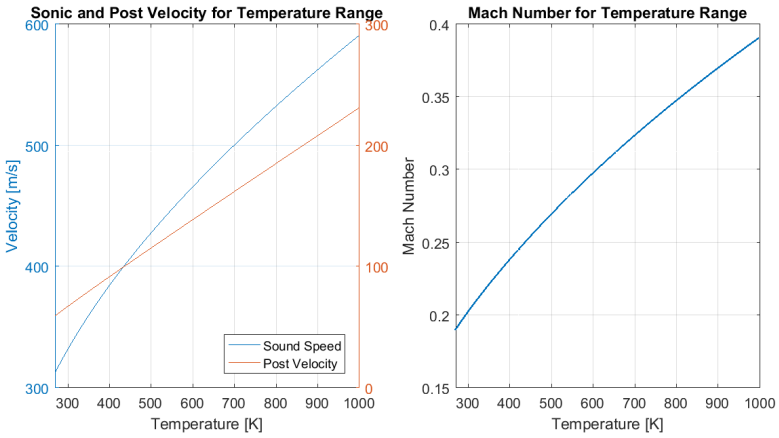

Figure 3.9.: Variation in sound speed and velocity (left), and Mach number (right) of oxidizer with temperature variation.

with a hydrogen/air mixture were both examined. For the methane/oxygen/argon mixture, the addition of 17% water led to an increase in ignition delay of two to three times that without water content, along with a reduction in reaction rate. For the hydrogen/air mixture, the difference in ignition delay between 0% and 25% water vapor content was often an order of magnitude.

Umphrey et al. [126] studied a kerosene-fueled GCSC injector with heated oxidizer. In this work, the injector was tested at low and high power configurations, with a short and long swirl cup. The low power with shortened swirl cup configuration is fairly representative of the DVRC operating at reduced oxidizer temperatures. In this simulation, a secondary recirculation is identified near the dump plane. With a longer cup, the resulting enhanced mixing causes this recirculation zone to deteriorate. Increasing combustor power level, which also increases oxidizer temperature, further eradicates the recirculation zone. The increased presence of the secondary recirculation zone is noted to coincide with a decrease in combustion stability. Following this work, a similar change may be expected to occur in the DVRC with a decrease in oxidizer temperature.

3.1.5 Fuel

Based on the requirements for acquiring the validation sets, the initial liquid fuel was RP-2. RP-2 is a hydrocarbon mixture containing 28 major constituents, comprising linear and branched paraffins, one- and two-ring cyclic paraffins of 11-16 carbon atoms, and does contain significant aromatic or olefin content [127]. n-Dodecane, a liquid linear alkane hydrocarbon with the chemical formula C12H26, and one of many constituents that comprise RP-2. A comparison of fuel properties is shown in Table 3.2.

Later, while examining the effects of oxidizer temperature, the RP-2 was replaced with dodecane. Dodecane is often used as a surrogate for RP-2 in simulations involving liquid hydrocarbon fuels [124, 126], which can be modeled computationally

Table 3.2.: Comparison of Thermophysical Properties for RP-2 and dodecane. RP-2 properties come from References [100, 128], dodecane properties from [100], and † [129].

Property	RP-2	Dodecane
Molecular Formula	$C_{11.74}H_{23.40}$	$C_{12}H_{26}$
Molecular Mass [kg/kmol]	164.6	170.3
Density [kg/m^3]	806	751
Critical Temperature [K]	678	658
Critical Pressure [MPa]	2.204	1.82
Kinematic Viscosity [cSt]	2.27	1.99
Thermal Conductivity [W/mK]	0.111†	0.137†
Specific Heat [kJ/kg K]	2.09	2.21

following a fourteen-step mechanism using nine species [130]. As is evident in Table 3.2, the two fluids have similar thermophysical properties. The most glaring discrepancy is in density, where there is approximately a 7% difference. This would suggest that, as long as chemical effects are similar, substituting dodecane for RP-2 should preserve injector characteristics, such as velocity or momentum flux ratio, and therefore the bulk hydrodynamics.

Another benefit of dodecane over RP-2 is the removal of aromatic components. While RP-2 already has a reduced amount of aromatics compared to its counterpart, RP-1, it still contains a very small percentage. Dodecane, on the other hand, is not a mixture but a single chemical formula, $CH_3(CH_2)_{10}CH_3$. As such, it does not contain aromatics like benzene, which could contribute to sooting [131]. A minimization of soot was desired for optical tests in order to achieve improved optical accessibility of the combustion.

Accurate modeling of dodecane combustion requires numerous element reactions and several dozen chemical species, representing only a fraction of the actual reactions and species involved [132,133]. In the more complicated models, the heat release field is shown to be much wider than that of one generated with fewer chemical reactions and intermediate species [107]. Following the Rayleigh Criterion, it would be expected that a less detailed reaction, yielding a narrower heat release field due to the artificial rapidity of the reaction, could generate higher levels of instabilities, provided the heat release field is located near and in sync with pressure oscillations. The full chemical pathway of the liquid fuel, then, provides a number of routes producing varying amounts of heat release. This would lead to a broader distribution of the heat release of kerosene combustion, compared to other fuels with less complex chemical pathways such as gaseous hydrogen or methane. This broader distribution would act to dampen instabilities by resisting the sharp organizing effects of a thermoacoustic coupling through the presence of low-scale de-tuning of increased heat release at the edges of the distribution. It was shown with several variations of kerosene that there can be an appreciable amount of time between initial to final point of combustion for

a single droplet. In the study of GTL kerosene, Exxsol D80 and Jet A-1, Burkert and Paa measured the initial and total ignition delay of droplets [134]. Initial ignition varied between 200 ms and 1200 ms, depending on fuel variant and temperature. Total ignition time then required between 400 ms to 1200 ms. Higher temperatures yielded lower delay times, both initial and total. In the context of the DVRC with dodecane injected at room temperature, a sizeable window between initial and total ignition time would be expected.

Similar results were found with China No. 3 aviation kerosene. Liang et al. [135] showed that there was a logarithmic relationship between temperature and ignition delay, where increasing the temperature exponentially decreased the delay.

3.1.6 Injector Design

The methodology of swirler design discussed in Section 2.2.2 will be applied to the DVRC as a means of characterizing it. Relevant geometrical parameters are listed in Table 3.3. These dimensions are shown in Figure 3.10

Table 3.3.: DVRC Injector Geometry Parameters

Parameter	Dimension [cm]
r_p	0.48
r_{sw}	0.57
r_{in}	0.53
$r_{f,in}$	0.05
h	0.06
n	8
L_{sw}	0.89
RR	0.94

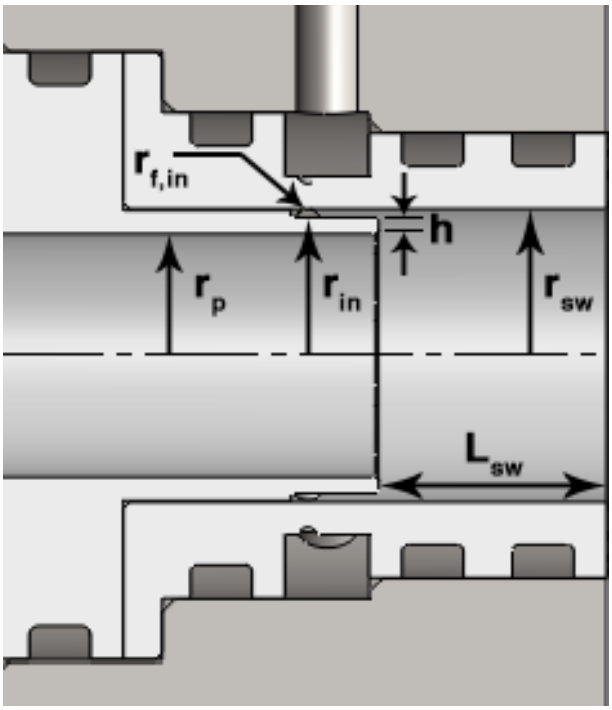

Figure 3.10.: Dimensions of the DVRC injector, as listed in Table 3.3.

Table 3.4.: DVRC Nominal Operating Conditions

Parameter	Variable	Value
Fuel Mass Flow Rate	$\dot{m}_f$	0.098 kg/s
Oxidizer Mass Flow Rate	$\dot{m}_{ox}$	0.249 kg/s
Fuel Density	ρ_f	765 kg/m^3
Oxidizer Density (285 K)	$\rho_{ox,amb}$	62.84 kg/m^3
Oxidizer Density (686 K)	$\rho_{ox,hot}$	24.07 kg/m^3

First, the geometric characterization constant, A, a ratio of the tangential velocity and normalized momentum arm to the axial velocity, is calculated,

$$A = \frac{r_{in} r_{ir}}{n r_{f,in}^2} = \frac{(0.525 \text{ cm})(0.574 \text{ cm})}{8(.050 \text{ cm})^2} = 15.34 \tag{3.1}$$

This value falls in the moderately high swirl range [62]. Values of A around this region are expected to have well-developed liquid sheets, where the centripetal acceleration forces the liquid against the outer wall, smoothing it [39]. The increased swirl associated with this geometric constant means a reduction in effective filling area. This is seen in both the calculation of the coefficient of filling, via Equation (2.2), and the discharge coefficient, Equation (2.3). The coefficient of filling, ϕ, can be calculated from the geometric constant,

$$A = 15.34 = \frac{(1-\phi)\sqrt{(2)}}{\phi\sqrt{\phi}} \tag{3.2}$$

where solving yields $\phi = 0.179$. The discharge coefficient is then calculated.

$$\mu = \frac{\phi\sqrt{\phi}}{\sqrt{2-\phi}} = \frac{0.179\sqrt{0.179}}{\sqrt{2-0.179}} = 0.056 \tag{3.3}$$

This value falls within the expected range of discharge coefficients at this high of a geometric constant. Further increasing the geometric constant, and thereby forcing

the fuel closer to the wall, would increase the gap between the fuel and the inner gas core, effectively reducing the effective cross-sectional area and lowering the discharge coefficient. Conversely, a lower geometric constant would ultimately lead to a higher discharge coefficient.

The termination of the collar provides a void where both the liquid and gas could expand to fill in. As mentioned above, the fuel is likely pressed tightly against the wall, allowing the gas core to expand into both the step behind the collar, as well as into the gap that existed in the fuel annulus between the collar and inner radius of the fuel. This ratio of the gas core diameter to the injection recess diameter, S, is calculated using Equation (2.4). Plugging in values for the discharge coefficient and geometric constant, S can be solved for. For the DVRC, the gas core diameter to injection recess diameter ratio is $S = 0.963$. For a injection recess diameter of 1.148 cm, the gas core diameter is 1.106 cm with a film thickness of 0.021 cm.

Estimates of the tangential and axial velocities of the liquid fuel based on the geometrical parameters. First, the total velocity needs to be calculated via the Bernoulli equation. Experimental results determined the pressure drop across the fuel inlets to be around 0.965 MPa. Density of the fuel, dodecane, is calculated through REFPROP, using pressure and temperature measurements from the fuel manifold.

$$v_{f,tot} = \sqrt{\frac{2}{\rho}\Delta P} = \sqrt{\frac{2}{765 \text{ kg/m}^3} 0.965 \text{ MPa}} = 50.23 \text{ m/s} \tag{3.4}$$

Axial and tangential velocities are then derived using the following equations, respectively.

$$v_{f,ax} = \sqrt{1 - \frac{4\mu^2 A^2}{(1+S)^2}} v_{f,tot} = \sqrt{1 - \frac{4(0.056)^2(15.34)^2}{(1+0.963)^2}} 50.23 \text{ m/s} = 24.02 \text{ m/s} \tag{3.5}$$

$$v_{f,tan} = \frac{2\mu A}{1+S} v_{f,tot} = \frac{2(0.056)(15.34)}{1+0.963} 50.23 \text{ m/s} = 43.84 \text{ m/s} \tag{3.6}$$

With velocities and densities known, momentum flux ratio can be calculated. Momentum flux ratios are calculated based on both axial and total liquid velocities.

Table 3.5.: DVRC Injection Parameters

Parameter	Value
$\dot{m}_f$	0.098 kg/s
$\dot{m}_{ox}$	0.249 kg/s
ρ_f	765 kg/m^3
$\rho_{ox,amb}$	62.8 kg/m^3
$\rho_{ox,hot}$	24.1 kg/m^3
$v_{f,tot}$	50.23 m/s
$v_{f,ax}$	24.02 m/s
$v_{f,tan}$	43.84 m/s
$v_{ox,amb}$	63.23 m/s
$v_{ox,hot}$	158.5 m/s
$a_{ox,amb}$	322.4 m/s
$a_{ox,hot}$	495.4 m/s
$M_{ox,amb}$	0.20
$M_{ox,hot}$	0.32
$J_{ax,amb}$	0.51
$J_{ax,hot}$	1.27
$J_{tot,amb}$	0.12
$J_{tot,hot}$	0.29

DVRC injection parameters are listed in Table 3.5. Oxidizer values are calculated for both heated temperatures of 685 K and cooler temperatures at ambient.

It can be seen that the change in the oxidizer temperature brings with it numerous other changes related to changing the thermophysical state. Cooling the oxidizer increases the density by nearly a factor of three while reducing the velocity by more

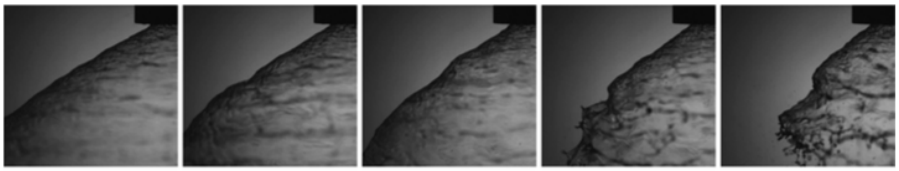

Figure 3.11.: Effect of momentum flux ratio on spray angle in a gas-centered swirl coaxial injector. Adapted from [24]

than half. The momentum flux ratio is reduced from 0.29 to 0.12 for the total velocity definition as a result, or from 1.27 to 0.51 with the axial velocity definition.

A momentum flux ratio on the order of 1 places the parameter in a region where the liquid momentum dominates. Based on the injector geometry and conditions for the DVRC listed above, a liquid-only spray (half) angle of 1.070 radians (61.3°) is expected. Correlations by Anand et al. [62] suggest the spray angle will open up with the inclusion of the gas core. Predictions of 1.287 radians (73.4°) with the hot oxidizer and 1.347 radians (77.2°) with the cold oxidizer are made based on their work. The work of Im et al. [32] predicts narrower spray angles, of 1.079 radians (61.9°) with the hot oxidizer and 1.135 radians (65.0°) with the cold oxidizer. This agrees with the results of Park et al. [60], who predict spray angles around 1.082 radians (62°) and 1.117 radians (64°) for the hot and cold oxidizer, respectively. In all three instances, the expected change in spray angle between the hot and cold oxidizer is around 5%, suggesting similar mixing profiles for both the hot and cold oxidizer cases.

According to Reference [60], the momentum of the liquid continues to dominate such that the spray angle does not begin to appreciably change until a momentum flux ratio around 1.62 is reached.

Figure 3.11 is a comparison of liquid sheets across a range of momentum flux ratios. It can be seen that at the lower values, the liquid sheet remains intact, minimally affected by gas core. Empirical correlations produced by Fu et al. [31], based on the work of References [53, 136] and modified to include injector geometry, present

a dimensionless breakup length as the breakup length divided the diameter of the injection recess, $L_{bu}/2r_i r$.

$$L_{bu}/2r_i r = 3935A^{-0.621}Re_p^{-0.465} \tag{3.7}$$

where Re_p represents the Reynolds number in the fuel inlets,

$$Re_p = \frac{2\dot{m}_l}{\pi\sqrt{n}r_p\mu} \tag{3.8}$$

Following Equation (3.7), a breakup length of 7.54 cm is predicted. This length corresponds to the spreading arm, and the axial breakup length can be calculated using the spreading angle. Using the angle based on the liquid only velocity ratio, the axial breakup length is 3.62 cm.

Reference [62] provides some insight into what the droplet distribution of the DVRC injector. The droplet size and size distribution were obtained using laser diffraction based on Mie scattering on an injector with a recess ratio and swirl number nearly identical to the injector of the DVRC and are shown in Figure While the droplet distribution presented by Reference [62] will not exactly match that of the DVRC, it does offer a glimpse of what can be expected, as well as general trends.

Figure 3.12 shows a pair of still images of the injector operating with momentum flux ratios of 5.0 and 3.5. It is clear that increasing momentum flux ratio increases mixing, as the gas core is much more intact at the lower value. The effect is also visible on the spray particle diameter distribution, shown in Figure 3.13 for four different ratios: MFR = 2, 3, 4 and 5. Note that the right y-axis is halved for Figure 3.13d. There are two distinct spray regions, one yielding a large percentage of larger diameter droplets (100 - 1000 μm), and another comprising a much smaller percentage producing very fine drops (10 - 100 μm). The shear layer produces the finest particles, where the oxidizer jet interacts most heavily with the fuel spray. Increasing momentum flux ratio naturally leads to increased atomization at the shear layer, made evident by the increase in particle distribution at the smaller diameters as the momentum ratio increases. On the periphery exists the outer edge of the spray which is not disrupted

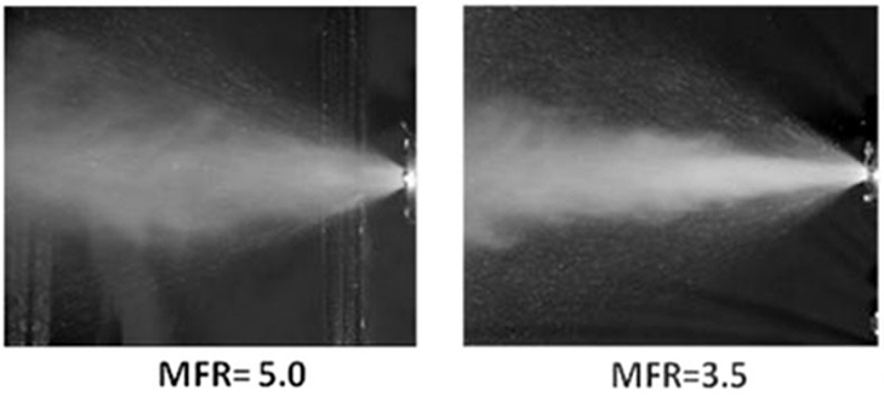

Figure 3.12.: Visual comparison of spray structures at momentum flux ratios of 5.0 and 3.5 for the same injector [62].

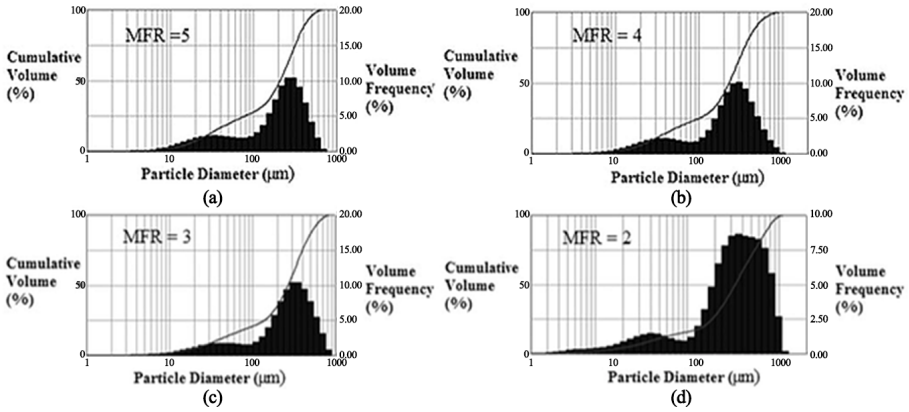

Figure 3.13.: Distribution of particle diameters as a function of momentum flux ratios. Increased momentum flux ratio leads to more, finer particles. Adapted from [62].

by the inner oxidizer jet. With no dominant atomization mechanism at work, droplets remain large in the hundreds of microns. With momentum flux ratios of 0.51 and 1.27 for the DVRC in the cold and hot oxidizer cases, an even greater distribution of particles at larger diameters would be expected.

This analysis suggests that the DVRC injector does not create a well-distributed, uniform spray. Instead, it is expected to find a heavily stratified distribution of

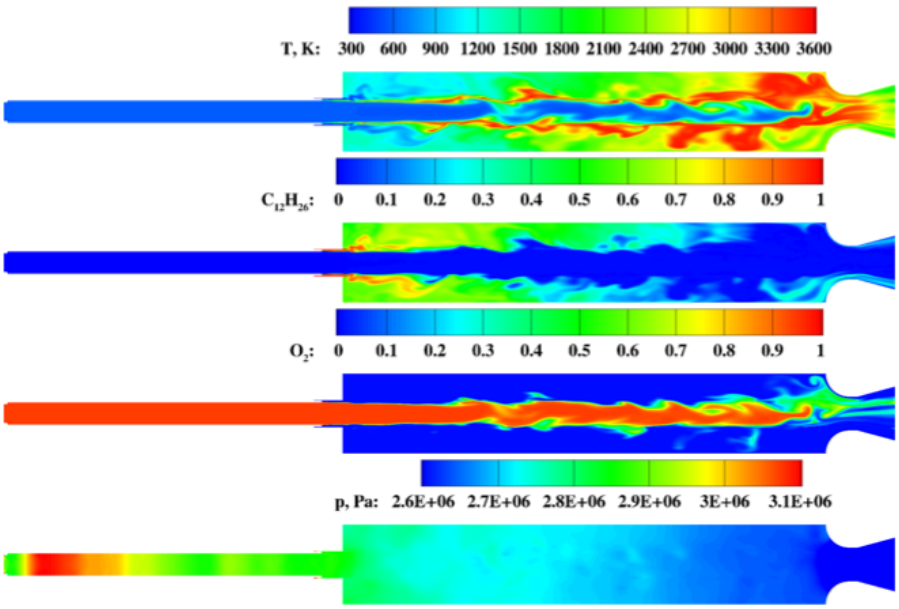

Figure 3.14.: Predictions of temperature, oxidizer and fuel mass fraction and pressure taken from a single time step from simulation of the DVRC. Configuration modeled has a 0.205 m long chamber and 0.144 m long oxidizer post with a choked inlet [124].

propellants, with oxidizer in the center, a a well-mixed region along the shear layer, and fuel along the outer edge.

Simulations of the DVRC predict this radial distribution. Lietz et al. [124] modeled the DVRC configured with a short chamber length of 0.205 m and an oxidizer post length of 0.144 m with a choked inlet.

Coinciding with this radial distribution is the prediction of incomplete combustion. This would be a product of poor mixing by the injector. As a result, impingement of the unburnt fuel on the hot nozzle promotes intermittent spikes in the pressure.

For comparison, the injector geometries and injection parameters for the UEC and the RD-170 are provided in Table 3.6.

Table 3.6.: Comparison of geometries and parameters for DVRC, UEC [99] and RD-170 [137] GCSC injectors.

	L_{post} [cm]	d_{post} [cm]	L_{cup} [cm]	d_{cup} [cm]	$\dot{m}_{ox}$ [kg/s]	$\dot{m}_{fuel}$ [kg/s]	v_{ox} [m/s]	$v_{fuel_{ax}}$ [m/s]	J_{ax} [-]
DVRC_{hot}	5.3 - 14.4	0.95	0.89	1.15	0.249	0.098	158.5	24.02	0.51
DVRC_{amb}	5.3 - 14.4	0.95	0.89	1.15	0.249	0.098	63.23	24.02	1.27
UEC	17.1	2.05	0.51	2.31	0.462	0.073	219.5	4.0	25.58
RD-170	9.3	1.12	1.05	1.27	1.33	0.477	186.69	49.06	0.38

3.2 Acoustics

3.2.1 Acoustic Impedance

At the injector, the two propellants are mixed and combusted. This leads to discrete distributions of the propellants, generating a landscape of varying temperatures, densities, composition and sound and fluid speeds. Those parameters have a direct influence on local acoustics, such as mean-flow effects or acoustic impedance.

Acoustic waves traveling between two media will undergo both transmission through, as well as reflection from, the interface. This is governed by the acoustic impedance ratio between the two media. The impedance, Z, is the product of density, ρ and local sonic velocity, c,

$$Z = \rho c. \tag{3.9}$$

The reflection, $\mathbb{R}$, or transmission, $\mathbb{T}$, of a given acoustic wave then depends on the impedance of the media,

$$\mathbb{R} = \frac{Z_2 - Z_1}{Z_2 + Z_1}, \tag{3.10}$$

$$\mathbb{T} = \frac{2Z_2}{Z_2 + Z_1}, \tag{3.11}$$

where the subscript 1 represents the medium the acoustic wave originates in, and the subscript 2 the medium the acoustic wave is entering. It can be seen that for two fluids of identical impedance, $Z_1 = Z_2$, the the acoustic pulse is fully transmitted with no reflection. For a pulse moving from a fluid of low impedance to high, the reflection coefficient approaches unity, and the transmission value approaches a value of two. This value of the reflection coefficient implies that the wave is mostly reflected at the interface. A transmission greater than one indicates some portion of the pulse is transmitted to the second medium, with an increase of amplitude nearly double the incident wave. While it appears that the wave is effectively doubled, or perhaps nearly tripled, power is conserved between the incident wave and the reflected and transmitted waves. For pressure amplitudes of the same magnitude, the intensity of the acoustic wave will be greater in a medium of lower impedance.

In the opposite case, where an acoustic wave enters a medium of lower impedance, the reflection coefficient decreases, approaching a value of -1 at the most extreme case. This value is simply the negative of the reflection coefficient for a wave traveling in the opposite direction. The transmission value also decreases, approaching zero. The summation of the transmission values in both directions equals two.

With the variation in oxidizer temperature, the impedance within the oxidizer post of the DVRC varies, altering the transmission and reflection rates of acoustic waves. The impedance of the oxidizer, fuel and combustion gas are provided in Table 3.7, with the reflection and transmission coefficients between the three media detailed in Table 3.8.

The dodecane has the highest impedance of the group, having a much higher density to compensate for the low velocity. The oxidizer is on the same order of magnitude for the two temperatures, but differ by almost a factor of two, with the cooler oxidizer having the higher impedance. The combustion gas, with both low density and low velocity is an order of magnitude lower than the oxidizer.

Table 3.7.: Impedance of propellants and combustion gas in DVRC.

Fluid	Impedance $[\frac{Pa \cdot s}{m}]$
Hot Oxidizer (685 K)	$1.144 \cdot 10^4$
Gaseous Oxygen (285 K)	$1.944 \cdot 10^4$
Dodecane	$4.277 \cdot 10^3$
Combustion Gas (2860 K)	$1.014 \cdot 10^6$

Table 3.8.: Reflection and transmission coefficients between media in DVRC.

Fluid 1	Fluid 2	$\mathbb{R}$	$\mathbb{T}$
Combustion Gas	Hot Oxidizer	0.46	1.46
Combustion Gas	Gaseous Oxygen	0.64	1.64
Combustion Gas	Dodecane	0.99	1.99
Hot Oxidizer	Dodecane	0.98	1.98
Gaseous Oxygen	Dodecane	0.96	1.96

When comparing the impedance between media and calculating the reflection and transmission coefficients, it can be seen that the largest differences appear at the interface between oxidizer and the combustion gas. The reflection is close to unity between dodecane and any other fluid. Between the combustion gas and the hot oxidizer, the reflection coefficient is 0.46. This value increases to 0.64 with the cooler oxidizer, about a 40% rise. The transmission coefficient also increases by the same amount, from 1.46 to 1.64, or about a 12% jump.

The dodecane, being a very dense fluid, has a high specific impedance and as a results has reflection coefficients near unity for all other fluids in the system, as well as transmission coefficients around 2. Very little changes at the interface between oxidizer and fuel as the temperature is reduced.

Based on the these predicted coefficients, it is expected that the cooler oxidizer will better promote resonant behavior as it permits both reflections and transmissions at stronger amplitudes. The ambient oxidizer presents a more favorable scenario to promote coupling between the oxidizer post and chamber. Although the transmission back from the post into the chamber is attenuated, allowing for the increased transmission into the post gives acoustic pulses generated in the chamber a better opportunity to resonate. This is compared to the situation presented with the hot oxidizer, where chamber-generated pulses are weaker entering the post. Pulses coming

from the oxidizer post are transmitted better, but are generally weaker than those from the combustion field.

Acoustic impedance was used to describe part of the discrepancy between pressure amplitudes in a multi-element transverse combustor where injection of fuel into select elements created an asymmetric combustion field [138].

3.2.2 Linearized Euler Equation Analysis of Acoustics

Linearized Euler Equations (LEE) provides numerical solutions of the acoustics of a system. Acoustic analysis through the wave equation, shown in Equation (3.12) as derived by Lighthill [139], is limited as it can only be applied to a homogeneous medium within a simple geometry without mean flow.

$$\frac{\delta^2 \rho`}{\delta t^2} - c_0^2 \nabla \rho` = \frac{\delta^2 \rho u v}{\delta x \delta y} \tag{3.12}$$

A one-dimensional approach through LEE can provide numerical solutions of acoustics modes, while also accounting for mean flow effects, compressiblity, heat addition, as well as changes in geometry or flow conditions [140–142]. A full description of the underlying LEE model used in this work can be found in Reference [103].

The system and chamber modes in this work were calculated by LEE. As the acoustic profile of the system, based on oxidizer post and chamber length, was a studied variable in this work, LEE was used to generate frequency maps to assist in choosing the geometries to study at given injection conditions. These maps have been calculated for previous experiments (see Figure 2.16 for the UEC and Figure 2.23 for the CVRC). The steps to using LEE to examine the acoustic modes of the system are provided below.

First, a selection of geometries at a given set of conditions is chosen. For this example, the oxidizer post length is fixed at 5.27 cm at the ambient oxidizer condition while the chamber length is varied between 20.32 and 40.64 cm. Baseline operating conditions, as listed in Section 3.1.6, are used. Second, the NASA Chemical Equi-

librium with Applications (CEA) code is run to make predictions of the combustion field, including temperature, composition and sound speed. Third, the CEA code is rerun with a fixed reduced temperature to simulate a reduction in c* efficiency. Full combustion efficiency is impossible to achieve, and a reduction in efficiency would naturally lead to a change in thermophysical properties of the combustion field. A non-ideal combustion efficiency can be predicted using previous work. In this example, combustion efficiency from preliminary tests on the DVRC was used.

The combustion efficiency for each test was calculated by taking the ratio between the calculated c* based on test measurements and the theoretical c*. The actual c* efficiency is calculated as the ratio between the product of the chamber pressure and throat area, and the mass flow rate. The theoretical c* efficiency is calculated from the output of CEA, using Equation (3.13).

$$c*_{theo} = \sqrt{\gamma \left(\frac{\gamma+1}{2}\right)^{\left(\frac{\gamma+1}{\gamma-1}\right)} \frac{RT}{MW}} \tag{3.13}$$

The c* efficiency was found to be around 88 to 91% for the ambient oxidizer and 93 to 95% for the hot oxidizer.

The adiabatic temperature is then multiplied by the square of the c* effiency to obtain the reduced temperature for use in the rerun of the CEA code. The updated CEA output, along with geometry and the oxidizer and fuel properties determined through manifold measurements and REFPROP, are then put into LEE, where the acoustic modes are generated.

The effect of c* efficiency on the LEE results is shown in Figure 3.15. Horizontal trends are calculated system modes that are dominated by the oxidizer post, as they do not change with the chamber length. Chamber modes are represented by the sloping lines, as the longitudinal frequencies are proportional to chamber length. Vertical lines are provided to indicate geometries tested at these conditions, with asterisks denoting persistent frequencies measured in the pressure signals. There is no change between the post-dominated system modes between the two maps, as the flow conditions in the post are unchanged. There is a noticeable reduction in

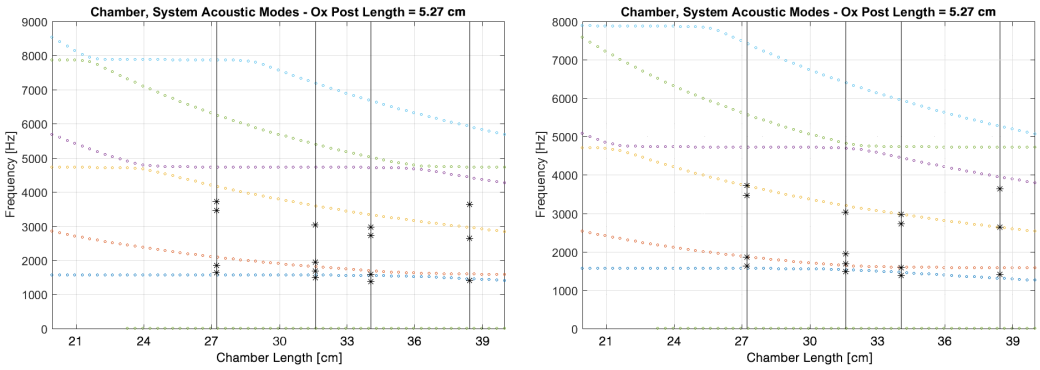

(a) Adiabatic (100% Efficiency)

(b) Heat Loss (89% Efficiency)

Figure 3.15.: Comparison of the frequency maps produced by LEE at (a) adiabatic chamber temperature and (b) reduced chamber temperature based on non-ideal c* efficiency. This example is based on a fixed oxidizer post length of 5.27 cm and with the ambient oxidizer temperature, sweeping across chamber lengths.

the chamber frequencies with the heat loss, which is amplified at higher harmonics. It can be seen that the frequency markers are much more closely aligned with the predicted frequencies at the reduced temperature than the adiabatic temperature. This is evident for both system and chamber modes.

The available geometry limits the potential acoustic profiles that can be tested. Presented in Tables 3.9 and 3.10 are the possible acoustic profiles based on the available oxidizer post and chamber lengths, referring to the hot and ambient oxidizer cases, respectively.

Four tests are discussed in Chapter 4. These four tests are in pairs, with two using the hot oxidizer and two with the ambient oxidizer. The tests are also paired such that a hot and ambient oxidizer test is conducted near one acoustic profile, while the other pair of tests conducted near a different acoustic profile to examine the effect of geometry. The acoustic profiles were chosen based on the results from LEE taken at those geometries.

The calculated pressure mode shapes for the longitudinal modes for those four tests are provided in Figure 3.16. The axis starts at the oxidizer post inlet and ex-

Table 3.9.: Acoustic profiles based on available geometry with hot oxidizer. Background color relates to magnitude, with increased values having darker colors.

L/λ		Chamber Length [cm]					
		20.46	24.83	27.28	31.65	34.10	38.47
Post Length [cm]	5.27	0.28	0.23	0.21	0.18	0.17	0.15
	7.18	0.38	0.31	0.29	0.25	0.23	0.20
	12.44	0.66	0.54	0.50	0.43	0.40	0.35
	14.36	0.76	0.63	0.57	0.49	0.46	0.41

Table 3.10.: Acoustic profiles based on available geometry with ambient oxidizer. Background color relates to magnitude, with increased values having darker colors.

L/λ		Chamber Length [cm]					
		20.46	24.83	27.28	31.65	34.10	38.47
Post Length [cm]	5.27	0.42	0.36	0.32	0.28	0.26	0.23
	7.18	0.59	0.48	0.44	0.38	0.35	0.31
	12.44	1.02	0.84	0.76	0.66	0.61	0.54
	14.36	1.17	0.97	0.88	0.76	0.70	0.62

tends to the end of the chamber. The dump plane can typically be identified by a jump in the profile, due to the change in conditions and geometry between the oxidizer post and chamber. The modes exist as standing waves, which are the superposition of a pair of traveling waves. Nodes exist for each mode where the amplitudes drop to zero. These points represent phase shifts in the signal. Anti-nodes are where the pressure oscillations reach a maximum. The spatial distribution of the nodes and anti-nodes are important to combustion stability based on the fundamental of thermoacoustic instabilities predicated on the Rayleigh Criterion. If pressure oscillations are generated, in phase, in the same location where heat release occurs, an instability is driven. By tailoring flow conditions or geometry, specific acoustic profiles can be used to drive or dampen thermoacoustic instabilities in certain regions of the combustor.

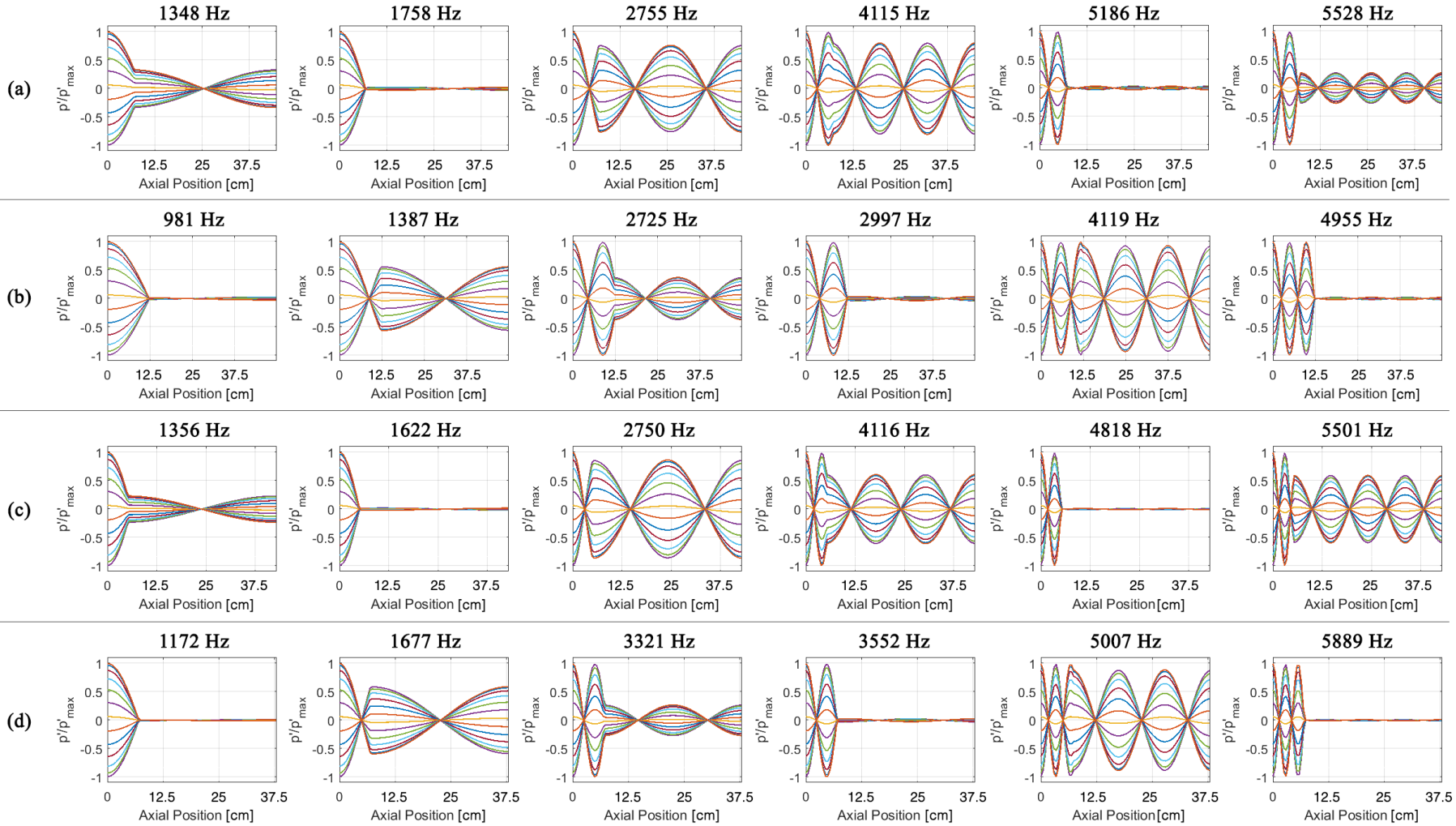

Figure 3.16.: A compilation of the pressure mode shapes for the longitudinal modes calculated by LEE for the tests analyzed in the Results chapter. Includes (a) Test 363 (hot oxidizer) at $L/\lambda = 0.20$, (b) Test 359 (hot oxidizer) at $L/\lambda = 0.36$, (c) Test 360 (ambient oxidizer) at $L/\lambda = 0.23$, and (d) Test 366 (ambient oxidizer) at $L/\lambda = 0.38$.

There are different levels of acoustic pressure ratios, which are the ratios of calculated maximum p' of the chamber to that of the post, and based on the acoustic profile. The oxidizer post-dominated system modes are easy to spot, as they have pressure ratios close to zero. These modes are expected to be heavily damped based on acoustic theory. Other modes are expected to be more prone to excitation, such as the chamber 2L modes seen in Figure 3.16(a) and (c), where a high acoustic pressure ratio is achieved.

As mentioned above, tests near two acoustic profiles were chosen, with a hot and ambient oxidizer test picked for each profile. The similarities can be seen in the mode shapes, such as comparing Figure 3.16(a) and (c), or Figure 3.16(b) and (d), which feature different geometries and oxidizer temperatures, but similar acoustic profiles. Other tests were run, filling in the L/λ spectrum between 0.2 and 0.5, or roughly between quarter-wave and half-wave resonators. This range was covered in the CVRC, although chamber length was kept constant. Likewise, the UEC experiment also covered this range of acoustic profiles, although based the calculations on the chamber 2L mode.

3.3 Testing and Facility

3.3.1 Design and Testing Requirements

As stated before, the primary focus of this work is the collection of data sets for validating computational models. Design and testing requirements were implemented to facilitate the modeling of the experiment. These requirements are listed below:

1. Propellants
    - Warm (1100 R [611 K]) O_2 at the main injector manifold
    - RP-2
2. Main Chamber Injector

- Gas-centered swirl coaxial injector
- Momentum flux ration within 1/2 order of magnitude of selected injector
- Oxidizer post Mach No. of 0.3 - 0.5
- Subsonic oxidizer post inlet

3. Configurations
   - Test configurations shall present discriminating stability behavior
   - Self-excited pressure oscillations shall present amplitudes of p'/p_{mean} < 0.05 and p'/p_{mean} > 0.10 at acoustic (axial) mode frequency
4. Main Chamber
   - Mean pressure of 600 psia [4.14 MPa]
   - Resonant frequency of 1500 - 2000 Hz
5. Instrumentation
   - High frequency pressure measurements to provide ox post and chamber modal information up to third longitudinal mode
   - Pressure amplitude measurement accuracy better than 1%
   - Propellant temperatures measured to within ±10 R [5.6 K]
   - Flow rates and mean pressure measurement accuracy within 5%
6. Design for modeling
   - Fluid inlets are understood
   - Heat loss shall be measured with sufficient spatial resolution in active combustion areas and integrated in throat
   - Geometries and size of domain shall be reasonable
7. Test duration

- Test duration shall be sufficient to obtain steady flow and limit cycle amplitudes

3.3.2 Validation Data Set Acquisition

The DVRC was prepared for testing following the design and testing requirements discussed in the previous section. Two configurations were initially chosen, but ultimately 14 configurations were tested. The 14 configurations are listed in Table 3.11 The first two configurations were sized from the results of the CVRC, with one having a post close to a half-wave resonator length, and the other close to a 3/8-wave. Based on operation of the CVRC at these conditions, the former was expected to be stable and the latter unstable. Both demonstrated to be very stable. More configurations were added and tested to find an unstable test point. Changes towards this goal include a reduction in the pressure drop across the subsonic inlet, a switch to a choked inlet, sweeps through a range of O/F ratios, testing at lower chamber pressure and varying post and chamber length.

3.3.3 Instrumentation

Low frequency pressure transducers were used to monitor pressure levels at metering and inlet locations, as well as to measure the static pressure signal from manifolds and main chamber. Unik 5000 transducers from GE were used, with ranges spanning between 1000 psi and 5000 psi (6.89 MPa and 34.47 MPa), depending on the expected pressure levels for the installed system. These transducers were chosen for their accuracy, which are reported to be 0.04% of the full scale signal, based on a best fit line. This is in comparison to the 0.1% of Honeywell TJE transducers, or the 0.25% of Druck PMP 1260 transducers. In locations that required a high accurate measurement, such as the chamber and inlet locations like the manifolds, the Unik 5000 was chosen. For other locations and scenarios, like system diagnostics, the PMP 1260 was installed.

Table 3.11.: Configurations tested to gather validation data. * denotes that the first chamber section was replaced with a section of smaller ID. † represents tests where highest amplitudes were localized to only the head end. ‡ indicates tests ran at lower chamber pressure (2.76 MPa [400 psi]). $^{*}_{*}$ represents tests where the igniter section was moved one section downstream to isolate potential effects.

Config.	L_{post} [cm]	L_c [cm]	L/λ	Inlet (ΔP [%Pc])	O/F	P'/Pc
1	7.18	34.10	0.55	Subsonic (20)	2.60	1%
2	5.27	34.10	0.40	Subsonic (20)	2.61	1%
3	5.27	20.46	0.67	Subsonic (20)	2.63	2%
4*	7.18	32.36	0.58	Subsonic (20)	2.29 - 2.76	2%
5*	7.18	32.36	0.58	Subsonic (12)	2.32 - 2.86	2%
6	7.18	34.10	0.55	Subsonic (12)	2.40 - 2.79	2%†
7	5.27	34.10	0.40	Subsonic (12)	2.36 - 2.82	4%
8‡	7.18	34.10	0.55	Subsonic (12)	2.35 - 2.77	4%
9	7.18	34.10	0.55	Choked (–)	2.29 - 2.76	3%
10	5.27	34.10	0.40	Choked (–)	2.32 - 2.86	2%
11	7.18	20.46	0.91	Subsonic (12)	2.48	5%†
12	14.36	20.46	0.91	Choked (–)	2.47	4%†
13	14.36	25.54	0.73	Choked (–)	2.57	5%
14^{*}_{*}	14.36	20.46	0.91	Choked (–)	2.67	8%†

Thermocouples from OMEGA were installed throughout the system to measure fluid and chamber wall temperatures. Type K thermocouples were chosen, as they had the highest operating range, up to 1523 K. Small diameter probes, at 1/16" (1.59 mm), were used for increased response time, as were exposed junction ends. Model KQXL-116E-12 provided the necessary parameters. Measurements have an accuracy of 2.2 K, or 0.75%. Quick disconnect interfaces allow for simple installation, a benefit for when making hardware changes.

One Type E thermocouple, with a narrower range but more accurate measurement than a Type K, was used to measure the temperature of liquid nitrogen in a dewer to serve as a reference temperature. This Type E thermocouple, and the thermocouples in the oxidizer and fuel manifolds, were installed into the flowfield, where disruption of the local flowfield was unimportant, for more accurate measurements

Both the low frequency pressure transducers and thermocouples were sampled at 1 kHz.

High frequency pressure transducers were installed for measuring dynamic changes in the pressure field. Measurements were taken with sampling speeds of 250 kHz, far above the frequencies of the behavior being studied. Kulite WCT-312M piezoelectric transducers, shown in Figure 3.17 were installed in manifolds, the oxidizer post and throughout the chamber. Transducers are water cooled to permit operation where high thermal loads are expected. Accuracy within 0.5% of full scale output is achieved with these sensors.

Porting for the high frequency pressure transducers considered the axial location within the chamber to target placement of the sensors near either pressure nodes or anti-nodes. In order to resolve the individual effects of the first three longitudinal modes, multiple sensors were required. These sensors would be installed at the head end of the combustor, which would serve as a pressure anti-node for all chamber acoustic modes, as well as the quarter-, third- and half-length axial locations, which would permit isolation of any of the first three longitudinal modes. An example of all of the instrumentation locations can be seen in Figure 3.18.

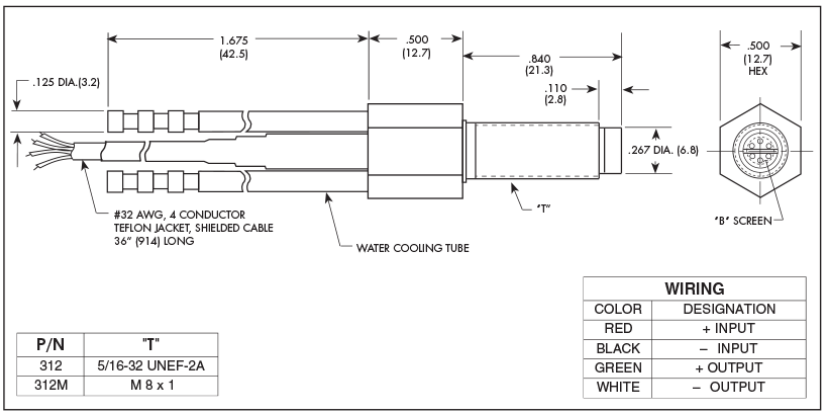

Figure 3.17.: Diagram of the WCT-312M kulite high frequency pressure transducer. Dimensions are in english units with metric units in parantheses [143].

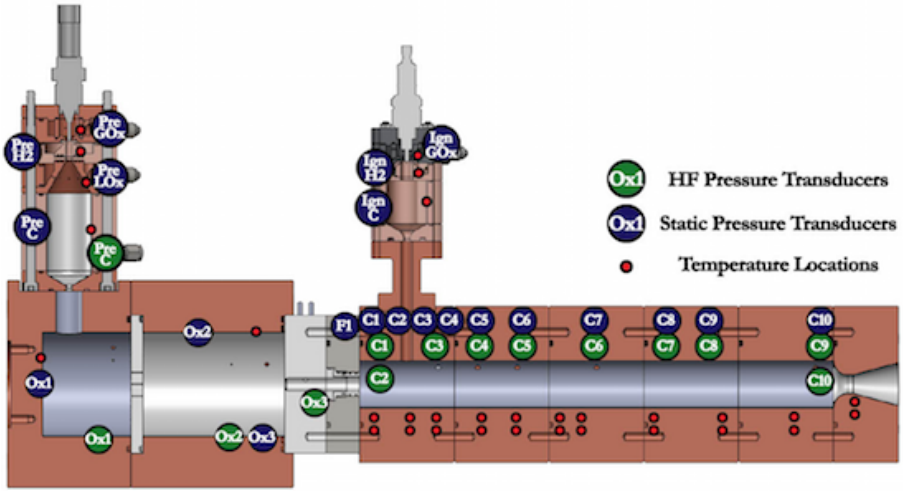

Figure 3.18.: Illustration of the instrumentation locations for the baseline configuration of the DVRC.

Also shown here are pairs of thermocouples within the chamber wall. These thermocouples were embedded into the walls with each pair having two depths. The first was 0.318 cm [0.125 in] away from the inner diameter of the chamber, and the second 0.732 cm [0.288 in] away from the inner diameter. Together, these pairs would allow for back calculation of the local heat flux. Through these 11 pairs, the heat loss to chamber walls would have spatial resolution.

The instrument selections as well as installation locations were considered sufficient to meet the stated requirements.

3.3.4 Test Facility and Procedures

The DVRC was installed on Stand B of the Rocket Cell in the High Pressure Lab (HPL) at Zucrow Laboratories, part of the Purdue University campus. The facility is equipped with 14.2 m^3 of gaseous nitrogen at 41.5 MPa, used for purging and pressurization of propellants, such as the liquid fuel. The test stand is plumbed to flow liquid fuel at 0.390 kg/s at pressures up to 12.41 MPa. Gaseous oxygen flow rates up to 1.013 kg/s are possible, at pressures up to 17.24 MPa. The test stand is also equipped with gaseous hydrogen to fuel the preburner and igniters.

The test stand itself, shown in a Figure 3.19, utilizes a hydraulic jack to compress the test article with a compressive force up to 68.9 MPa. Rapid compression/decompression supports quick modifications of the hardware, such as adding, removing or swapping oxidizer post or chamber sections to affect geometry.

An example of a system pressure profile is shown for Test 359 in Figure 3.20 for a hot oxidizer test. The autosequence begins with inert nitrogen purge through both oxidizer and fuel systems. Then the preburner system is brought on line, starting with the preburner igniter. Failure to light the preburner igniter triggers an abort (minimum igniter chamber pressure not met). The spark igniter induces noise in the signals, which is apparent around 1.2 seconds in the figure. Once the igniter is lit, the preburner propellant run valves open. Red lines check the preburner chamber

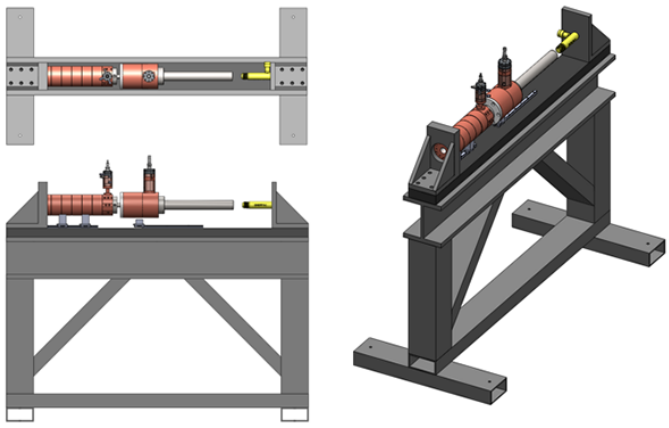

Figure 3.19.: Model of the original DVRC configuration on the test stand.

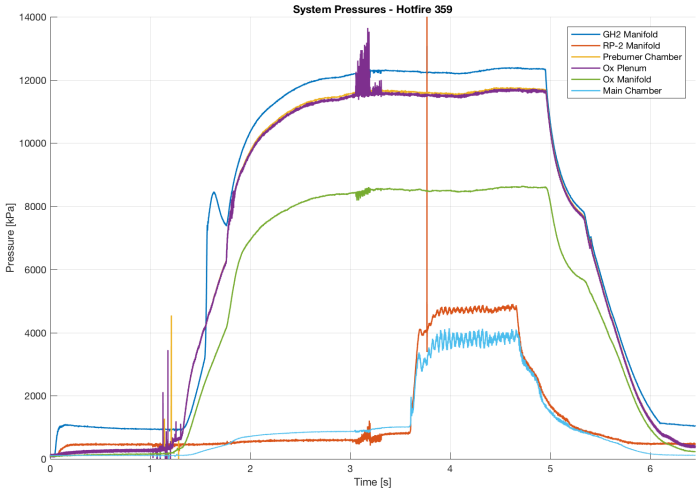

Figure 3.20.: Example pressure profiles from Test 359. Preburner manifold and chamber pressures reach between 11.03 and 12.41 MPa during steady state, with a pressure drop to around 8.27 MPa in the oxidizer manifold. Fuel manifold pressure nears 4.83 MPa while chamber pressure is around 3.79 MPa. Noise in signals is triggered when spark igniters are active (around 1.1 and 3.2 seconds).

pressure to ensure it is lit by comparing it to an acceptable minimum value. Another red line checks the preburner chamber for overpressurization.

Once the preburner reaches steady state, the main chamber igniter is brought online. Noise is again induced in the pressure signals by the spark igniter, seen around 3.2 seconds. Red line monitoring then checks the igniter chamber pressure to ensure it has lit. If it has, the main propellant run valves open. Similar to the preburner, red lines check for ignition and will abort if the chamber pressure is to low. Overpressurization will also lead to an abort.

Hot fire lasts for one second, and defined as the time the main fuel run valve is open. Steady state is often achieved within the first quarter second. An example of the chamber pressure during hot fire taken from high frequency pressure trandsucers is shown in Figure 3.21. In this example, a low frequency mode emerges shortly after ignition and persists for the first two thirds of the test before dying off. The end

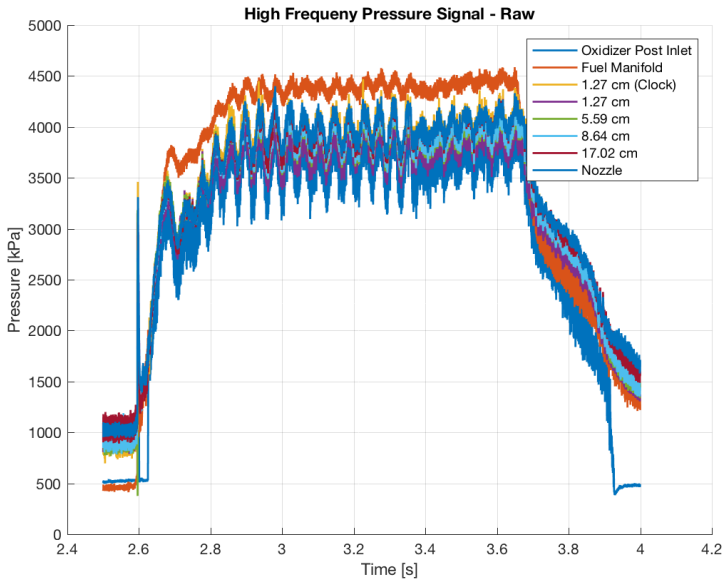

Figure 3.21.: Example HF pressure profiles from Test 359. A bulk mode is present in the system, evident in chamber and fuel manifold signals.

of the test is marked by the drop in pressures, as fuel is no longer being supplied. Shortly after the main fuel run valve closes, the preburner is shut down.

Tests conducted with the ambient oxidizer do not use the preburner. In these tests, the preburner igniter and the preburner fuel are not activated. Otherwise, timing is the same between hot and ambient oxidizer tests.

4. RESULTS

The primary goal of this work was to capture validation data. This was done at a number of configurations, listed in the previous section in Table 3.11. Throughout testing, all configurations were observed to be stable, with pressure oscillations below 10% of the mean chamber pressure. Preliminary comparisons of the experimental results to computational models were reported by Reference [124].

The lack of unstable operating points prompted the secondary objective of this work, which was to reduce the oxidizer temperature as a method of achieving higher pressure oscillation amplitudes. Two temperatures of oxidizer were tested. The first relied on hot oxidizer, where oxygen was burned with hydrogen in the preburner before entering the oxidizer manifold. Tests were conducted with an oxidizer temperature measured around 685 K, as measured in the oxidizer manifold. Note that as combustion products are formed, the oxidizer is no longer purely oxygen, but approximately 95% diatomic oxygen and 5% water vapor, by weight. For cooler temperatures, oxygen from compressed gas cylinders was used. The temperature of the pure oxygen remains near room temperature, measured around 285 K in the oxidizer manifold.

Different geometries were studied at both oxidizer temperatures. Oxidizer post resonance with the chamber can instigate combustion instabilities. It was expected that modifying the geometries to attain certain acoustic profiles would generate pressure oscillations strong enough to drive instabilities. While consistent, high amplitude unstable behavior was not observed, there were some geometry effects noticed.

This section discusses the results obtained through testing. First, low frequency measurements are presented, providing a background of the test conditions and typical testing profiles. Following this are high frequency pressure transducer results. High-pass filtered results are first presented and compared These results represent the mean-subtracted dynamic pressure signal (p'). Included in the analysis of this

grouping of signals are comparisons of waveforms, and cross-correlations between different locations and provide phase relationships. The phase between measurements can be used to gauge timing and levels of acoustic interactions. Following this, time-independent statistics based on the distribution of the pressure signal are discussed. These include the root mean square (RMS) and standard deviation of the signals, as well as the skewness and kurtosis, which are the third and fourth standardized moments. As all tested configurations remained stable, with little sustained acoustic forcing, a statistical approach provides a quantitative base in which to compare the different data sets. Frequency analysis of the signals is presented and discussed, first using power spectral densities and spectrograms, then by using the continuous wavelet transform. These methods capture the dominant frequencies within the signals, along with determining amplitude and variability of the frequency content through time.

Application of this suite of analytical techniques to the pressure signals obtained in this work provided insight into the state of the thermoacoustic field as a function of the oxidizer inlet temperature. The pressure field was considerably more stable with the higher inlet temperature. Pressure fluctuations increased in amplitude with the cooler inlet temperature proportional to the increase in the acoustic reflection and transmission coefficients, a product of the changing specific impedance of the oxidizer in relation to the combustion gas. Similar frequency content was found in both settings, borne from the acoustic modes of the system, primarily the chamber. Organization was observed to increase with the cooler temperature, where acoustic energy was distributed to narrower bandwidths at the acoustic modes with sharper peaks in the frequency domain. Further augmentation of pressure oscillation amplitudes was achieved through geometry changes, but only observed in the ambient oxidizer cases. The relationship between amplitude and acoustic profile matched that of previous similar experiments, in general. Deviation was observed with two different geometries at very similar acoustic profiles, where one configuration promoted strong amplitudes, and the other much weaker amplitudes. A more fitting trend was found

Table 4.1.: Geometry and operating parameters for representative tests of the DVRC.

Test ID	L_{post} $[cm]$	L_c $[cm]$	L/λ	$\dot{m}_{ox}$ $[kg/s$	$\dot{m}_{fuel}$ $[kg/s]$	T_{ox} $[K]$	T_{fuel} $[K]$	O/F
363	7.18	38.47	0.20	0.255	0.096	691	1	2.66
359	12.44	38.47	0.36	0.254	0.098	675	1	2.58
360	5.27	38.47	0.23	0.253	0.096	283	1	2.64
366	7.18	31.65	0.38	0.251	0.098	285	1	2.57

based on the timing between expected vortex generation and impingement, and the subsequent arrival of a traveling pressure wave in the chamber.

4.1 General Performance

The general performance of a handful of representative tests are will first be presented. Four tests have been chosen, with two system geometries for each oxidizer temperature. Geometry and operating parameters for these four tests are listed in Table 4.1. A summary of results are provided in Table 4.2. The first pair of tests listed, Tests 363 and 359, were run with hot oxidizer and oxidizer posts acting as resonators with equivalent wavelengths of 0.20 and 0.36. The second pair of tests, Tests 360 and 366, were run with ambient oxidizer, hitting similar equivalent wavelengths of 0.23 and 0.38. The equivalent wavelengths were chosen to compare effects of the equivalent wavelength at the same temperature, as well as to compare similar wavelengths at different conditions. It should also be noted that twice a new fuel collar was installed prior to testing, once before operation heated oxidizer conditions and again before ambient. The collar was then examined and showed discoloration at the tip in both heated and cooler conditions, an indication of flame anchoring at the tip.

Table 4.2.: Summary of general results from representative tests of the DVRC.

Test ID	Pc [MPa]	Overall P'/Pc [peak-to-peak %]	c* efficiency [%]	J_{total}	J_{axial}
363	3.800	3.90	93.8	0.49	2.11
359	3.827	3.88	93.2	0.43	1.83
360	3.565	6.25	91.0	0.17	0.74
366	3.468	8.25	87.4	0.21	0.91

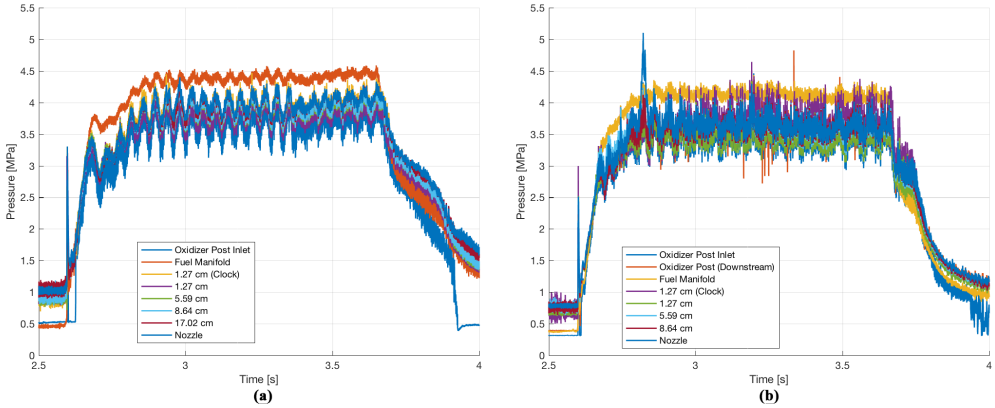

Figure 4.1.: Raw high frequency profiles from (a) Test 359 using hot oxidizer and (b) Test 366 using ambient oxidizer.

4.2 High Frequency Pressure Results

Raw high frequency pressure traces from Tests 359 and 366 are shown in Figure 4.1, with the former being a good representation of hot oxidizer tests, and the latter of ambient oxidizer tests, respectively. A low frequency bulk mode around 25 Hz appeared, with different presentations depending on oxidizer temperature. At higher temperatures, such as in Figure 4.1a, the bulk mode is dominant throughout most of the test. At lower temperatures, such as in Figure 4.1b, the bulk mode is weaker and heavily modulated by what appears to be higher frequency content.

Interpretation of the differences in the results is not immediately apparent. A number of methods and techniques were applied to the high frequency pressure signals to extract relevant, useful information on how the oxidizer temperature impacts the thermoacoustics, and therefore the stability of the system.

4.2.1 High-Pass Filtered Results

The raw pressure traces obtained by the high frequency pressure transducers are high-pass filtered, removing the static component to leave the dynamic or fluctuating

component. A 5 millisecond window of the signals shown in Figure 4.1 was high-pass filtered. The results are broken into four groupings for comparison, based on both location and appearance of waveforms. The first grouping contains all signals, while the second grouping contains only measurements taken in the injector. The third grouping is limited to only measurements near the dump plane, and the last grouping the remaining chamber measurements.

Presented first are signals from Test 359 with hot oxidizer, shown in Figure 4.2. It is apparent that a diverse range of waveforms are present. Within the injector, two main waveforms can be seen. The upstream oxidizer post signal shows little obvious organization but strong, rapid high frequency modulation. Further downstream, at the downstream oxidizer post and fuel manifold locations, the signals do not show the high amplitude, high frequency modulation. Instead, it is replaced with weaker, lower frequency behavior. These two signals lack coherence, as they switch between being in and out of phase.

The chamber signals were split into two waveform types, with one waveform at the dump plane and another elsewhere. These two measurements are taken from the same axial location, 1.27 cm downstream of the injector face, but are installed at different circumferential angles. One is installed at the same angle as the high frequency instrumentation array, placing it 0.785 radians (45 °) from a twelve-o-clock position. The second, denoted as "clocked", is placed at nine-o-clock when facing upstream, 4.712 radians (270 °). Both of these signals exhibit relatively strong amplitudes and a periodic structure. A slight phase shift between the two signals is also evident, despite the measurements coming from the same axial location. For a longitudinal acoustic mode, it is expected that signals from the same axial location would have the same phase, despite whether the wave is traveling or standing. This suggests some other acoustic or hydrodynamic mode is present at the chamber head end.

In comparison, the downstream chamber measurements have much smaller amplitudes and no dominant frequency present. The signal from the most central measurement, located at 17.02 cm, is the weakest of the group. This is consistent with a nodes

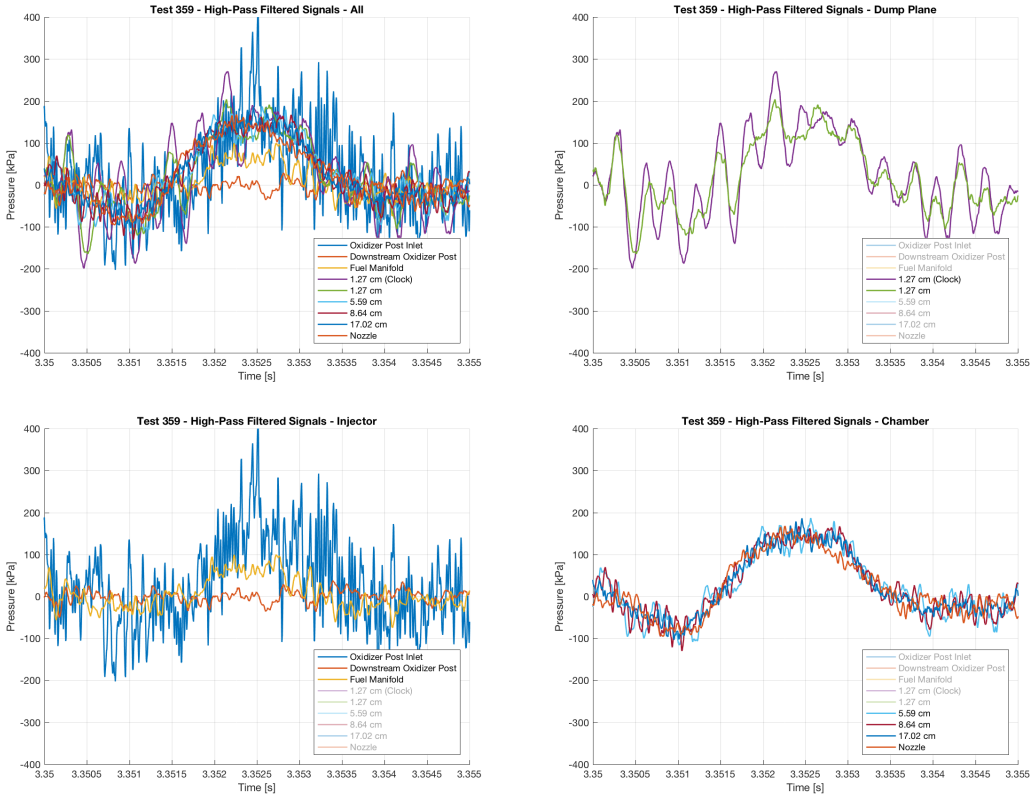

Figure 4.2.: Waveform comparison for Test 359 for a 0.005 second window. Signals are divided into like groups: all high frequency measurements (top-left), injector measurements (bottom-left), upstream chamber measurements (top-right), and downstream chamber measurements (bottom-right).

for odd-numbered acoustic modes. Further supporting weak acoustic organization is the phase shift of the signals. The further upstream locations, at 5.59 and 8.64 cm, along with the 17.02 cm, are occasionally out of phase with the nozzle location at 37.13 cm, which is consistent with the first longitudinal mode. However amplitudes remain small, suggesting acoustic forcing is limited.

High-pass filtered measurements from Test 366 are presented in Figure 4.3. Again, the signals fall into the same three groupings, although amplitudes are stronger globally.

The injector measurements are similar to those of Test 359 with the hot oxidizer. The upstream oxidizer post signal is the strongest of the grouping. It does not appear to be embedded with higher frequency content than the rest of the injector, but still differs from the downstream oxidizer post and fuel manifold locations, which remain similar to each other. These two measurements shift in and out of phase, despite their strong similarity.

The strongest oscillations are seen at the head end of the chamber, as shown in Figure 4.3c, with peak-to-peak amplitudes ranging from 140 kPa to 410 kPa. The two measurements at 1.27 cm are similar to each other, although the clocked position waveform maintains a more sinusoidal shape. The peaks are smooth, while the non-clocked position appears more broken. There is an apparent phase shift between the two signals, similar to the hot oxidizer case.

Downstream chamber measurements are much weaker and broken compared to the upstream signals. The phase shifts between these signals serve as evidence of weak standing wave behavior of the first longitudinal mode, more so than the hot oxidizer test. The two measurements in the upstream half, at 5.59 and 8.64 cm, are completely out of phase with the nozzle measurement at 30.31 cm. This behavior is intermittent, however, as the waveforms collapse into noise before organizing again. This suggests that either the acoustic perturbations are unable to couple with a heat release or hydrodynamic mode, or are actively damped.

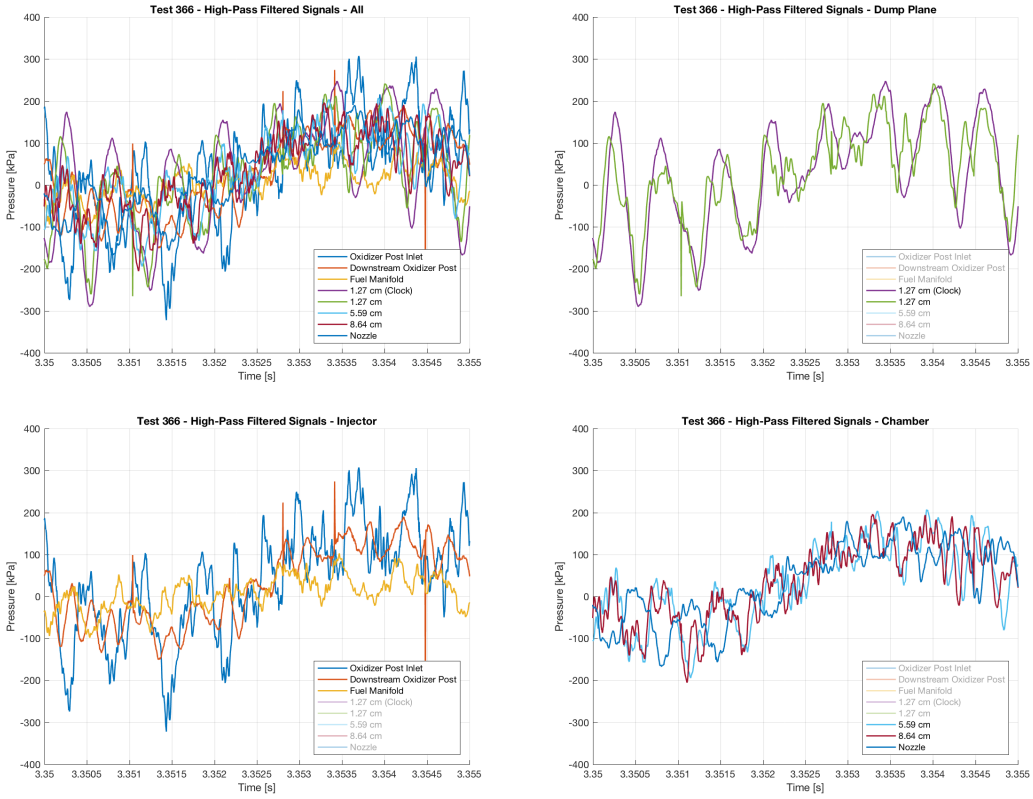

Figure 4.3.: Waveform comparison for Test 366 for a 0.005 second window. Signals are divided into like groups: all high frequency measurements (top-left), injector measurements (bottom-left), upstream chamber measurements (top-right), and downstream chamber measurements (bottom-right).

The configuration tested in Test 366 did not have a mid-chamber measurement location to examine the pressure signal near the center acoustic node. However, the companion ambient oxidizer test, Test 360, does have a central measurement which does show a much weaker acoustic response than the locations further away from the node of the first longitudinal acoustic mode.

4.2.2 Cross-Correlation

High-pass filtered results were cross-correlated to assess signal similarity and identify phase relationships. For the four representative tests, three reference transducers were chosen which the various transducer signals are cross-correlated against. The three reference locations are the oxidizer post inlet, the 1.27 cm location, and the nozzle. The reference locations are based off of their nodal locations, each being at a global anti-node. This is designed to prevent inaccurate measurements arising from attenuated signals.

The two representative hot oxidizer tests, Test 363 and 359, are discussed first. The results are shown in Figure 4.4, broken up into reference location. Dashed lines indicate oxidizer post signals, dotted lines for the fuel manifold, and solid lines for the chamber locations. The first results discussed are cross-correlations with the upstream oxidizer post inlet location, Figure 4.4a for Test 363 and Figure 4.4d for Test 359. The only strong correlation appears for the oxidizer post inlet to itself, or the autocorrelation. It has a sharp drop off on either side, indicating that the self-similarity is not preserved through time. Two small, jagged peaks appear on either side of the central peak, suggesting the potential for very weak periodicity that gets lost past the first period, as no more peaks appear. The only other notable correlation is with the two 1.27 cm locations, which show a shallow peak that lags the oxidizer post inlet signal, as indicated by it appearing on the positive side of the axis of ordinates. For Test 363, the peaks are around 0.15 ms, while for Test 359 the time lag is around 0.31 ms. This would suggest an acoustic pulse emitting from near the

dump plane that travels upstream through the post, perturbing the flowfield near the choked inlet. Test 363 uses a shorter post length of 7.18 cm compared to the 12.44 cm length of Test 359, resulting in a shorter travel time. The time lags are similar to what would be expected for a pulse traveling along this length against the mean flow, where a simple calculation postulates an acoustic travel time of 0.21 and 0.37 ms for Tests 363 and 359, respectively. The lack of a paired peak on the negative side of the auto-correlation peak indicates that this pulse either is not reflected or is attenuated by the time it returns to the dump plane. No other significant peaks appear for this cross-correlation pairing.

Stronger correlation appears with the 1.27 cm reference location for both hot oxidizer tests. The two 1.27 cm locations have the strongest correlations by a wide margin, primarily around a time lag of zero, but also subsequent peaks in both directions, indicating periodic behavior. The time lag is around 0.36 ms for both tests. This matches the period of a single cycle for the first chamber longitudinal mode, as both tests share the same chamber length. A weaker correlation with the upstream oxidizer post location is visible, matching the results where that measurement was used as the reference location. No other significant peaks are apparent, with maximum correlations below 0.4 for the remaining signals.

The cross-correlation relationships with the nozzle location as the reference are shown in Figure 4.4c and Figure 4.4f for Test 363 and 359, respectively. Overall the level of correlation increases, but not as an indication of periodicity in the form of singular, repeated peaks. The highest correlations are from auto-correlation with the nozzle signal, and also with the upstream oxidizer post signal. The auto-correlation naturally reaches a peak around zero. For Test 363, the oxidizer post inlet peaks at 0.02 ms and -0.65 ms, while for Test 359 it peaks at -0.14 and -0.74 ms. Test 363 has a downstream post measurement, which shows similar time lags as the upstream location, with peaks at 0.02 and -0.65 ms. For each test, the spacing between the two oxidizer post inlet peaks and the next strongest correlation, the 1.27 cm locations, is consistent. For Test 363, the spacing is 0.24 ms between post inlet and 1.27 cm

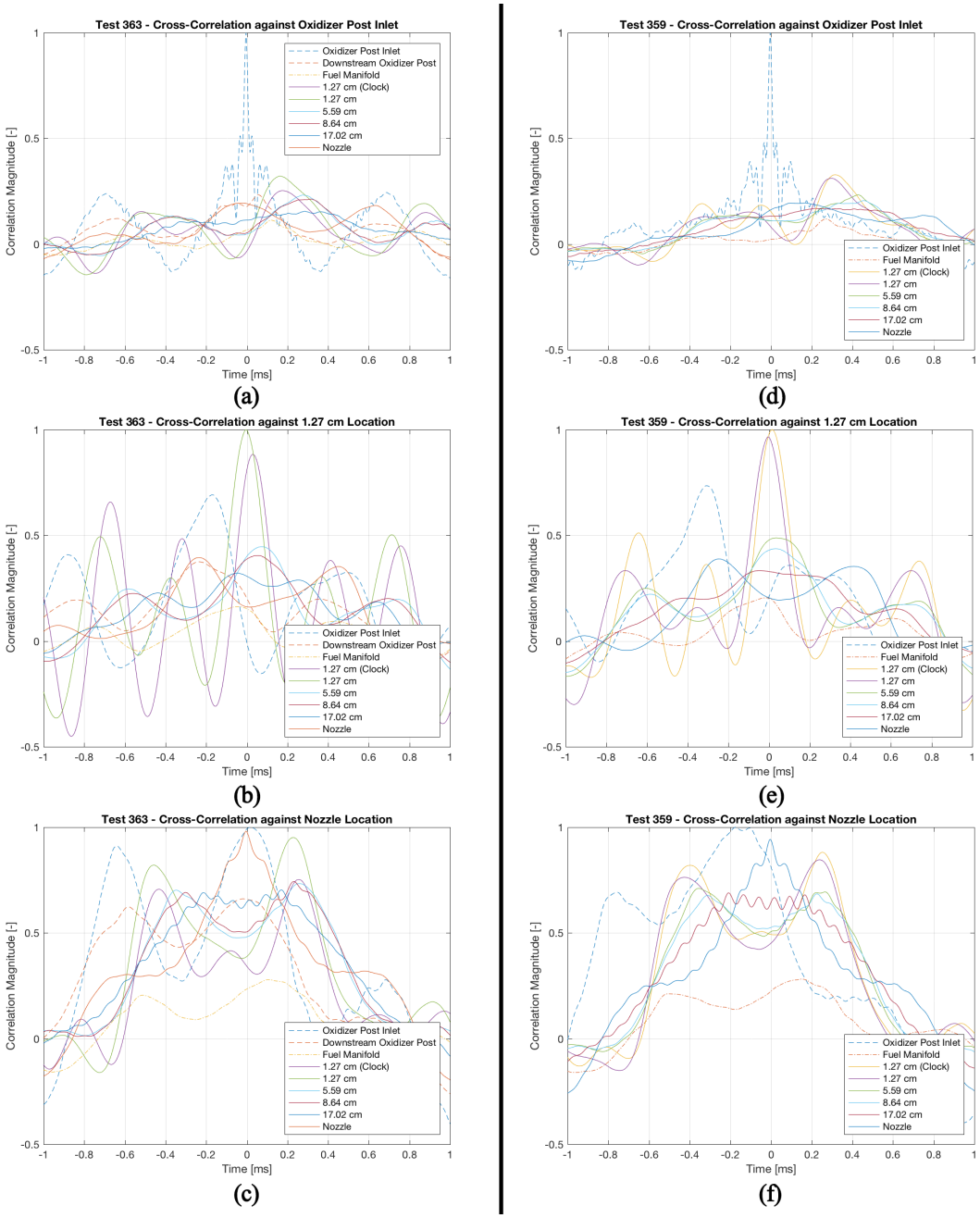

Figure 4.4.: Cross-correlation of signals from hot oxidizer tests. Test 363, with $L/\lambda = 0.20$, makes up the left column and Test 359, with $L/\lambda = 0.36$, makes up the right. Reference signals are the oxidizer post inlet for (a) and (d), 1.27 cm location for (b) and (e), and nozzle location for (c) and (f).

location peaks, while it is around 0.45 ms for Test 359. These values are consistent with an acoustic pulse traveling upstream through the oxidizer post.

While they do not have strong, well-defined peaks, the chamber measurements capture interesting behavior. As Figure 4.5 illustrates, between the central peak for the nozzle location auto-correlation and the outer dump plane peaks rests weak but present peaks for the remaining chamber measurements. There is not a single, sharp peak for these signals, instead the peaks are quite broad and remain a high degree of correlation across a wide range of time lags. However, the maxima do follow a trend with the peaks occurring in order of axial location. This would serve as an indication of an acoustic wave emanating from the dump plane, losing coherence along the way through the chamber, reaching the nozzle where its interaction creates a stronger pulse that is reflected and travels back upstream to the dump plane where it leads to the generation of another pressure pulse. The time lags match for a pressure wave traveling downstream, sped up by mean flow with a Mach number of 0.1. Likewise, the time lags fit a return pulse, slowed by mean flow at a Mach number of 0.1. The return pulse also appears to slow down as it approaches the head end, reducing in speed from approximately 990 m/s to 762 m/s at the 5.59 cm location, then 330 m/s at the dump plane.

For each reference location, the fuel manifold consistently had very weak correlation.

The same analysis is conducted on the two ambient oxidizer tests, Tests 360 and 366. The results are visualized in Figure 4.6. The same three reference signals are used as the hot oxidizer cases, with the upstream oxidizer post measurement for Figure 4.6a and Figure 4.6d, the dump plane at 1.27 cm for Figure 4.6b and Figure 4.6e, and the nozzle for Figure 4.6c and Figure 4.6f.

The cross-correlation results with respect to the oxidizer post inlet vary differently between the hot and ambient oxidizer tests. Whereas the hot oxidizer test had weak correlations with the inlet signal, apart from auto-correlation, the ambient oxidizer tests show substantially stronger correlations, along with evidence of periodicity. The

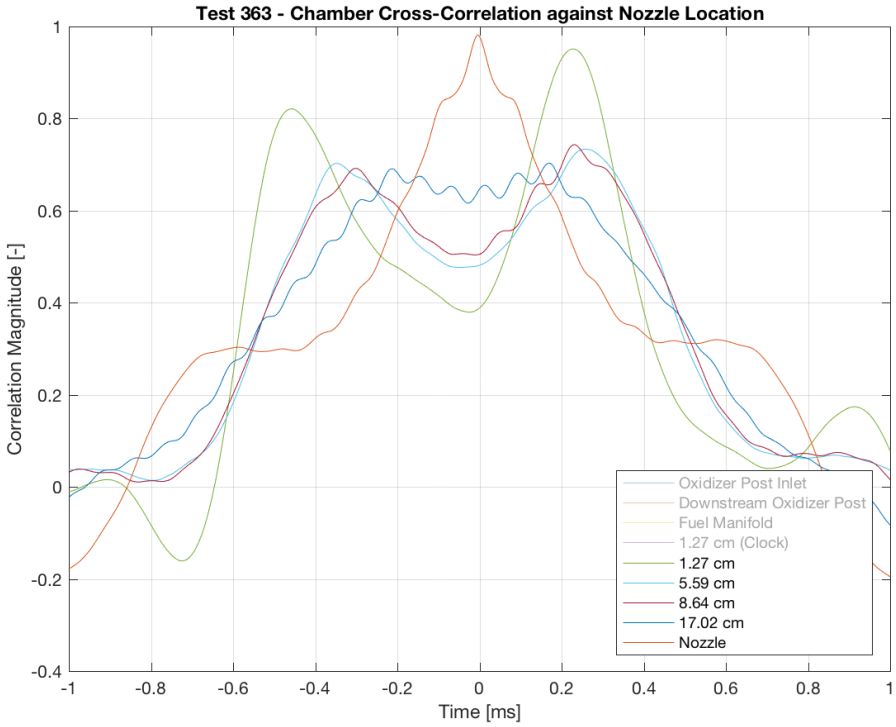

Figure 4.5.: Cross-correlation of chamber signals with the nozzle signal as the reference for hot oxidizer Test 363. Time shift of peaks between locations indicates traveling wave emanating from the nozzle and reflecting back at the dump plane.

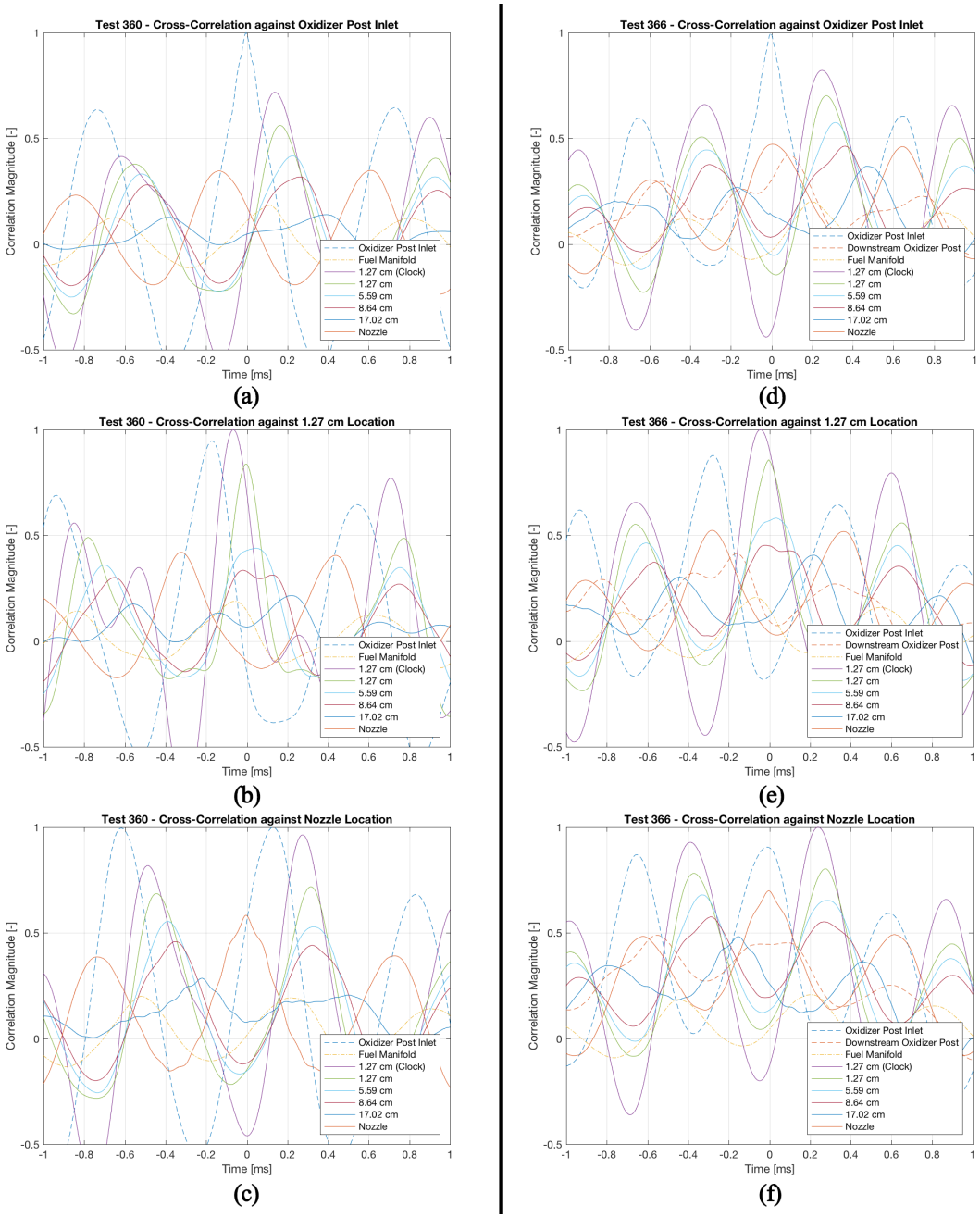

Figure 4.6.: Cross-correlation of signals from ambient oxidizer tests. Test 360, with $L/\lambda = 0.23$, makes up the left column and Test 366, with $L/\lambda = 0.38$, makes up the right. Reference signals are the oxidizer post inlet for (a) and (d), 1.27 cm location for (b) and (e), and nozzle location for (c) and (f).

auto-correlation again produces the strongest correlations, peaking not only around zero but also with secondary peaks, either leading or lagging the central peak by 0.73 ms for Test 360, and 0.63 ms for Test 366. This matches the expected timing for the fundamental longitudinal chamber mode, for a pulse to travel from the dump plane to the nozzle and back.

The chamber cross-correlation results capture dynamics similar to what was seen in the hot oxidizer nozzle results, where a pulse traveling along the chamber is visible. Unlike the hot oxidizer tests, the pulse can only be seen traveling upstream instead of both up and downstream. For Test 360, the peaks at the various chamber locations moves in sequence, starting at the nozzle at 0.61 ms, moving up to 0.39 ms at 17.02 cm, 0.26 ms at 8.64 cm, 0.22 ms at 5.59 cm, then reaching the dump plane 0.15 ms before the post inlet. This translates to a pulse that is decelerating as it travels upstream, starting around the expected sound speed at 975 m/s, then slowing to around 620 m/s at the head end.

In Test 366, the upstream traveling chamber pulse is also evident. The nozzle location leads the post by 0.636 ms, the 8.64 cm location by 0.34 ms, 5.59 cm by 0.31 ms, and 1.27 cm by 0.27 ms. The 17.02 cm location in the middle of the chamber shows a very weak correlation with the inlet reference location. The remaining time shifts capture a traveling pulse emanating from the nozzle, traveling around 780 m/s in the downstream half and accelerating to 1000 m/s in the upstream half. In comparison to Test 360, the cross-correlation results for Test 366 appear to capture a complete standing wave system mode shape. Besides the chamber itself displaying a much more uniform pulse speed throughout, the oxidizer post also shows a 1L standing wave profile, with the inlet and dump plane out of phase. It appears that stronger organization is achieved when the geometry better accommodates a full acoustic mode through the system. Despite this, both the fuel manifold and the downstream oxidizer post measurements are not strongly correlated with the upstream post signal.

Relying on the post inlet and dump plane signals, an estimate of the upstream velocity inside the post was made based on time lag and distance between the sensors.

For Test 360, the estimate is around 380 m/s, while the estimate for Test 366 is lower, around 280 m/s. The estimate of 380 m/s is much higher than the predicted mean flow-adjusted velocity of 260 m/s, while the estimate for Test 366 is much closer to the expected value.

The results from cross-correlation with the 1.27 cm reference location are very similar to those with the inlet post reference, achieving time lags consistent with a pulse traveling around 1000 m/s for Test 360 and around 1200 m/s for Test 366. The 1000 m/s value is close to the expected chamber sound speed of 1081 m/s, while the 1200 m/s result is slightly higher than expected.

There is an unusual bifurcation visible near a time lag of 0.045 ms for the 8.6 cm measurement in Test 360 and 0.024 ms for Test 366. The appearance it takes on suggests it could be the result of reflection of the upstream traveling pulse. Relying on the timing between the non-clocked dump plane location and both the midpoint sensor and nozzle sensor shows the timing to be consistent with a downstream pulse traveling at a mean velocity of 1150 m/s for Test 360 and 1130 m/s for Test 366, close to the mean flow-adjusted velocity of around 1190 m/s.

A difference that is highlighted with the dump plane location is the time shift between the two 1.27 cm locations. As these two measurements are taken from the same location, it is expected that a longitudinal chamber pulse would result in the same phase shift between these and any other location. For Test 360, the shift is 0.064 ms, while it is 0.032 ms for Test 366. The combination of acoustics and energy production at the head end, and perhaps the swirling nature or the fuel, could be suitable for weak excitation of the first or second tangential mode. The fundamental tangential mode is predicted to be around 16010 Hz, having a period of 0.063 ms. Taking the cross power spectral density it is possible to determine the shared frequency content between two signals. For Test 360, there is a clear rise in magnitude for frequencies in this range for the two dump plane sensors, as shown in Figure 4.7. A similar rise is not found in the cross power spectral density of the

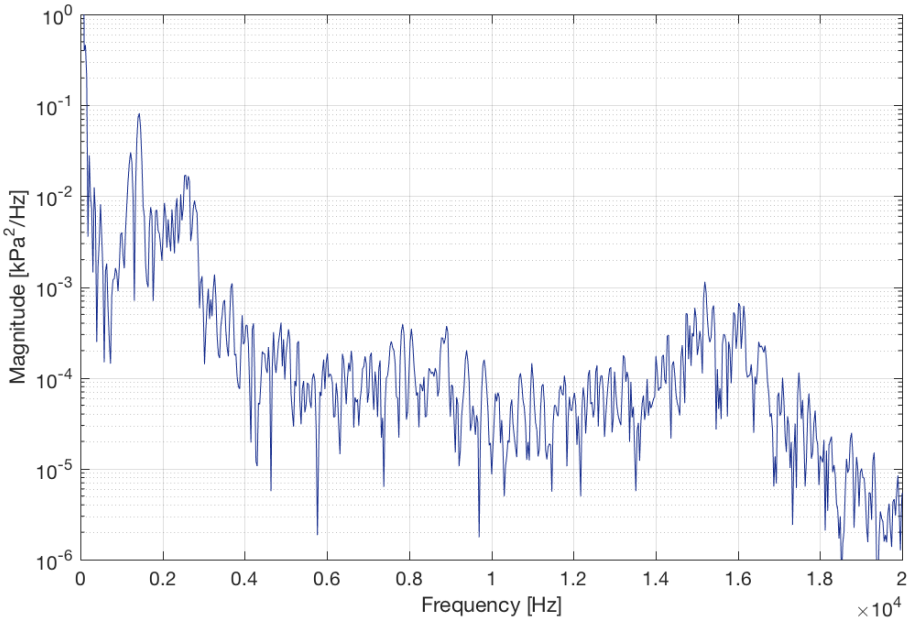

Figure 4.7.: The cross power spectral density for the two sensors installed at 1.27 cm at different circumferential locations. Shared frequency content near the first tangential mode around 16 kHz is evident.

dump plane sensors for Test 366, at either the fundamental or first harmonic of hte tangential mode.

The results from the nozzle reference match those from the oxidizer post inlet reference results. In Test 360, a pulse is seen traveling upstream through the chamber, starting around 930 m/s then slowing to 840 m/s as it nears the dump plane. In the oxidizer post the pulse slows with the lower fluid temperature, to around 350 m/s. This is higher than the expected mean flow-adjusted sound speed of 260 m/s, but is very similar to the value calculated from the post inlet reference. The nozzle reference results for Test 366 also match those with the post inlet reference, as the upstream pulse is calculated to have a velocity around 1000 m/s throughout the chamber. It then slows to a value of 290 m/s inside the oxidizer post, more closely resembling the

expected speed. The bifurcation seen when the dump plane reference was used is not visible here.

The timing discerned from the cross-correlation results was compared to expected travel times for acoustic pulses within the chamber. It was thought that when the acoustics of the system more closely matched expected acoustic speeds, it would become easier to resonate with the natural modes of the chamber. The timing backed out of the peaks in the cross-correlation demonstrated that the chamber had a strong propensity for upstream traveling acoustic pulses emanating from the nozzle, where as time moved forward, the various locations peaked in order from the downstream sensors up towards the dump plane, and even to the oxidizer post inlet. The evidence for a returning wave is seen in a few ambient oxidizer tests, but not all. However, the timing between the dump plane peak, when the pulse is considered to be at the far upstream end, and the next nozzle peak were compared to the theoretical mean-flow adjusted sound speed. Generally, as the difference in timing decreased, the RMS amplitude of the pressure signals increased, and vice versa. For tests with the same acoustic profile, the timing should be the same, when normalized by the fundamental chamber frequency. The discrepancy between the two tests around $L/\lambda = 0.32$ but different geometry shows that acoustic profile alone does not fully account for the acoustics within the chamber.

A possible explanation is that vortices are being generated at the head end of the chamber by the backstep. These vortices were shown in simulations of the UEC, formed when a favorable pressure gradient appears at the dump plane, rolling up oxidizer and fuel and shooting the vortices outwards towards the wall. With the UEC, it was demonstrated that by tailoring the step height of the backstep, and thereby altering the travel time of the vortex, the system could be tuned to have the vortex impinge on the hot wall and combust at the same time an acoustic pulse traveling through the chamber - after being produced by the same initial pulse that generated the vortex - reaches it. This led to a configuration that was originally stable become unstable with a small geometry change.

In the DVRC, the results are much less severe, as RMS amplitudes range between 10 and 60 kPa. Using a method akin to that of the UEC, the time between local pressure pulse at the dump plane and final vortex impingement on the wall was calculated and compared to the travel time of that pulse down the chamber and back. This was then normalized by the fundamental longitudinal chamber mode, as shown in Equation (4.1).

$$\Phi = \frac{t_a - t_v}{T} \tag{4.1}$$

Here, t_a represents a stretch of time starting from a localized pressure pulse at the dump plane, through the subsequent expansion that then provides the pressure gradient that generates a vortex, up to the impingement of the vortex on the nearby wall. The time from that initial pressure pulse, through the traveling down to the end of the chamber, reflected, and up to traveling back to the dump plane is captured in t_v. T is the period of the fundamental longitudinal chamber mode. As the chamber length increases, so does both t_v and T. Increasing oxidizer post length increases t_a. In this way, two geometries with similar acoustic profiles would have different timings between vortex impingement and chamber pulse return.

Comparisons of the value Φ and the measured RMS pressure amplitudes for each ambient oxidizer geometry are shown in Figure 4.8. There is a clear trend observed. The amplitude increases linearly with the value of Φ, rising from one up to nearly two. There is a lone outlier around 1.55 that comes from the single test at L/λ greater than 0.5. Both hot and ambient oxidizer tests exhibited a sharp change in behavior at values beyond 0.5, and this is further evidence of that.

The timing between vortex generation to impingement compared to the chamber pulse travel time is out of phase by more than a full chamber cycle. That is, a full cycle within the chamber occurs before the initial driving pulse at the injector face produces a vortex which propagates to the wall. At a phase lag around one, the amplitudes are at the weakest. They continue to grow to the most extreme Φ tested around a full two cycles. The fact that more than a single cycle passes

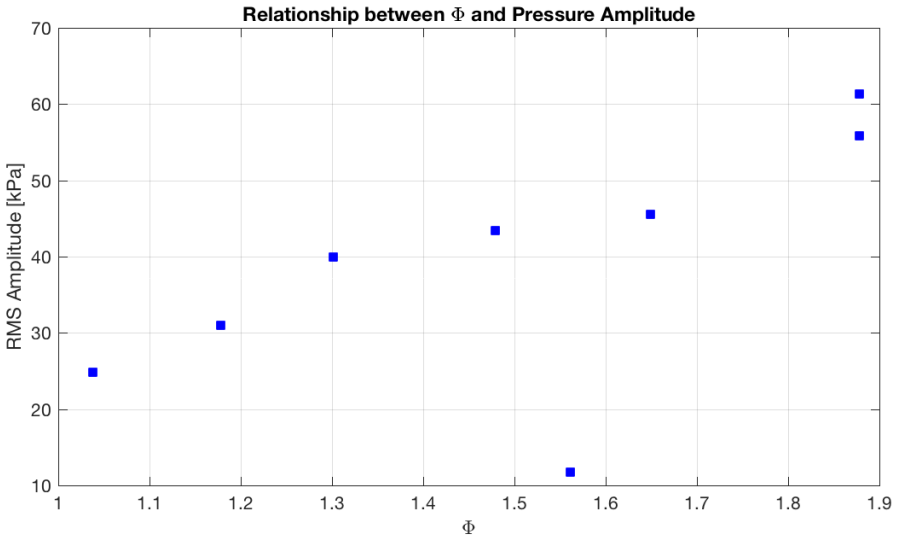

Figure 4.8.: Comparison of RMS pressure amplitude as a function of normalized difference between vortex impingement time and chamber pulse travel time.

between vortex impingement and localized compression in the chamber carries with it interesting ramifications. This would make it difficult to couple the acoustics with the localized heat release, as any pressure fluctuations generated by the release of heat will not have an impact on the next cycle or two of vortices. This delay would act as a buffer, stabilizing the combustion field. It is possible that the assumption of vortex impingement at an axial length of 4.5 times that of the step height is not correct, nor the assumption the vortex travels at approximately two-thirds the velocity of the oxidizer jet. While those assumptions fit the results of the UEC, the difference in oxidizer temperature and composition, as well as injector dynamics such as O/F and momentum flux ratio, could lead to different vortex speeds and impingement locations. But based on previous results and those shown here, it does appear that proper tuning of the system can utilize vortices generated of the backstep to induce pressure fluctuations that can ultimately lead to thermoacoustic coupling.

Comparison of the results from cross-correlation between pressure signals identify differences between the tests run with hot and ambient oxidizer. Strength of correlation is the key identifier. Tests run with hot oxidizer produced cross-correlation values that were either very weak, or would show high degrees of correlation for a short period of time. No signals correlated strongly with the oxidizer post inlet reference apart from itself but only without any time lag. Correlation increased with the dump plane reference signal, although only the dump plane measurements themselves maintained correlations above 0.5 for time lags indicative of multiple cycles. With the nozzle reference signal, stronger correlations were obtained but captured very wide peaks instead of narrow ones, a possible indication of transient behavior. Estimates of pressure pulse traveling speeds were calculated using time lag and distance between signals which captured pressure fluctuations that appeared to emanate near the nozzle and propagate upstream at a velocity close to that of the fluid sound speed, adjusted for mean flow velocity.

For the ambient oxidizer tests, the cross-correlation results generated stronger, sharper peaks for a greater number of signals. Correlation was relatively consis-

tent regardless of reference signal. Each reference signal captured upstream traveling pulses at velocities near the expected mean flow-adjusted sound speed. For Test 360, the pulse was near the expected value at the downstream end of the chamber and slower near the head end. Oxidizer post speeds were also higher than expected. For Test 366, the pulse maintained a consistent speed throughout the chamber matching the expected value. This also held true in the oxidizer post. Test 366, with an acoustic profile of L/λ of 0.38 captured stronger correlations compared to those from Test 360, with an acoustic profile of L/λ of 0.23. The time lag between signals for Test 366 showed that the system better accommodated a full wavelength than Test 360, where the post and chamber both individually exhibited half-wave mode shapes.

A constant through both tests was the weak presence of both the downstream oxidizer post and the fuel manifold signals, which correlated the weakest with the reference signals, although the correlations were higher for the ambient oxidizer tests. The lack of strong peaks suggests that these two locations do not directly capture the effect of pressure perturbations.

4.2.3 Statistics-Based Analysis

Statistical methods were applied to pressure data for all tests, both hot and ambient oxidizer. These statistics provide a foundation on which to compare not only the tests, but also the various sensor locations. Two metrics are examined. First is the range of the pressure fluctuations, the extent to which amplitudes were exhibited, sans any outliers. To achieve this, the lowest and highest 1% of the amplitudes were removed, leaving the central 98%. Second is the root mean square of the signals. Both metrics aim to provide a quantitative measure for comparison. With both the hot and ambient oxidizer temperatures, limited organization was present. Fluctuations varied in amplitude with each pulse. The RMS was considered to be a sufficient measurement of amplitude.

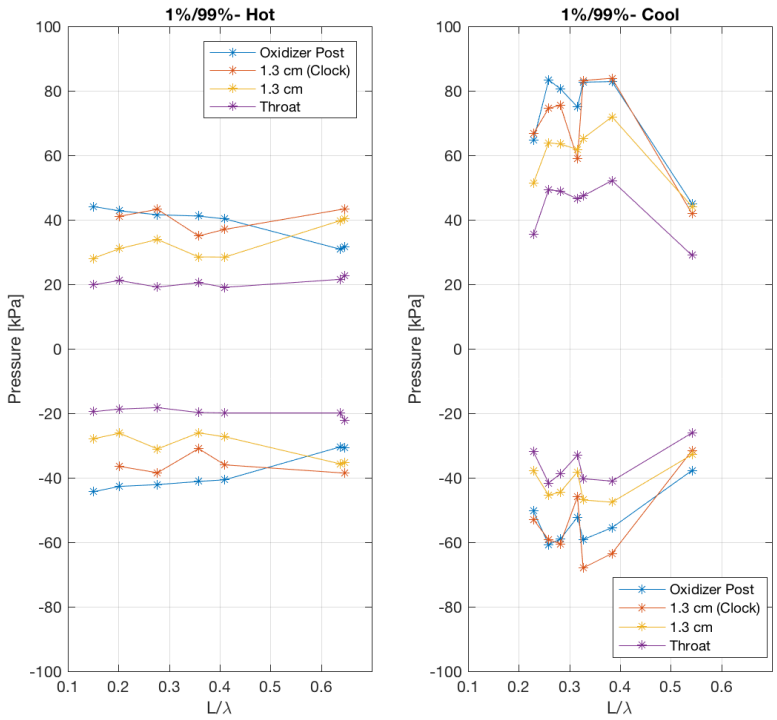

Figure 4.9.: Effect of acoustic profile on range of pressure fluctuations amplitude, comparing hot and ambient oxidizer tests.

The first comparison, shown in Figure 4.9, contrasts the range of the dynamic pressure signals. On the left hand side are the results with the ambient oxidizer, while on the right are the results from hot oxidizer tests. The acoustic profile, represented by L/λ, is featured along the x-axis. Two groupings are presented on each plot, capturing the upper and lower limits of the dynamic range with the extreme 1% of the values removed. The signals are high-pass filtered, so the results are roughly centered around zero.

The hot oxidizer tests exhibit very little variation at values of L/λ below 0.5. The oxidizer post inlet and throat locations remain constant, while the dump plane locations fluctuate some around 0.3. More variation exists between the different locations at the same L/λ value. The throat exhibits the narrowest range, which then expands for the dump plane measurements. The oxidizer post inlet has the greatest dynamic range, at around $\pm$40 kPa. While at the same axial position, the 1.27 cm locations have different ranges. The clocked position experiences a greater amplitude range, with amplitudes pushing 40 kPa and the non-clocked sensor around 30 kPa.

The single test with an L/λ value beyond 0.5 shows a drastic change in amplitude range for the post inlet and dump plane locations. The post inlet range drops from 40 kPa to 30 kPa while the dump plane locations make the reverse change, with both 1.27 cm signals converging to the same value. The throat signal appears unchanged.

Results with the ambient oxidizer exhibit a stronger response compared to the hot oxidizer. The oxidizer post inlet has the largest range, followed by the dump plane locations, then throat, similar to the hot oxidizer. In this case, the difference between the two 1.27 cm locations is greater, with the clocked position nearly converging to the range seen at the post inlet. Unlike with the hot oxidizer, the lower bound is not quite symmetric across the x-axis with the upper bound. The magnitude of the lower is reduced, and the 1.27 cm clocked location exceeding that of the post inlet.

The effect L/λ has on the range is also greater with the cooler oxidizer inlet temperature. In the range between 0.2 and 0.5, the bounds generally take on a

parabolic form, reaching a maximum 0.32. Another geometry was tested near this same acoustic profile, but with much more subdued amplitudes. This was consistent across all sensor locations, and seen in each test for this configuration. Similar to the hot oxidizer case, tests at configurations where the acoustic profile exceeded 0.5 showed a drastic change. Beyond $L/\lambda = 0.5$, the range narrowed for all measurement locations, appearing to converge towards a shared value.

The RMS of the pressure signals trends very similar to the 1%/99% distribution for both hot and ambient oxidizer, shown in Figure 4.10. With the hot oxidizer, there is minimal change in RMS amplitude with change in geometry. The oxidizer post continues to exhibit the strongest amplitudes, followed by the clocked, then non-clocked 1.27 cm locations, and finally the throat, matching the order of the previous section. The sudden change in behavior with the jump to L/λ greater than 0.5 is also seen in the RMS data.

Likewise, the ambient oxidizer test RMS amplitudes capture the same general parabolic relationship between RMS and L/λ, including the drop in amplitudes around 0.32. The order of greatest to least amplitude again matches between RMS and the 1%/99% measurements. One observed change between the two is a noticeable increase for the clocked 1.27 cm signal at the dump plane. This is not matched by the other 1.27 cm location. Apart from that, the trends are maintained between the RMS and distribution of the pressure signals.

Similar results were obtained through reducing the data through the two statistical methods. Generally, the hot oxidizer had a weak to no observable dependency on the acoustic profile at L/λ values. At values below 0.5, both the dynamic range and RMS of the signals are flat, although different magnitudes are obtained depending on sensor location. The strongest amplitudes are observed at the oxidizer post inlet, followed by the dump plane locations, although the two exhibit different amplitudes despite being located at the same axial position. The sensor near the throat was noticeably weaker than the others.

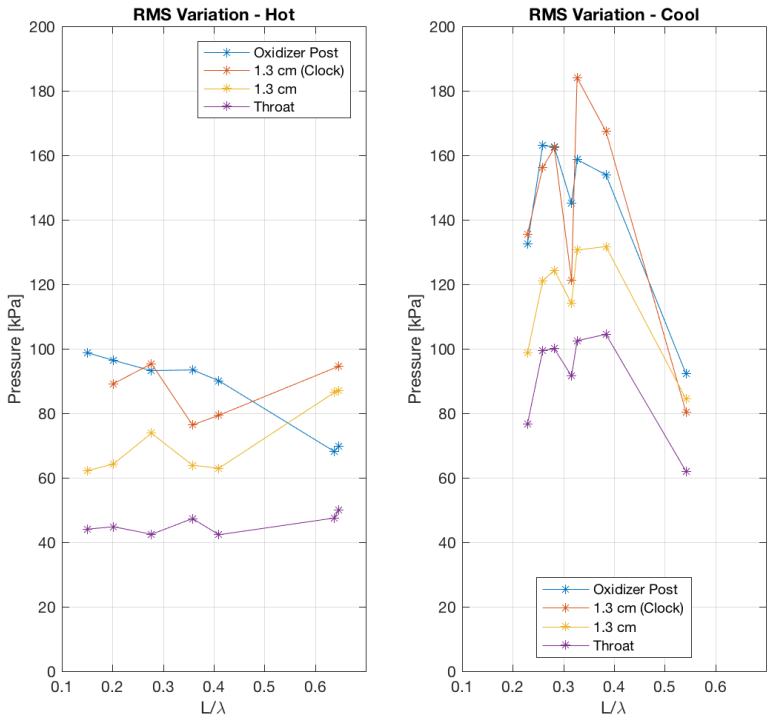

Figure 4.10.: Effect of acoustic profile on the RMS of pressure fluctuations amplitude, comparing hot and ambient oxidizer tests.

The behavior changed for the single test case beyond L/λ of 0.5, where the amplitudes of the post inlet and the two dump plane locations switched. There was minimal impact on the throat signal. It is not possible to gauge the effects at these higher values from a single test point, and instead this work examines only tests with the behavior changed below 0.5

A drastic change is observed with the ambient oxidizer, as a clear dependency between L/λ and amplitude manifests. For all cooler tests, the magnitudes of the RMS and dynamic range are greater than those from the same sensors in hot oxidizer. In general, a parabolic trend is observed, where at the extreme L/λ values tested the amplitudes decreased. In between these values, the amplitudes rose to a maximum near $L/\lambda = 0.32$. This is not consistent with all tests, as a test at $L/\lambda = 0.31$ demonstrated weaker amplitudes. The same stratification between sensor locations observed with the hot oxidizer is present here, with the same order. The two dump plane locations have disparate values, with the clocked location stronger and more closely attached to the post inlet signal rather than the non-clocked pairing.

Like the hot oxidizer, a change occurs at higher L/λ values, with all values dropping and converging to a similar value.

As mentioned in the previous section, and shown in Figure 4.8, the change in oxidizer temperature also augmented the specific impedance of the fluid, and thereby the acoustic reflection and transmission coefficients between the oxidizer and combustion gases. This increase, from hot to ambient oxidizer inlet temperature, is around 40% for both reflection and transmission, which matches with the increase in the dynamic range and RMS at the lowest amplitudes of the ambient oxidizer cases. This does not explain the further modulation of the magnitudes with variation in L/λ.

4.2.4 Power Spectral Density and Spectrogram

The power spectral density (PSD) of a signal breaks it down into the frequency components. Identifying frequency responses within the pressure measurements is key

to understanding the system, from oscillations from the feed supply to thermoacoustic instabilities. Analysis of the PSD provides a window into the system behavior. Comparison of the PSD of multiple signals can provide further useful, albeit limited, spatial information.

A sample PSD is shown in Figure 4.12a. The example is taken from hot oxidizer Test 359 from the non-clocked 1.27 cm signal. The parent figure is created from a time slice of 0.30 seconds of continuous hot fire. Several peaks can be observed, although none are particularly strong or narrow. Instead, they are somewhat broad, with the peaks acting more like plateaus. Despite the wide and smeared appearance of the peaks, they still approach the expected frequencies for acoustic modes. The solid black lines are the frequencies of predicted chamber modes, based on measured equivalence ratio. The dashed red lines are the frequencies of predicted oxidizer post modes, assuming an closed-open configuration, based on oxidizer manifold temperature. The predicted chamber modes appear to be close to reality. The first mode appears to coincide with the first major peak, and the second appears to be in the midst of a plateau. The third mode, however, is caught between two peaks. The oxidizer post modes appear to overpredict what is observed in experiment. Evidence for this is the shift between the higher prediction for the first post mode and the lower small peak around 850 Hz. The second mode is caught between two small peaks, while the third one falls on a single peak between two others. If the first mode is adjusted to a lower frequency, coinciding with the first peak, that would also shift the second mode onto the larger of the two nearby peaks, and the third mode to the isolated peak around 4300 Hz.

This signal was broken into six sequential slices, then the frequency response presented via PSD, shown in Figure 4.12b-g. The PSDs generated for the six time slices are not consistent. The most pronounced peak, seen around 3000 Hz, rises and falls between 0.1 and 1. Similarly, the wide peak observed around 1500 Hz undergoes dramatic changes throughout the 0.3 second window. Between 0.90 and 0.95 seconds, this peak is fairly narrow and near its strongest. As it moves into the 0.95 - 1.00

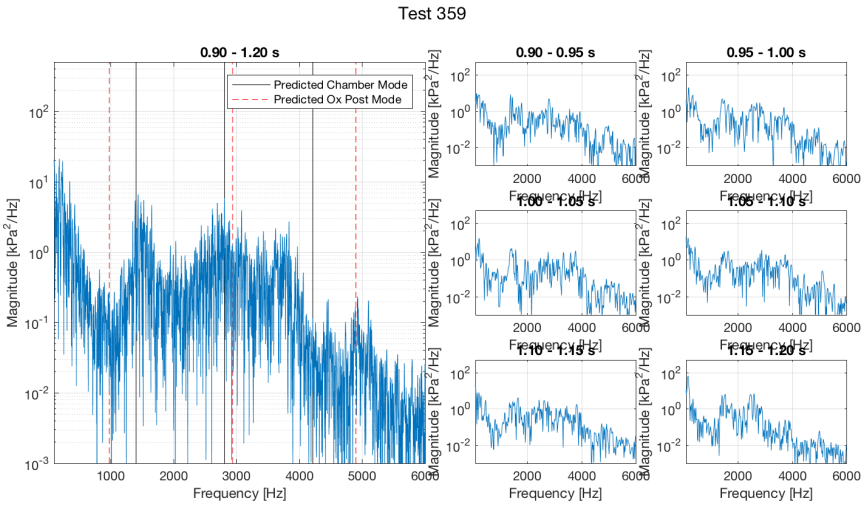

Figure 4.11.: Variation in power spectral density through time for Test 359 with hot oxidizer with $L/\lambda = 0.36$. Main figure shows frequency content from a window of 0.30 seconds. Subfigures capture the frequency content from 0.05 second windows within the parent time frame.

s window, then the 1.00 - 1.05 s window, the peak widens. At 1.05 - 1.10 s the excited frequency range drops in amplitude, followed by an increase in frequency content around 1700 Hz. It is this rapid change in both the frequency range of a given response and the amplitude that causes the smeared presentation in the parent figure.

The same analysis was applied to the clocked dump plane signal from Test 363 with hot oxidizer. This test has a smaller L/λ at 0.20, acting more like a quarter-wave resonator. Compared to Test 359, Test 363 has a less smeared appearance. Although there are not any strong, narrow peaks typical of thermoacoustic instabilities, there is clear presence of organized content. The first two chamber modes appear to be predicted fairly well. The predicted frequency of the first mode falls nearly on top of the first major peak, while the second prediction is shifted slightly higher than the observed harmonic. The third mode does not appear to be excited, as no peaks are nearby. The oxidizer post modes are also near that of the predictions. While the first post mode is a little lower than the expected frequency, the second mode falls right on a peak near 5100 Hz.

While the predicted and observed modes are similar, there is still moment-to-moment variation in the frequency content, as captured by the children plots. For example, the first major peak around 1460 Hz undergoes significant changes. Between the first two subplots the single peak split apart into two adjacent peaks. It then rises again in the next snapshot, surrounded by two other peaks. The central peak appears to shift frequencies throughout. The larger peak around 2743 Hz exhibits similar transient behavior, shifting between 2600 and 2750 Hz through the 0.3 second time trace, the two rising and falling in amplitude together.

Operating with ambient oxidizer resulted in a sharpening of peaks at a small number of frequencies at the fundamental mode. Higher modes remained weaker and smeared. Test 366 provides an example of this at L/λ of 0.38. The first two chamber modes compare well between prediction and simulation. There is a slight shift between the strongest peak and the first chamber mode prediction, with the

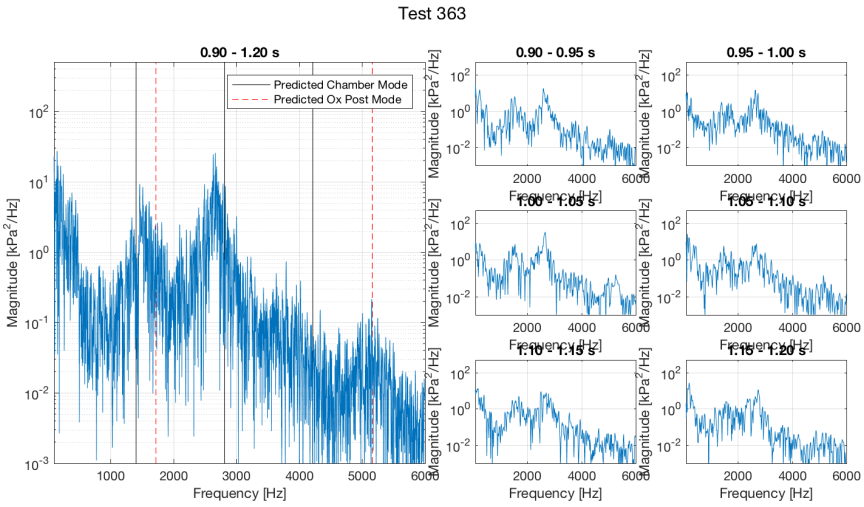

Figure 4.12.: Variation in power spectral density through time for Test 363 with hot oxidizer with $L/\lambda = 0.20$. Main figure shows frequency content from a window of 0.30 seconds. Subfigures capture the frequency content from 0.05 second windows within the parent time frame.

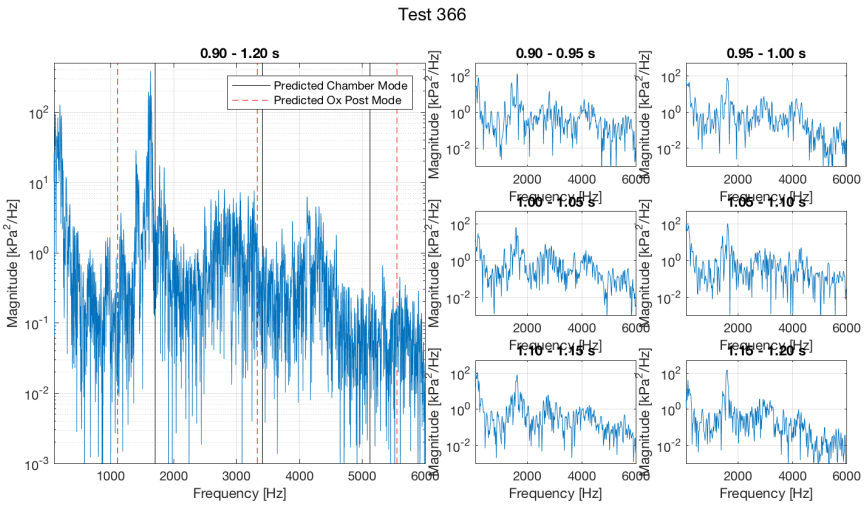

Figure 4.13.: Variation in power spectral density through time for Test 366 with ambient oxidizer with L/λ = 0.38. Main figure shows frequency content from a window of 0.30 seconds. Subfigures capture the frequency content from 0.05 second windows within the parent time frame.

prediction slightly overshooting. The expected frequency of the second mode does not fall directly on a peak, but is very close to one. The third prediction is not quite near a peak, with the only significant peak higher than the prediction, which is opposite of the expected shift. This suggests that harmonics beyond the second mode are not excited, similar to the hot oxidizer cases.

There is a grouping of peaks surrounding the predicted fundamental oxidizer post mode. The mode is predicted at 1110 Hz, while there are nearby peaks at 1400, 1160 and 950 Hz, and even another at 673 Hz. The 1160 Hz mode most closely matches the predicted mode, and also lines up with a peak around the second mode around 3280 Hz. The third expected post mode also falls on a peak, but not the strongest one in the vicinity. The strongest peak falls directly between the expected third chamber and post modes.

Of the grouping of peaks at low frequencies, only two are likely to be directly attributable to the fundamental chamber and post modes. This is unlikely to be a

beating effect, as the beating of two similar frequencies in this range would result in third frequency in the hundreds of Hertz. It is also unlikely that these adjacent peaks are artificial, due to the behavior of the frequency spectrum through time and the lack of synchronized organization between them. In each time slice, the largest peak, attributed to the chamber mode, is present. In all but one slice, the adjacent peak around 1450 Hz is present. The one odd time slice does not have a peak, between 1.10 and 1.15 seconds, instead has two broad shoulders. An artifact would likely have a uniform effect, either across a wide frequency band, or synchronized in time.

The 1160 Hz peak appears to be independent of the others, not trending with either the higher frequency pairing, nor the two at 950 and 673 Hz. If this mode is related to the oxidizer post and the post and chamber modes do not trend together, then that would suggest a failing of the post and chamber to couple. The lower frequency pairing generally trend together. They are typically present at the same time, although sometimes one changes amplitude more than the other. They do not immediately show a connection to the higher frequency pairing. There is no clear indication as to what drives these peaks.

Test 360, where the acoustic profile featured an L/λ of 0.20, provides a similar PSD profile to that of Test 366. A grouping of sharp peaks exists at low frequencies around that of the fundamental modes for both the chamber and post, while the harmonics exhibit weak, less defined peaks. The predicted frequency for the first chamber mode falls right on top of the experimentally defined one. The expected harmonics, pure multiples of the fundamental, overpredict the actual harmonics, which are not exactly multiples.

The predicted fundamental frequency for the post falls between the sharp, central peak and a higher secondary shoulder peak. The next harmonic appears around 4500 Hz, falling at a frequency somewhat less than the nearest peak that looks to be most likely the fourth chamber mode. Back near the first predicted post mode are four obvious, well-defined peaks. Besides the most central one at 1400 Hz attributed to the chamber mode, three others are found at 1040, 1232 and 1575 Hz. As stated

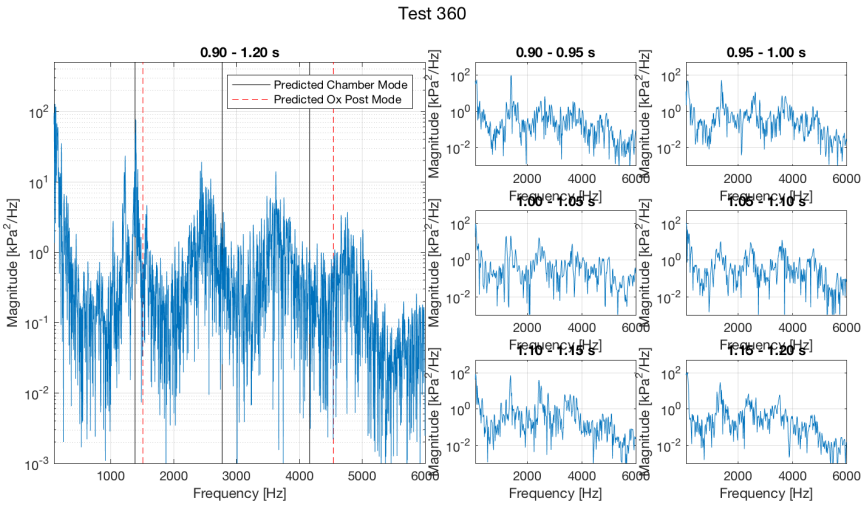

Figure 4.14.: Variation in power spectral density through time for Test 360 with ambient oxidizer with $L/\lambda = 0.23$. Main figure shows frequency content from a window of 0.30 seconds. Subfigures capture the frequency content from 0.05 second windows within the parent time frame.

above, the highest frequency peak at 1575 Hz is closest to the predicted frequency. The lower pair do not match any expected frequencies, like with Test 366.

A sense of the persistence of these peaks can be gleaned from sequence of PSDs constructed from slice of the original 0.30 seconds. In each child plot, the fundamental chamber mode around 1400 HZ is prominent, being the strongest response in each time interval. The next strong response is around 1230 Hz and is more variable than the 1400 Hz peak. At times its power in on par with the fundamental chamber mode, such as between 1.00 and 1.05 seconds, while other times it barely registers, such as between 0.95 and 1.00 seconds, or 1.15 and 1.20 seconds. The 1040 Hz peak shows itself to be more ephemeral, appearing only in a few of the time slices. Similarly, the higher frequency peak that matches the predicted fundamental post mode varies greatly, where it appears only in some time slices. Although this mode is weaker than the 1230 Hz response, the two appear to trend together somewhat in their amplitude variation.

In the parent figure, it appears that only two peaks are in the vicinity of the expected second chamber mode, one a broadened and blurry peak and another right at the expected 2L frequency as a obviously distinct peak. Based on the time slices, the broadened peak may in fact be a combination of different response. The main response falls around 2450 Hz, featured in most of the time slices. Occasionally the response in this mode falls in amplitude, revealing a response around 2650 Hz, such as in the 0.90 to 0.95 seconds or 1.15 to 1.20 seconds slices, or a lower frequency around 2300 Hz, seen in the 1.05 to 1.10 and 1.15 to 1.20 seconds slices. The variation between the three responses are not obviously connected. The peak sitting at the expected chamber 2L mode around 2700 Hz remains distinct from this collection of responses.

Analyzing the frequency content of pressure signals via the power spectral density provides a window into identifying system behavior. Excitation of the acoustic modes of both the chamber and the oxidizer post can be observed through the organization of frequency content into peaks at the resonant frequencies. Strength of the acoustic

resonance is measured by the amplitude of the peak, and level of organization of by width of the peak.

With both oxidizer temperatures, the fundamental chamber mode was easily identifiable and usually the strongest response. The first two harmonics were also identifiable for the ambient oxidizer, yet only the first harmonic for the hot oxidizer. In both, the harmonics were not simply integer multiples of the fundamental mode, with the actual frequencies being less than the predicted values. This is most visible in the second harmonic for the ambient oxidizer cases.

The effect of the post modes is more subtle than that of the chamber modes. In some instances peaks can be found at expected frequencies, such as the second and third post modes in hot oxidizer Tests 363 and 359, respectively. This is also evident in ambient oxidizer Tests 360 and 366. In the former, the predicted first post mode is just shy of the peak associated with it, while the second post mode is shifted even further lower than the experimental result. In the latter, the predicted first post mode is also near a local peak, although a bit underestimated, while the second predicted mode slightly overpredicting a weak peak. The third predicted mode is caught between a very close weak peak and a further stronger peak, causing difficulties in determining which it belongs to.

Observation of the peaks reveals that the associated amplitudes appear to vary greatly. Typically for chamber modes, the fundamental frequency exhibits the greatest excitation, which weakens with subsequent harmonics. For the post modes, this is not the case. Instead, the results bolster the underlying theory of tuning the post to passively dampen chamber modes. In Test 363, where $L/\lambda = 0.20$, the first chamber harmonic shows the strongest response. This mode is separated from post modes by a fair margin. Compare this to Test 359 where $L/\lambda = 0.36$, where the first chamber harmonic frequency is very close to the first post harmonic. Treating the post as an open-close system with a choked inlet, post resonance would put a pressure node at the dump plane, while the chamber mode, a close-close system, would place an anti-node there. This would discourage coupling and actively dampen any behavior

at that frequency. It is only at higher frequencies that the post mode is seen to be separate from the chamber mode, weakening any potential interference between the two. A weak but obvious peak is found right at the expected post mode.

Similar results are found with the ambient oxidizer tests. In Test 360, where the post is effectively a quarter-wave resonator, the fundamental post and chamber modes are nearly at the same frequency. The fundamental chamber mode for Test 360 has an amplitude nearly an order of magnitude less than of Test 366, where the post is closer to a 3/8-wave resonator and the spacing between fundamental frequencies much greater.

The behaviors described above are transient, as the children plots illustrate, In neither the hot or ambient oxidizer cases is there a feedback loop fully closed, leading to a sustained thermoacoustic instability. Instead, various levels of interaction between chamber and oxidizer post acoustics are observed.

The above analysis considered a single signal from near the dump plane. This analysis is expanded to all of the signals for the representative tests. Doing so assists in identifying acoustic modes, as spatial effects can be visualized, such as frequency response attenuation at acoustic nodes. The following section examines the difference in frequency content in signals from different locations within the system. Pressure signals from a time slice of 0.15 seconds are taken from each location and compared within groups of similar measurement locations: the oxidizer post, the dump plane, and the remaining chamber locations.

The PSDs of the various signals for Test 363 with hot oxidizer is shown in Figure 4.15, alongside the predicted acoustic chamber and post modes. The first grouping, Figure 4.15a, contains the upstream and downstream oxidizer post and fuel manifold locations. The profiles of the frequency spectra are similar in energy distribution. The sole peak around the fundamental chamber mode is clearly visible in all three locations. Harmonics may be identified in the upstream post location, but with difficulty as the amplitudes are so low. The most apparent difference is the broadband increase in power for the upstream post location, indicated by the higher noise floor.

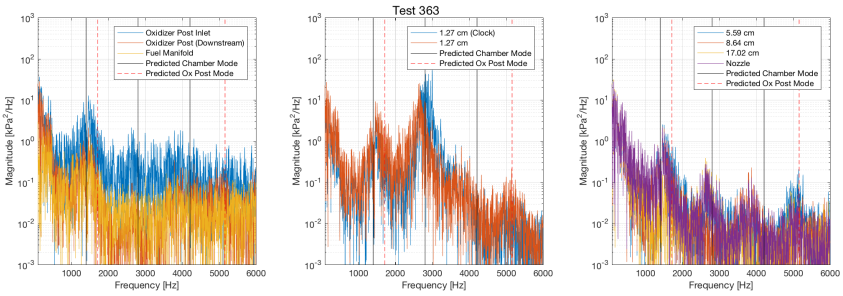

Figure 4.15.: Power spectral density from Test 363 with hot oxidizer from a window of 0.15 seconds. Signals are grouped by location.

This is not unexpected, as the transducer is located near the choked orifice marking the inlet. This would instigate a high level of turbulence within the far upstream section of the post flowfield.

Stronger responses are observed at the upstream chamber locations, as shown in Figure 4.15b. Similar to Test 359, the two 1.27 cm locations are nearly identical for the majority of the spectrum. The fundamental chamber mode is clearly identified in both signals, as is the third post mode. It is between 2700 and 3600 Hz that the profiles for the two signals diverge. The non-clocked signal peaks around the predicted second chamber more frequency, which matches the upstream results in Figure 4.15a. The frequency content amplitude drops, then rises again at what may be the third chamber mode shifted to a lower frequency. The spectrum then drops in amplitude beyond this point. The clocked dump plane signal follows along with the second chamber mode peak, but continues to rise to a peak around 3080 Hz. The amplitude then decreases to where it converges with the other transducer at the same axial location. The peak for this clocked measurement falls next to the second post mode. This is a peak that was not registered in the post and manifold signals.

Remaining chamber measurements capture weak acoustic behavior, with general similarities found between the four locations. The most prominent mode shared between the locations is the fundamental chamber mode. The 17.02 cm location near the chamber midpoint is unlike the others, featuring a sharp drop in amplitude which

is consistent with a 1L chamber mode shape. The second chamber mode is weak across all four transducers, most significantly with the 8.64 cm signal which is near a 2L acoustic node. At the higher frequency of 3840 Hz is the third chamber mode, as indicated by the weakened 17.02 cm signal near the modal node. Typically, the amplitude drops with each subsequent harmonic. Here, it appears as if the second harmonic is nearly skipped over. Following the discussion presented in the previous test case above, it is likely that the proximity to the second post mode, acting as a quarter-wave resonator, is dampening the second chamber mode.

The two dump plane locations at 1.27 cm are captured in the second grouping, Figure 4.15b. Both signals capture nearly identical response to the fundamental chamber mode seen in the upstream locations. The dump plane, however, responds differently at the first chamber and post harmonics. While a very weak peak was observed at the post inlet for the first chamber harmonic, the response at the dump plane is the strongest observed response. However, the two signals at the 1.27 cm location capture slightly different spectra. The non-clocked location captures a single peak around 2665 Hz, just short of the expected 2810 Hz. The clocked position captures a plateau-like rise, starting at 2665 Hz and stretching to 3000 Hz. Beyond that, the two spectra begin to converge to the same amplitudes, matching around 3500 Hz. Of note is the similarity in the small-scale profile of the two signals. This would suggest that the two signals are not dissimilar in their composition, but observe markedly difference change in amplitude across a narrow range of frequencies for the same, or at least similar, behavior. The first post harmonic, beyond the point of convergence for the frequency spectra, are captured around 5150 Hz. Here, the clocked signal appears to be slightly weaker than its counterpart.

The last grouping contains the remaining chamber locations: 5.59 cm, 8.64 cm, 17.02 cm and near the nozzle. Comparison of this grouping of signals assists in identifying the peaks as chamber acoustic modes. The 17.02 cm location, near the chamber midpoint, captures limited content at the fundamental chamber mode as is expected near the nodal point. This also occurs for the third chamber mode for

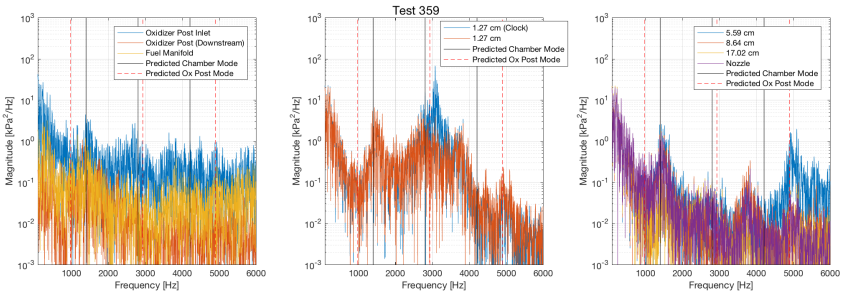

Figure 4.16.: Power spectral density from Test 359 with hot oxidizer from a window of 0.15 seconds. Signals are grouped by location.

the same reason. Likewise, the 8.64 cm location sits very close to a node for the second chamber mode and accordingly observes no content at this frequency. The second post mode is strongest for the 5.59 cm location, while the remaining chamber locations register similar but weaker responses. This appears to be less due to the nodal location of the transducer and more of a proximity effect, as the 5.59 cm location is the signal closest to the post in this grouping.

Comparisons of frequency spectra from hot oxidizer Test 359 with $L/\lambda = 0.36$ are shown in Figure 4.16. Also included are predicted frequencies of chamber and post modes, in solid black and dotted red lines, respectively. These results are similar to that of Test 363.

The three signals presented in Figure 4.16 share similar spectra. The two post locations and fuel manifold are relatively quiet. A weak peak falls at the first predicted chamber mode. The second predicted chamber mode slightly overpredicts the second major peak in the PSD. Several peaks are in the vicinity of the predicted third chamber mode. Narrower peaks also appear around the predicted post modes. These modes are marginally weaker than the chamber modes. The noise floor for the upstream post location again exceeds that of the downstream location and fuel manifold by a large margin.

At the dump plane, the two transducers produce signals that are nearly identical. Several peaks are present. The fundamental and first harmonic of the chamber mode

falls near the predicted frequencies, The second harmonic, is close to the predicted peak, but is overpredicted. Around this prediction is another small peak which is not immediately clear what it is associated with.

Oxidizer post modes make a weak appearance. The first predicted post mode falls in a low amplitude frequency band, with a single sharp peak in the vicinity that may be associated with the mode. The second predicted mode is very close to the second chamber mode and falls in the frequency band where the two signals diverge greatly. While the frequency spectra of these two dump planes signals are virtually identical, even when examining the profiles across an extremely narrow bandwidth, the 1.27 cm clocked position continues to increase in amplitude with increased frequency from the predicted second chamber mode, around 2700 Hz. The magnitude increases, becoming the strongest peak by a wide margin at 3080 Hz, where it then decreases and converges directly with the non-clocked 1.27 cm measurement. This peak seen only in the clocked location is very near to the second post mode. There is also the third post mode in the upper frequency range, in Figure 4.16b. This weak but conspicuous peak lines up with the predicted value. There is also an adjacent peak of nearly equal value, which would fall near a fourth chamber mode when compensating for the increased shift between predicted and experimentally-determined frequencies for higher harmonics.

The modes observed at the dump plane are also present in the remaining chamber signals, save for the peak near the second post mode that was limited to only the clocked measurement. As Figure 4.16c shows, these modes are much weaker further into the chamber, and in the case of the second chamber mode, almost non-existant. The 17.02 cm signal, being located near a node for odd-numbered chamber modes, identifies the first and third chamber modes via a reduction in amplitude. Likewise, the 8.64 cm near the 2L node experiences weakened amplitudes for the same mode. As for the post modes, the first two predictions are not accompanied by an obvious response at those frequencies. These two predictions fall near chamber modes. As

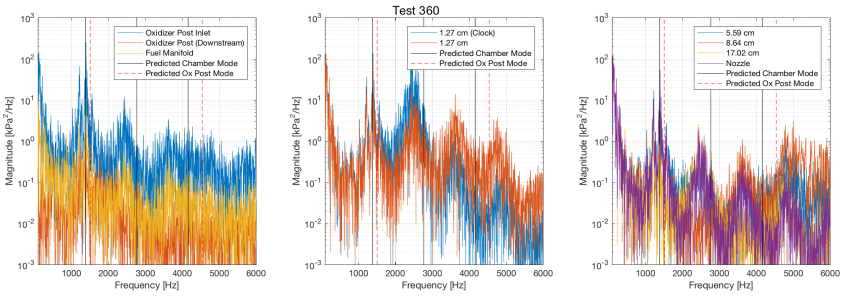

Figure 4.17.: Power spectral density from Test 360 with ambient oxidizer from a window of 0.15 seconds. Signals are grouped by location.

these modes feature a closed-open mode shape in the post, and closed-closed in the chamber, the two would act to dampen each other out.

An event not observed in Test 363 but present here is the sharp rise in amplitude at 4890 Hz, right on a predicted third post mode. While present in all four signals, it is the 5.59 cm location where it is most prominent, matching the amplitude of the first chamber mode. If this is indeed a post mode, it is not surprising it would be stronger near the head end. However, this level of response was not observed at the dump plane.

Tests with ambient oxidizer capture increased amplitudes throughout the post, fuel manifold and chamber. Presented first, in Figure 4.17, are PSDs of signals taken from Test 360 with a $L/\lambda = 0.23$. Following the trends observed in the hot oxidizer cases, the post and fuel manifold signals exhibit similar profiles with the post inlet spectra amplitude nearly an order of magnitude higher than the downstream post and fuel manifold signals. Fitting the acoustic profile of the configuration, the predicted fundamental chamber and post modes are nearly the same. The expected and actual first chamber mode fall at the same frequency of 1400 Hz. Multiple peaks surround the fundamental chamber mode. One peak falls at the higher frequency of 1575 Hz, slightly higher than the predicted first post mode. At lower frequencies are the peaks at 1230 and 1040 Hz. These are not obviously tied to any particular mode.

The second chamber mode is predicted around 2775 Hz. Both the post inlet and fuel manifold capture a nearby peak around 2450 Hz. The downstream post does not capture this behavior, likely due to the proximity of the sensor to a node for this mode. The actual and predicted third chamber modes have drifted further apart, following the example of the second mode. Similar to the second mode, this mode is further weakened at the downstream post location. There is no peak near the predicted second post mode.

The signals recorded from the dump plane measurements capture peaks at the same frequency as the post and fuel manifold locations. Several peaks are visible around the fundamental post and chamber modes, with the strongest peak falling right at the first chamber mode frequency and the first post mode near a side peak. Two other pronounced peaks are observed at frequencies lower than either fundamental mode. Amplitudes for these locations are nearly identical up to around the first chamber mode.

The frequency range around the second chamber mode captures a small deviation to the spectra measured upstream. There is still a strong peak somewhat lower than the predicted second chamber mode, but there is a clear change in amplitude between the two 1.27 cm locations with the clocked version being the strongest of the two. This changes around 3000 Hz where the overall amplitude of the clocked signal falls and stays below the amplitude of the non-clocked signal. There is a small but prominent peak in both signals right at the predicted second chamber mode frequency that, while not very powerful, is quite narrow compared to the other observed modes. The third chamber mode does not match the predicted frequency, with the expected frequency overpredicting by around 500 Hz, placing the prediction between two peaks. The higher frequency peak is close to the expected second post mode.

Further downstream, the remaining chamber locations for Test 360 in Figure 4.17c capture similar frequency profiles to the dump plane signals but at an overall lower amplitude. The first grouping of peaks near the predicted fundamental chamber mode show a sharp drop in amplitude at the 17.02 cm location compared to the other

locations. While this points to general acoustic mode shape behavior, it does not directly explain the several adjacent prominent sharp peaks at all four locations in this plot. The first post mode is also predicted around this frequency, which would make it likely that the post is driving some of this behavior. The second chamber mode is identified by the drop in amplitude near the node at the chamber midpoint, as measured by the 8.64 cm signal. No measurable response to the second chamber mode is registered at this sensor while the three others clearly capture periodic behavior at this around the predicted frequency. The third chamber mode, like the first, is clearly present by the drop in amplitude for the 17.02 cm sensor in comparison to the other signals. This is despite the approximately 500 Hz shift between predicted and actual 3L frequency.

Another organization of frequency content occurs around 4800 Hz. This is near the predicted second post, but also a fourth chamber mode, based on the shifts seen between predicted and actual chamber modes. There is not a clear acoustic mode shape to the response around this frequency. The amplitude is higher for the further upstream measurements, 5.59 and 8.64 cm, then drops for the 17.02 cm and nozzle locations as opposed to a single reduction in amplitude at the expected node location around 8.64 cm. Like the peaks around the fundamental chamber mode, this could be an indication of post driven physics.

Presented next, in Figure 4.18, are the PSDs of the signals from Test 366 at $L/\lambda = 0.38$. The spectra closely resembles the other ambient oxidizer test, having stronger responses than the hot oxidizer tests. This test also demonstrates a stronger response than near the quarter-wave resonator case. As in the previous cases discussed, the sensor near the post inlet observes the highest amplitudes and generally has a higher broadband noise floor. The other two locations have roughly similar amplitudes except between 2600 and 5100 Hz, where the downstream post signal exceeds that of the fuel manifold.

There are a number of individual peaks around the predicted fundamental chamber mode. The strongest peak is near the predicted fundamental chamber frequency, with

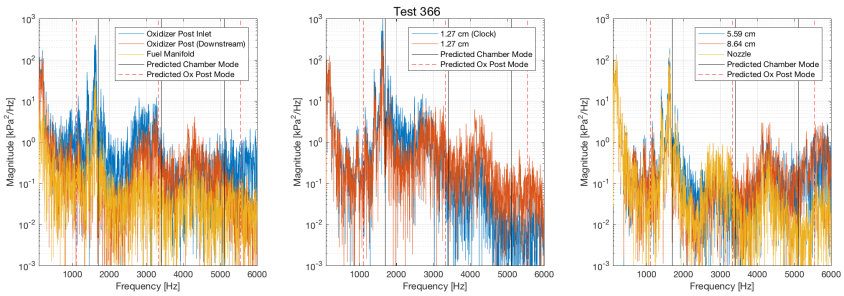

Figure 4.18.: Power spectral density from Test 366 with hot oxidizer from a window of 0.15 seconds. Signals are grouped by location.

three adjacent peaks at lower frequencies. The center of these three is close to the expected fundamental post mode frequency. The response near the second chamber mode is much less organized. There is not a single sharp response here. As a whole, this response falls short of both the predicted second post and chamber modes, a trait seen in the previously discussed tests. What appears to be the third chamber mode is short of the predicted frequency. There are no observed responses at either of the third chamber or post modes.

Profiles of the frequency spectra are not too different between the upstream signals and those at the dump plane. The grouping of peaks near the fundamental chamber mode exhibits increased amplitude, primarily at the strongest frequency adjacent to the predicted chamber mode. Up until about this peak, the two signals have equal strength. Beyond it, across a narrow bandwidth, the clocked position is stronger, then drops below the non-clocked signal strength from around 3400 Hz and higher.

There is not a strong second mode response evident for either the post or the chamber mode. The wide rise in amplitude seen upstream is weaker near the dump plane. This could be tied to the damping effects of the closed-open post mode on the open-open chamber mode. There is a weak rise in strength around the third chamber mode, showing a wide peak reaching up from the noise floor. Very little coherent signal is observed at higher frequencies.

Comparison of the frequency spectra for the remaining chamber signals provides insight into the acoustic excitation of the system. Due to the configuration of this test, there was no measurement at the chamber midpoint to aid in identifying the odd-numbered modes. The signals captured downstream of the dump plane for this configuration include the 5.59 cm, 8.64 cm and nozzle locations. The PSDs for all three are similar. The grouping of peaks near the fundamental chamber mode especially shows near identical responses on both sides of the chamber. Likewise, all three signals show a weak 2L mode, corroborating the results from the dump plane. There is an observed different at the third chamber mode, as the 8.64 cm location, close to the acoustic node, is much weaker than the other two locations near anti-nodes.

Similar to Test 360, at the higher frequency around 5500 Hz, near the predicted post mode, is a difference between upstream and downstream responses. The two upstream signals capture generally stronger noise than the far downstream sensor. This would be expected for an active post mode.

Discriminating behavior is apparent when comparing the frequency spectra from pressure signals of tests with different oxidizer temperatures. While both hot and ambient oxidizer tests exhibit the effects of acoustic resonance from both the chamber and the post, there is a clear increase in amplitude with the ambient oxidizer, primarily at chamber modes. There is also a sharpening of the peak along with the increased amplitude. For the ambient oxidizer tests, chamber modes are dampened when the frequencies approach that of the post modes. This is the expected consequence of the posts acting either as resonators, where a quarter-wave resonator of a closed-open system would place a pressure node at the dump plane, where chamber oscillations would be at their greatest.

For the ambient oxidizer tests, the fundamental chamber mode was accompanied by multiple adjacent peaks. These peaks typically have spacing between 100 and 200 Hz and can fall on either side of the first chamber mode frequency, though typically appear at lower frequencies. They do not appear for any chamber harmonics.

Frequency spacing between adjacent peaks were examined to investigate the impact of similar post and chamber modes had on the amplitude of the RMS pressure signal. Up to five peaks can appear within this region, with the fourth peak having the strongest amplitude and attributed to the chamber mode, while the next strongest peak, peak number three, is attributed to the oxidizer post mode. For each ambient oxidizer test, the spacing between adjacent peaks was compared to the RMS of the pressure signal at the fundamental chamber frequency. The results are shown in Figure 4.19. Peaks 1 and 5 were not always present in the PSD, and were typically quite weak when they did appear. The data points relying on those peaks, the blue circles and purple diamonds, contain a high degree of scatter, although there is some trending towards higher amplitudes with increased spacing. This trend is much more easily

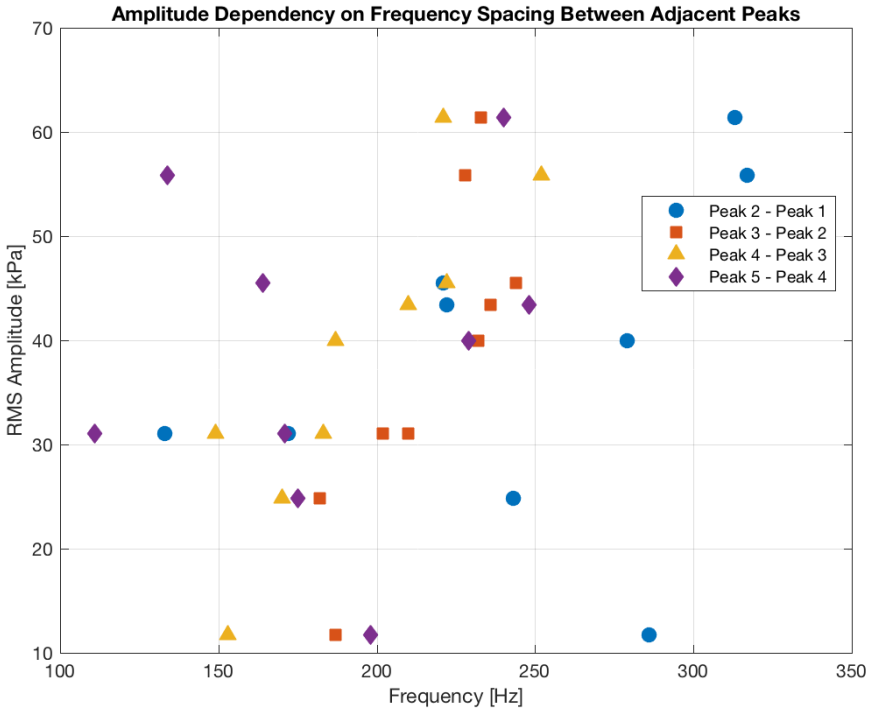

Figure 4.19.: The dependency of RMS amplitude of pressure signal on the spacing between adjacent peaks for ambient oxidizer tests at a variety of acoustic profiles. A high degree of scatter is found in the comparisons between Peaks 1 and 2, and Peaks 4 and 5. A linear trend is observed for Peaks 2 and 3, and Peaks 3 and 4 where increased spacing led to increased amplitudes.

observed in the comparison of frequency spacing of Peaks 2 and 3, orange squares, and Peaks 3 and 4, yellow triangles. Both pairings capture the trend of increased amplitudes with increased spacing in the frequencies of the adjacent peaks.

These results are unsurprising in the context of the particular mode shapes of the post and chamber. The oxidizer post is treated as a closed-open resonator, which places a pressure anti-node at the choked inlet and a node at the end of the injector. The chamber is considered a closed-closed cavity. Pressure anti-nodes would then be found at either end. When the frequencies of the fundamental modes for the post and chamber converge, there would be active damping at the dump plane as perturbations

from the chamber mode shapes would be attenuated by the pressure node of the post mode. As the frequencies of the two domains diverge, this effect is lessened, allowing for stronger oscillations to occur.

Consistent in all tests was a low frequency bulk mode. This bulk mode has been identified in numerous experiments and simulations similar to the DVRC featuring kerosene-fueled GCSC injectors, including multi-element configurations [124,126]. The bulk mode is attributed to the cyclic build up and burning of fuel near the dump plane.

The PSD, while useful for deciphering frequency content of the pressure signals, suffers from an inability to capture distinguish transient and steady events, as shown earlier in this section. Momentary periodic events would then get appear in a PSD, even if the event is not a good representation of steady state behavior. Temporal resolution of the frequency content is required to capture this information. One means of accomplishing this is through the spectrogram, which is presented next.

Similar to the PSD, the spectrogram presents the frequency content of a segment of the signal as a function of time. A given signal is broken into numerous bins, with the PSD of each bin calculated and placed side-by-side to give a temporal history of the frequency component of the signal.

Spectrograms from Test 363 with hot oxidizer at $L/\lambda = 0.20$ are presented first in Figure 4.20. These spectrograms are based on the signals from the oxidizer post inlet, the two dump plane locations, and the nozzle. Time slices shown capture the ignition transient, indicated by the abrupt shift between the low amplitude blue background noise to the higher amplitude combustion noise in yellow and red. Peaks presented in the PSDs shown above appear in the spectrograms as red regions. The width of the red regions represents the breadth of the peaks. Superimposed on the actual results are the predicted chamber and post modes, in solid and dashed lines, respectively. Each PSD has the same color bar, which is also kept constant for all four tests presented to aid in comparison.

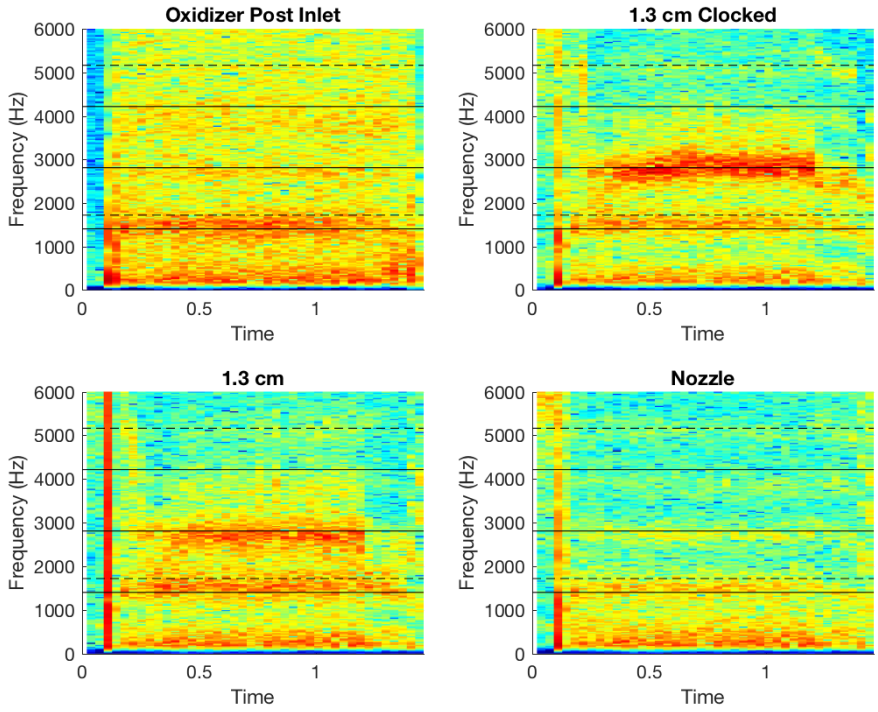

Figure 4.20.: Spectrograms of pressure signals taken from the oxidizer post inlet (upper-left), clocked 1.27 cm location (upper-right), non-clocked 1.27 cm location (bottom-left), and nozzle (bottom-right) for Test 363 with hot oxidizer at $L/\lambda = 0.20$. Solid horizontal lines represent predicted chamber modes, dashed lines represent predicted post modes.

The excited bands are aligned with the chamber modes of the system. Harmonics are also clearly visible. The amplitudes of the peaks differ with sensor location. The excitation of the fundamental chamber mode is visible in all four locations, but weakest near the throat and strongest at the oixizer post inlet. The second chamber mode is most prominent near the dump plane and barely visible in other locations. Further harmonics are registered but quite weak. The fundamental post mode is close to the first chamber mode and hard to separate the effects of the two. There is also a strong low frequency response present in all locations.

There is a delay in the manifestation of the first and second chamber modes. The fundamental mode appears right at ignition, while the second mode appears around 0.20 seconds later. This is something that has been observed in previous experiments performed at Purdue, including the UEC and CVRC.

During this window a shift in frequency is evident, shifting from the fundamental mode to the first harmonic where it becomes stationary. The response around this mode is very wide, with the edges of the peak - marked by the transition out of the red region - shifting throughout the test. As was seen in the PSDs of the dump plane signals, there is a different response around the 2L mode. Initially the two signals have a similar, shifted to a lower frequency than the predicted second chamber mode. Approximately half a second into hotfire, the clocked signal shifts to a higher frequency and at a higher amplitude, remaining around this frequency for the remainder of the test. This shift in frequency is not seen elsewhere. No other frequency shifts are observed, although many of the excited modes do show variation in amplitude. There is also significantly more background noise for the oxidizer post inlet signal. This matches the observed increase in noise floor in the PSD for this location and is likely connected to the turbulence generated by the choked inlet.

Spectrograms from the same comparison signal locations from the second representative hot oxidizer test, Test 359 at $L/\lambda = 0.36$, are shown in Figure 4.21. The results are not dissimilar to those of Test 363. There are clear bands indicating excitation at the first chamber mode at all locations and weaker excitation of the second

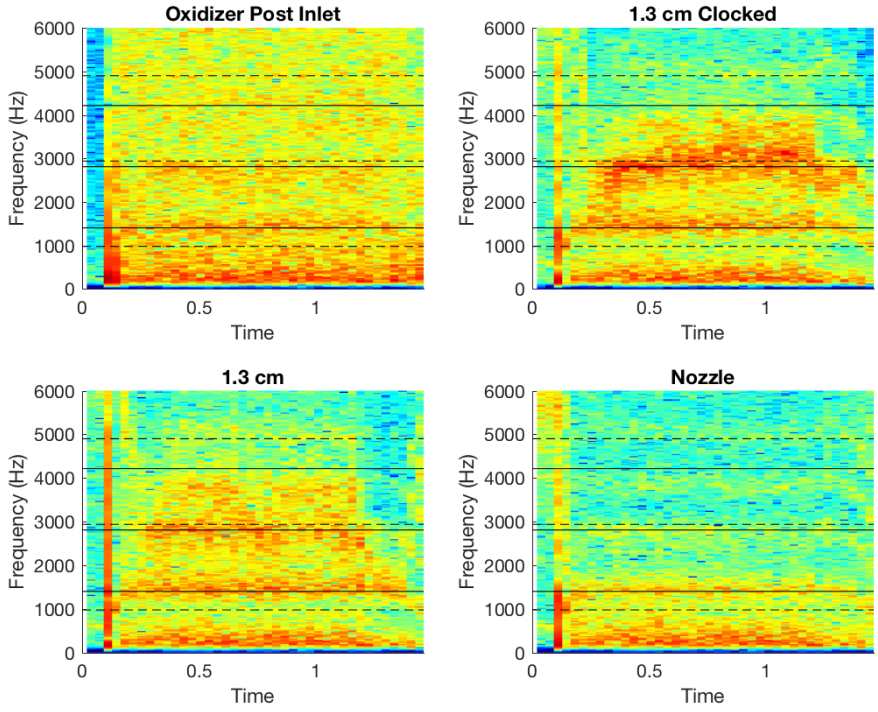

Figure 4.21.: Spectrograms of pressure signals taken from the oxidizer post inlet (upper-left), clocked 1.27 cm location (upper-right), non-clocked 1.27 cm location (bottom-left), and nozzle (bottom-right) for Test 359 with hot oxidizer at $L/\lambda = 0.36$. Solid horizontal lines represent predicted chamber modes, dashed lines represent predicted post modes.

chamber mode. The post modes nearly coincide with the chamber modes and the effects of the two cannot be separated apart from the third post mode which stands alone and produces a measurable response at all locations but the post inlet. The third chamber mode response is relatively hidden, shifted to a lower frequency and only discernible at the nozzle.

The fundamental chamber mode is excited right after ignition. Shortly thereafter is a split in this response that leads to an excitation of the second chamber mode. This response initially is constrained in a tight frequency band with a strong amplitude before it widens and disperses around 0.5 seconds, primarily observed at the clocked

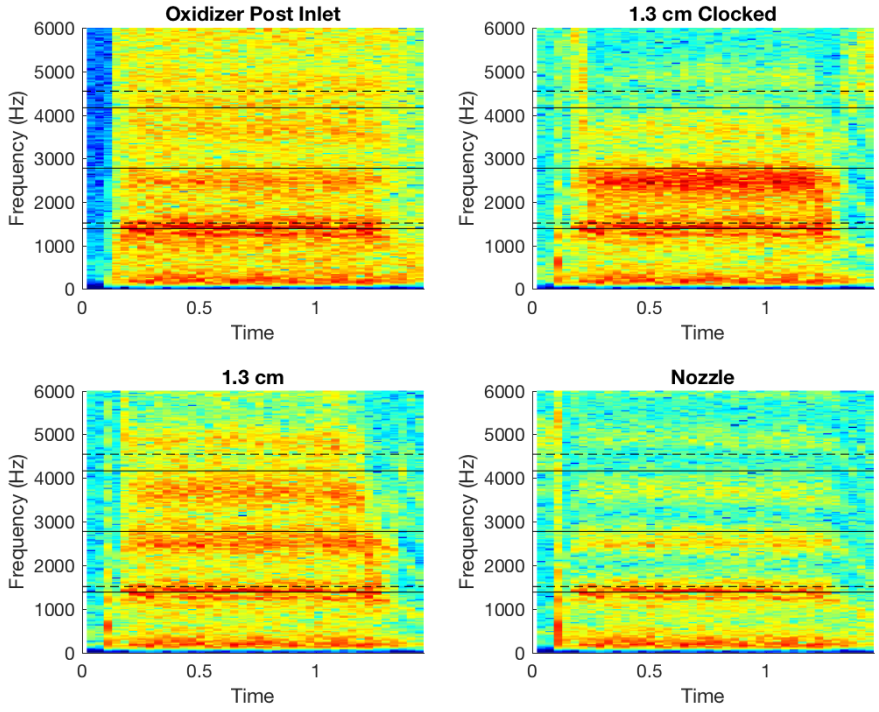

Figure 4.22.: Spectrograms of pressure signals taken from the oxidizer post inlet (upper-left), clocked 1.27 cm location (upper-right), non-clocked 1.27 cm location (bottom-left), and nozzle (bottom-right) for Test 360 with ambient oxidizer at $L/\lambda = 0.23$. Solid horizontal lines represent predicted chamber modes, dashed lines represent predicted post modes.

1.27 cm location. This widened peak is quite broad, extending towards the third chamber mode which itself is weakly excited and only cleanly visible at the nozzle.

The same analysis is conducted on the ambient oxidizer tests, starting with Test 360 at $L/\lambda = 0.23$ in Figure 4.22. Color axis is kept constant between tests and signals to make for more direct comparison. It is clear that the response in this test exhibits a stronger response than the two hot oxidizer tests as the excited modes result in darker, narrower red bands for several harmonics, an indication of a stronger amplitude and more organized response.

Excited bands appear near the chamber modes, each subsequent mode shifted further towards a lower frequency, an effect observed in the PSDs. The post modes are difficult to detect, as the fundamental post mode frequency falls close to first chamber mode, muddling the effects of the two. Only the second chamber mode is without a nearby post mode. Similar to the hot oxidizer cases, the fundamental chamber mode is present immediately following ignition while the first harmonic is slightly delayed. The delay is less pronounced here than in the hot oxidizer case. Not seen here is the visible shift in frequency at startup, moving from the fundamental chamber up to first harmonic.

The first two chamber modes have very different appearances. The fundamental mode around 1425 Hz is denoted by a very narrow band, with another thin band at 1250 Hz. These two bands maintain a consistent frequency of excitation throughout the test, unlike the hot oxidizer tests. While the frequency remain constant, the amplitude does vary throughout the test.

The second chamber mode does not have such a tightly bound appearance. Instead the response is spread across a much wider frequency band with no clear dominant peak. This is most prominent for the clocked dump plane location.

Higher harmonics are evident in all four locations. It is not immediately clear whether the high frequency excited bands are tied to the chamber or post modes, but the spacing between the bands suggests it to be related to the chamber.

Lower frequency content is also visible throughout the test, observed at the same amplitudes in all chamber and post sensor locations.

Presented in Figure 4.23 are the spectrograms for the oxidizer post inlet, two dump plane and nozzle pressure signals for the full duration of hot fire. Operating with ambient oxidizer, this test resembles the previously discussed Test 360. The first three chamber modes are excited, visible at all locations except for the third chamber mode at the post inlet. There is no immediately obvious effect of the post modes.

The first two chamber modes have drastically different appearances. This is similar to the previous test, which also operated with ambient oxidizer but at a different

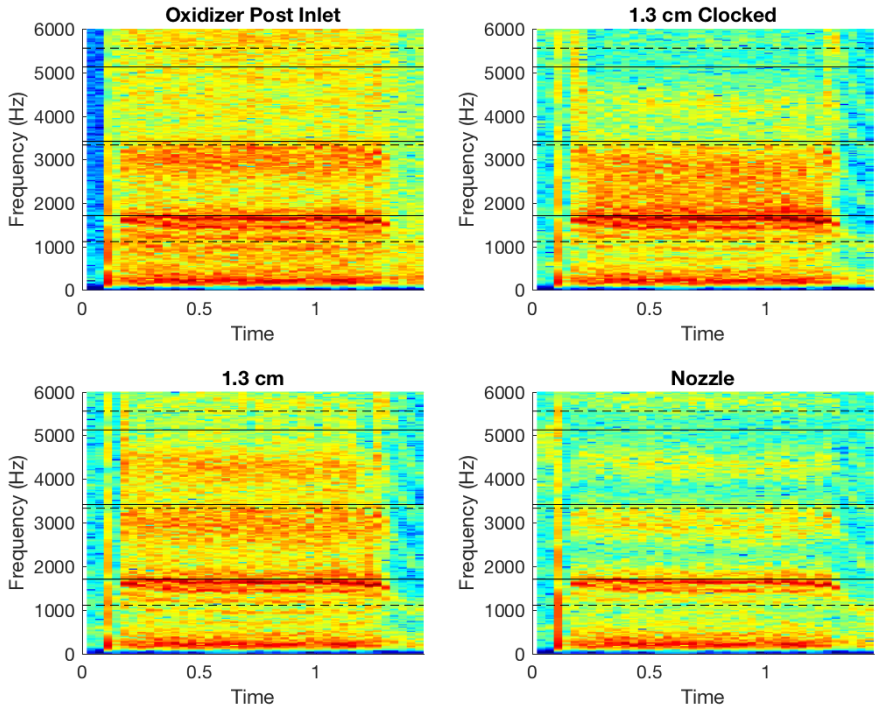

Figure 4.23.: Spectrograms of pressure signals taken from the oxidizer post inlet (upper-left), clocked 1.27 cm location (upper-right), non-clocked 1.27 cm location (bottom-left), and nozzle (bottom-right) for Test 366 with ambient oxidizer at $L/\lambda = 0.38$. Solid horizontal lines represent predicted chamber modes, dashed lines represent predicted post modes.

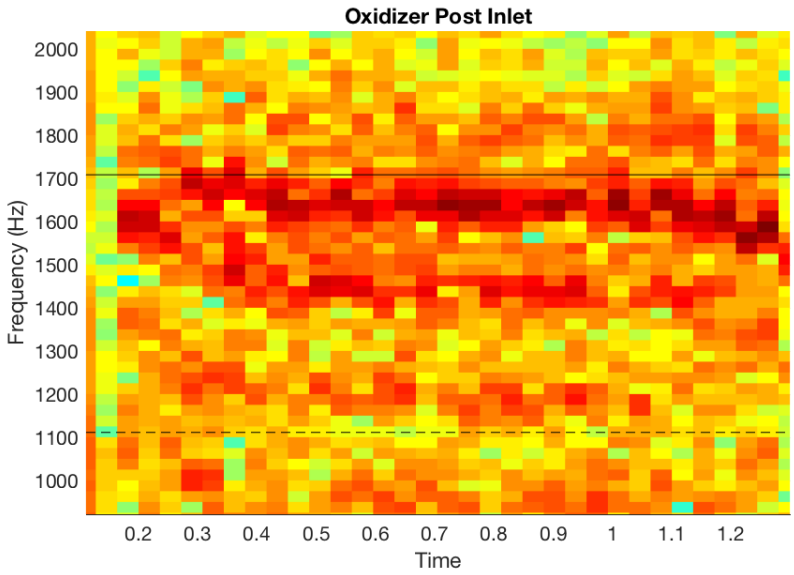

Figure 4.24.: Close up of the spectrogram for the oxidizer post inlet signal for Test 366 with ambient oxidizer, capturing the frequencies between 900 and 2050 Hz. The solid line represents a predicted chamber mode, dashed line represent a predicted post modes

acoustic profile. A pair of peaks are prominent around the fundamental chamber mode, the stronger at 1650 Hz and the weaker at 1425 Hz. They are both clearly defined despite being so close to each other, with the 1650 Hz mode being the strongest of the two. Something of note is the shift in frequency observed at the start of the test, highlighted in Figure 4.24. At ignition there is an excited response at 1600 Hz that then splits in two. The higher frequency component jumps up to around 1700 Hz before it falls back down and stays around 1650 Hz for the duration of the test. The lower frequency component shifts to the 1425 Hz mode and remains there. This is mirrored in another lower frequency peak that was observed in the PSD, shifting from around 1400 Hz to 1200 Hz. The spacing between the peaks are nearly equidistant. With the 1650 Hz mode being near a predicted chamber mode and the 1200 Hz near a predicted post mode, it is possible that the central 1425 Hz mode is the effect of beating between the two modes.

The second chamber mode is much less organized than the first. Instead of any single sharp, well-defined frequency, the response is spread across a wide range. The orange and red region within the spectrograms covers from 2700 to 3300 Hz. Higher modes are similar, spread across narrower ranges but at much reduced amplitudes with the increase in frequency.

Unlike the previously discussed tests, the first two chamber modes appear at the same time instead of with the second one appearing after the first with a short delay. Immediately following ignition, both modes are excited to approximately the same degree as they are throughout the remainder of the test.

Another trait of this test is the consistent frequencies of the peaks around the fundamental chamber mode. There appears to be very little drift throughout hotfire, with the excited band centered around a tight band of frequencies. The amplitudes, however, appear to vary with time.

Low frequency content is present for this test as well, covering a range of frequencies from around 150 to 300 Hz.

The spectrograms build on the results from the PSD results discussed above. The chamber modes are easily recognized for both hot oxidizer and both ambient oxidizer tests, generally appearing at or slightly below predicted frequencies. The post modes are generally not directly visible, either overpowered by background noise, obscured by chamber modes, or simply do not play a major role. For the hot oxidizer tests, a delay in the onset of the first and second chamber modes was observed. The first chamber mode would be driven immediately following ignition, with the second mode manifesting approximately a quarter second later. In the ambient oxidizer tests, this delay was greatly reduced in Test 360 or not observed in Test 366.

The increase in organization for the ambient oxidizer, primarily at the first chamber mode, is very apparent in these plots. The excited bands are generally wide and cover a large frequency band. The fundamental chamber modes for the ambient oxidizer cases exhibit a few sharp, very narrow peaks. In Test 360, where the oxidizer post is nearly a quarter-wave resonator, there are two peaks that may correspond to

the fundamental chamber and post modes. In Test 366, where $L/\lambda = 0.38$, there is a spacing between the fundamental modes, with another mode, neatly bisecting the two, which may indicate a beating of these two modes. In the hot oxidizer tests, the response is much more muddled and spread across a wider range. Beyond the fundamental mode, the responses weaken and become more dispersed, losing any organization.

As was also described above, the pressure signals observe both frequency and temporal variation throughout the test. Primarily in the hot oxidizer tests the response to chamber modes did not adhere to a single frequency. Instead, the response was spread across a wide band that shifted during the test. This was most evident at the clocked 1.27 cm location. In the ambient oxidizer cases the frequency shift is greatly diminished. Both cases experience variations in the amplitude at the chamber mode frequencies. The variations are greater for the ambient oxidizer case, likely due to overall increase in amplitude. However, the resolution provided through the power spectral density is limited to 25 Hz and approximately 0.035 ms. This prompts the use of an analysis technique that can better capture the rapid fluctuations in both frequency and time.

4.2.5 Continuous Wavelet Transform

Continuous wavelet transform (CWT) of the high-pass filtered data presented the spectral content of the signals from a new perspective than what was provided by PSD. While similar to the spectrogram, the CWT is not nearly dependent on window sizing Instead, the result of the CWT is based on the type of wavelet family used in the transform. The wavelet is scaleable, making it appropriate to use across any frequency or time range. There is a tradeoff between the two akin to the Heisenberg uncertainty principle, where increased time resolution comes at the cost of a decrease in frequency resolution. The various wavelet families provide augment this tradeoff in different ways, making some families more effective at certain scales. In this work,

the 'bump' wavelet is used to increase frequency resolution and better capture the variations in frequency that were observed in the PSDs.

Similar to the presentation of the spectrogram results, the CWTs of the oxidizer post inlet, dump plane, and nozzle sensor locations are discussed. In general, the frequency content is similar to what was observed in the spectrograms. Provided by the CWTs is a refining of the frequency bins, making the distinction between different acoustic mode responses clearer.

The CWTs for Test 363 with hot oxidizer and $L/\lambda = 0.20$ are shown in Figure 4.26. In general, the frequency distribution greatly matches that of the spectrograms for the same test, shown in Figure 4.20. The excited acoustic modes stretch across wide frequency ranges and the bands show some level of drift in the central frequency. The discrepancy between the two 1.27 cm location signals for the second chamber mode is still evident. Likewise, the shift observed in the dump plane locations at startup, bridging the first and second chamber modes is also present in the CWTs. The shift does not have any apparent organization.

A similar story is presented in the CWT results from Test 359 at $L/\lambda = 0.36$, shown in Figure 4.26. The discrepancy seen between the two dump plane locations is more dramatic. For the non-clocked 1.27 cm location, the second and third chamber modes are both captured as independent bands, with some variability in central frequency in both bands. In the clocked location, however, the two bands are hidden behind a third stronger band. This third band starts near the second chamber mode frequency and drifts higher throughout the test This third band is not observed anywhere else.

Testing of the ambient oxidizer at $L/\lambda = 0.23$ in Test 360 reveals behaviors in the acoustic responses that were not evident in either the spectrogram or PSD results. As can be seen in Figure 4.27, the acoustic responses of the first three chamber modes are visible throughout the system, along with the fundamental post mode. These excited bands are both tighter and at greater amplitudes than those seen in the hot oxidizer tests. However, the most striking difference here is the pattern in the variation of the amplitudes of the fundamental chamber and post modes.

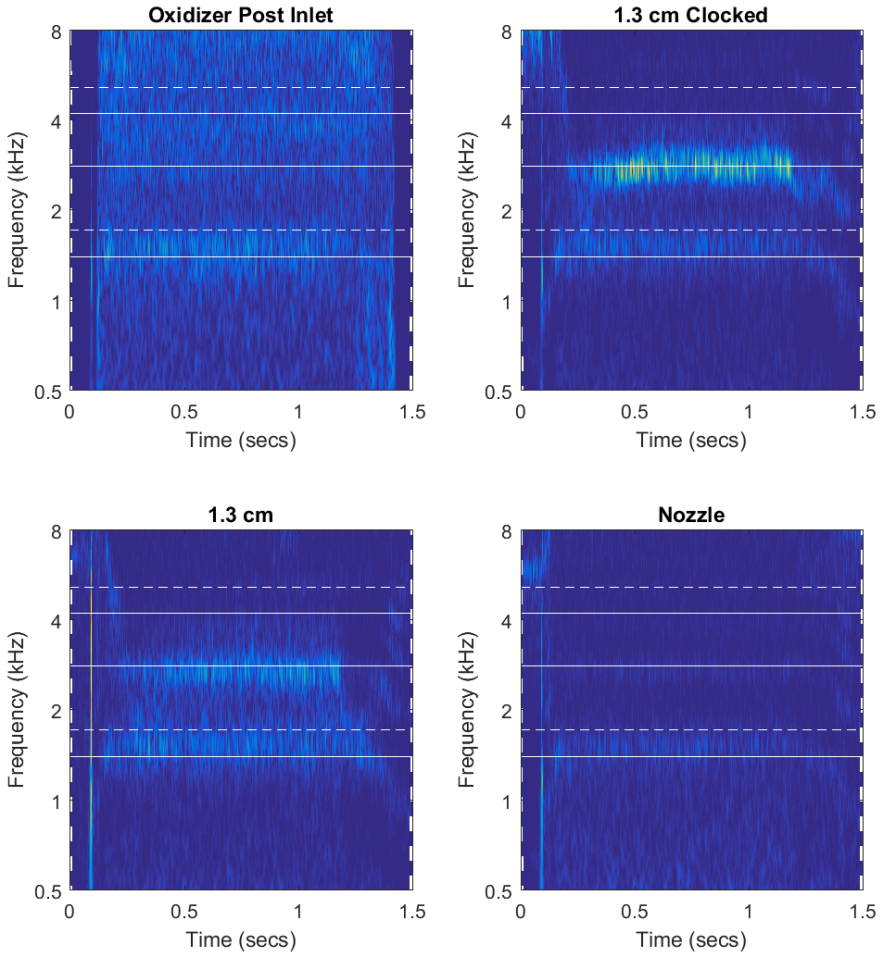

Figure 4.25.: Continuous wavelet transforms of pressure signals taken from the oxidizer post inlet (upper-left), clocked 1.27 cm location (upper-right), non-clocked 1.27 cm location (bottom-left), and nozzle (bottom-right) for Test 363 with hot oxidizer at $L/\lambda = 0.20$. Solid horizontal lines represent predicted chamber modes, dashed lines represent predicted post modes.

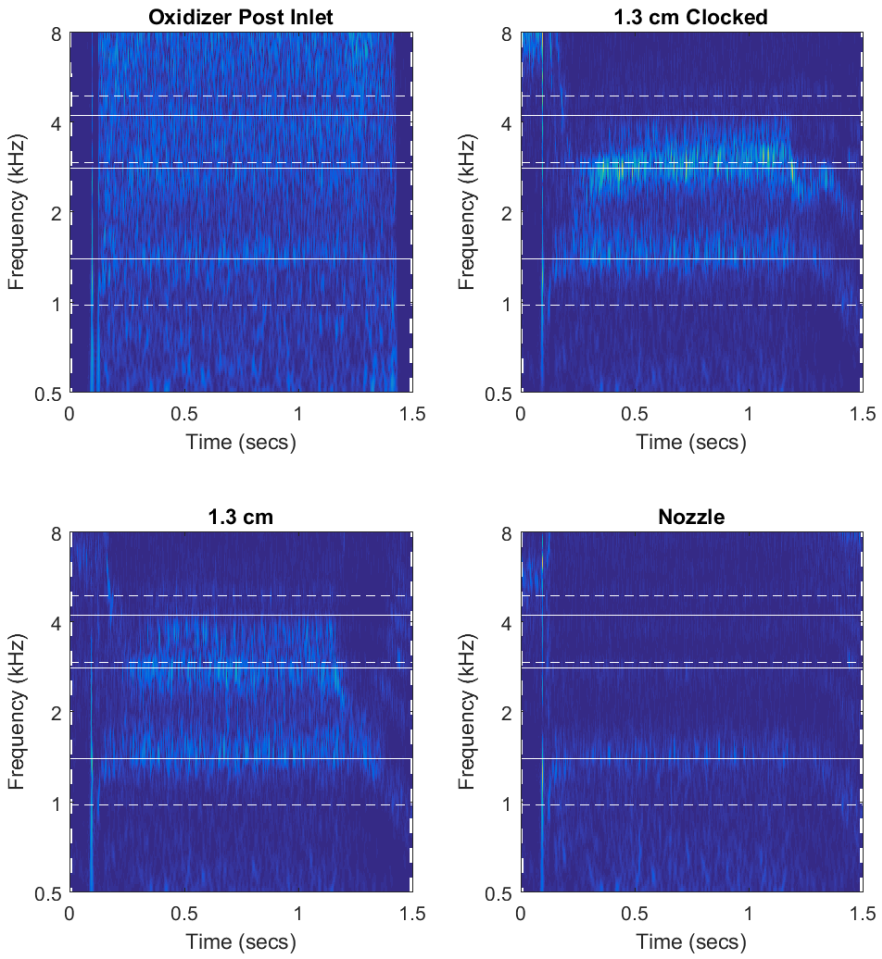

Figure 4.26.: Continuous wavelet transforms of pressure signals taken from the oxidizer post inlet (upper-left), clocked 1.27 cm location (upper-right), non-clocked 1.27 cm location (bottom-left), and nozzle (bottom-right) for Test 359 with hot oxidizer at $L/\lambda = 0.36$. Solid horizontal lines represent predicted chamber modes, dashed lines represent predicted post modes.

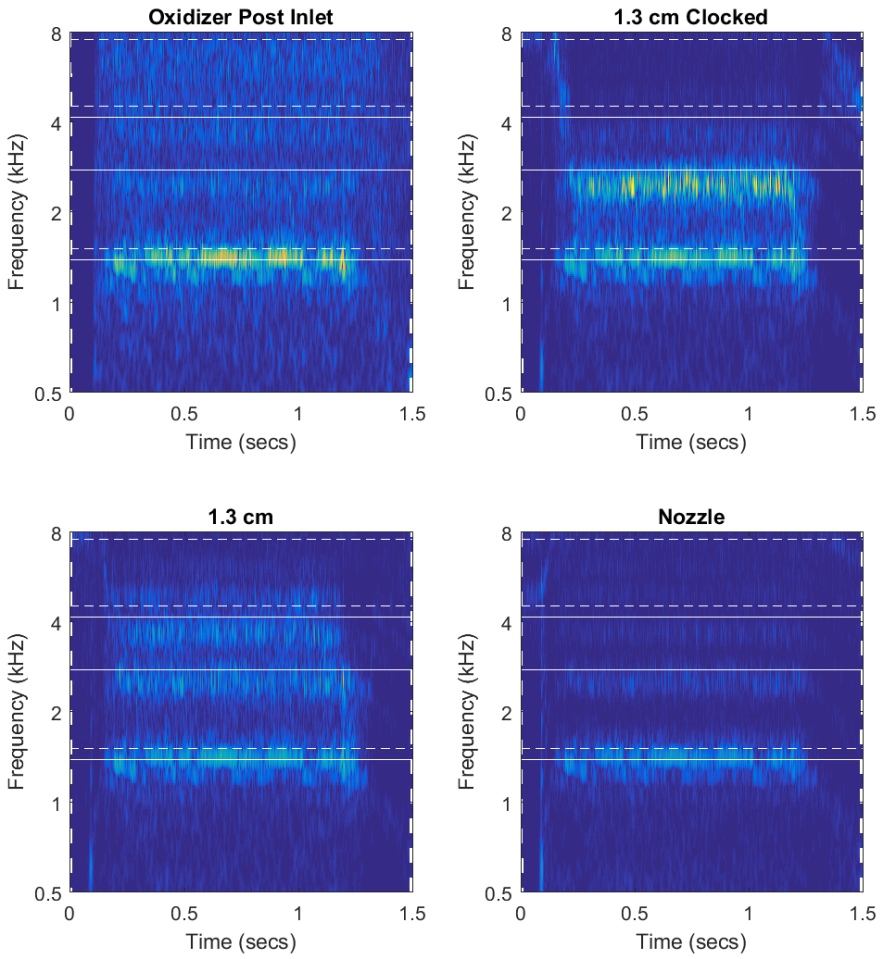

Figure 4.27.: Continuous wavelet transforms of pressure signals taken from the oxidizer post inlet (upper-left), clocked 1.27 cm location (upper-right), non-clocked 1.27 cm location (bottom-left), and nozzle (bottom-right) for Test 360 with hot oxidizer at $L/\lambda = 0.23$. Solid horizontal lines represent predicted chamber modes, dashed lines represent predicted post modes.

The two bands are distinct, although there is some overlap between them. The higher frequency band is the stronger one and sits at the predicted fundamental chamber mode. The fundamental post mode is expected at a frequency higher than the chamber mode, while the weaker of the two modes is lower than the chamber mode. Either the stronger mode does pertain to the chamber, and the post mode is much weaker and skewed to a lower frequency, or the post mode is the stronger of the two, with both modes shifted down slightly in frequency. Most often, it is the chamber mode that is dominant, suggesting that it is the post mode that was shifted to a lower frequency.

In either case, there appears to be periodic trade-offs between the two bands. After the ignition transient, the higher frequency mode is dominant. During a short period of time, the lower frequency mode varies in amplitude. Then, approaching the 0.5 second mark, the amplitudes switch and the lower mode becomes dominant. This switching then occurs twice more in a short stretch before the higher mode once again becomes dominant. It is dominant for a long stretch of time while the lower mode drifts between little and some amplitude. Around 0.8 seconds, the higher band drops in amplitude for about a tenth of a second. There is not a direct switch in modal activity, as the lower frequency mode is also relatively inactive for the first half of this intermission, then increases in amplitude for the latter half. It then recedes as the higher mode again becomes dominant. This shifting continues for a little longer, and is evident at each chamber location. There are also no other related shifts in behavior observed in other modes. This indicates that the two modes are both attempting to exist in a dominant state, but the associated mode shapes are incompatible and act to dampen the system, or at least prevent post-chamber coupling around the fundamental resonant frequencies.

Adjacent fundamental post and chamber bands are also present in Test 366 at $L/\lambda = 0.38$. In this test, the predicted post mode frequency is less than that of the chamber mode. The stronger, higher mode frequency is right at the predicted chamber mode frequency. The weaker band is at a much higher frequency than the

predicted post mode, and instead is very close to the chamber mode. The switching of amplitudes between the two bands is not nearly as prominent in this case. The first example appears around 0.32 seconds where the dominant higher band drops in amplitude and a rise in amplitude to the strongest levels of the lower frequency band appears. For the most part, the manifestation of interaction between the two modes does not appear to be a switch of amplitudes like in Test 360. Instead it appears that a further reduction in the lower amplitude band leads to a further rise in amplitude in the stronger band, or perhaps vice versa as time dependency is not made clear. These events are brief but occur several times throughout the test fire.

Amplitude modulation of the various bands were tracked by taking the maximum value within the bands for each time step. Presented are the bands from the 1.27 cm non-clocked location. This axial location provided the largest amplitudes and the non-clocked location compared more closely to other signals through both post and chamber. The first two or three evident modes, chamber and/or post, are tracked and presented. The amplitude traces are reduced to a window of 0.15 seconds, matching the windows shown in the PSDs of Section 4.2.4.

Presented first, in Figure 4.29, are the amplitudes for the first two chamber modes for Test 363, with hot oxidizer at $L/\lambda = 0.20$. The frequencies for these modes are around 1639, and 2818 Hz, respectively. Two behaviors emerge in the comparison of the amplitudes of these modes. The two signals go back-and-forth between being directly in-sync and directly out-of-sync. The signals appear to generally be more asynchronous, with examples of the two being out-of-sync in this 0.15 long time slice appearing at 3.413, 3.430, 3.444, 3.512 and 3.533 seconds, to name a few. During this time slice, only one strong example of synchronous behavior appears, at 3.466 seconds.

As this test is conducted with the oxidizer post nearly in a quarter-wave configuration, the post mode shape corresponding to the first chamber mode will have a pressure anti-node at the choked inlet and node near the dump plane. This will have a dampening effect, overall, as any chamber resonance associated with the fundamental

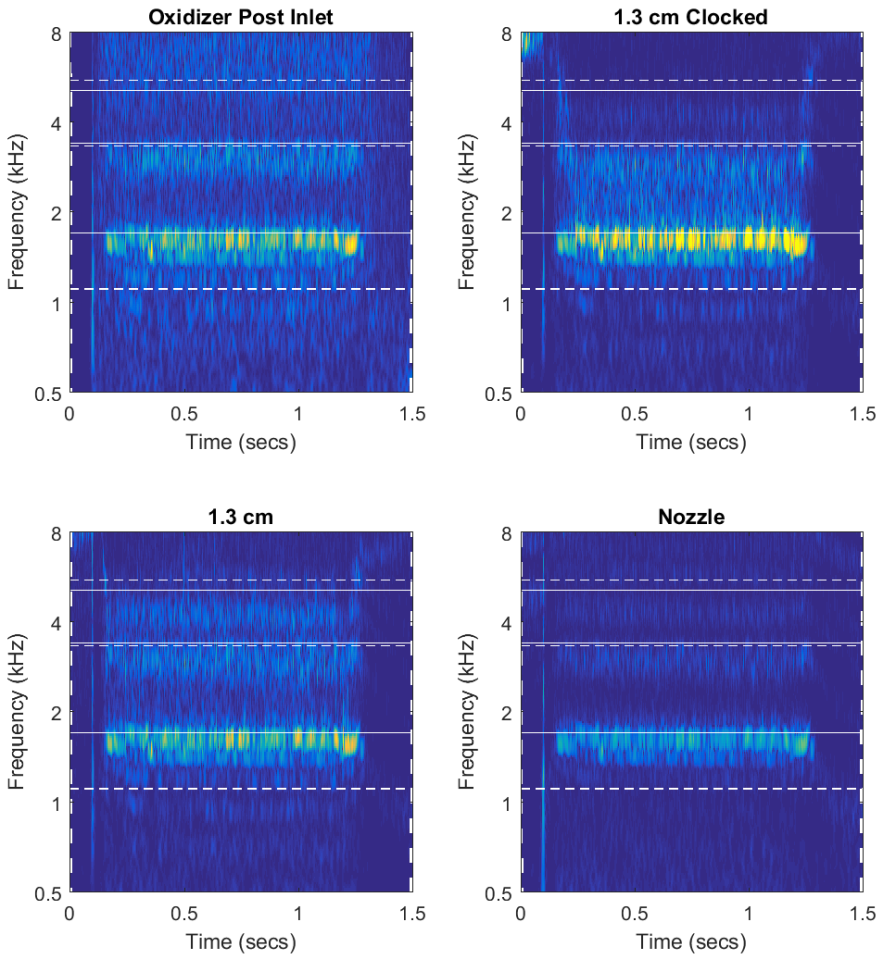

Figure 4.28.: Continuous wavelet transforms of pressure signals taken from the oxidizer post inlet (upper-left), clocked 1.27 cm location (upper-right), non-clocked 1.27 cm location (bottom-left), and nozzle (bottom-right) for Test 366 with hot oxidizer at $L/\lambda = 0.38$. Solid horizontal lines represent predicted chamber modes, dashed lines represent predicted post modes.

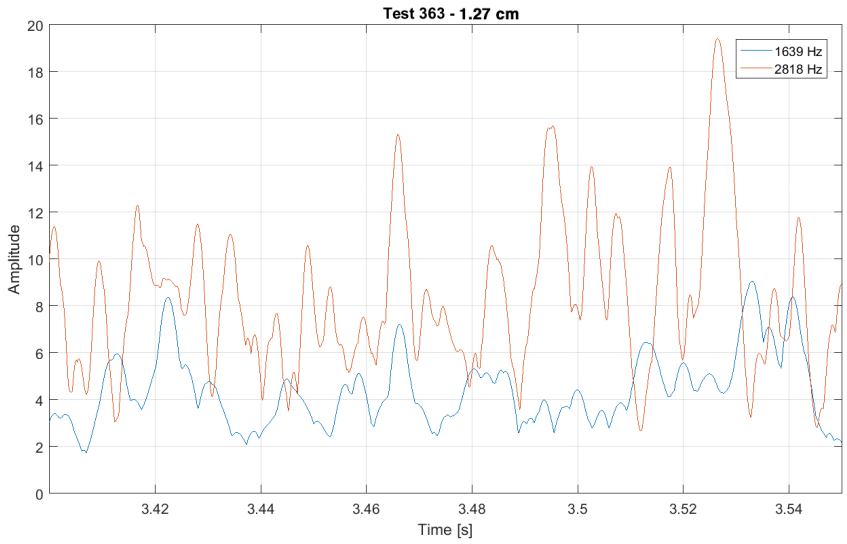

Figure 4.29.: Variation in the amplitudes of frequency content for Test 363 with hot oxidizer at $L/\lambda = 0.20$. The two strongest modes, the first two chamber modes at 1639 and 2818 Hz, are compared.

chamber mode will struggle to excite the post mode. The second harmonic of the chamber would not yield a direct harmonic in the post, but the corresponding mode shapes would place pressure anti-nodes from both domains near the dump plane. The fact that the two modes appear to compete for dominance suggests that neither mode is exactly self-sustaining, nor compatible with the other. The fact the amplitudes are higher for the second chamber mode would be expected for the corresponding post mode shape that better completes the full acoustic mode shape throughout the system.

The acoustic profile for Test 359 with hot oxidizer, with $L/\lambda = 0.36$, shifts away from the quarter-wave resonator to the 3/8-wave resonator. In this configuration, the pressure node at the post mode corresponding to the fundamental chamber mode is no longer a node but approaching an anti-node. This allows the post to behave more as a resonance tube for the fundamental chamber mode. This would also be the case for the first few chamber harmonics.

The amplitude traces for the first three chamber acoustics modes, 1493, 2817, and 3816 Hz, are shown in Figure 4.30. Generally, amplitudes for the first two modes reach comparable magnitudes, while the third mode is consistently weaker with occasional strong pulses. Both in- and out-of-sync behavior is observed here, with the inclusion of the third mode leading to more complicated interconnected behavior. There are occasional moments where only one mode sees a peak, such as the 1L mode around 3.480 or 3.502 seconds, the 2L mode at 3.409 or 3.512 seconds, or the 3L mode around 3.455 seconds. Occasionally only two modes coincide, like 1L and 3L around 3.412 seconds, or the 2L and 3L at 3.522 seconds. More common are the times when all three modes rise in amplitude together, seen at 3.423, 3.498, 3.518 and 3.539 seconds. In either event, the variation in amplitudes show that no single mode is ever consistently excited.

Tests with the ambient oxidizer showcase stronger, more organized fluctuations in the amplitude traces. Results from Test 360 at $L/\lambda = 0.23$ are shown in Figure 4.31.

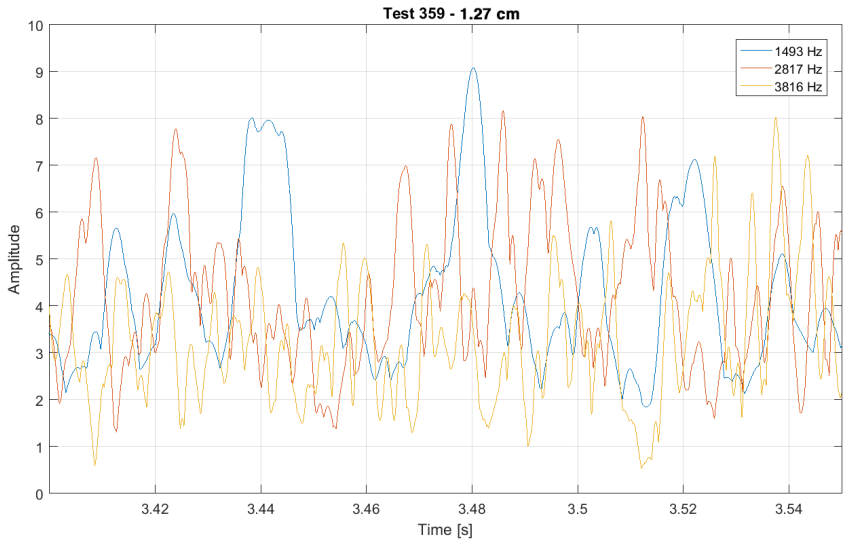

Figure 4.30.: Variation in the amplitudes of frequency content for Test 359 with hot oxidizer at $L/\lambda = 0.36$. The three strongest modes, the first three chamber modes at 1493, 2817, and 3816 Hz, are compared.

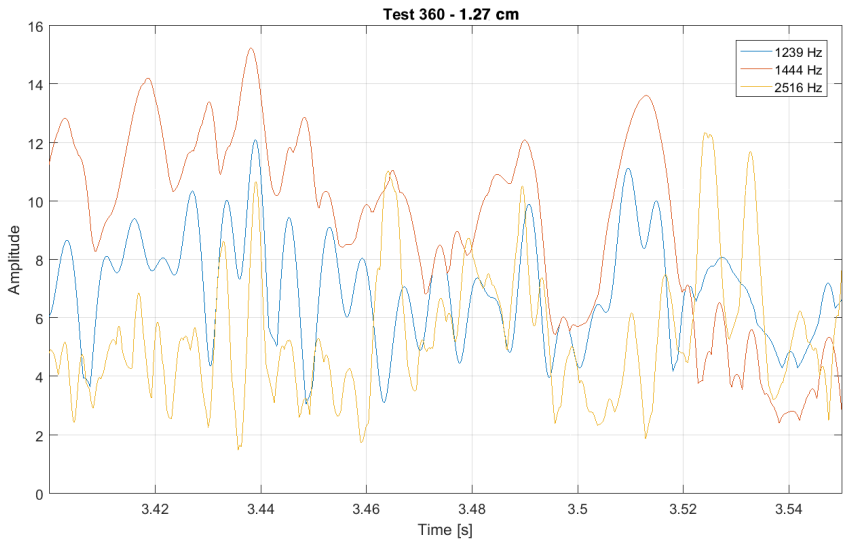

Figure 4.31.: Variation in the amplitudes of frequency content for Test 360 with ambient oxidizer at $L/\lambda = 0.23$. The three strongest modes, the first post mode and first two chamber modes at 1239, 1444, and 2516 Hz, are compared.

The fundamental post and chamber modes are close, at 1239 and 1444 Hz respectively. The second chamber mode at 2516 Hz is also shown.

Despite the incompatible mode shapes of the fundamental post and chamber modes, both rise and fall in amplitude, often together. The second chamber mode also often falls in line with the beat of the other two modes. Strong resonance amongst the three is most evident at 3.423 and 3.439 seconds, and again at 3.490 seconds. It is more difficult to tell when the two fundamental modes are out-of-sync, as it is also possible that due to the rapid increase and drop in amplitude the desynchronization is instead a phase shift between the two.

The results from ambient oxidizer Test 366 at $L/\lambda = 0.38$, shown in Figure 4.32, generally compare well to those of Test 360, but also show a strong increase in amplitudes observed in the fundamental chamber mode at 1655 Hz, that greatly overpowers the fundamental post mode at 1410 Hz and second chamber mode at 2784 Hz. At its

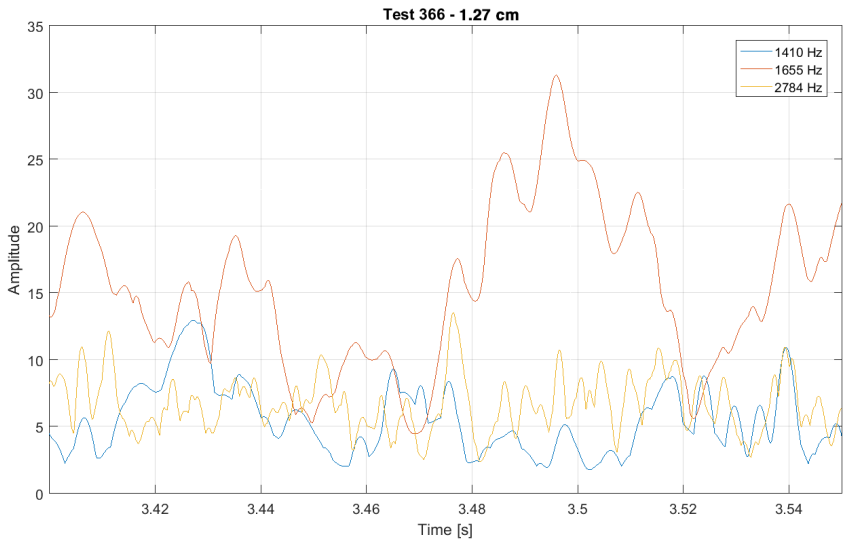

Figure 4.32.: Variation in the amplitudes of frequency content for Test 366 with ambient oxidizer at $L/\lambda = 0.38$. The three strongest modes, the first post mode and first two chamber modes at 1410, 1655, and 2784 Hz, are compared.

strongest during this 0.15 second long time slice, the 1655 Hz mode reaches amplitudes twice that of what was observed in the other ambient oxidizer test.

There are multiple times where all three modes shown have coinciding peaks, such as 3.406, 3.476, 3.496, and 3.540 seconds. While the amplitudes may differ, the general profile of the two fundamental modes are often similar. Despite these similarities, sustained high amplitudes are not observed.

On the surface, the CWT provides information similar to that of the spectrogram: the frequency spectrum of a signal as a function of time. The reliance on wavelets, with the inherent ability to scale with frequency, increases the resolution as compared to the spectrogram. The higher degree of resolution reveals behaviors not easily seen in the spectrograms.

In the hot oxidizer tests, the excited bands associated with the chamber acoustic modes are clearly defined within a wide bandwidth that varied throughout the test. In one test, Test 359, a frequency between the observed 2L and 3L modes was sustained

for the duration of hotfire, but only observed at the 1.27 cm clocked location. This response drifted upwards in frequency with time and was much stronger than any other measured responses.

Tracking the amplitudes of the excited bands provided a glimpse into the stability of the system. Sustained high amplitude thermoacoustic instabilities are marked by acoustic modes and harmonics all being excited. In the hot oxidizer cases, strong amplitudes for any given mode are not sustained. Typically, the fluctuations in amplitude for any given mode are erratic, with the occasional synchronized rise in amplitude across multiple modes. These simultaneous peaks are then quickly quenched.

The excitation of individual adjacent modes at lower frequencies seen in the ambient oxidizer tests greatly benefit from the increased resolution of the CWT. The excited bands are much tighter and without the frequency drift seen with the hot oxidizer. The multiple peaks around the fundamental chamber are distinct at all sensor locations. The amplitude variation in the excited bands at the lower frequency capture what appears to be an exchange of dominance between the two strongest. In both discussed cases, the highest frequency in the grouping generally has the highest amplitudes. Periodically, the amplitude of the higher frequency mode drops, coinciding with an increase in amplitude for the lower mode. This effect is more apparent in the amplitude traces. Along with the temporary switching of the dominant mode, there are also more occasions where multiple modes rise in amplitude at the same time. The peaks in amplitude are also generally stronger than the hot oxidizer tests. This increase synchronized behavior suggests the ambient oxidizer encourages coupling behavior, or at least dampens it less than that of the hot oxidizer.

5. CONCLUSIONS

The DVRC is built following the legacy of similar combustors at the Maurice J. Zucrow Laboratories at Purdue University in exploring the fundamentals of combustion stability. In this document, two earlier combustors were recalled and compared to the DVRC for their similarity in operation or injector design. These two experiments presented both stable and unstable operation, determined by the geometry. Scaling methods devised from and tested on these combustors were adapted and applied to the DVRC to promote similar discriminating behavior.

The primary goal of the DVRC is the production of high-resolution quantitative data sets for use in the validation of models for prediction of injector dynamics and combustion instability. This data set would not only serve as a surrogate for oxidizer-rich staged combustion cycle engines through the use of a preburner for the generation of heated oxidizer, but would also capture the behavior of liquid fuel injected at transcritical conditions. This invoked a test article with a modular design, well-defined boundary conditions, and sufficient instrumentation to accurately reconstruct the acoustic mode shapes of the combustor as well as temperature measurements within the combustor walls to estimate heat loss. To this end, 14 configurations were tested, varying oxidizer post and chamber lengths and oxidizer post inlet configurations.

A goal within the generation of the validation data set was the demonstration of discriminating stability behavior. This was defined as the data set including cases where the amplitude of pressure oscillations were less than 5% of the mean chamber pressure, as well as cases where the amplitudes exceed 10% of the mean chamber pressure. The collected data set showed that the scaling methods used in previous combustors to achieve discriminating behavior did not have the same effect on the DVRC, as pressure oscillations remained at low levels at acoustically damping and driving geometries.

This prompted an examination into the oxidizer composition, the primary difference between the DVRC and the Uni-Element Combustor, which tested at similar geometries and injector design. The UEC operated with decomposed hydrogen peroxide, compared to the pre-combusted hot oxidizer of the DVRC. One possible explanation for the difference is the production of water vapor in the decomposition of hydrogen peroxide, which has been shown to increase ignition delay. Long ignition delays lead to lifted flames, which are inherently unstable. Through varying the oxidizer inlet temperature on the DVRC, the ignition delay can similarly be modulated.

While unable to replicate the same high-level amplitudes seen in the previous experiments, the DVRC presented discriminating behavior between tests conducted with hot oxidizer and those at cooler temperatures. Assessment of the stability at the two operating conditions relied on varying oxidizer post and chamber geometry to drive or damp pressure oscillations. Potential causes for the inability to achieve thermoacoustic instabilities like on previous similar combustors include operating at higher pressures by a factor of about two or more, injection of transcritical fuel which can drastically alter mixing and the ignition process, and the main difference of using heated oxidizer from a preburner instead of decomposed hydrogen peroxide.

The modular design permitted testing at a number of geometries for the two oxidizer temperature inlet conditions, with discrete options for both oxidizer post length and chamber length. Oxidizer post lengths of 5.27, 7.18, 12.44 and 14.36 cm were available, as were chamber lengths of 20.46, 24.83, 27.28, 34.10 and 38.47 cm, making a wide range of permutations available for study. The inlet temperature was kept close to one of two temperatures: hot, around 685 K, and cool at ambient temperature. Corresponding to these available options, a number of acoustic profiles are possible, ranging from 0.15 to 0.76 with the hot oxidizer, and 0.23 to 1.17 for the ambient. This work focuses on results from the range consistent with previous experiments: 0.15 to 0.41.

Discriminating behavior was observed between the two oxidizer temperature conditions. At high temperatures, the acoustic field remained stable across all geometries

tested. With the cooler oxidizer, pressure oscillation amplitudes increased at all testing configurations when compared to the hotter oxidizer. Amplitudes were further augmented with modifications to the geometry. It is postulated that this increase in amplitude is associated with a change in acoustic impedance between the oxidizer post and chamber domains. Furthermore, the cooler oxidizer acoustic field is modulated by the acoustic timing defined by the geometry.

Amplitudes throughout the post and chamber were low with little variation between domains. For the hot oxidizer, the peak-to-peak amplitudes ranged from 140 to 200 kPa at the oxidizer post inlet, 200 kPa around the dump plane, and around 75 kPa downstream in the chamber. At cooler oxidizer conditions, the peak-to-peak amplitudes increased, as did the range of amplitudes. Oscillations up to 275 kPa were observed in the post, between 275 and 350 kPa at the dump plane, and between 140 and 200 kPa downstream in the chamber.

Statistical analysis of the pressure oscillations revealed that at the low amplitude cases, when the acoustic profile was near the low value of 0.20 and high value of 0.45, the increase from hot oxidizer to ambient oxidizer levels was around 40%, based on the full range of fluctuation magnitudes, with the top and bottom 1% value removed, and the RMS amplitude.

The acoustic impedance of the oxidizer varies between the two temperatures tested. This value regulates the reflection and transmission of acoustic energy between two media at an interface. It would be expected that a change in impedance of one of the two media would alter the transfer of pressure pulses. Based on the densities and local velocities of the oxidizer and combustion gases, the shift to ambient led to a 40% and 12% increase in reflection and transmission coefficients, respectively. This increase does not immediately indicate that the post and chamber are more likely to couple due to an increase in pulse amplitude, but that due to the change in oxidizer specific impedance higher amplitude pressure fluctuations would be expected.

The amplitude increase is also evident within the frequency of the pressure signals. The power spectral density of the signals revealed that the increase in amplitudes is

not tied to a broadband rise in signal strength, as the noise floor remains constant between oxidizer temperatures. Instead, organization is observed at individual modes attributed to acoustic modes. While operating with hot oxidizer, peaks are found near the first three to four chamber modes, and occasionally around oxidizer post modes. These peaks are broad, and amplitudes rise above the noise floor an order of magnitude or less. Tests with ambient oxidizer are identifiable by a sharp rise in amplitude and narrowing of the acoustic mode peaks. The peaks rise by one to two orders of magnitude above the nearby noise floor. The width of the peaks decreases from several hundred Hertz to one or two dozen.

Apart from the increased magnitude, other signs of acoustic organization are evident in the frequency spectrum. With the hot oxidizer, a high degree of variation is observed in the frequency of the acoustic peaks. Through the duration of hot fire, acoustic mode frequencies drift around a central frequency. Simultaneously, the amplitudes at these frequencies are inconsistent, greatly fluctuating. Testing with the ambient oxidizer showed a reduction in the amplitude variations, although variation was still present. The frequency drift was not present.

Comparisons of the amplitude variation between the chamber modes illustrated the increased organization associated with the ambient oxidizer. With the hot oxidizer, the amplitude variations between the first few modes did not correlate well. While occasionally two or three modes would simultaneously rise or fall, this was an uncommon event. Variation was present with the ambient oxidizer, but to a much smaller degree. Multiple modes often rose or fell together, indicating a stronger interaction and dependency between the modes.

The interaction between oxidizer post and chamber was identified as a key factor in earlier experiments to initiate unstable combustion behavior. While strong, sustained pressure fluctuations were not observed in the DVRC, the ambient oxidizer permitted similar variation in the acoustic field based on the lengths of the oxidizer post and chamber. The acoustic profile, defined as effective wavelength of the post as a resonator for the chamber and denoted by L/λ, was varied at both oxidizer inlet

temperature conditions. At the low amplitude oscillations of hot oxidizer testing, no dependence on L/λ was noted. A general trend observed for the ambient oxidizer was the appearance of lower pressure oscillations at the low and high end of the tested L/λ range, around 0.20 and 0.50 respectively. The amplitudes increased between these values, peaking near a post length equal to a 3/8-wave resonator. These results match those from earlier work on other experiments. However, tests at other configurations but similar L/λ values to the 3/8-wave resonator presented unexpectedly lower oscillations. This prompted a re-examination of the relationship between the geometry and acoustics.

The presence of the acoustic modes was made clear in the cross-correlation results. Using four reference signals - oxidizer post inlet, the dump plane locations, and nozzle - similarities between two signals were examined. With hot oxidizer, low levels of cross-correlation values were observed between most pressure signals. Notable increases in correlation were observed between the two dump plane locations, as well as between various signals and the nozzle. Remaining correlation values were at insignificant levels. Operating with ambient oxidizer led to a sharp rise in correlation, regardless of reference signal. The increased correlation allowed for accurate measurements of time lag between locations throughout the post and chamber. These phase lags matched the expected travel times for acoustic pulses traveling through the domains, modified by mean flow effects. The pulses are recorded traveling primarily upstream, having been generated near the nozzle. In some cases, a reflection at the dump plane is believed to be observed. This manifests as a bifurcation in midchamber measurements near the head end, such as the 5.59 and 8.64 cm locations. The bifurcation causes a pair of peaks, one associated with the initial upstream pulse, and another that fits the timing of a possible reflected pulse. These traveling pulses can be weakly observed in the hot oxidizer tests, but only for those moving upstream.

Further identification of the presence of the acoustic modes is found in the frequency content for sensors within the chamber. The axial distribution of the chamber pressure sensors allowed for the detection of acoustic nodes. As sensors near the

chamber midpoint had severely reduced responses to odd-numbered chamber acoustic modes. Similarly, sensors near the one-quarter chamber length position registered reduction of the second chamber acoustic mode. This can be detected in tests with both hot and ambient oxidizer, although the increased amplitudes greatly aid in making the observation.

The identification of modes through this method assisted in determining whether a peak in the frequency spectrum was associated with a chamber or an oxidizer post mode for scenarios where the two had similar frequencies. This method was particularly useful in the ambient oxidizer cases, where the multiple distinct peaks were present around the first chamber mode. The strongest of the peaks was associated with the chamber mode, and the second strongest to the nearby oxidizer post mode. The remaining peaks were not directly tied to any specific acoustic mode, nor fit a beating relationship with other modes. Instead, these peaks often varied in amplitude independent of the variations in the other nearby peaks. However, a trend was observed, pairing the observed amplitudes of the pressure signals to the frequency distance between adjacent peaks. As many as five peaks within a span of 1000 Hz were identified. Comparing the spacing to the amplitudes revealed that as the spacing between adjacent peaks increased, so did the amplitude of the pressure signals. This trend has limited presence in pairings that include the first and last peaks, which were consistently the weakest, but held fast for pairings that included the chamber and post mode frequencies. This suggests, as expected by acoustic theory, that the closed-open post mode shape and closed-closed mode shape of the chamber are incompatible, such that as the two modes have similar frequencies, pressure oscillations amplitudes are dampened. As the spacing increases, and the interaction between the two decreases, amplitudes increase. This behavior provides an explanation to the observed differences between the two ambient oxidizer tests conducted at nearly identical acoustic profiles.

This finding was corroborated by an examination of the effectiveness of the chamber geometry to resonate with itself. This was determined by comparing the spacing

between adjacent upstream traveling pressure pulses within the chamber to the travel time of a returning pulse, reflected at the dump plane. As the difference between the two decreased, signifying a geometry more accommodating to acoustic resonance, the overall RMS amplitude increased in a linear fashion. This is expected, as a discrepancy between the two would indicate a de-tuning, leading to a reduction in the conversion of energy from one pulse to the next. However, the fact that this discrepancy exists indicates that the simple standing wave model for the acoustic field within the chamber is inadequate. The strongest correlations capture the passing of an acoustic pulse emanating from the nozzle, not the dump plane where the bulk of heat release and likely combustion noise is generated. Generation of acoustic perturbations at the nozzle comes from the combustion of unburnt fuel on the hot converging wall section. In the context of the two tests with similar L/λ values but dissimilar amplitudes, Test 370, which exhibited the stronger amplitudes, also had a chamber length shorter than all others tested at 27.28 cm. A reduction in chamber length could further exacerbate the issue of incomplete combustion, possibly leading to increased fuel ignition at the nozzle. A c* efficiency of 84% for this configuration, compared to the 87% efficiency of the more stable configuration with the longer chamber, supports this idea.

There is also evidence that the timing of vortex impingement compared to the travel time of a chamber pulse has a connection to the amplitude of pressure oscillations. When the phase lag of the vortex impingement to the returning chamber pulse is around a single cycle, the pressure fluctuations were at their weakest in ambient oxidizer operation. As this phase lag increased, so did the amplitude of the fluctuations to a maximum reached at nearly two cycles. This deviates from the expected trend, where generally having the two events in phase, such as at integer values, would promote coupling, while events out of phase would exhibit a decrease in amplitude. This may suggest that the assumption of the vortex generation timing or traveling speed may not be fully accurate. It is also possible that an unaccounted for coupling is leading to increased interaction at even-numbered phase shifts.

The change in oxidizer temperature would also dramatically alter several thermophysical properties of the fluid. Reducing the temperature from 685 K to ambient, the density increases by a factor of 2.5 and a 10% increase in specific heat ratio. The post sound speed is thus affected, reduced by 35%. Together, this leads to a 60% decrease in oxidizer post velocity. These effects are typically discussed in aggregate in the form of the momentum flux ratio, which is historically used in the scaling of GCSC injectors. In this work, the momentum flux ratio decreases from a value of 1.27 with heated oxidizer down to 0.51 with ambient oxygen.

Literature shows that there are two critical momentum flux ratios where for a given set of conditions in a GCSC injector. The lower critical value defines the point where the inner oxidizer jet attains a high enough momentum flux that it lowers the pressure between the jet and outer fuel spray, pulling the spray inwards and reducing the spray angle. The second, higher critical value defines the point where increasing the oxidizer momentum flux further has no apparent effect on the spray angle, with this point considered the value of highest mixing. While the critical values for the DVRC injector were not defined, literature points to the lower critical value hovering around unity, where the momentum fluxes of the two propellants are similar. Both the ambient and hot oxidizer have low momentum flux ratios, indicating that there is minimal interaction between the fuel spray and the oxidizer core jet. While it is possible that the higher momentum flux ratio of the heated oxidizer would lead to a higher degree of mixing and atomization, literature indicates this change is minimal: A third region, distinct from the outer fuel spray and inner oxidizer jet, would appear between the other two, where a finer distribution of atomized fuel begins to appear. An increased quantity of finer fuel droplets might appear in the fuel droplet size distribution, but very slightly. The change in momentum flux ratio is then expected to have minimal impact on the mixing characteristics of the injector.

This work discussed instability mechanisms found in previous, similar instability tests. Operating conditions that target exploitation of these mechanisms were identified and tested when possible. Of the three discussed mechanisms - vortex shedding

and impingement driven, acoustic timing driven, and baroclinic torque driven - only the first two were deemed possible, as liquid fuel is much less sensitive to baroclinic torque than gaseous methane.

The remaining two mechanisms rely on timing to synchronize heat release events with localized acoustic compression. The acoustic timing driven mechanism considers the oxidizer post as a resonator sized to synchronize return pressure pulses at the dump plane. Constructive interference leads to a strong localized pulse that temporarily cuts off fuel supply, which is then consumed in a subsequent pulse one period later, closing the feedback loop. This scenario is recreated in the DVRC when L/λ is around 0.32. With the hot oxidizer, this configuration did not exhibit any difference in behavior compared to any other configuration.

The remaining mechanism observed in past experiments relies a vortices shed at the injector backstep to mix unburnt fuel products and deliver them to the chamber wall where they are ignited. Coinciding with a returning acoustic pulse closes the feedback loop. This scenario requires specific timing to match the timing of the return pulse to the impingement of the vortex on the hot chamber wall, relying on sound and convection speeds in the post and lengths in both the post and chamber. The DVRC is capable of recreating the scenario of synchronized vortex impingement and return pulse presented in earlier work only with the hot oxidizer in the case of the shortest available oxidizer post and longest chamber, tuning the system to where the vortex impingement happens nearly simultaneously with the returning acoustic wave. At this condition, the DVRC did not exhibit any significant change in behavior compared to any other configuration.

The same geometry with the ambient oxidizer results in more than a full period of the 1L chamber mode before the vortex is expected to impinge on the walls. This timing could prevent the mechanism from taking place, as any shed vortex may be disrupted before reaching the chamber wall. However, a clear linear trend was observed between this timing and the RMS amplitude of the pressure oscillations, with the lowest amplitudes around a phase of one and the strongest amplitudes near

a phase of two. The one outlier was at $L/\lambda = 0.54$, which had already demonstrated atypical behavior.

In this work, an experiment was designed and tested to generate data sets for the use of validating computational models to help predict combustion instabilities. This experiment is well instrumented with high and standard frequency pressure transducers and thermocouples to characterize the behavior of the propellant manifolds, oxidizer post and chamber. The combustor demonstrated very stable operation across a wide range of tested configurations. Data sets of unstable combustion were desired, which prompted testing at different oxidizer inlet temperature. Reduction of the inlet temperature to ambient did not generate self-excited instabilities, but modulation of the acoustic field was achieved through variation of the oxidizer inlet temperature and further modulated through changes to the system geometry, although only observed at the cooler oxidizer condition. The oxidizer temperature had the strongest impact on pressure amplitudes, with an increase in magnitude of 40% or higher with the cooler oxidizer compared to the hot oxidizer. This was attributed to the change in acoustic impedance in the oxidizer, which resulted in an increase in acoustic reflection and transmission coefficients between the combustion gas and oxidizer interface around 40% and 12%, respectively. This would suggest that the ambient oxidizer did not lead to further coupling between the heat release and acoustic field, but that the reduced specific impedance of the oxidizer at ambient condition generated stronger pressure amplitudes.

The pressure field was further augmented by variations in geometry which either promoted or discouraged acoustic resonance. Resonant behavior and increased pressure fluctuations in the post and chamber were encouraged when the difference in the frequencies of the post and chamber modes increased. As the post was considered a closed-open acoustic domain and the chamber a closed-closed domain, the matching of frequencies would place a pressure node at the dump plane in the post standing wave and an anti-node near the same location from the chamber, resulting in a damping situation according to the Rayleigh Criterion. A trend was observed in comparing

the timing between a pressure pulse at the dump plane and the subsequent generation and impingement of a vortex to the travel time for that pulse to traverse the chamber and back. Normalizing this difference in timing by the period of the fundamental longitudinal chamber mode, a prominent linear trend was observed. All tests had phase lags between the return pulse and impinging vortex between one and two chamber cycles. Weakest amplitudes were found at a phase lag of one cycle, while the strongest were found at a phase lag of two. The sole outlier was at the highest acoustic profile tested which had demonstrated atypical behavior. It is expected from previous work that integer phase lags would be the likeliest timing schemes to promote a thermoacoustic coupling, but that behavior is not exhibited. It is possible that the assumptions used in the analysis of the vortex generation and convection are not entirely correct, such as the vortex impinging 4.5 step heights away, or travels at two-third the velocity of the oxidizer jet. The oxidizer velocity drops from 172 m/s to 66 m/s with the ambient oxidizer, a substantial drop that could greatly alter the vortex shedding and traveling properties.

Strong self-sustained thermoacoustic instabilities were not identified at any testing condition or configuration. Pressure oscillations were insufficient to drive any sustained or organized modulation of the heat release field, either through periodic variation of propellant inflow or triggering sudden localized combustion events. The reluctance of the system to enter unstable operation can be tied to a few items. First, the propellants in this combustor largely differed from previous experiments by using transcritically injected fuel and heated oxidizer from a preburner instead of decomposed hydrogen peroxide. The atomization of the fuel and subsequent generation of heat release through combustion can be drastically altered as a liquid fuel moves towards trans- and supercritical injection. How this would then affect combustion stability is not well known. The choice of heated oxygen as opposed to hydrogen peroxide products will also alter both injector hydrodynamics and the ignition process through the change in thermophysical properties and the inclusion of a substantial amount of water in the decomposed peroxide. It is believed that due to discoloration

of the collar tip, the flame is anchored to the collar lip on the injector, a known stabilizer of combustion. This stabilization was not present in previous experiments and could explain the stable operation that was persistent at all tested configurations and conditions.

5.1 Future Work

Potential future work could build from the results presented in this document in a few ways. First, it may be prudent to explore the effects of testing at acoustic profiles beyond L/λ of 0.5, where the spatial distribution of pressure fluctuations and relationship between vortex timing and pressure oscillations were drastically different compared to lower values. This was observed for both the hot and ambient temperature oxidizer. Further testing at higher values corresponding to oxidizer posts behaving as half-wave resonators and beyond could illuminate how and why this behavior shifts.

This work also serves as a preliminary investigation into the effects of the oxidizer inlet temperature on a single element gas-centered swirl coaxial injector combustor. A theory based on acoustic impedance and the reflection and transmission of acoustic pulses at the interface of oxidizer post and chamber was developed based on two set points, one hot and one at ambient. Testing at intermediary temperatures, or at temperatures beyond those tested would provide further validation of the claims made in this document. While much work has been published discussing the role geometry has in a rocket combustor, primarily in the sense of tuning (or de-tuning) injectors to promote (or dampen) instabilities, there is very little discussion of the effects of the specific acoustic impedance of the various media. An experiment designed to study this particular effect, while removing the contributions of other factors such as the momentum flux ratio, would serve to enlighten the relationship between impedance and expected amplitudes of pressure perturbations.

A more practical avenue of future work could be further investigation into how trans- and supercritical fuel injection affect combustion stability, as this is a scenario that occurs frequently in industry. The DVRC injects the liquid fuel at a reduced pressure around 2 and a reduced temperature around 0.5. After injection, the fuel heats up before combusting, transitioning from a transcritical state to supercritical. During this transition, the fluid properties undergo rapid changes, such as in density, specific heat and surface tension, which could all drastically alter combustion properties. The RD-170, which utilizes the GCSC design, injects fuel near a reduced temperature of 1. This injector design is of great interest, and further understanding of injector operation and behavior near critical pressures or temperatures could leverage the design in next generation domestic liquid rocket engines.

Another suggested course of study is the effects of inter-element interaction of GCSC injectors at low momentum flux ratios. In general, literature often discusses the effectiveness of mixing and atomization of these injectors at configurations around the critical momentum flux ratio where mixing is considered optimized. The injection element that served as the template for the one studied in this work has a momentum flux ratio around one, which is considered to carry with it poor performance due to the limited interaction between gaseous oxidizer jet and the swirling liquid fuel. Why this injector operates at this condition is unknown and it is possible that it relies on inter-element interaction to drive the atomization process. This could serve as means of further decoupling the heat release field from potential acoustic modulation at the injection site, as well as distribute the combustion field across a wider volume further from the injector face, alleviating heating.

REFERENCES

REFERENCES

[1] Warren Ferster. Ula to invest in blue origin engine as rd-180 replacement, September 2014.

[2] SpaceX. Making life multiplanetary, September 2017.

[3] Brian Berger. Aerojet rocketdyne pitches ar1 as the only direct replacement for rd-180. http://spacenews.com/aerojet-rocketdyne-pitches-ar1-as-the-only-direct-replacement-for-rd-180/, April 2016.

[4] Rayleigh. The explanation of certain acoustic phenomena. *Royal Institution Proceedings*, 8:536–542, 1878.

[5] F. E. C. Culick, M. V. Heitor, and J. H. Whitelaw. *Unsteady Combustion (NATO Science Series E: (closed))*. Springer, New York, 1996.

[6] V. Nori and J. Seitzman. Ch* chemiluminescence modeling for combustion diagnostics. *Proceedings of the Combustion Institute*, 32:895–893, 2009.

[7] V. Nori and J. Seitzman. Evaluation of chemiluminescence as a combustion diagnostic under varying operating conditions. In *46th AIAA Aerospace Sciences Meeting and Exhibit, Aerospace Sciences Meeting*, 2008.

[8] H. Najm, P. Paul, C. Mueller, and P. Wyckoff. On the adequacy of certain experimental observables as measurements of flame burning rate. *Combustion and Flame*, 113:312–332, 1998.

[9] B. Ayoola, R. Balachandran, J. Frank, E. Mastorakos, and C. Kaminski. Spatially resolved heat release rate measurements in turbulent premixed flames. *Combustion and Flame*, 144:1016, 2006.

[10] M. J. Bedard, S. V. Sardeshmukh, T. L. Fuller, W. E. Anderson, and M. Tanabe. Chemiluminescence as a diagnostic in studying combustion instability in a practical combustor. In *50th AIAA/ASME/SAE/ASEE Joint Propulsion Conference*, 2014.

[11] Tristan L. Fuller. Review of chemiluminescence as an optical diagnostic tool for high pressure unstable rockets. Master's thesis, Purdue University, August 2015.

[12] A. F. Ghoniem, A. J. Chorin, and A. K. Oppenheim. Numerical modelling of turbulent flow in a combustion tunnel. *Philosophical Transactions of The Royal Society*, 304:303–325, 1982.

[13] Hideaki Kobayashi. Experimental study of high-pressure turbulent premixed flames. *Experimental Thermal and Fluid Science*, 26:375–387, 2002.

[14] Hideaki Kobayashi, Teppei Nakashima, Takashi Tamura, Kaoru Maruta, and Takashi Niioka. Turbulence measurements and observations of turbulent premixed flames at elevated pressures up to 3.0 mpa. *Combustion and Flame*, 108:104–117, 1997.

[15] Hideaki Kobayashi, Takashi Tamura, Kaoru Maruta, and Takashi Niioka. Burning velocity of turbulent premixed flames in a high-pressure environment. In *Twenty-Sixth Symposium (International) on Combution*, number 389-396. The Combustion Institute, 1996.

[16] Li Li, Fu Shan, and J. J. Witton. Schlieren methods for high pressure turbulent jet flames. *Journal of the Energy Institute*, 82(2):114–117, 2009.

[17] Matthew Kenneth Wierman. *Measurement of Combustion Response to Transverse Modes at High Pressure.* PhD thesis, Purdue University, December 2014.

[18] Jonas P. Moeck, Jean-Francois Bourgouin, Daniel Durox, Thierry Schuller, and Sebastien Candel. Tomographic reconstruction of heat release rate perturbations induced by helical modes in turbulent swirl flames. *Experiments in Fluids*, 54(1498):1–17, 2013.

[19] J. Frank, M. Miller, and M. Allen. Imaging of laser-induced fluorescence in a high-pressure combustor. In *37th Aerospace Sciences Meeting and Exhibit*, 1999.

[20] Delphine Salgues, Anne-Geraldine Mouis, Seong-Young Lee, Danielle Kalitan, Sibtosh Pal, and Robert Santoro. Shear and swirl coaxial injector studies of lox/gch4 rocket combustion using non-intrusive laser diagnostics. In *44th AIAA Aerospace Sciences Meeting and Exhibit*, 2006.

[21] C. Slabaugh, A. Pratt, and R. Lucht. Simultaneous 5 khz oh-plif/piv for the study of turbulent combustion at engine conditions. *Applied Physics B*, 118(1):109–130, 2014.

[22] R. Sadanandan, W. Meier, and J. Heinze. Experimental study of signal trapping of oh laser induced fluorescence and chemiluminescence in flames. *Applied Physics B*, 106(3):717–724, 2012.

[23] Justin S. Hardi, W. Zach Hallum, Cheng Huang, and Wi. Approaches for comparing numerical simulation of combustion instability and flame imaging. *Journal of Propulsion and Power*, 32(2):279–294, March 2016.

[24] Jaehyoung Jeon, Moongeun Hong, Yeoung-Min Han, and Soo Yong Lee. Experimental study on spray characteristics of gas-centered swirl coaxial injectors. *Journal of Fluid Mechanics*, 133(12), 2011.

[25] James Canino, Stephen Heister, Venkateswaran Sankaran, and Sergey Zakharov. Unsteady response of recessed-post coaxial injectors. In *41st AIAA/ASME/SAE/ASEE Joint Propulsion Conference and Exhibit*, 2005.

[26] Vasin et al. Liquid-propellant rocket engine chamber and its casing. Patent, June 2001.

[27] R. K. Cohn, P. A. Strakey, R. W. Bates, D. G. Talley, J. A. Muss, and C. W. Johnson. Swirl coaxial injector development. In *41st Aerospace Sciences Meeting and Exhibit*, 2003.

[28] J. Hulka, J. S. Forde, R. E. Werling, V. S. Anisimov, V. A. Kozlov, and I. P. Kositsin. Modification and verification testing of a russian nk-33 rocket engine for reusable and restartable applications. In *34th AIAA/ASME/SAE/ASEE Joint Propulsion Conference and Exhibit*, 1998.

[29] Mark L. Dranovsky. *Combustion Instabilities in Liquid Rocket Engines*, volume 221. AIAA, 2007.

[30] Matthew R. Long, Vladimir G. Bazarov, and William E. Anderson. Main chamber injectors for advanced hydrocarbon booster engines. In *39th AIAA/ASME/SAE/ASEE Joint Propulsion Conference and Exhibit*, 2003.

[31] Qing-Fei Fu, Li-Jun Yang, and Yuan-Yuan Qu. Measurement of annular liquid film thickness in an open-end swirl injector. *Aerospace Science and Technology*, 15:117 – 124, 2010.

[32] Ji-Hyuk Im, Seongho Cho, and Youngbin Yoon. Comparative study of spray characteristics of gas-centered and liquid-centered swirl coaxial injectors. *Journal of Propulsion and Power*, 26(6):1196 – 1204, 2010.

[33] Detlef Manski, Christoph Goertz, Hagen-D. Sabnick, James R. Hulka, B. David Goracke, and Daniel J. H. Levack. Cycles for earth-to-orbit propulsion. *Journal of Propulsion and Power*, 14(5):588 – 604, September-October 1998.

[34] Vladimir Bazarov. Design of injectors for self sustaning of combustion chambers stability. In *International Symposium on Energy Conversion Fundamentals*, 2004.

[35] F. E. C. Culick. Combustion instabilities in liquid-fueled propulsion systems. Technical report, California Institute of Technology, 1988.

[36] P. A. Strakey, R. K. Cohn, and D. G. Talley. The development of a methodology to scale between cold-flow and hot-fire evaluations of gas-centered swirl coaxial injectors. In *52nd JANNAF Propulsion Meeting*, 2004.

[37] J. A. Muss, C. W. Johnson, R. K. Cohn, P. A. Strakey, R. W. Bates, and D. G. Talley. Swirl coaxial injector development. part i - test and results. In *Proceedings of 38th JANNAF Joint Propulsion Meeting*, 2002.

[38] Vladimir G. Bazarov and Vigor Yang. Liquid-propellant rocket injector dynamics. *Journal of Propulsion and Power*, 14(5):797–806, September-October 1998.

[39] S. A. Schumaker, S. Danczyk, and M. Lightfoot. Effect of swirl on gas-centered swirl-coaxial injectors. In *47th AIAA/ASME/SAE/ASEE Joint Propulsion Conference and Exhibit*, 2011.

[40] J. L. Santolaya, L. A. Aisa, E. Calvo, I. Garcia, and J. A. Garcia. Analysis by droplet size classes of the liquid flow structure in a pressure swirl hollow cone spray. *Chemical Engineering and Processing: Process Intensification*, 49:125 – 131, 2010.

[41] Malissa D. A. Lightfoot, Stephen A. Danczyk, and Douglas G. Talley. Atomization rate of gas-centered swirl-coaxial injectors. In *ILASS Americas, 21st Annual Conference on Liquid Atomization and Spray Systems*, 2008.

[42] M. D. A. Lightfoot, S. A. Danczyk, and D. G. Talley. Atomization in gas-centered swirl-coaxial injectors. In *ILASS Americas, 19th Annual Conference on Liquid Atomization and Spray Systems*, 2006.

[43] S. A. Rahman, S. Pal, and R. J. Santoro. Swirl coaxial atomization: Cold-flow and hot-fire experiments. In *33rd Aerospace Sciences Meeting and Exhibit*, 1995.

[44] M. Sasaki, H. Sakamoto, M. Takahashi, T. Tomita, and H. Tamura. Comparative study of recessed and non-recessed swirl coaxial injectors. In *33rd Joint Propulsion Conference and Exhibit*, 1997.

[45] G. Obermaier, G. Taubenberger, and D. Feyhl. Coaxial injector development for storable propellant upper stage turbopump engines. In *33rd Joint Propulsion Conference and Exhibit*, 1997.

[46] Fumiaki Takahashi, W. John Schmoll, and John L. Dressler. Characteristics of a velocity-modulated pressure-swirl atomizing spray. *Journal of Propulsion and Power*, 11(5):955–963, September-October 1995.

[47] V. G. Bazarov. Influence of propellant injector dynamic characteristics on combustion stability and efficiency. In *43rd International Astronautical Congress*, 1992.

[48] V. G. Bazarov. Liquid flow pulsation damping in feed lines and injectors of liquid rocket engines. In *44th Congress of International Astronautical Federation*, 1993.

[49] Yuriy Khavkin. About swirl atomizer mean droplet size. *Atomization and Sprays*, 11(6):757 – 774, 2001.

[50] V. G. Bazarov and L. A. Lul'ka. Self-pulsation of liquid flow in coaxial air stream. *Soviet Aeronautics*, 3, 1978.

[51] United Launch Alliance. *Atlas V Launch Services User's Guide.*

[52] Sebastian Soller, Robert Wagner, Hans-Peter Kau, Philip Martin, and Chris Mading. Combustion stability characteristics of coax-swirl-injectors for oxygen/kerosene. In *43rd AIAA/ASME/SAE/ASEE Joint Propulsion Conference and Exhibit*, 2007.

[53] Q. Fu, L. Yang, and X. Wang. Linear stability analysis of a conical liquid sheet. *Journal of Propulsion and Power*, 26:955 – 968, 2010.

[54] L. Bayvel and Z. Orzechowski. *Liquid Atomization.* Taylor and Francis, 1993.

[55] Qing-Fei Fu, Li-Jun Yang, Wei Zhang, and Kun-Da Cui. Spray characteristics of an open-end swirl injector. *Atomization and Sprays*, 22(5):431 – 445, 2012.

[56] Gary C. Cheng, Rory R. Davis, Curtis W. Johnson, Jeffrey A. Muss, Daniel A. Greisen, and Richard K. Cohn. Development of gox/kerosene swirl-coaxial injector technology. Technical report, Sierra Engineering Inc., 2003.

[57] A. H. Lefebvre. *Atomization and Sprays.* Hemisphere Publishing Corporation, New York, 1989.

[58] N. K. Rizk and A. H. Lefebvre. Internal flow characteristics of simplex swirl atomizers. *Journal of Propulsion and Power*, 1:193 – 199, 1985.

[59] M. Suyari and A. H. Lefebvre. Film thickness measurements in a simplex swirl atomizer. *Journal of Propulsion and Power 2*, 2(6):528 – 533, 1986.

[60] Gujeong Park, Ingyu Lee, Jungho Lee, and Youngbin Yoon. Measurement of film thickness in gas-centered swirl coaxial injectors. In *50th AIAA/ASME/SAE/ASEE Joint Propulsion Conference*, 2014.

[61] Gujeong Park, Jungho Lee, Ingyu Lee, Youngbin Yoon, and Chae Hoon Sohn. Geometric effect on spray characteristics of gas-centered swirl coaxial injectors: Recess ratio and gap thickness. *Atomization and Sprays*, 27(7):579 – 589, 2017.

[62] Rahul Anand, P. R. Ajayala, Vikash Kumar, A. Salih, and K. Nandakumar. Spray and atomization characteristics of gas-centered swirl coaxial injectors. *International Journal of Spray and Combustion Dynamics*, 0(0):1 – 14, 2016.

[63] R. J. Kenny, James R. Hulka, Marlow D. Moser, and Noah O. Rhys. Effect of chamber backpressures on swirl injector fluid mechanics. *Journal of Propulsion and Power*, 25(4):902 – 913, July-August 2009.

[64] V. Bazarov. *Dynamics of Liquid Injectors*. Mashinostroenie, 1979.

[65] M. D. A. Lightfoot. Atomization of wall-bounded two-phase flows. In *ILASS Americas, 19th Annual Conference on Liquid Atomization and Spray Systems*, 2006.

[66] T. Sarpkaya and C. F. Merrill. Spray generation from turbulent plane water wall jets discharging into quiescent air. *AIAA Journal*, 39(7):1217 – 1229, 2001.

[67] Donald E. Woodmansee and Thomas J. Hanratty. Mechanism for the removal of droplets from a liquid surface by a parallel air flow. *Chemical Engineering Science*, 24(2):299 – 307, February 1969.

[68] Z. Dia, W. H. Chou, and G. M. Faeth. Drop formation due to turbulent primary breakup at the free surface of plane liquid wall jets. *Physics of Fluids*, 10(5):1147 – 1157, 1998.

[69] Jong Gyu Kim, Yeoung Min Han, Hwan Seok Choi, and Youngbin Yoon. Study on spray patterns of gas-centered swirl coaxial (gcsc) injectors in high pressure conditions. *Aerospace Science and Technology*, 27:171 – 178, 2013.

[70] Wolfgang O. H. Mayer, Axel H. A. Schik, Bruno Vielle, Christian Chauveau, Iskender Gokalp, Douglas G. Talley, and Rodger D. Woodward. Atomization and breakup of cryogenic propellants under high-pressure subcritical and supercritical conditions. *Journal of Propulsion and Power*, 14(5):835 – 842, September-October 1998.

[71] P. A. Strakey, A. K. Cohn, and D. G. Talley. Gas-centered swirl coaxial liquid injector evaluations. In *Fifth International Symposium on Liquid Space Propulsion*, 2005.

[72] E. Mayer. Theory of liquid atomization in high velocity gas streams. *ARS Journal*, 31:1783 – 1785, 1961.

[73] Nan Zong and Vigor Yang. Near-field flow and flame dynamics of lox/methane shear-coaxial injector under supercritical conditions. *Proceedings of the Combustion Institute*, 31:2309 – 2317, 2007.

[74] Joseph C. Oefelein and Vigor Yang. Modeling high-pressure mixing and combustion processes in liquid rocket engines. *Journal of Propulsion and Power*, 14(5):843 – 857, September-October 1998.

[75] W. Mayer, A. Schik, M. Schaffler, and H. Tamura. Injection and mixing processes in high-pressure liquid oxygen/gaseous hydrogen rocket combustors. *Journal of Propulsion and Power*, 16(5):823 – 828, September-October 2000.

[76] D. Kendrick, G. Herding, P. Scouflaire, C. Rolon, and S. Candel. Effects of a recess on cryogenic flame stabilization. *Combustion and Flame*, 118(3):327 – 339, 1999.

[77] G. Singla, P Scouflaire, J. C. Rolon, and S. Candel. Flame stabilization in high pressure lox/gh2 and gch4 combustion. *Proceedings of the Combustion Institute*, 31:2215 – 2222, 2007.

[78] Colette Nicoli, Pierre Haldenwang, and Bruno Denet. Flame holding downstream from a co-flow injector. *C. R. Mecanique*, 334:408 – 413, 2006.

[79] Matthew Juniper and Sebastien Candel. Edge diffusion flame stabilization behind a step over a liquid reactant. *Journal of Propulsion and Power*, 19(3):332 – 341, May-June 2003.

[80] Baoe Yang, Francesco Cuoco, and Micale Oschwald. Atomization and flames in lox/h2- and lox/ch4- spray combustion. *Journal of Propulsion and Power*, 23(4):763–771, July-August 2007.

[81] Yoshio Nunome, Takuo Onodera, Masaki Sasaki, Takeo Tomita, Kan Kobayashi, and Yu Daimon. Combustion instability phenomena observed during cryogenic hydrogen injection temperature ramping for single coaxial injectior elements. In *47th AIAA/ASME/SAE/ASEE Joint Propulsion Conference and Exhibit*, 2011.

[82] Jeongseok Kang and Hong-Gye Sung. Kerosene/gox dynamic combustion characteristics in a mixing layer under supercritical conditions using the les-fpv approach. *Fuel*, 203:579 – 590, 2017.

[83] Michael J. Bedard. *Detailed Measurement of ORSC Main Chamber Injector Dynamics*. PhD thesis, Purdue University, June 2017.

[84] V. Yang, M. Habiballah, M. Popp, and J. Hulka. *Progress in Astronautics and Aeronautics: Liquid Rocket Thrust Chambers*. AIAA, 2005.

[85] Holger Burkhardt, Martin Sippel, Armin Herbertz, and Josef Levanski. Comparative study of kerosene and methane propellant engines for resuable liquid booster stages. In *4th International Conference on Launcher Technology "Space Launcher Liquid Propulsion"*, 2002.

[86] Fengquan Zhong, Xuejun Fan, Gong Yu, Jianguo Li, and Chih-Jen Sung. Heat transfer of aviation kerosene at supercritical conditions. *Journal of Thermophysics and Heat Transfer*, 23(3):543–550, July-September 2009.

[87] Bruce Chehroudi. Recent experimental efforts on high-pressure supercritical injection for liquid rockets and their implications. *International Journal of Aerospace Engineering*, 2012, 2012.

[88] Dustin W. Davis and Bruce Chehroudi. Measurements in an acoustically driven coaxial jet under sub-, near- and supercritical conditions. *Journal of Propulsion and Power*, 23(2):364–374, March-April 2007.

[89] Justin M. Locke, Sibtosh Pal, Roger D. Woodward, and Robert J. Santoro. High speed visualization of lox/gh2 rocket injector flowfield: Hot-fire and cold-flow experiments. In *46th AIAA/ASME/SAE/ASEE Joint Propulsion Conference and Exhibit*, 2010.

[90] Seung-Han Kim, Yeoung-Min Han, Seonghyeon Seo, Il-Yoon Moon, Jong-Kyu Kim, and Woo-Seok Seol. Effects of lox post recess on the combustion characteristics for bi-swirl coaxial injector. In *41st AIAA/ASME/SAE/ASEE Joint Propulsion Conference and Exhibit*, 2005.

[91] Xingjian Wang and Vigor Yang. Supercritical mixing and combustion of liquid-oxygen/kerosene bi-swirl injectors. *Journal of Propulsion and Power*, 1(7), 2016.

[92] Kevin Miller. Experimental study of longitudinal instabilities in a single element rocket combustor. Master's thesis, Purdue University, 2005.

[93] B. T. Zinn. Longitudinal mode acoustic losses in short nozzles. *Journal of Sound and Vibration*, 22(1):93–105, 1972.

[94] L. E. Kinsler, A. R. Freq, A. B Coppens, and J. V. Sanders. *Fundamentals of Acoustics*. Wiley, New York, 4th edition, 2000.

[95] James C. Sisco. *Measurement and Analysis of an Unstable Model Rocket Combustor*. PhD thesis, Purdue University, 2007.

[96] R. Smith, G. Xia, W. Anderson, and C. L. Merkle. Computational simulations of the effect of backstep height on nonpremixed combustion instability. *AIAA Journal*, 48(9):1857 – 1868, September 2010.

[97] R. Smith, M. Ellis, G. Xia, V. Sankaran, W. Anderson, and C. L. Merkle. Computational investigation of acoustics and instabilities in a longitudinal-mode rocket combustor. *AIAA Journal*, 46(11):2659 – 2673, November 2008.

[98] G. Xia, M. Harvazinski, W. Anderson, and C. L. Merkle. Investigation of modeling and physical parameters on instability prediction in a model rocket combustor. In *47th AIAA/ASME/SAE/ASEE Joint Propulsion Conference and Exhibit*, 2011.

[99] Kevin Miller, James Sisco, Nicholas Nugent, and William Anderson. Combustion instability with a single-element swirl injector. *Journal of Propulsion and Power*, 23(5):1102 – 1112, September-October 2007.

[100] Eric W. Lemmon, Marcia L. Huber, and Mark O. McLinden. Nist standard reference database 23: Reference fluid thermodynamic and transport properties-refprop, version 9.1. Technical report, National Institute of Standards and Technology, 2013.

[101] Matthew E. Harvazinski, Cheng Huang, Venkateswaran Sankaran, Thomas W. Feldman, William E. Anderson, Charles L. Merkle, and Douglas G. Talley. Coupling between hydrodynamics, acoustics and heat release in a self-excited unstable combustor. *Physics and Fluids*, 27(4), 2015.

[102] Yen C. Yu, Loral O'Hara, James C. Sisco, and William E. Anderson. Experimental study of high-frequency combustion instability in a continuously variable resonance combustor. In *47th AIAA Aerospace Sciences Meeting*, 2009.

[103] Yen Ching Yu. *Experimental and Analytical Investigations of Longitudinal Combustion Instability in a Continuously Variable Resonance Combustor (CVRC)*. PhD thesis, Purdue University, May 2009.

[104] Yen C. Yu, James C. Sisco, Stanford Rosen, Ajay Madhav, and William E. Anderson. Spontaneous longitudinal combustion instability in a continuously variable resonance combustor. *Journal of Propulsion and Power*, 28(5):876 – 887, September-October 2012.

[105] R. Garby, L. Selle, and T. Poinsot. Large-eddy simulation of combustion instabilities in a variable-length combustor. *Comptes Rendux Mécanique*, 341(1-2):220 – 229, 2013.

[106] S. Srinivasan, R. Ranjan, and S. Menon. Flame dynamics during combustion instability in a high-pressure, shear-coaxial injector combustor. *Flow Turbulence Combustion*, 94:237 – 262, 2015.

[107] Swanand V. Sardeshmukh, William E. Anderson, Matthew E. Harvazinski, and Venkateswaran Sankaran. Prediction of combustion instability with detailed chemical kinetics. In *53rd AIAA Aerospace Sciences Meeting*, 2015.

[108] Luigi Crocco and Sin-I Cheng. *Theory of Combustion Instability in Liquid Propellant Rocket Motors*. Butterworths Publications, LTD., 1956.

[109] Swanand V. Sardeshmukh, Cheng Huang, William E. Anderson, Matthew E. Harvazinski, and Venkateswaran Sankaran. Impact of chemical kinetics on the predictions of bluff body stabilized flames. In *54th AIAA Aerospace Sciences Meeting*, 2016.

[110] D. A. Smith and E. E. Zukoski. Combustion instability sustained by unsteady vortex combustion. In *21st AIAA/ASME/SAE/ASEE Joint Propulsion Conference*, 1985.

[111] T. J. Poinsot, A. C. Trouve, D. P. Veynante, S. M. Candel, and E. J. Esposito. Vortex-driven acoustically coupled combustion instabiities. *Journal of Fluid Mechanics*, 177:265 – 292, 1987.

[112] K. H. Yu, A. Trouve, and J. W. Daily. Low-frequency pressure oscillations in a model ramjet combustor. *Journal of Fluid Mechanics*, 232:47 – 72, 1991.

[113] R. W. Pitz and J. W. Daily. Combustion in a turbulent mixing layer formed at a rearward-facing step. *AIAA Journal*, 21(11):1565 – 1570, 1983.

[114] Gerhard Heinzel, Albrecht Rüdiger, and Roland Schilling. Spectrum and spectral density estimation by the discrete fourier transform (dft), including a comprehensive list of window functions and some new flat-top windows. Technical report, Max Planck Society, 2002.

[115] Luis Aguiar-Conraria and Maria Joana Soares. The continuous wavelet transform: A primer. Technical report, NIPE - Universidade do Minho, 2011.

[116] Jonathan M. Lilly and Sofia C. Olhede. Higher-order properties of analytic wavelets. *IEEE Transactions on Signal Processing*, 57(1):146–160, 2008.

[117] M. Holschneider. *Wavelets: An Analysis Tool*. Oxford University Press, 1998.

[118] S. Olhede and A. T. Walden. Polarization phase relationships via multiple morse wavelets. i. fundamentals. *Proceedings of the Royal Society A*, 459(2030), February 2003.

[119] Praveen Kumar and Efi Foufoula-Georgiou. Wavelet analysis in geophysics: An introduction. *Wavelets in Geophysics*, 1994.

[120] Thomas W. Feldman, Matthew E. Harvazinski, Charles L. Merkle, and William E. Anderson. Comparison between simulation and measurement of self-excited combustion instability. In *48th AIAA/ASME/SAE/ASEE Joint Propulsion Conference and Exhibit*, 2012.

[121] R. Garby, L. Selle, and T. Poinsot. Analysis of the impact of heat losses on an unstable model rocket-engine combustor using large-eddy simulation. In *48th AIAA/ASME/SAE/ASEE Joint Propulsion Conference and Exhibit*, 2012.

[122] Matthew E. Harvazinski, Venkateswaran Sankaran, and Douglas G. Talley. Parametric trends in the combustion stability characteristics of a single-element gas-gas rocket engine. In *52nd Aerospace Sciences Meeting*, 2014.

[123] David R. Clarke and Simon R. Phillpot. Thermal barrier coating materials. *Materials Today*, 8(6), 2005.

[124] Christopher F. Lietz, Matthew E. Harvazinski, S. Alexander Schumaker, and Venkateswaran Sankaran. Time-resolved single-element gas-centered swirl-coaxial injector simulations for combustion stability prediction. In *53rd AIAA/SAE/ASEE Joint Propulsion Conference*, 2017.

[125] T. Le Cong and P. Dagaut. Experimental and detailed modeling study of the effect of water vapor on the kinetics of combustion of hydrogen and natural gas, impact on nox. *Energy and Fuels*, 23:725–734, 2009.

[126] Clancy Umphrey, Matthew E. Harvazinski, S. Alexander Schumaker, and Venke Sankaran. Large-eddy simulation of single-element gas-centered swirl coaxial injectors for combustion stability predictions. In *53rd AIAA/SAE/ASEE Joint Propulsion Conference*, 2017.

[127] M. L. Huber, E. W. Lemmon, L. S. Ott, and T. J. Bruno. Preliminary surrogate mixture models for the thermophysical properties of rocket propellants rp-1 and rp-2. *Energy and Fuels*, 23:3083 – 3088, 2009.

[128] Stephanie L. Outcalt, Arno Laesecke, and Karin J. Brumback. Thermophysical properties measurements of rocket propellants rp-1 and rp-2. *Journal of Propulsion and Power*, 25(5):1032 – 1040, September-October 2009.

[129] Thomas J. Bruno. The properties of rp-1 and rp-2. Technical report, NIST, 2008.

[130] Ten-See Wang, Paul McConnaughey, Yen-Sen Chen, and Saif Warsi. Computational pollutant environment assessment from propulsion-system testing. *Journal of Spacecraft and Rockets*, 33(3):386 – 392, May-June 1996.

[131] F. Defoeux, V. Dias, C. Renard, P. J. Van Tiggelen, and J. Vandooren. Experimental investigation of the structure of a sooting premixed benzen/oxygen/argon flame burning at low pressure. *Proceedings of the Combustion Institute*, 30:1407 – 1415, 2005.

[132] Wen Zeng, Shuang Liang, Hai xai Li, and Hong an Ma. Chemical kinetic simulation of kerosene combustion in an individual flame tube. *Journal of Advanced Research*, 5:357–366, 2014.

[133] A. M. Starik, N. S. Titova, and S. A. Torokhov. Kinetics of oxidation and combustion of complex hydrocarbon fuels: Aviation kerosene. *Combustion, Explosion, and Shock Waves*, 49(4):392–408, 2013.

[134] A. Burkert and W. Paa. Ignition delay times of single kerosene droplets based on formaldehyde lif detection. *Fuel*, 167:271–279, 2016.

[135] JinHu Liang, Su Wang, HongHao Hu, ShengTao Zhang, BingCheng Fan, and JiPing Cui. Shock tube study of kerosene ignition delay at high pressures. *Science China Physics, Mechanics and Astronomy*, 55(6):947–954, June 2012.

[136] Y. Moon, D. Kim, and Y. Yoon. Improved spray model for viscous annular sheets in a swirl injector. *Journal of Propulsion and Power*, 26:267 – 279, 2010.

[137] Yixing Li, Xingjian Wang, Liwei Zhang, Shiang-Ting Yeh, and Vigor Yang. Flow dynamics of gaseous oxygen/kerosene jet-swirl injectors at supercritical conditions. In *55th AIAA Aerospace Sciences Meeting*, 2017.

[138] Brian Pomeroy and William Anderson. Transverse instability studies in a subscale chamber. *Journal of Propulsion and Power*, 32(4):939–947, July-August 2016.

[139] M. J. Lighthill. On sound generated aerodynamically. *Proceedings of the Royal Society A*, 211(1107), March 1952.

[140] J. Portillo, James Sisco, Yen Yu, Venkateswaran Sankaran, and William Anderson. Application of a generalized instability model to a longitudinal mode combustion instability. In *43rd AIAA/ASME/SAE/ASEE Joint Propulsion Conference and Exhibit*, 2007.

[141] Yen Yu, James Sisco, William Anderson, and Venke Sankaran. Examination of spatial mode shapes and resonant frequencies using linearized euler solutions. In *37th AIAA Fluid Dynamics Conference and Exhibit*, 2007.

[142] Y. C. Yu, J. C. Sisco, V. Sankaran, and W. E. Anderson. Effects of mean flow, entropy waves and boundary conditions on longitudinal combustion instability. *Combustion Science and Technology*, 182(7):739 – 776, July 2010.

[143] June 2011.

APPENDICES

A. HIGH-PASS FILTERED RESULTS

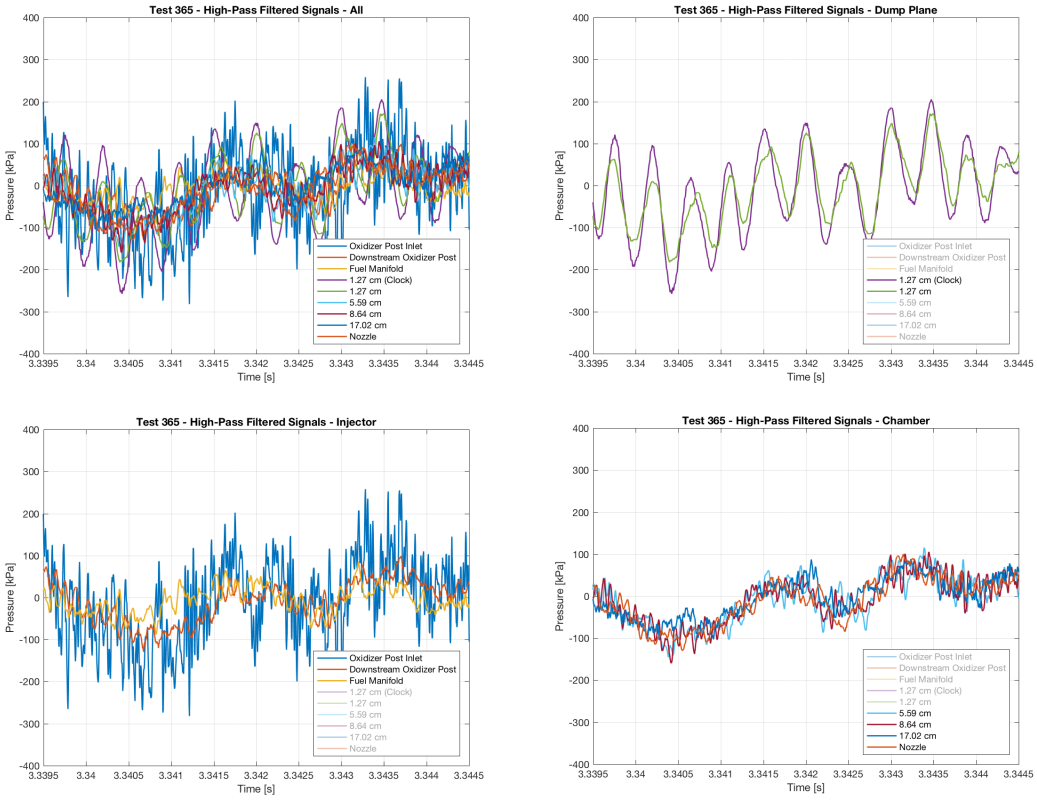

Figure A.1.: High-pass filtered results (top-left) and signal groupings, injector (bottom-left), dump plane (top-right), and chamber (bottom-right) for hot oxidizer Test 365 ($L/\lambda = 0.28$).

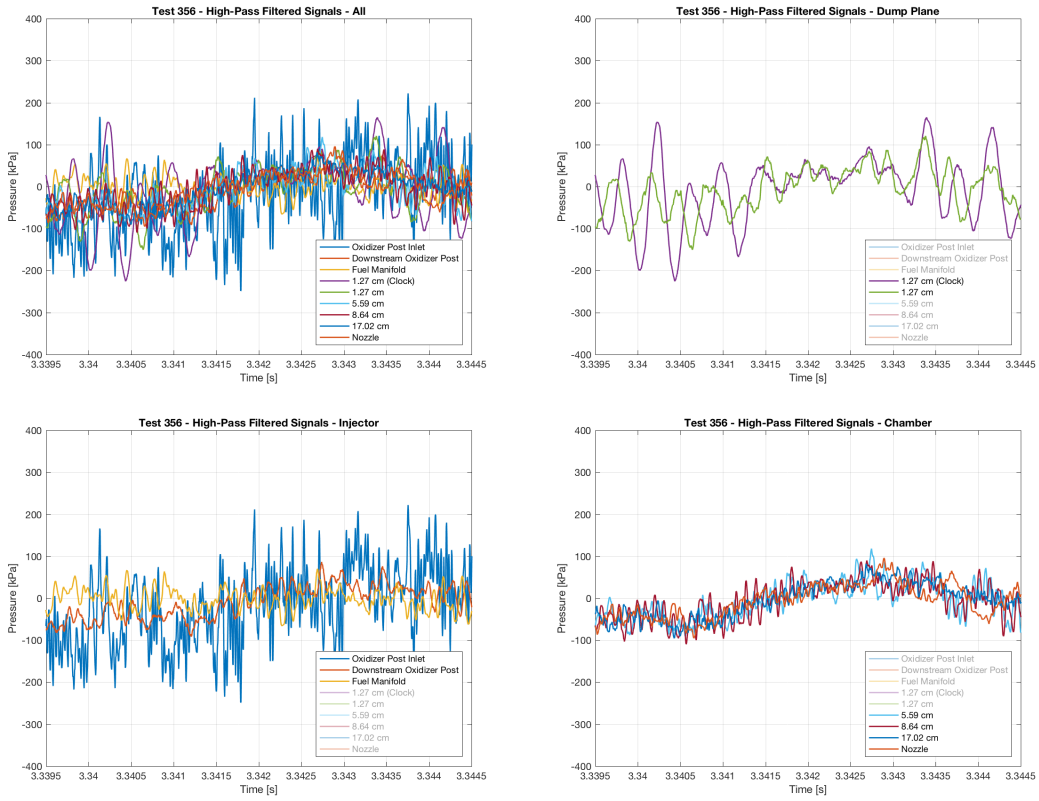

Figure A.2.: High-pass filtered results (top-left) and signal groupings, injector (bottom-left), dump plane (top-right), and chamber (bottom-right) for hot oxidizer Test 356 ($L/\lambda = 0.41$).

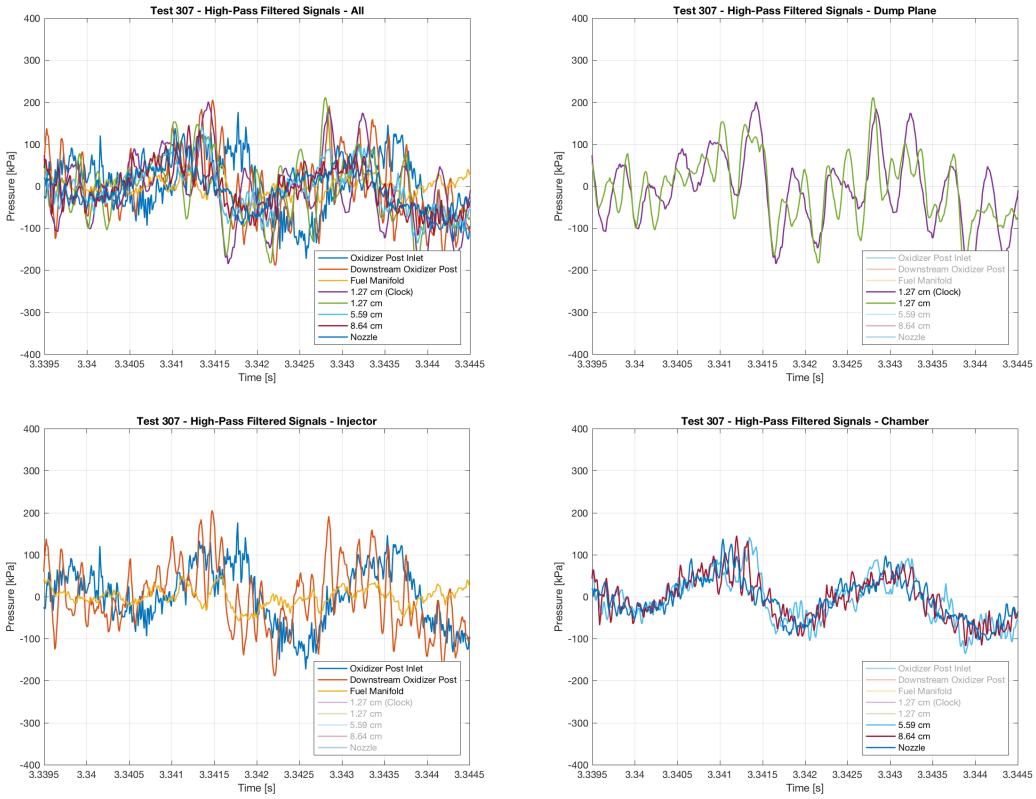

Figure A.3.: High-pass filtered results (top-left) and signal groupings, injector (bottom-left), dump plane (top-right), and chamber (bottom-right) for hot oxidizer Test 307 ($L/\lambda = 0.65$).

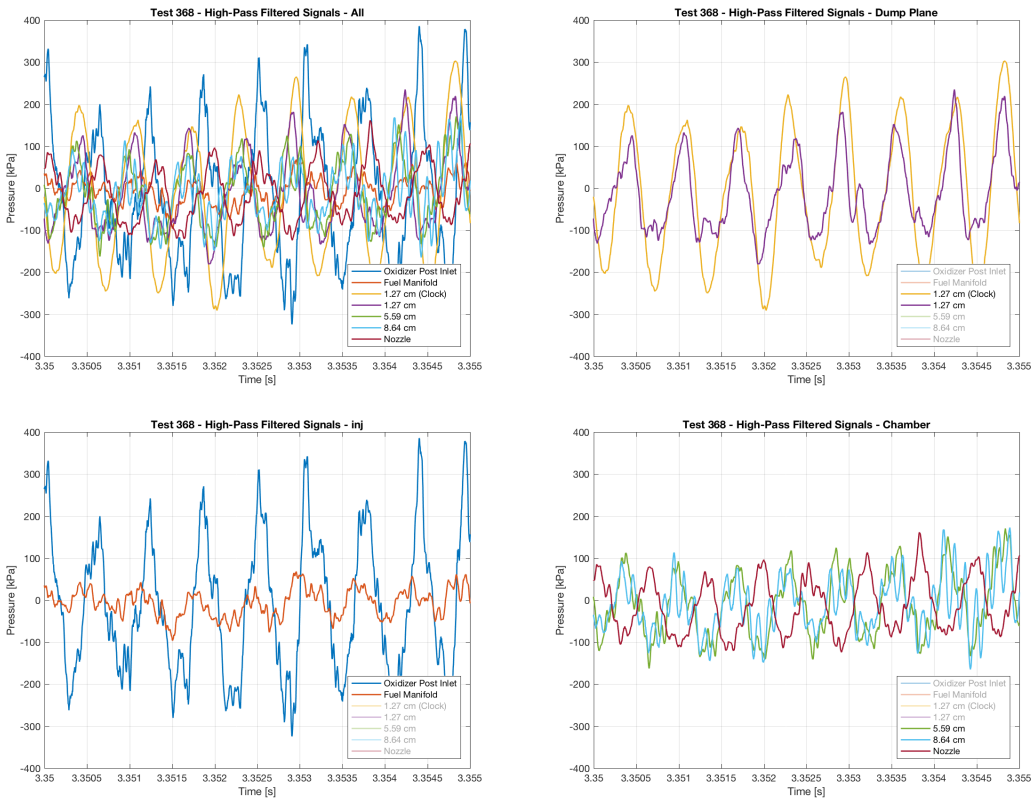

Figure A.4.: High-pass filtered results (top-left) and signal groupings, injector (bottom-left), dump plane (top-right), and chamber (bottom-right) for ambient oxidizer Test 368 ($L/\lambda = 0.26$).

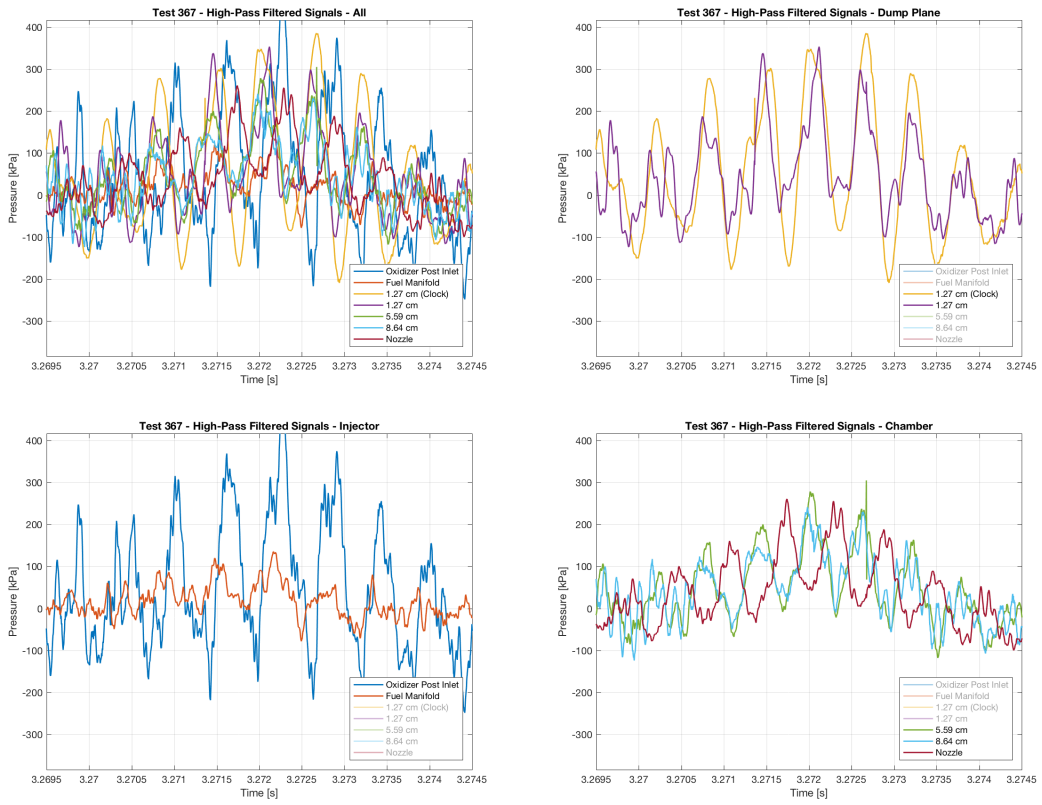

Figure A.5.: High-pass filtered results (top-left) and signal groupings, injector (bottom-left), dump plane (top-right), and chamber (bottom-right) for ambient oxidizer Test 367 ($L/\lambda = 0.28$).

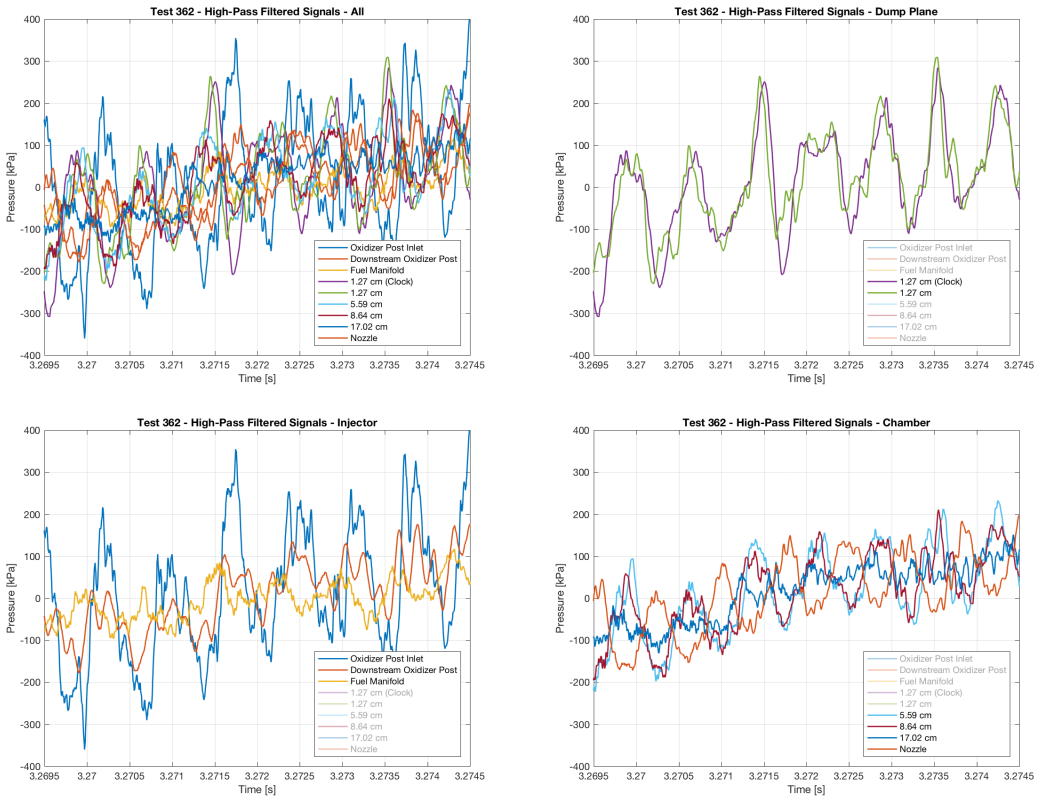

Figure A.6.: High-pass filtered results (top-left) and signal groupings, injector (bottom-left), dump plane (top-right), and chamber (bottom-right) for ambient oxidizer Test 362 ($L/\lambda = 0.32$).

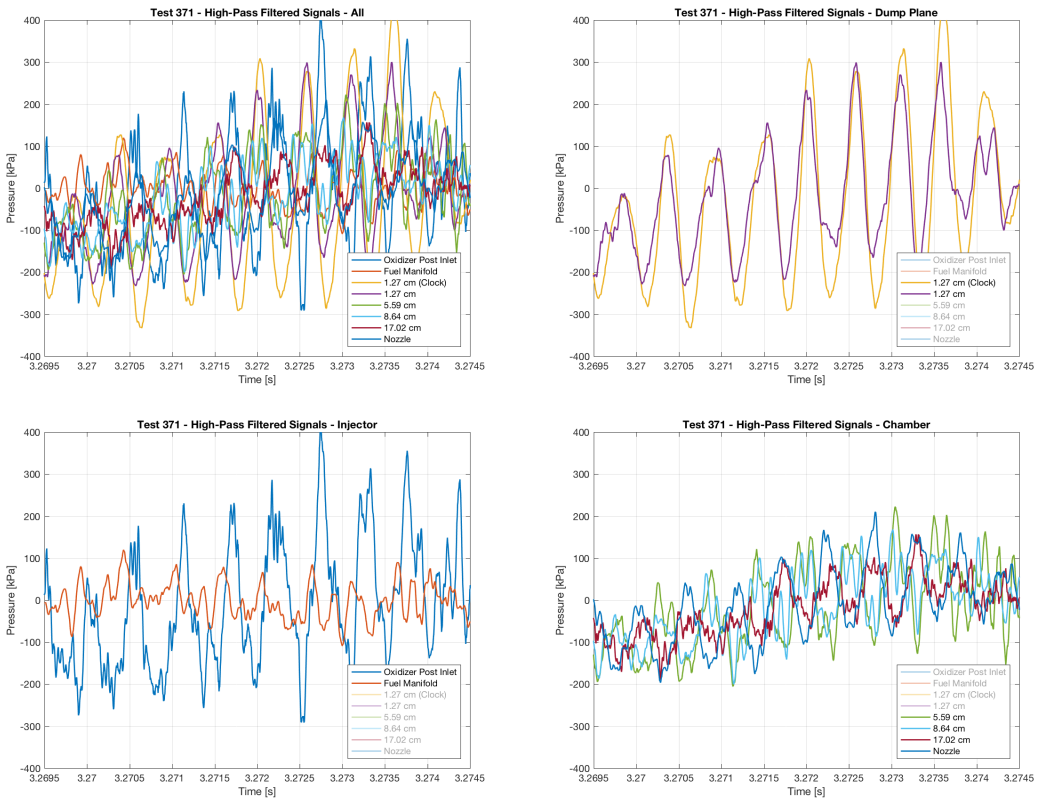

Figure A.7.: High-pass filtered results (top-left) and signal groupings, injector (bottom-left), dump plane (top-right), and chamber (bottom-right) for ambient oxidizer Test 371 ($L/\lambda = 0.33$).

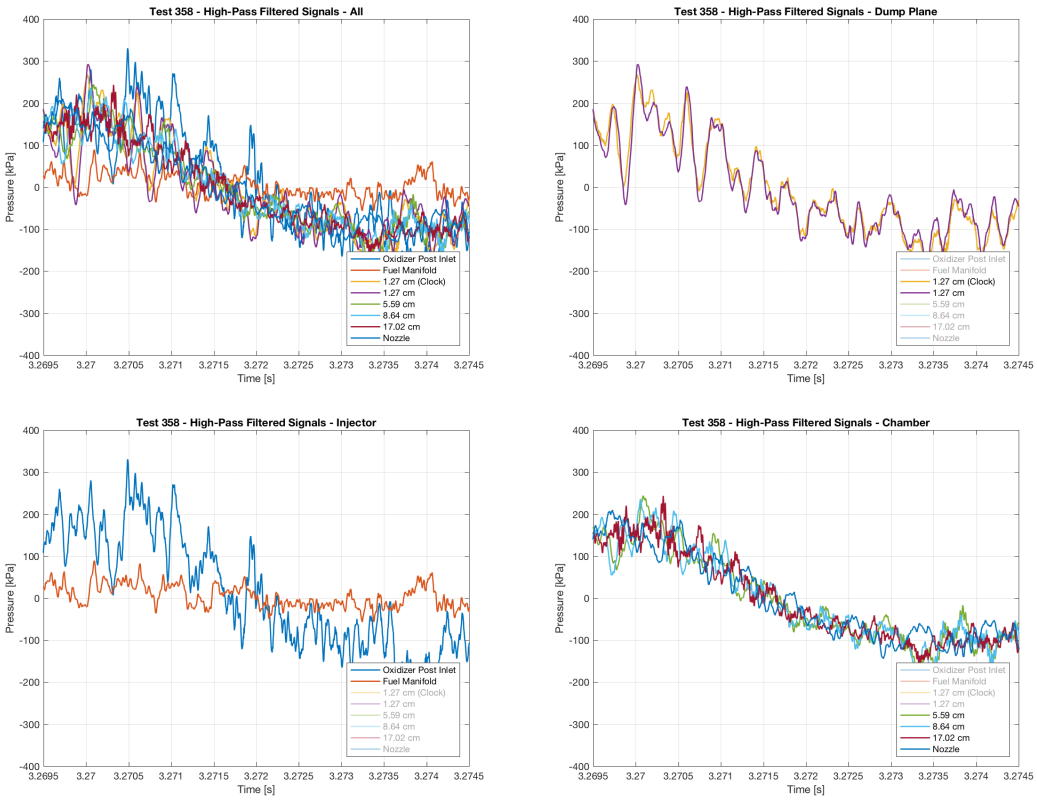

Figure A.8.: High-pass filtered results (top-left) and signal groupings, injector (bottom-left), dump plane (top-right), and chamber (bottom-right) for ambient oxidizer Test 358 ($L/\lambda = 0.54$).

B. CROSS-CORRELATION RESULTS

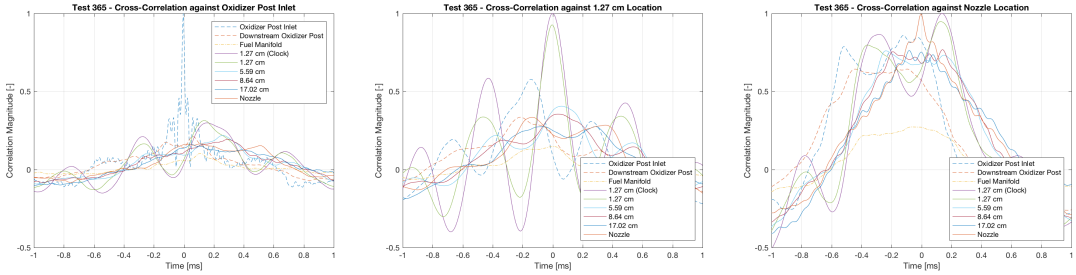

Figure B.1.: Cross-correlation with reference signals oxidizer post inlet (left), non-clocked 1.27 cm location (center), and nozzle (right) for hot oxidizer Test 365 ($L/\lambda = 0.28$).

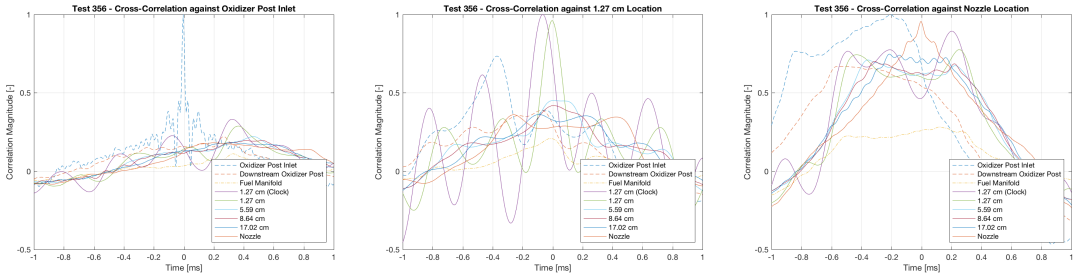

Figure B.2.: Cross-correlation with reference signals oxidizer post inlet (left), non-clocked 1.27 cm location (center), and nozzle (right) for hot oxidizer Test 356 ($L/\lambda = 0.41$).

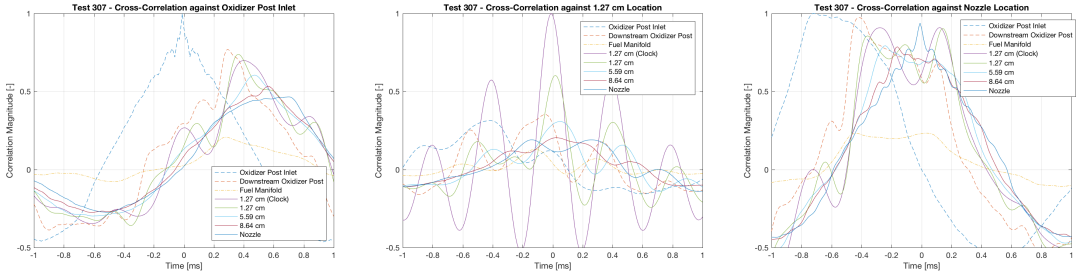

Figure B.3.: Cross-correlation with reference signals oxidizer post inlet (left), non-clocked 1.27 cm location (center), and nozzle (right) for hot oxidizer Test 307 ($L/\lambda = 0.65$).

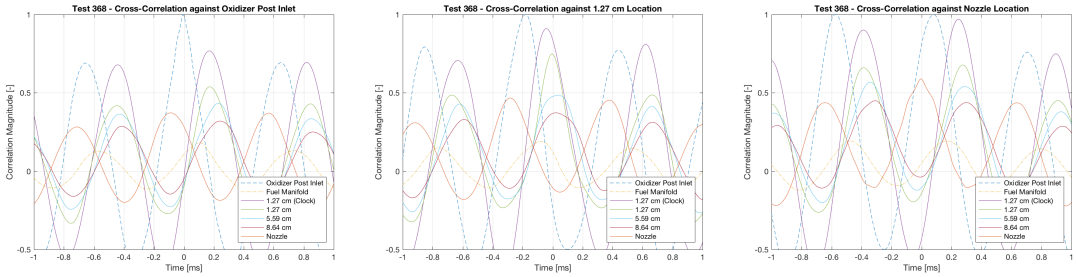

Figure B.4.: Cross-correlation with reference signals oxidizer post inlet (left), non-clocked 1.27 cm location (center), and nozzle (right) for ambient oxidizer Test 368 ($L/\lambda = 0.26$).

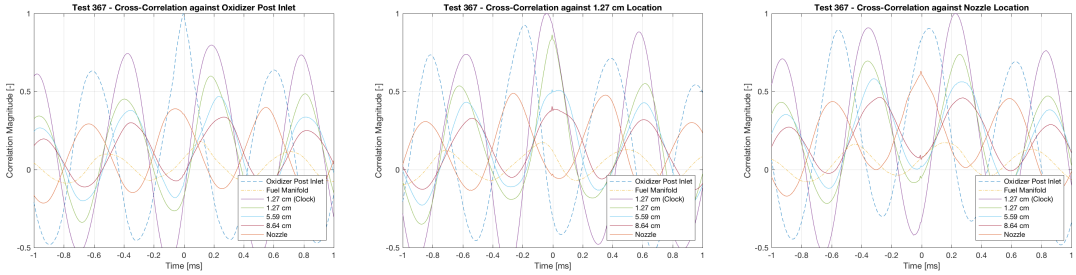

Figure B.5.: Cross-correlation with reference signals oxidizer post inlet (left), non-clocked 1.27 cm location (center), and nozzle (right) for ambient oxidizer Test 367 ($L/\lambda = 0.28$).

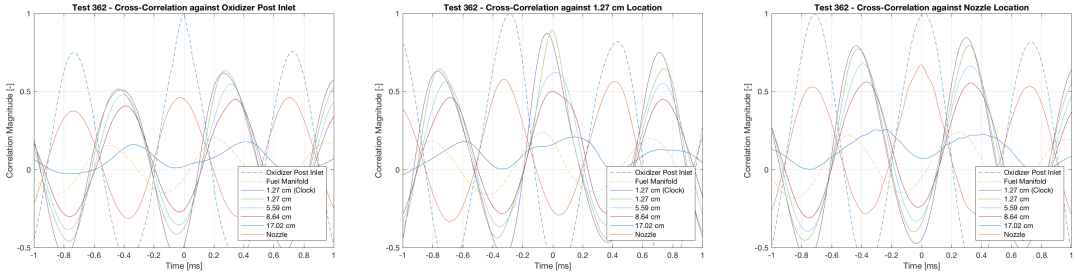

Figure B.6.: Cross-correlation with reference signals oxidizer post inlet (left), non-clocked 1.27 cm location (center), and nozzle (right) for ambient oxidizer Test 362 ($L/\lambda = 0.32$).

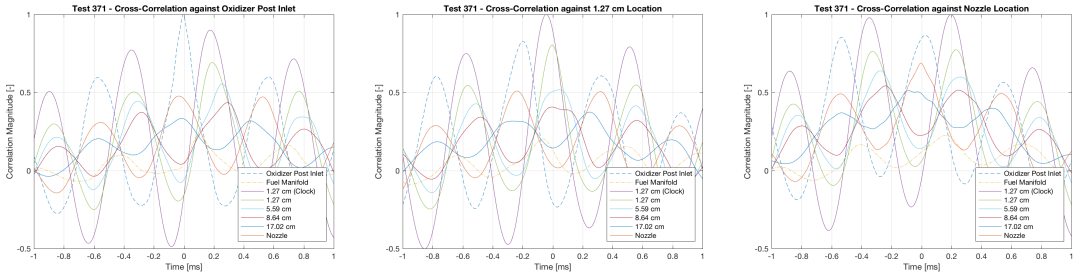

Figure B.7.: Cross-correlation with reference signals oxidizer post inlet (left), non-clocked 1.27 cm location (center), and nozzle (right) for ambient oxidizer Test 371 ($L/\lambda = 0.33$).

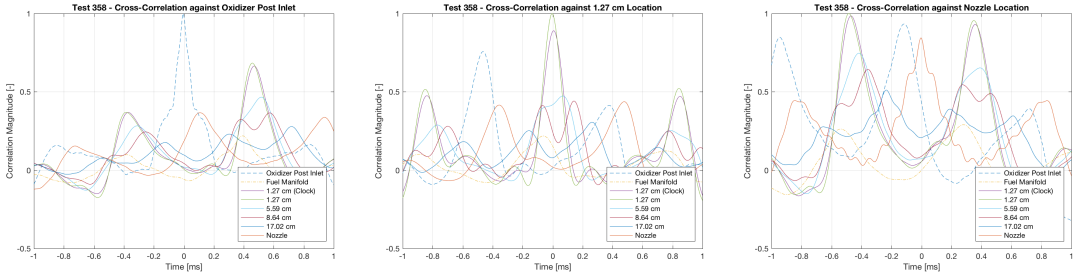

Figure B.8.: Cross-correlation with reference signals oxidizer post inlet (left), non-clocked 1.27 cm location (center), and nozzle (right) for ambient oxidizer Test 358 ($L/\lambda = 0.54$).

C. PSD RESULTS - FREQUENCY DISCREPANCY

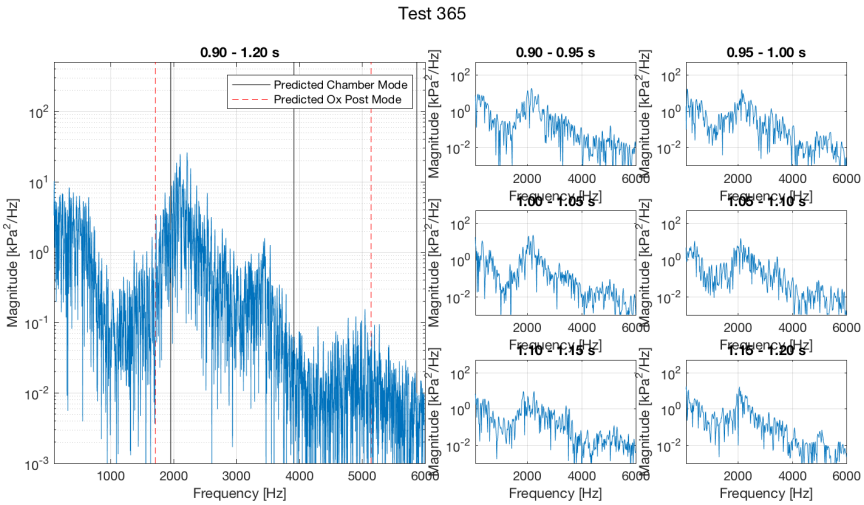

Figure C.1.: Variation in frequency content for hot oxidizer Test 365 ($L/\lambda = 0.28$).

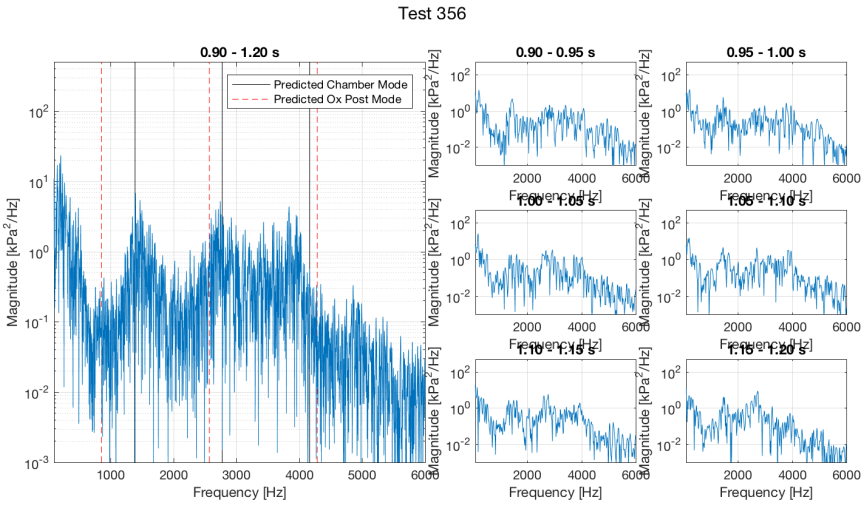

Figure C.2.: Variation in frequency content for hot oxidizer Test 356 ($L/\lambda = 0.41$).

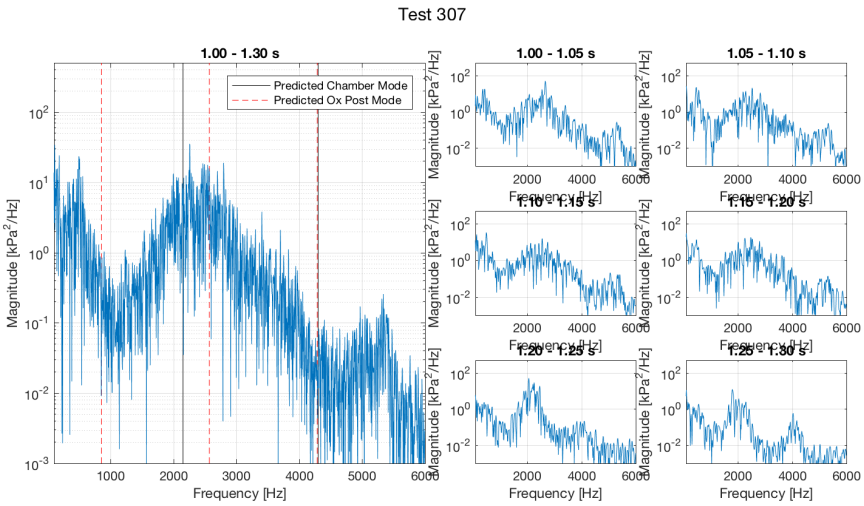

Figure C.3.: Variation in frequency content for hot oxidizer Test 307 ($L/\lambda = 0.65$).

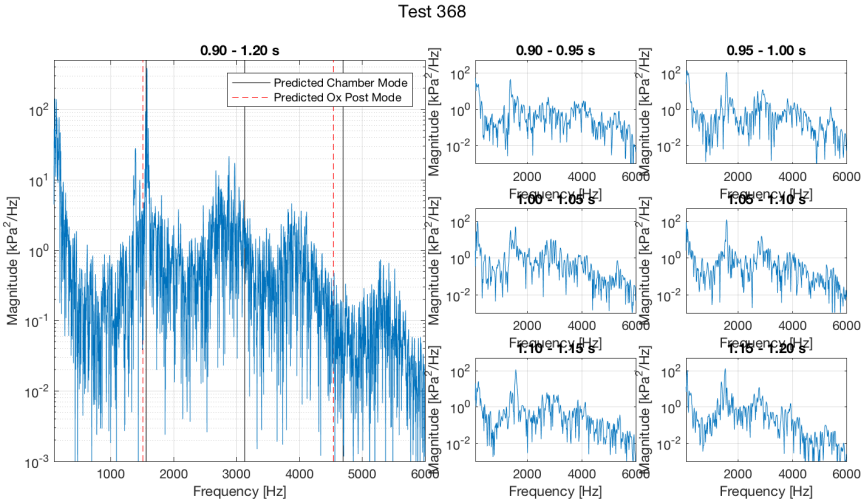

Figure C.4.: Variation in frequency content for ambient oxidizer Test 368 ($L/\lambda = 0.26$).

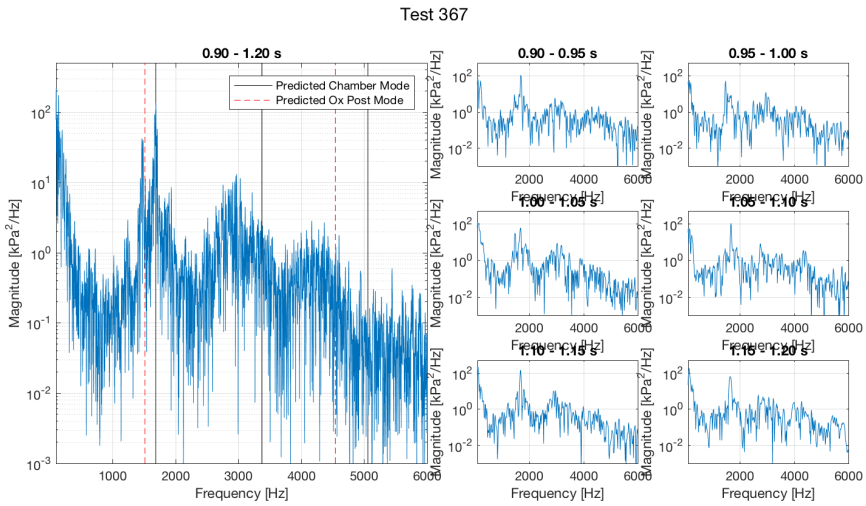

Figure C.5.: Variation in frequency content for ambient oxidizer Test 367 ($L/\lambda = 0.28$).

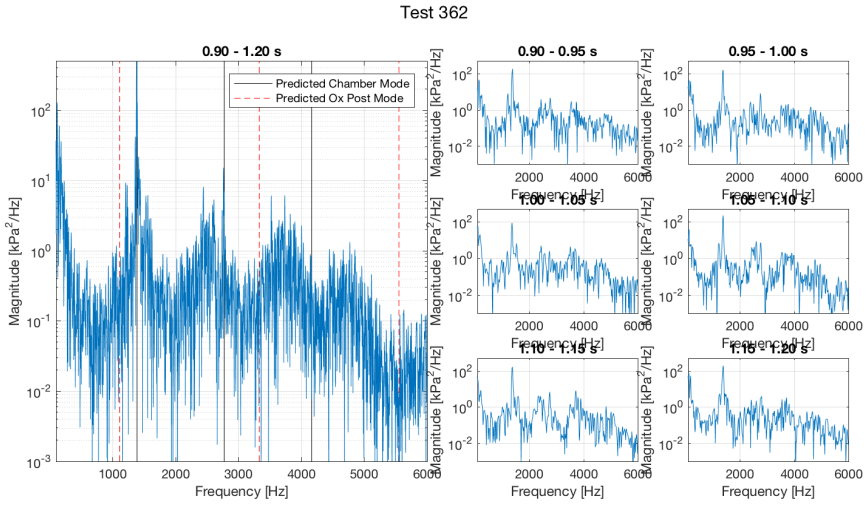

Figure C.6.: Variation in frequency content for ambient oxidizer Test 362 ($L/\lambda = 0.32$).

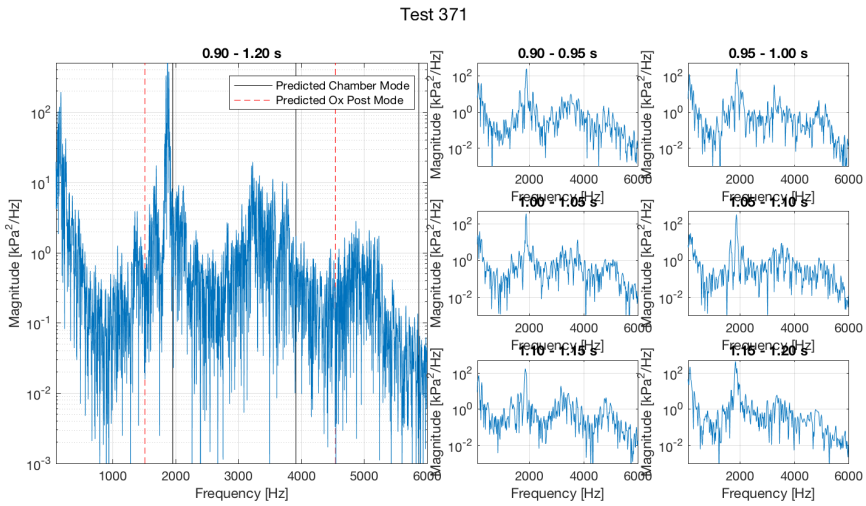

Figure C.7.: Variation in frequency content for ambient oxidizer Test 371 ($L/\lambda = 0.33$).

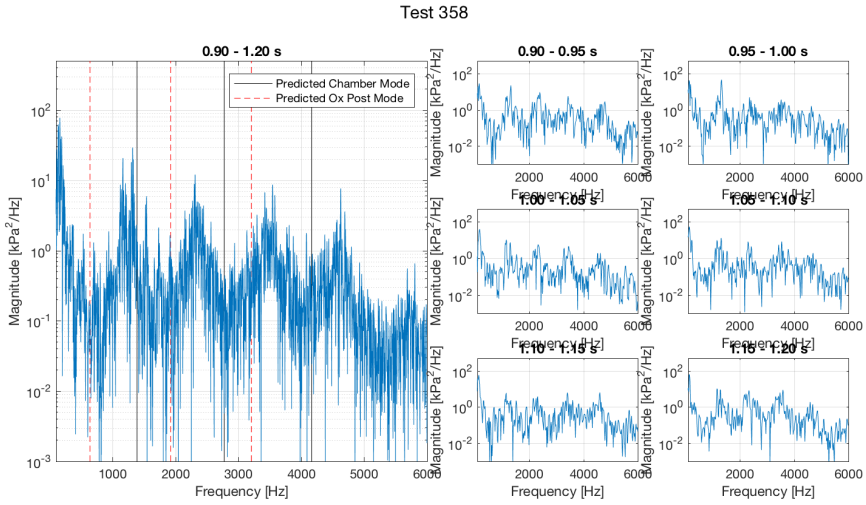

Figure C.8.: Variation in frequency content for ambient oxidizer Test 358 ($L/\lambda = 0.54$).

D. PSD RESULTS - GROUPINGS

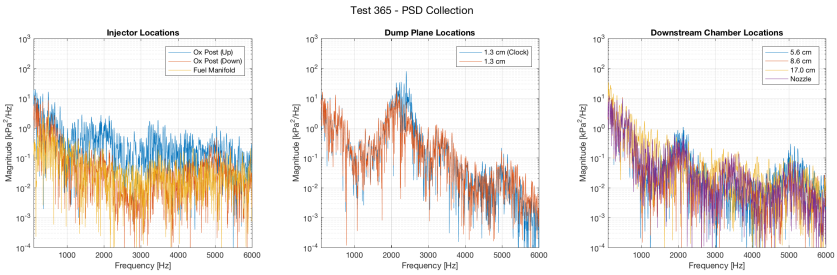

Figure D.1.: Power spectral density of pressure signals for hot oxidizer Test 365 ($L/\lambda = 0.28$), grouped by location.

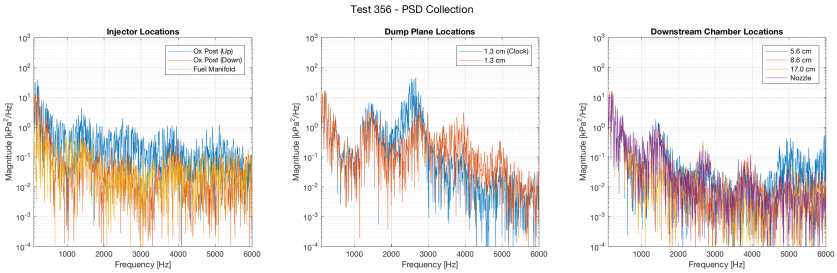

Figure D.2.: Power spectral density of pressure signals for hot oxidizer Test 356 ($L/\lambda = 0.41$), grouped by location.

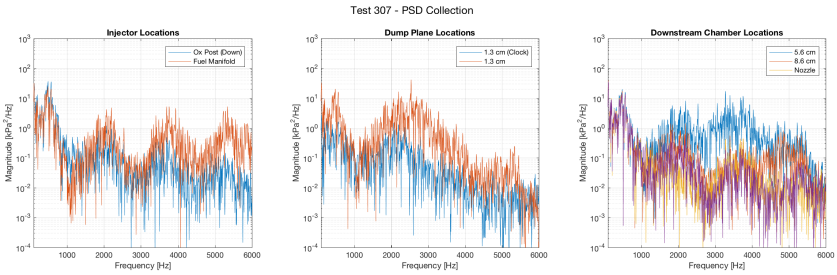

Figure D.3.: Power spectral density of pressure signals for hot oxidizer Test 307 ($L/\lambda = 0.65$), grouped by location.

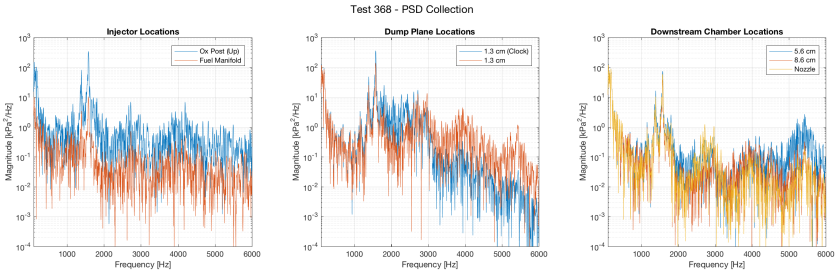

Figure D.4.: Power spectral density of pressure signals for ambient oxidizer Test 368 ($L/\lambda = 0.26$), grouped by location.

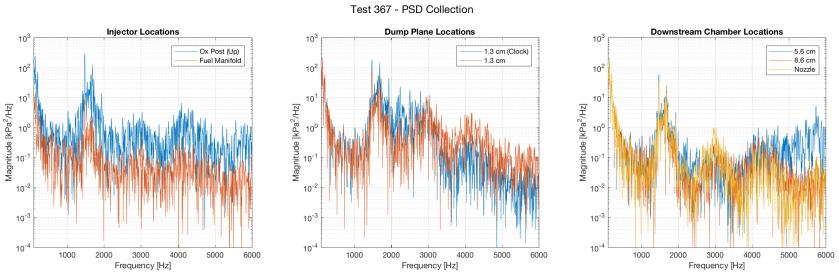

Figure D.5.: Power spectral density of pressure signals for ambient oxidizer Test 367 ($L/\lambda = 0.28$), grouped by location.

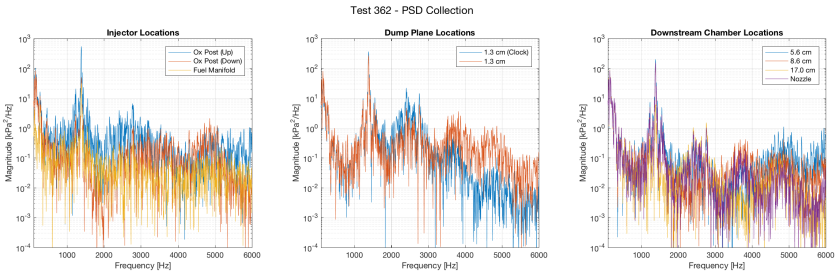

Figure D.6.: Power spectral density of pressure signals for ambient oxidizer Test 362 ($L/\lambda = 0.32$), grouped by location.

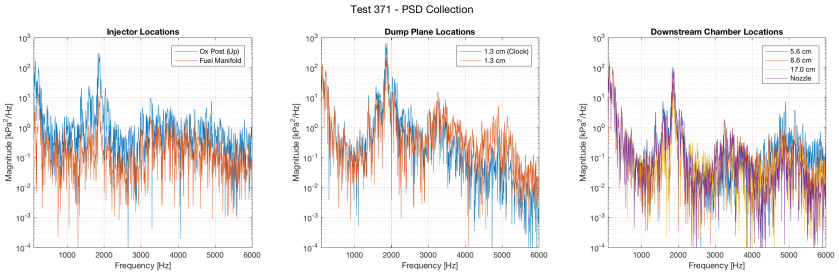

Figure D.7.: Power spectral density of pressure signals for ambient oxidizer Test 371 ($L/\lambda = 0.33$), grouped by location.

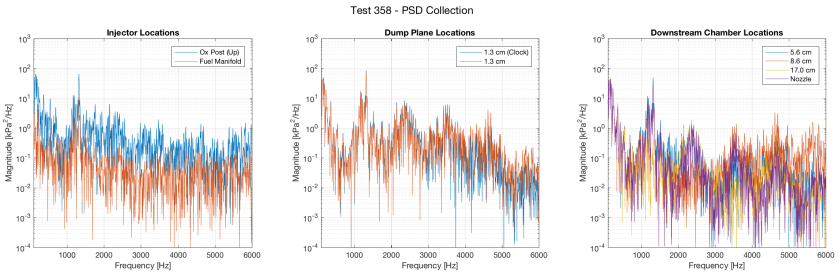

Figure D.8.: Power spectral density of pressure signals for ambient oxidizer Test 358 ($L/\lambda = 0.54$), grouped by location.

E. SPECTROGRAM RESULTS

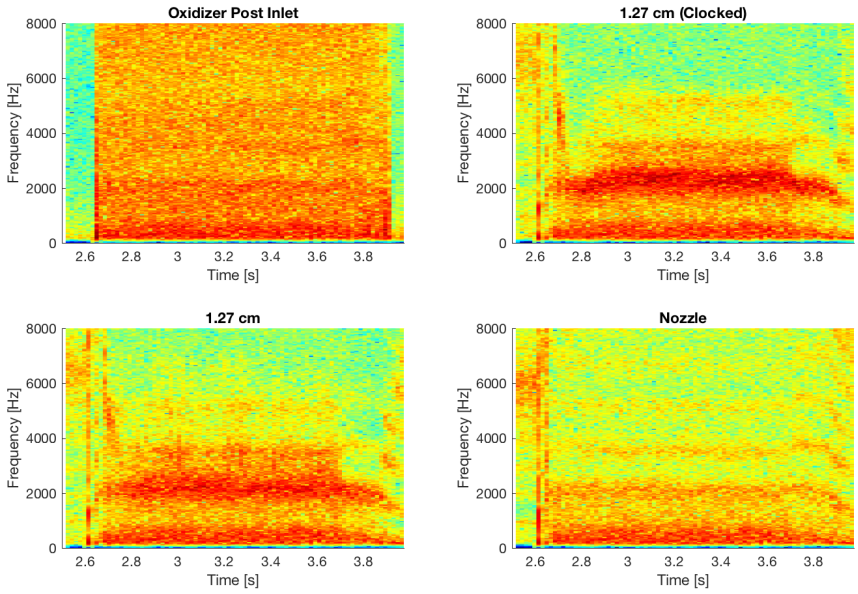

Figure E.1.: Spectrograms for the oxidizer post inlet (top-left), 1.27 cm (Clocked) location (top-right), 1.27 cm location (bottom-left), and chamber (bottom-right) for hot oxidizer Test 365 ($L/\lambda = 0.28$), grouped by location.

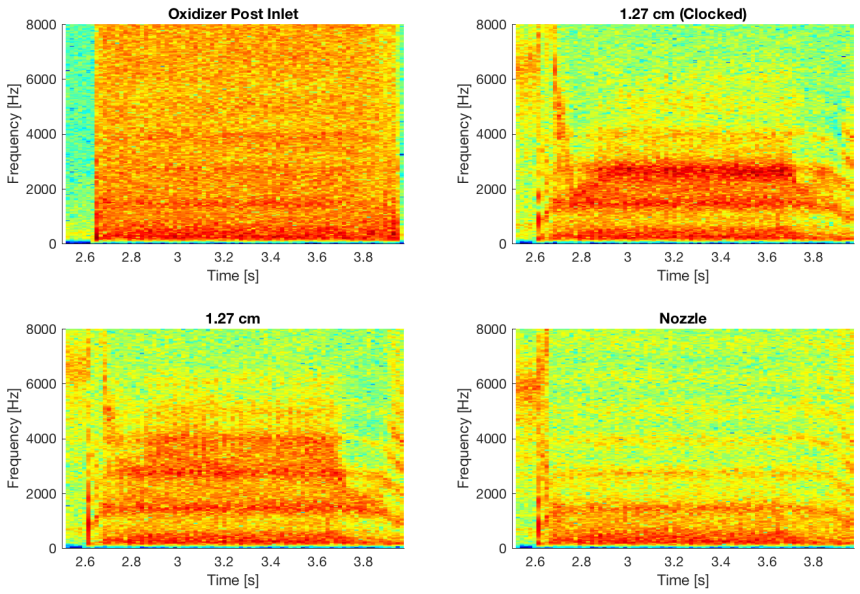

Figure E.2.: Spectrograms for the oxidizer post inlet (top-left), 1.27 cm (Clocked) location (top-right), 1.27 cm location (bottom-left), and chamber (bottom-right) for hot oxidizer Test 356 ($L/\lambda = 0.41$), grouped by location.

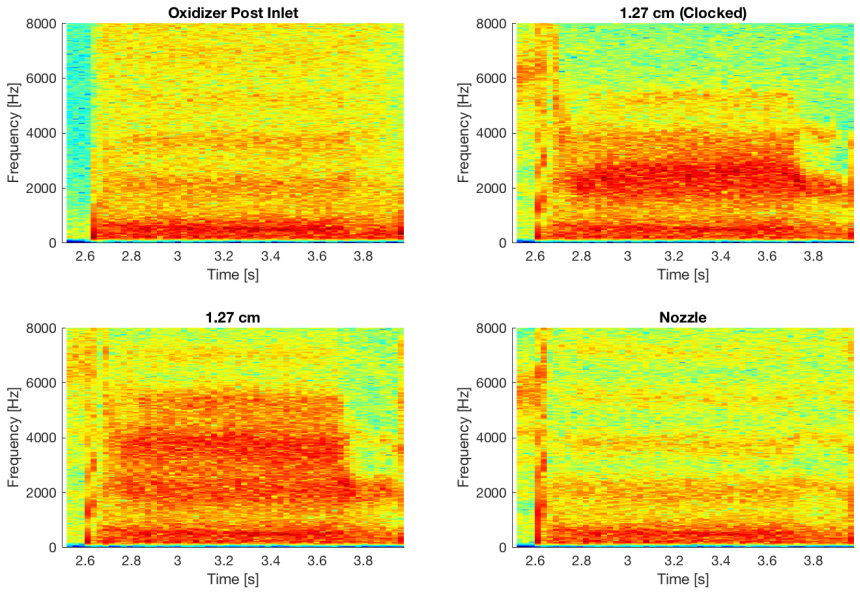

Figure E.3.: Spectrograms for the oxidizer post inlet (top-left), 1.27 cm (Clocked) location (top-right), 1.27 cm location (bottom-left), and chamber (bottom-right) for hot oxidizer Test 307 ($L/\lambda = 0.65$), grouped by location.

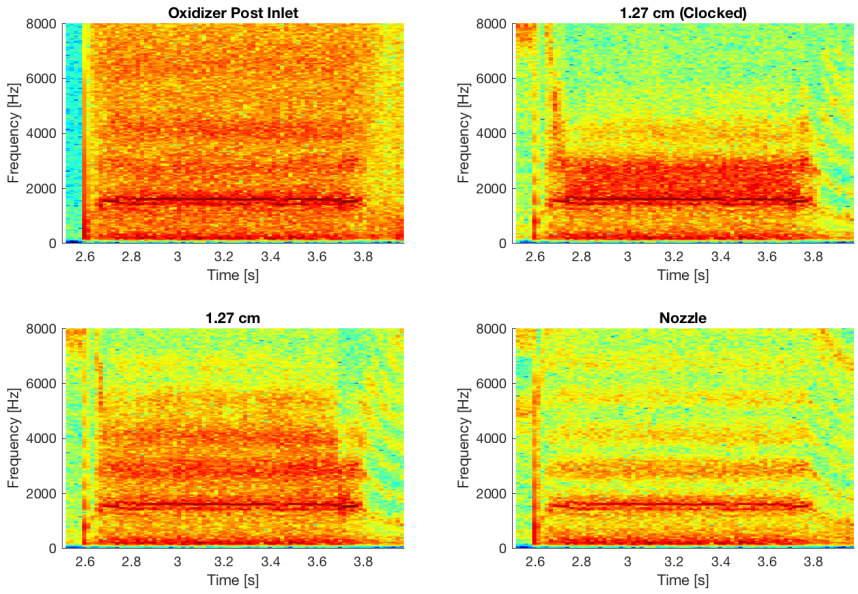

Figure E.4.: Spectrograms for the oxidizer post inlet (top-left), 1.27 cm (Clocked) location (top-right), 1.27 cm location (bottom-left), and chamber (bottom-right) for ambient oxidizer Test 368 ($L/\lambda = 0.26$), grouped by location.

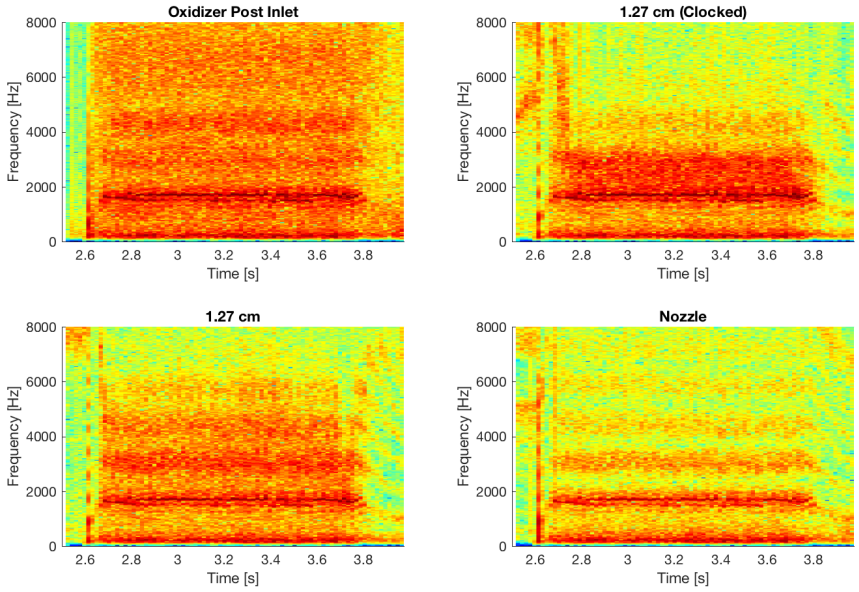

Figure E.5.: Spectrograms for the oxidizer post inlet (top-left), 1.27 cm (Clocked) location (top-right), 1.27 cm location (bottom-left), and chamber (bottom-right) for ambient oxidizer Test 367 ($L/\lambda = 0.28$), grouped by location.

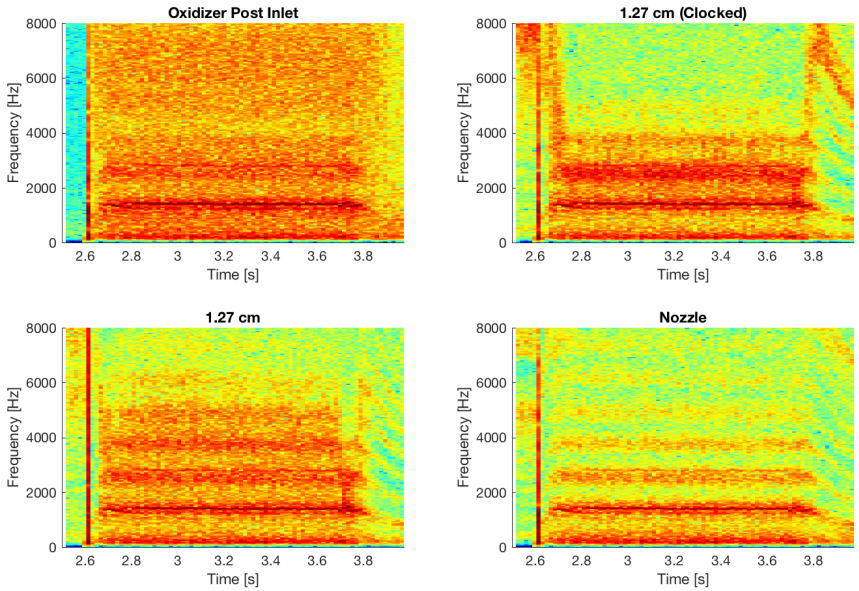

Figure E.6.: Spectrograms for the oxidizer post inlet (top-left), 1.27 cm (Clocked) location (top-right), 1.27 cm location (bottom-left), and chamber (bottom-right) for ambient oxidizer Test 362 ($L/\lambda = 0.32$), grouped by location.

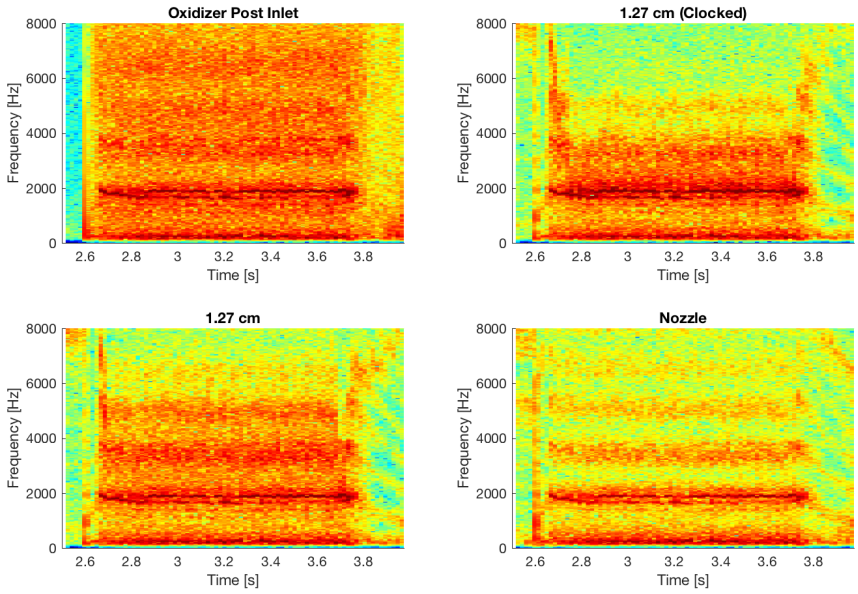

Figure E.7.: Spectrograms for the oxidizer post inlet (top-left), 1.27 cm (Clocked) location (top-right), 1.27 cm location (bottom-left), and chamber (bottom-right) for ambient oxidizer Test 371 ($L/\lambda = 0.33$), grouped by location.

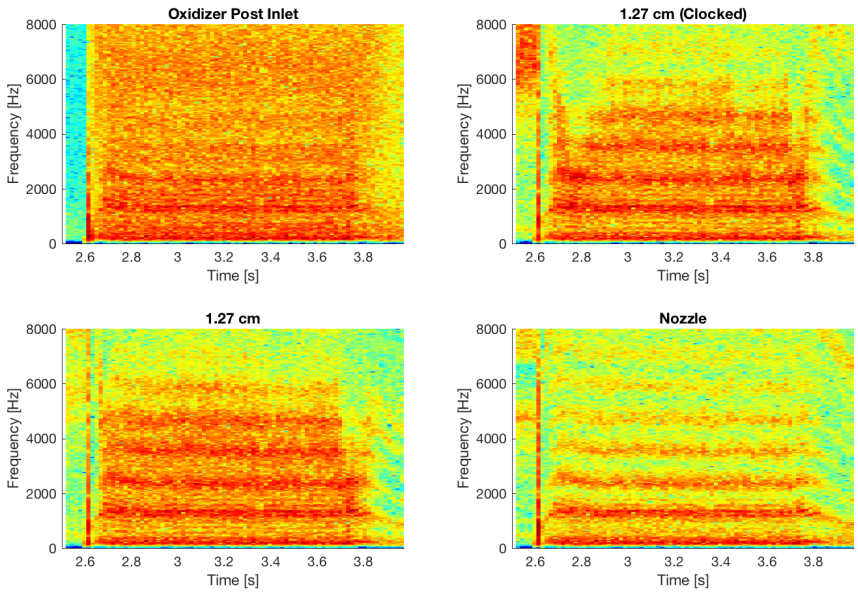

Figure E.8.: Spectrograms for the oxidizer post inlet (top-left), 1.27 cm (Clocked) location (top-right), 1.27 cm location (bottom-left), and chamber (bottom-right) for ambient oxidizer Test 358 ($L/\lambda = 0.54$), grouped by location.

F. CONTINUOUS WAVELET TRANSFORM RESULTS

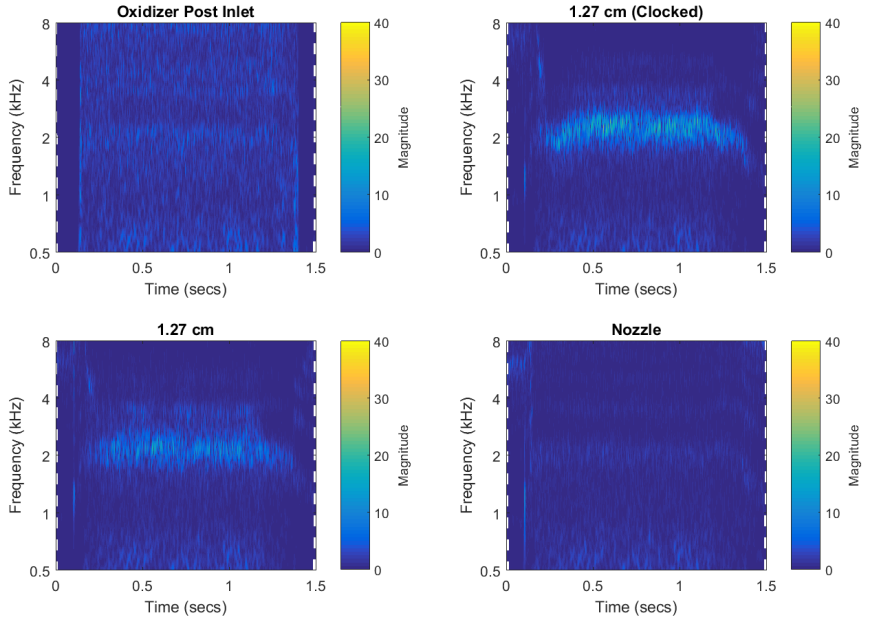

Figure F.1.: Continuous wavelet transforms for the oxidizer post inlet (top-left), 1.27 cm (Clocked) location (top-right), 1.27 cm location (bottom-left), and chamber (bottom-right) for hot oxidizer Test 365 ($L/\lambda = 0.28$), grouped by location.

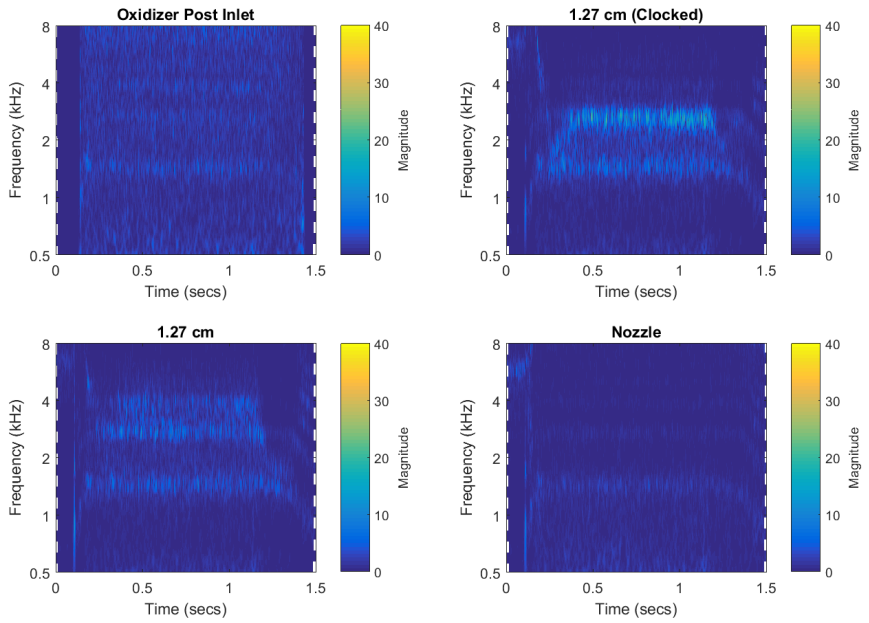

Figure F.2.: Continuous wavelet transforms for the oxidizer post inlet (top-left), 1.27 cm (Clocked) location (top-right), 1.27 cm location (bottom-left), and chamber (bottom-right) for hot oxidizer Test 356 ($L/\lambda = 0.41$), grouped by location.

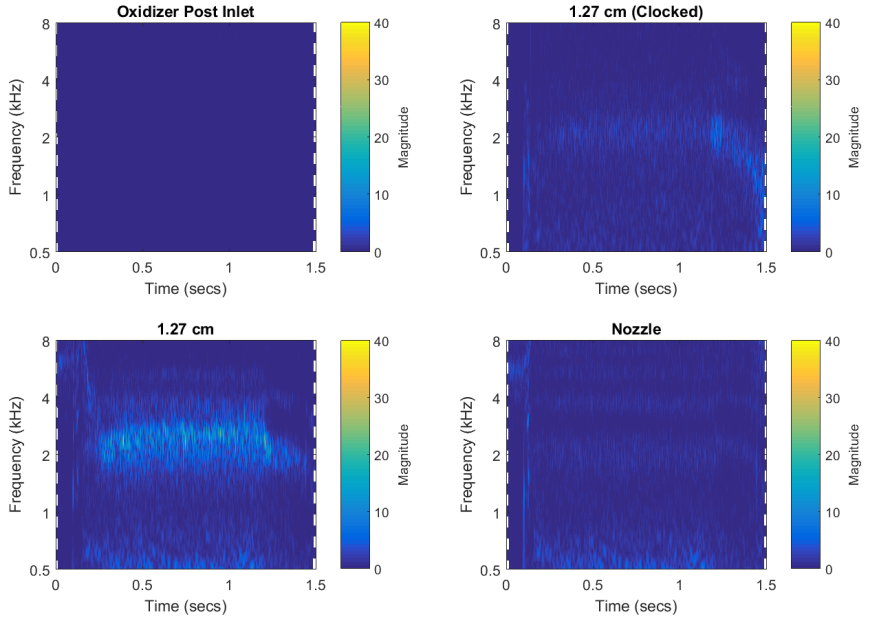

Figure F.3.: Continuous wavelet transforms for the oxidizer post inlet (top-left), 1.27 cm (Clocked) location (top-right), 1.27 cm location (bottom-left), and chamber (bottom-right) for hot oxidizer Test 307 ($L/\lambda = 0.65$), grouped by location.

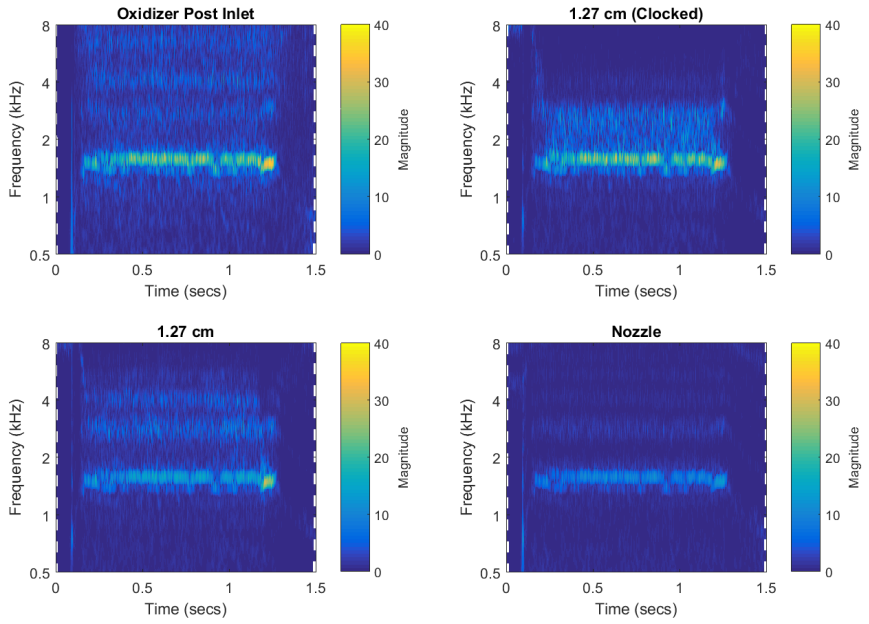

Figure F.4.: Continuous wavelet transforms for the oxidizer post inlet (top-left), 1.27 cm (Clocked) location (top-right), 1.27 cm location (bottom-left), and chamber (bottom-right) for ambient oxidizer Test 368 ($L/\lambda = 0.26$), grouped by location.

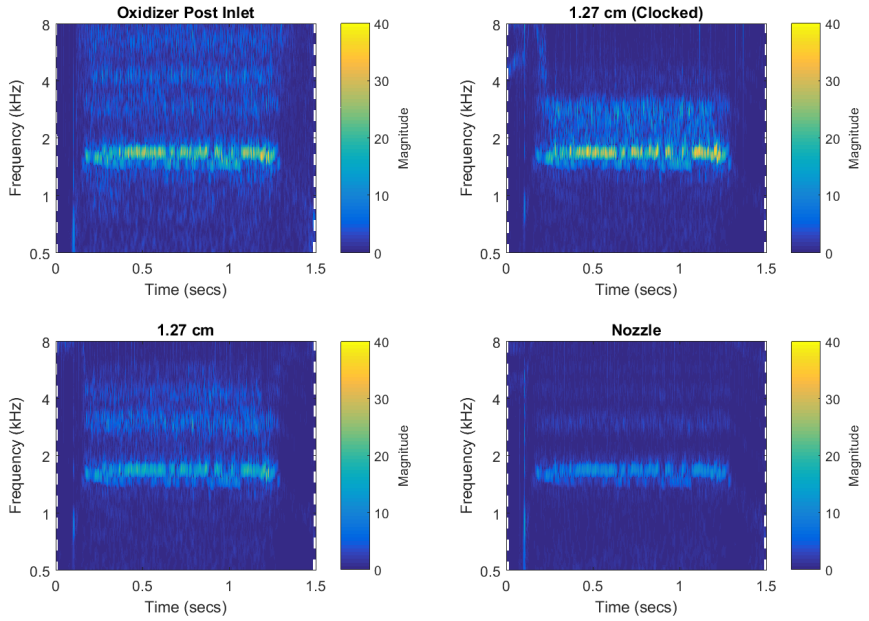

Figure F.5.: Continuous wavelet transforms for the oxidizer post inlet (top-left), 1.27 cm (Clocked) location (top-right), 1.27 cm location (bottom-left), and chamber (bottom-right) for ambient oxidizer Test 367 ($L/\lambda = 0.28$), grouped by location.

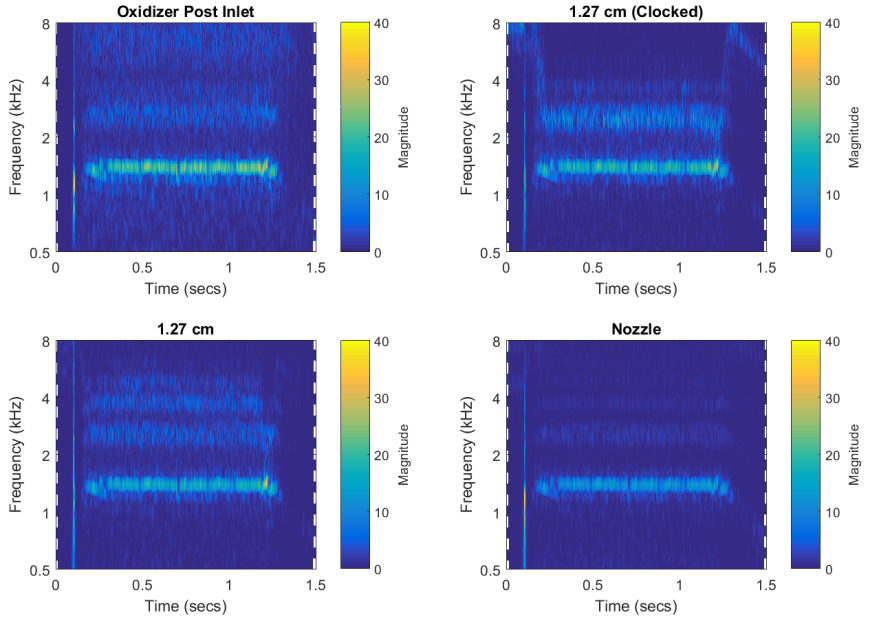

Figure F.6.: Continuous wavelet transforms for the oxidizer post inlet (top-left), 1.27 cm (Clocked) location (top-right), 1.27 cm location (bottom-left), and chamber (bottom-right) for ambient oxidizer Test 362 ($L/\lambda = 0.32$), grouped by location.

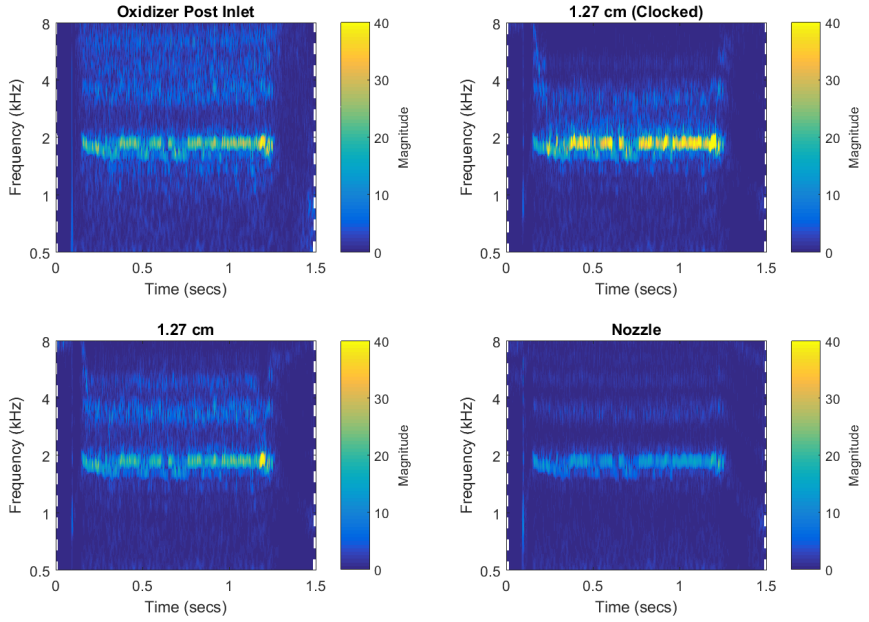

Figure F.7.: Continuous wavelet transforms for the oxidizer post inlet (top-left), 1.27 cm (Clocked) location (top-right), 1.27 cm location (bottom-left), and chamber (bottom-right) for ambient oxidizer Test 371 ($L/\lambda = 0.33$), grouped by location.

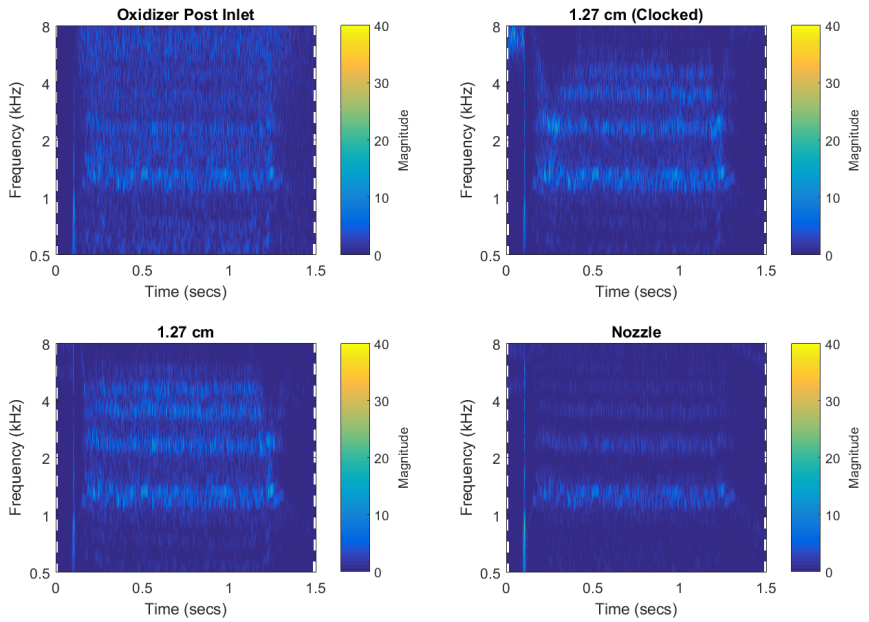

Figure F.8.: Continuous wavelet transforms for the oxidizer post inlet (top-left), 1.27 cm (Clocked) location (top-right), 1.27 cm location (bottom-left), and chamber (bottom-right) for ambient oxidizer Test 358 ($L/\lambda = 0.54$), grouped by location.

G. TEST ARTICLE DRAWINGS

REVISIONS				
ZONE	REV.	DESCRIPTION	DATE	APPROVED

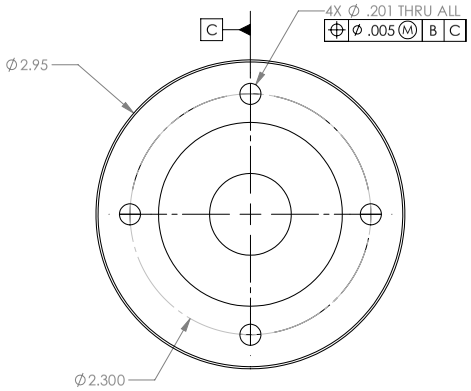

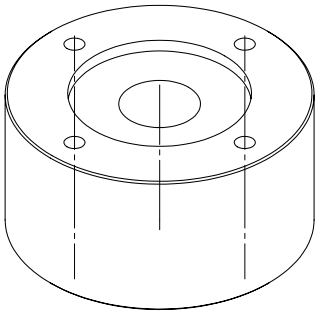

1. DEBURR HOLES
2. BREAK SHARP EDGES
3. PART SHALL BE FREE OF OIL, GREASE, SCALE, AND CHIPS

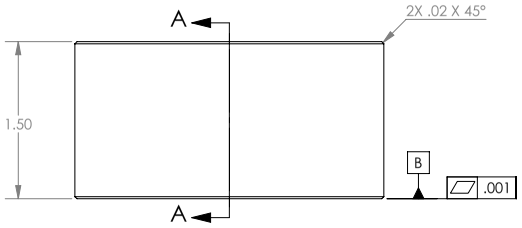

SECTION A-A

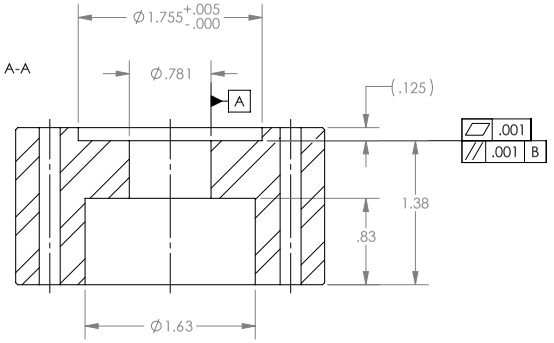

		NAME	DATE
DRAWN		BJA	01/09/17
CHECKED			
ENG APPR.			
M.FG APPR.			
Q.A.			
COMMENTS:			

UNLESS OTHERWISE SPECIFIED:

DIMENSIONS ARE IN INCHES
TOLERANCES:
FRACTIONAL ±1/64
ANGULAR: MACH ±1° BEND ±3°
TWO PLACE DECIMAL ±.005
THREE PLACE DECIMAL ±.003

INTERPRET GEOMETRIC TOLERANCING PER:

MATERIAL
AISI 304

FINISH

DO NOT SCALE DRAWING

IN Space, LLC

TITLE:
HYDRAULIC RAM INTERFACE
DVRC PREBUNER 030

SIZE	DWG. NO.	REV
B		

SCALE: 1:1 | WEIGHT: 2.25 | SHEET 1 OF 1

Printed: Tuesday, January 10, 2017

REVISIONS				
ZONE	REV.	DESCRIPTION	DATE	APPROVED

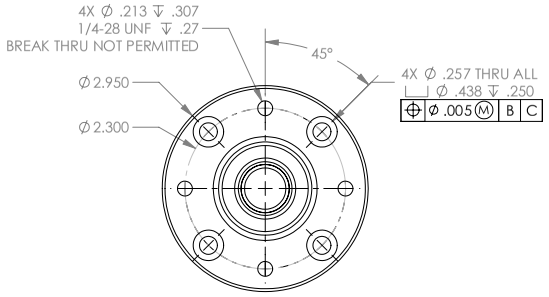

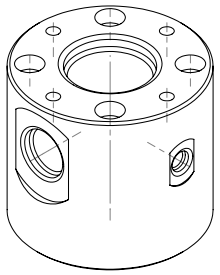

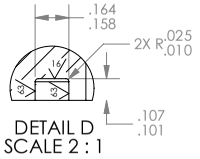

DETAIL D
SCALE 2 : 1

1. DEBURR HOLES
2. BREAK SHARP EDGES
3. PART SHALL BE FREE OF OIL, GREASE, SCALE, AND CHIPS
4. PROTECT SPECIFIED SURFACE FINISHES IN ALL PROCESSES

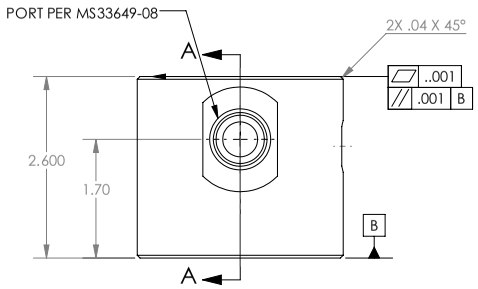

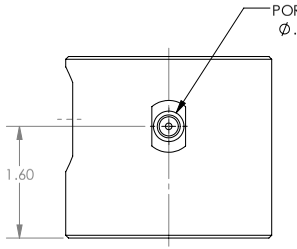

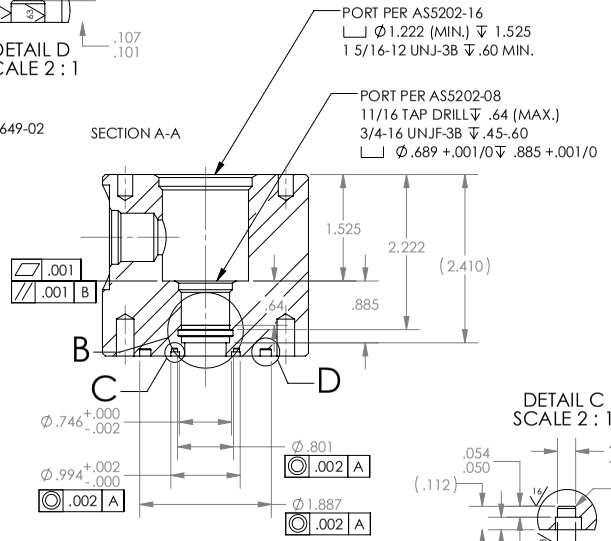

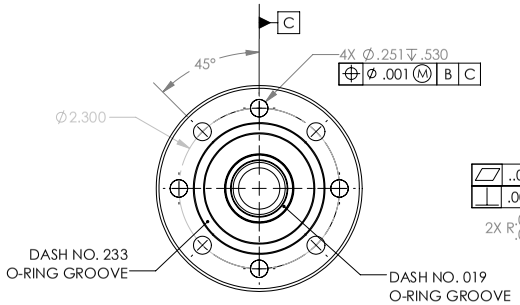

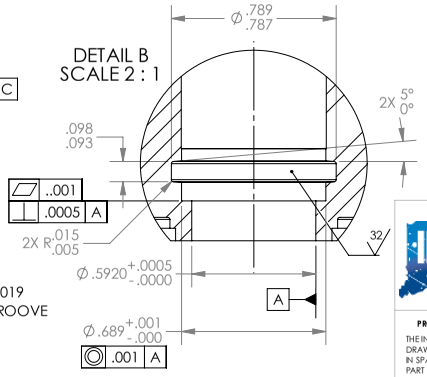

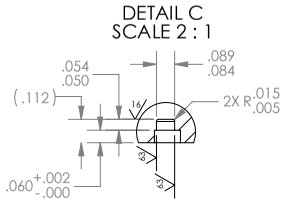

UNLESS OTHERWISE SPECIFIED:
DIMENSIONS ARE IN INCHES
TOLERANCES:
FRACTIONAL ±1/64
ANGULAR: MACH ±1° BEND ±3°
TWO PLACE DECIMAL ±.005
THREE PLACE DECIMAL ±.003
INTERPRET GEOMETRIC TOLERANCING PER:
MATERIAL: Monel 400
FINISH
DO NOT SCALE DRAWING

	NAME	DATE
DRAWN	BJA	12/16/16
CHECKED		
ENG APPR.		
MFG APPR.		
Q.A.		
COMMENTS:		

IN Space, LLC

TITLE:
OXIDIZER INJECTOR SEAT, RIGHT ANGLE INLET, PREBURNER 030

SIZE	DWG. NO.	REV
B	INS-PB030-OH2P-1161	

SCALE: 2:3 | WEIGHT: 0.45 | SHEET 1 OF 1

Printed: Tuesday, December 20, 2016

REVISIONS				
ZONE	REV.	DESCRIPTION	DATE	APPROVED

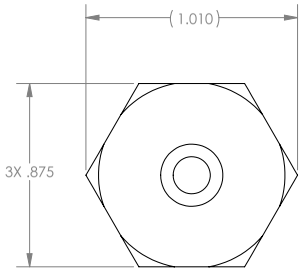

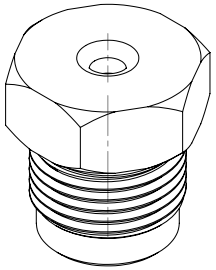

1. DEBURR HOLES
2. BREAK SHARP EDGES
3. PART SHALL BE FREE OF OIL, GREASE, SCALE, AND CHIPS
4. PROTECT SPECIFIED SURFACE FINISHES IN ALL PROCESSES

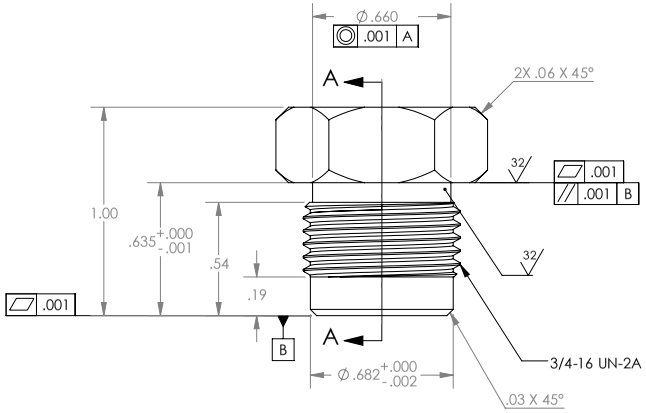

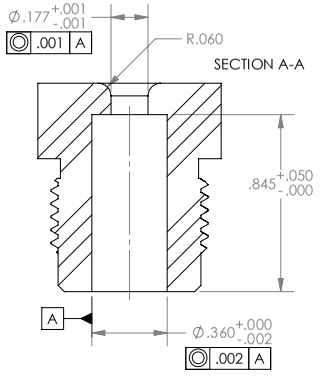

Printed: Tuesday, December 20, 2016

UNLESS OTHERWISE SPECIFIED:
DIMENSIONS ARE IN INCHES
TOLERANCES:
FRACTIONAL ±1/64
ANGULAR: MACH ±1° BEND ±3°
TWO PLACE DECIMAL ±.005
THREE PLACE DECIMAL ±.003
INTERPRET GEOMETRIC TOLERANCING PER:
MATERIAL: Inconel 600
FINISH:
DO NOT SCALE DRAWING

	NAME	DATE
DRAWN	BJA	12/16/16
CHECKED		
ENG APPR.		
MFG APPR.		
Q.A.		
COMMENTS:		

IN Space, LLC

TITLE:
OXIDIZER INJECTOR INLET, SINGLE INLET, D=0.177-IN, PREBURNER 030

SIZE	DWG. NO.	REV
B	INS-PB030-OH2P-1162	

SCALE: 2:1 | WEIGHT: 0.12 | SHEET 1 OF 1

REVISIONS				
ZONE	REV.	DESCRIPTION	DATE	APPROVED

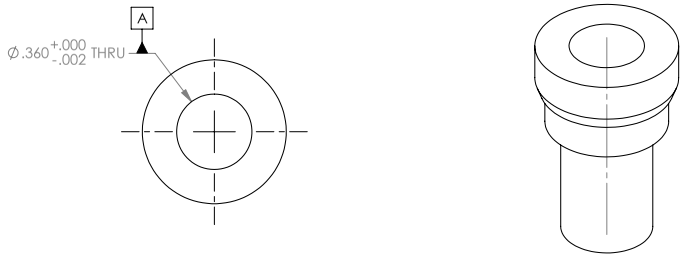

1. DEBURR HOLES
2. BREAK SHARP EDGES
3. PART SHALL BE FREE OF OIL, GREASE, SCALE, AND CHIPS
4. PROTECT SPECIFIED SURFACE FINISHES IN ALL PROCESSES

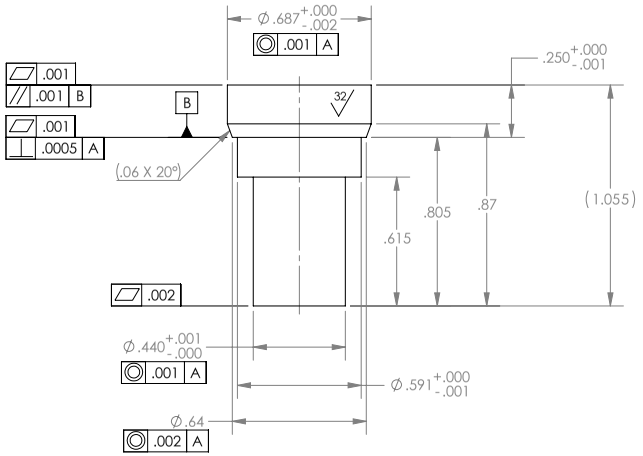

		NAME	DATE
UNLESS OTHERWISE SPECIFIED:	DRAWN	BJA	12/18/16
DIMENSIONS ARE IN INCHES TOLERANCES: FRACTIONAL ±1/64 ANGULAR: MACH ±1° BEND ±3° TWO PLACE DECIMAL ±.005 THREE PLACE DECIMAL ±.003	CHECKED		
	ENG APPR.		
	MFG APPR.		
INTERPRET GEOMETRIC TOLERANCING PER:	Q.A.		
MATERIAL: Inconel 600	COMMENTS:		
FINISH			
DO NOT SCALE DRAWING			

IN Space, LLC

TITLE: OXIDIZER INJECTOR POST V2.2, PREBURNER 030

SIZE	DWG. NO.	REV
B	INS-PB030-OH2P-1172	

SCALE: 2:1 | WEIGHT: 0.04 | SHEET 1 OF 1

Printed: Tuesday, December 20, 2016

REVISIONS				
ZONE	REV.	DESCRIPTION	DATE	APPROVED

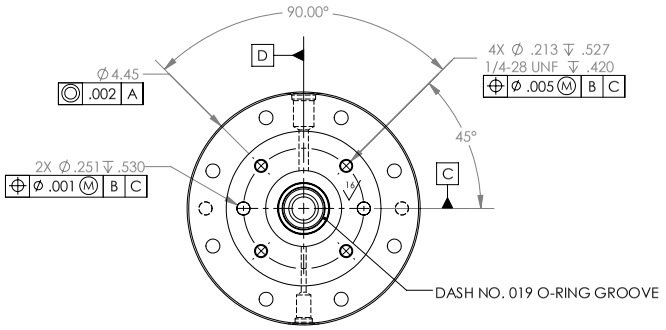

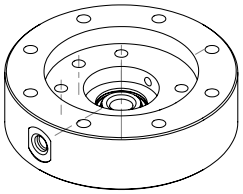

1. DEBURR HOLES
2. BREAK SHARP EDGES
3. PART SHALL BE FREE OF OIL, GREASE, SCALE, AND CHIPS
4. PROTECT SPECIFIED SURFACE FINISHES IN ALL PROCESSES

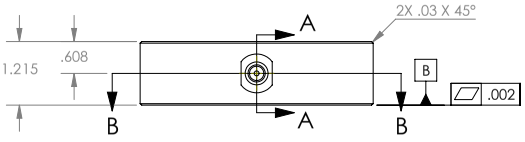

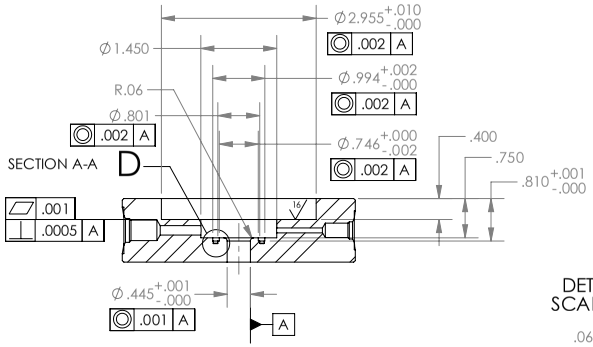

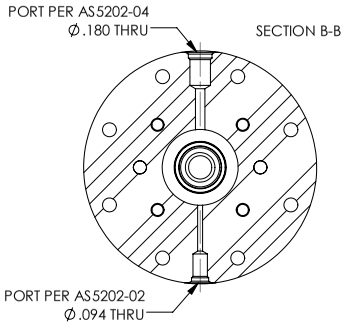

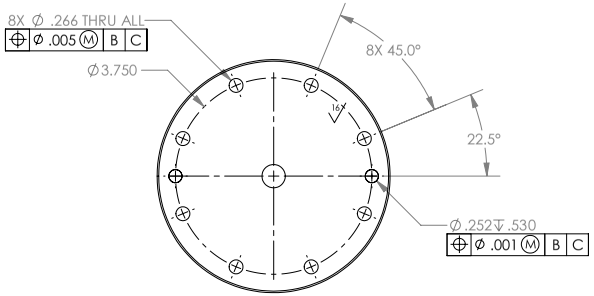

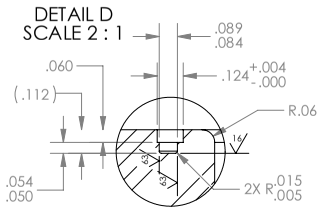

UNLESS OTHERWISE SPECIFIED:		NAME	DATE
DIMENSIONS ARE IN INCHES TOLERANCES: FRACTIONAL ±1/64 ANGULAR: MACH ±1° BEND ±3° TWO PLACE DECIMAL ±.005 THREE PLACE DECIMAL ±.003	DRAWN	BJA	12/16/16
	CHECKED		
	ENG APPR.		
	MFG APPR.		
INTERPRET GEOMETRIC TOLERANCING PER:	Q.A.		
MATERIAL: Inconel 600	COMMENTS:		
FINISH			
DO NOT SCALE DRAWING			

IN Space, LLC

TITLE: FUEL INJECTOR SEAT V2, PREBURNER 030

SIZE	DWG. NO.	REV
B	INS-PB030-OH2P-1112	-

SCALE: 1:2 | WEIGHT: 4.42 | SHEET 1 OF 1

Printed: Tuesday, December 20, 2016

REVISIONS				
ZONE	REV.	DESCRIPTION	DATE	APPROVED

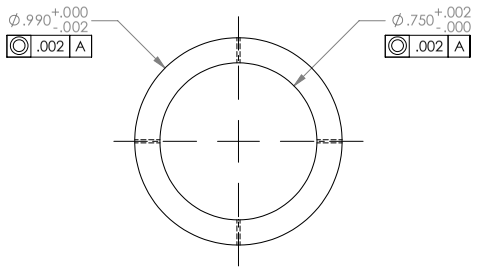

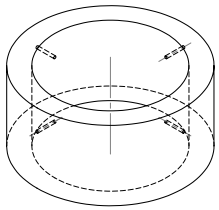

1. DEBURR HOLES
2. BREAK SHARP EDGES
3. PART SHALL BE FREE OF OIL, GREASE, SCALE, AND CHIPS
4. PROTECT SPECIFIED SURFACE FINISHES IN ALL PROCESSES

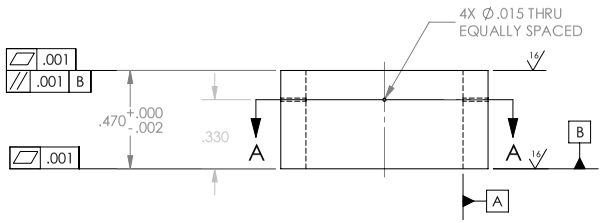

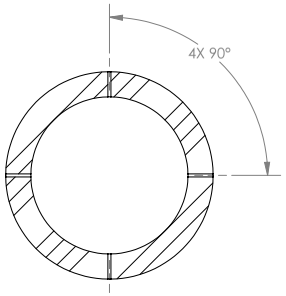

SECTION A-A

Printed: Tuesday, December 20, 2016

UNLESS OTHERWISE SPECIFIED:		NAME	DATE
DIMENSIONS ARE IN INCHES TOLERANCES: FRACTIONAL ±1/64 ANGULAR: MACH ±1° BEND ±3° TWO PLACE DECIMAL ±.005 THREE PLACE DECIMAL ±.003	DRAWN	BJA	12/16/16
	CHECKED		
	ENG APPR.		
	MFG APPR.		
INTERPRET GEOMETRIC TOLERANCING PER:	Q.A.		
MATERIAL: Inconel 600	COMMENTS:		
FINISH			
DO NOT SCALE DRAWING			

IN Space, LLC

TITLE: FUEL INJECTOR INLET V2.2, PREBURNER 030

SIZE	DWG. NO.	REV
B	INS-PB030-OH2P-1122	

SCALE: 2:1 | WEIGHT: 0.05 | SHEET 1 OF 1

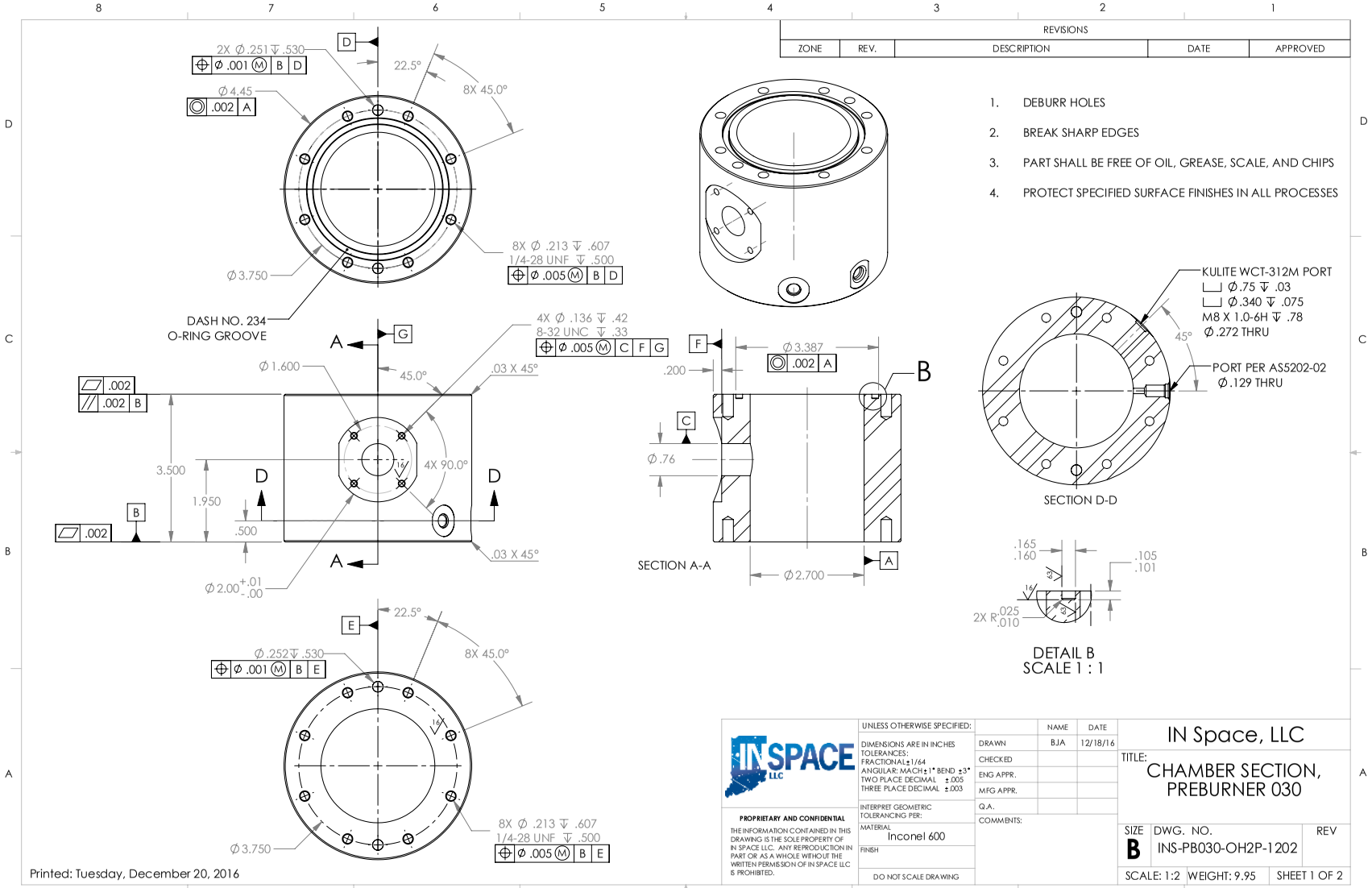
REVISIONS
ZONE | REV. | DESCRIPTION | DATE | APPROVED
1. DEBURR HOLES
2. BREAK SHARP EDGES
3. PART SHALL BE FREE OF OIL, GREASE, SCALE, AND CHIPS
4. PROTECT SPECIFIED SURFACE FINISHES IN ALL PROCESSES
2X Ø.251↧.530
Ø .001 M B D
22.5°
8X 45.0°
Ø4.45
.002 A
8X Ø .213 ↧ .607
1/4-28 UNF ↧ .500
Ø .005 M B D
Ø3.750
DASH NO. 234
O-RING GROOVE
4X Ø .136 ↧ .42
8-32 UNC ↧ .33
Ø .005 M C F G
Ø1.600
45.0°
.03 X 45°
.002
.002 B
3.500
1.950
.500
4X 90.0°
.002 B
Ø2.00 +.01 -.00
SECTION A-A
Ø3.387
.002 A
.200
Ø.76
Ø2.700
KULITE WCT-312M PORT
⌴ Ø.75 ↧ .03
⌴ Ø.340 ↧ .075
M8 X 1.0-6H ↧ .78
Ø.272 THRU
45°
PORT PER AS5202-02
Ø.129 THRU
SECTION D-D
.165
.160
.105
.101
2X R .025 .010
DETAIL B
SCALE 1 : 1
22.5°
8X 45.0°
Ø.252↧.530
Ø .001 M B E
8X Ø .213 ↧ .607
1/4-28 UNF ↧ .500
Ø .005 M B E
Printed: Tuesday, December 20, 2016
IN SPACE LLC
UNLESS OTHERWISE SPECIFIED:
DIMENSIONS ARE IN INCHES
TOLERANCES:
FRACTIONAL ±1/64
ANGULAR: MACH ±1° BEND ±3°
TWO PLACE DECIMAL ±.005
THREE PLACE DECIMAL ±.003
INTERPRET GEOMETRIC TOLERANCING PER:
MATERIAL Inconel 600
FINISH
DO NOT SCALE DRAWING
NAME DATE
DRAWN BJA 12/18/16
CHECKED
ENG APPR.
M.FG APPR.
Q.A.
COMMENTS:
PROPRIETARY AND CONFIDENTIAL
THE INFORMATION CONTAINED IN THIS DRAWING IS THE SOLE PROPERTY OF IN SPACE LLC. ANY REPRODUCTION IN PART OR AS A WHOLE WITHOUT THE WRITTEN PERMISSION OF IN SPACE LLC IS PROHIBITED.
IN Space, LLC
TITLE:
CHAMBER SECTION, PREBURNER 030
SIZE B
DWG. NO. INS-PB030-OH2P-1202
REV
SCALE: 1:2 WEIGHT: 9.95 SHEET 1 OF 2

REVISIONS				
ZONE	REV.	DESCRIPTION	DATE	APPROVED

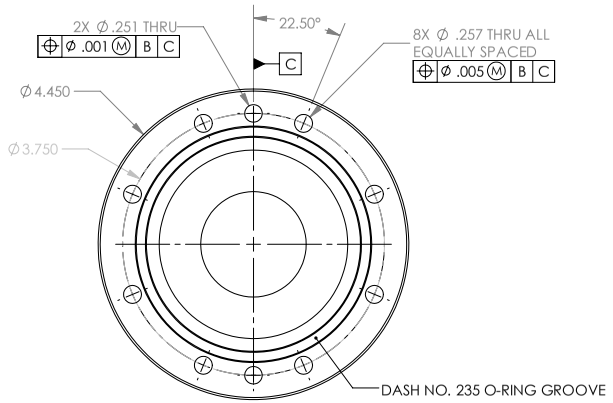

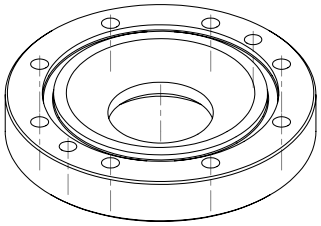

1. DEBURR HOLES
2. BREAK SHARP EDGES
3. PART SHALL BE FREE OF OIL, GREASE, SCALE, AND CHIPS
4. PROTECT SPECIFIED SURFACE FINISHES IN ALL PROCESSES

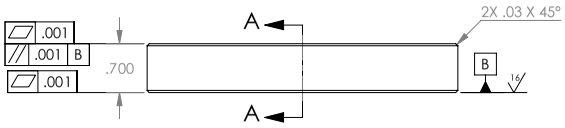

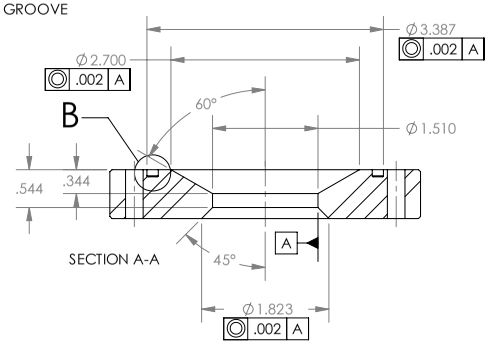

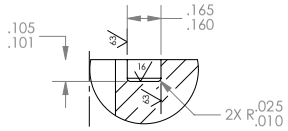

DETAIL B
SCALE 2 : 1

UNLESS OTHERWISE SPECIFIED:		NAME	DATE
DIMENSIONS ARE IN INCHES TOLERANCES: FRACTIONAL ±1/64 ANGULAR: MACH ±1° BEND ±3° TWO PLACE DECIMAL ±.005 THREE PLACE DECIMAL ±.003	DRAWN	BJA	12/19/16
	CHECKED		
	ENG APPR.		
	MFG APPR.		
	Q.A.		
	COMMENTS:		
INTERPRET GEOMETRIC TOLERANCING PER:			
MATERIAL: Inconel 600			
FINISH			
DO NOT SCALE DRAWING			

IN Space, LLC

TITLE: TURBULENCE RING, D = 1.51-IN, PREBURNER 030

SIZE	DWG. NO.	REV
B	INS-PB030-OH2P-1221	

SCALE: 2:3 | WEIGHT: 2.56 | SHEET 1 OF 1

Printed: Tuesday, January 03, 2017

REVISIONS				
ZONE	REV.	DESCRIPTION	DATE	APPROVED

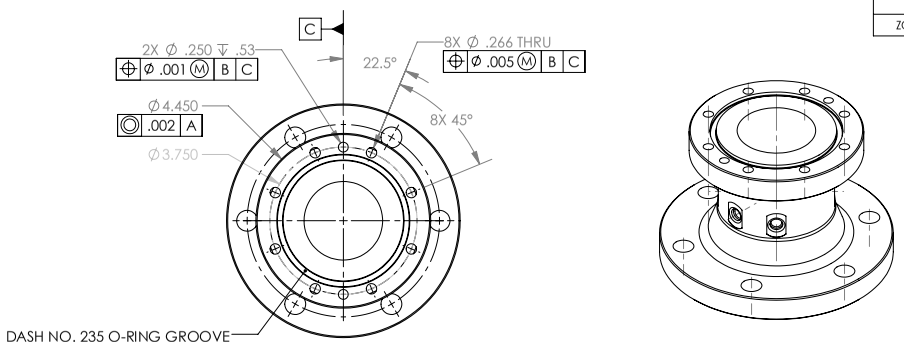

1. DEBURR HOLES
2. BREAK SHARP EDGES
3. PART SHALL BE FREE OF OIL, GREASE, SCALE, AND CHIPS
4. PROTECT SPECIFIED SURFACE FINISHES IN ALL PROCESSES

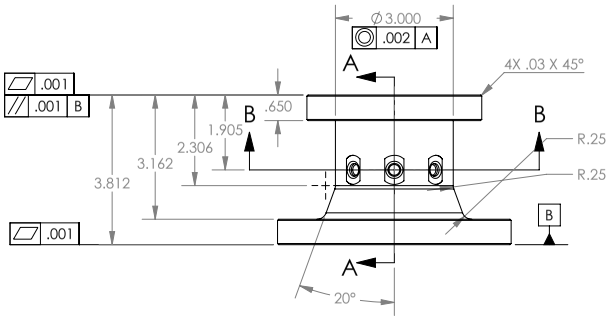

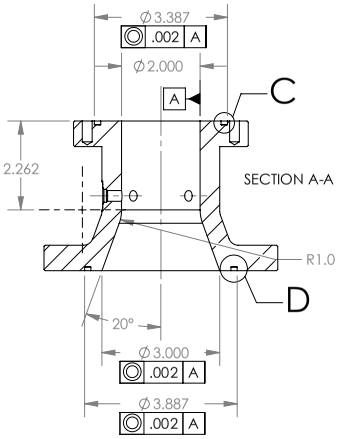

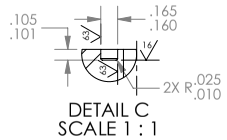

DETAIL C
SCALE 1 : 1

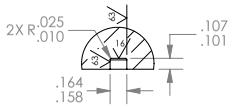

DETAIL D
SCALE 1 : 1

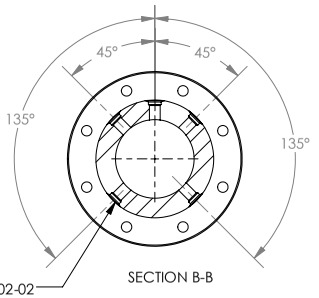

SECTION B-B

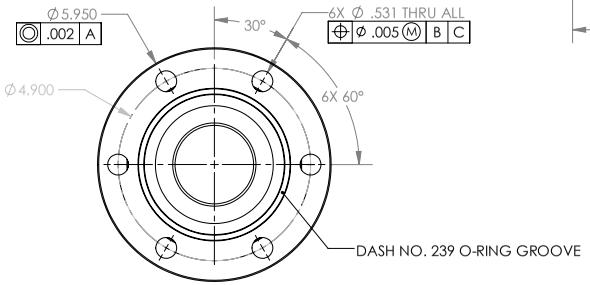

Printed: Tuesday, January 03, 2017

UNLESS OTHERWISE SPECIFIED:		NAME	DATE
DIMENSIONS ARE IN INCHES	DRAWN	BJA	12/19/16
TOLERANCES: FRACTIONAL ±1/64 ANGULAR: MACH ±1° BEND ±3° TWO PLACE DECIMAL ±.005 THREE PLACE DECIMAL ±.003	CHECKED		
	ENG APPR.		
	MFG APPR.		
INTERPRET GEOMETRIC TOLERANCING PER:	Q.A.		
MATERIAL: Inconel 600	COMMENTS:		
FINISH			
DO NOT SCALE DRAWING			

IN Space, LLC

TITLE: PREBURNER 030 DVRC INTERFACE

SIZE	DWG. NO.	REV
B	INS-PB030-OH2P-1303	

SCALE: 3:8 | WEIGHT: 9.40 | SHEET 1 OF 1

ITEM NO.	PART NUMBER	DESCRIPTION	QTY.
1	INS-41402-DVRC-1111	DVRC-2 OXIDIZER MANIFOLD INLET	1
2	INS-41402-DVRC-1121	DVRC-2 OXIDIZER MANIFOLD INLET PLATE	1
3	INS-41402-DVRC-1131	DVRC-2 OXIDIZER MANIFOLD, TYPE 2	1
4	MMC 97365A120	1/4 IN DIAM, 1 IN LENGTH DOWEL PIN	2
5	MMC 91950A033	1/2 IN SAE FLAT WASHER, TYPE 316 STAINLESS	6
6	MMC 93827A245	1/2-13 HEX NUT, ZINC ALUMINUM COATED STEEL	6
7	MMC 91251A122	1/2-13, 8.5 IN LENGTH, SOCKET HEAD CAP SCREW, BLACK OXIDE ALLOY STEEL	6

REVISIONS				
ZONE	REV.	DESCRIPTION	DATE	APPROVED

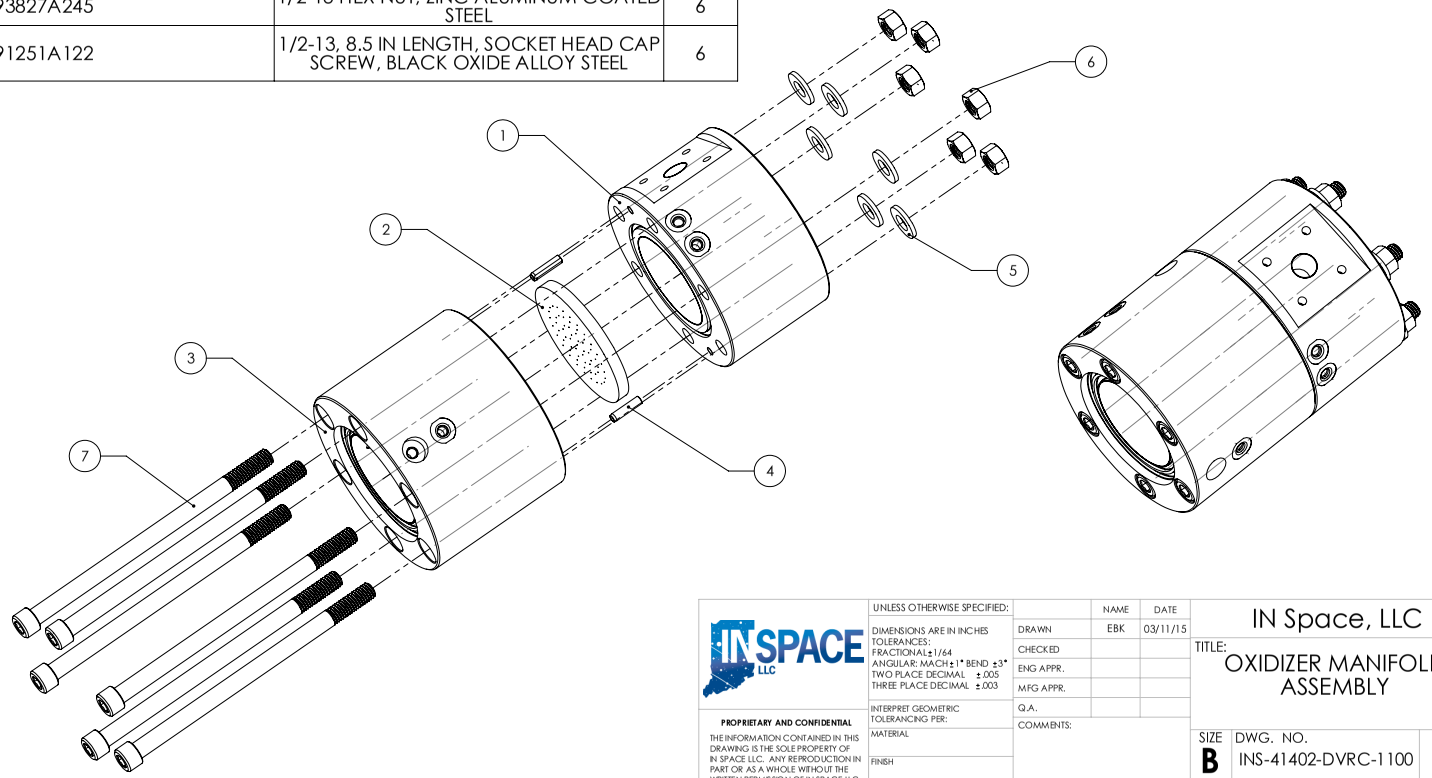

Printed: Wednesday, March 18, 2015

UNLESS OTHERWISE SPECIFIED:
DIMENSIONS ARE IN INCHES
TOLERANCES:
FRACTIONAL ±1/64
ANGULAR: MACH ±1° BEND ±3°
TWO PLACE DECIMAL ±.005
THREE PLACE DECIMAL ±.003
INTERPRET GEOMETRIC TOLERANCING PER:
MATERIAL
FINISH
DO NOT SCALE DRAWING

	NAME	DATE
DRAWN	EBK	03/11/15
CHECKED		
ENG APPR.		
MFG APPR.		
Q.A.		
COMMENTS:		

IN Space, LLC

TITLE: OXIDIZER MANIFOLD ASSEMBLY

SIZE	DWG. NO.	REV
B	INS-41402-DVRC-1100	

SCALE: 1:3 | WEIGHT: | SHEET 1 OF 1

REVISIONS				
ZONE	REV.	DESCRIPTION	DATE	APPROVED

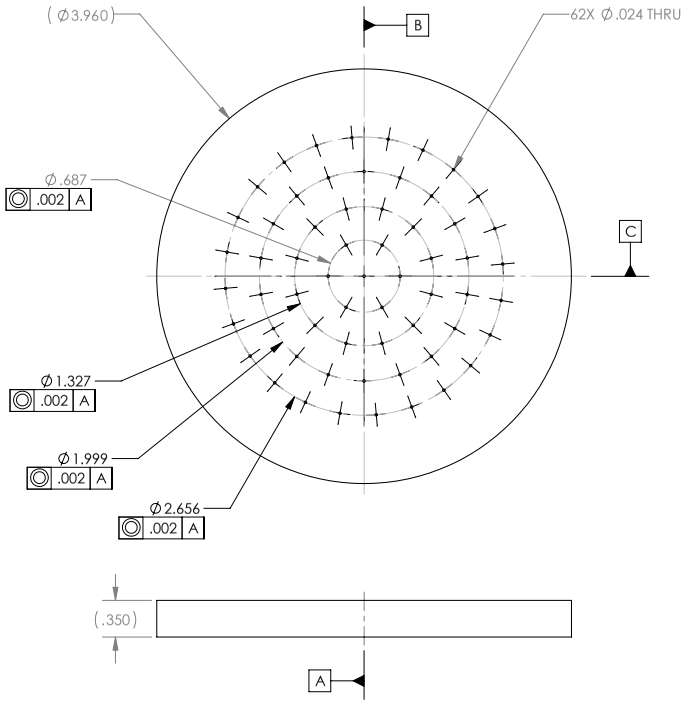

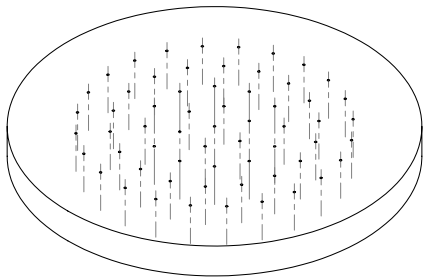

Printed: Thursday, March 12, 2015

PROPRIETARY AND CONFIDENTIAL

THE INFORMATION CONTAINED IN THIS DRAWING IS THE SOLE PROPERTY OF IN SPACE LLC. ANY REPRODUCTION IN PART OR AS A WHOLE WITHOUT THE WRITTEN PERMISSION OF IN SPACE LLC IS PROHIBITED.

UNLESS OTHERWISE SPECIFIED:

DIMENSIONS ARE IN INCHES
TOLERANCES:
FRACTIONAL ±1/64
ANGULAR: MACH ±1° BEND ±3°
TWO PLACE DECIMAL ±.005
THREE PLACE DECIMAL ±.003

INTERPRET GEOMETRIC TOLERANCING PER:

MATERIAL: INCONEL 600

FINISH

DO NOT SCALE DRAWING

	NAME	DATE
DRAWN	EBK	03/11/15
CHECKED		
ENG APPR.		
MFG APPR.		
Q.A.		

COMMENTS:

IN Space, LLC

TITLE: DVRC-2 OXIDIZER MANIFOLD INLET PLATE, EDM

SIZE	DWG. NO.	REV
B	INS-41402-DVRC-1121	

SCALE: 1:2 | WEIGHT: 1.31 | SHEET 1 OF 1

REVISIONS				
ZONE	REV.	DESCRIPTION	DATE	APPROVED

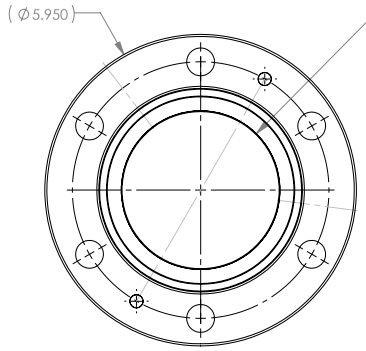

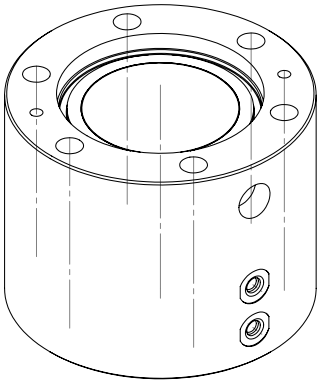

1. ALL SURFACES OTHER THAN CENTRAL INNER DIAMETER TO BE FREE OF TBC
2. THRU HOLES TO BE OPEN AFTER TBC APPLICATION

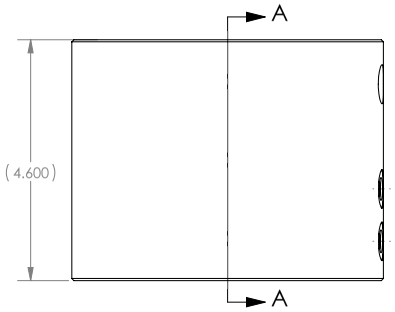

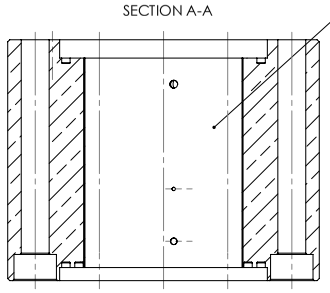

Printed: Friday, March 13, 2015

IN SPACE LLC

PROPRIETARY AND CONFIDENTIAL

THE INFORMATION CONTAINED IN THIS DRAWING IS THE SOLE PROPERTY OF IN SPACE LLC. ANY REPRODUCTION IN PART OR AS A WHOLE WITHOUT THE WRITTEN PERMISSION OF IN SPACE LLC IS PROHIBITED.

UNLESS OTHERWISE SPECIFIED:

DIMENSIONS ARE IN INCHES
TOLERANCES:
FRACTIONAL ±1/64
ANGULAR: MACH ±1° BEND ±3°
TWO PLACE DECIMAL ±.005
THREE PLACE DECIMAL ±.003

INTERPRET GEOMETRIC TOLERANCING PER:

MATERIAL: COPPER

FINISH

DO NOT SCALE DRAWING

	NAME	DATE
DRAWN	EBK	03/10/15
CHECKED	BJA	03/13/15
ENG APPR.		
M.FG APPR.		
Q.A.		

COMMENTS:

IN Space, LLC

TITLE: DVRC-2 OXIDIZER MANIFOLD, TYPE 2, TBC APPLICATION

SIZE	DWG. NO.	REV
B	INS-41402-DVRC-1131	

SCALE: 1:2 | WEIGHT: 26.89 | SHEET 1 OF 1

ITEM NO.	PART NUMBER	DESCRIPTION	QTY.
1	INS-41402-DVRC-1211	INJECTOR OXIDIZER POST AND INLET	1
2	INS-41402-DVRC-1251	INJECTOR OXIDIZER POST COLLAR	1
3	INS-41402-DVRC-1263	DVRC-2 INJECTOR, FUEL INJECTOR 03	1
4	INS-41402-DVRC-1280	DVRC-2 FUEL INJECTOR SEAT	1
5	WCT-312	KILITE PRESSURE TRANSDUCER	1
6	MMC 97365A150	1/4 IN DIAM, 1-3/4 IN LENGTH DOWEL PIN	2

REVISIONS				
ZONE	REV.	DESCRIPTION	DATE	APPROVED

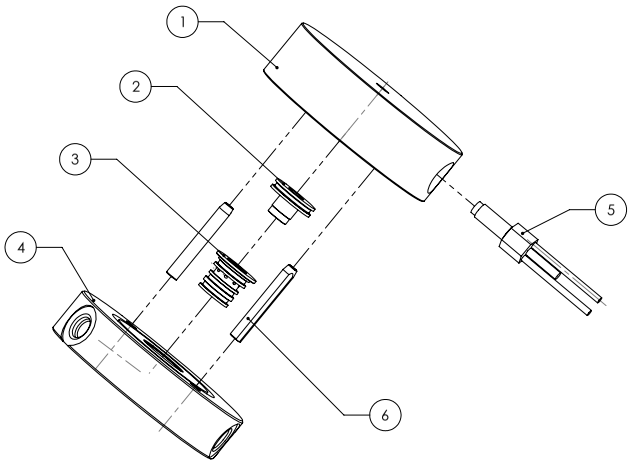

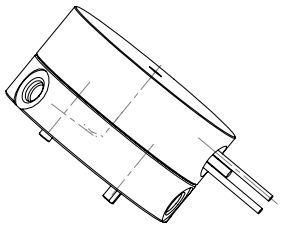

Printed: Tuesday, March 17, 2015

		NAME	DATE
DRAWN		EBK	03/11/15
CHECKED			
ENG APPR.			
MFG APPR.			
Q.A.			
COMMENTS:			

UNLESS OTHERWISE SPECIFIED:
DIMENSIONS ARE IN INCHES
TOLERANCES:
FRACTIONAL ±1/64
ANGULAR: MACH ±1° BEND ±3°
TWO PLACE DECIMAL ±.005
THREE PLACE DECIMAL ±.003
INTERPRET GEOMETRIC TOLERANCING PER:
MATERIAL
FINISH
DO NOT SCALE DRAWING

IN Space, LLC

TITLE:
DVRC-2 MAIN CHAMBER INJECTOR ASSEMBLY

SIZE	DWG. NO.	REV
B	INS-41402-DVRC-1203	

SCALE: 1:2 | WEIGHT: | SHEET 1 OF 2

REVISIONS				
ZONE	REV.	DESCRIPTION	DATE	APPROVED

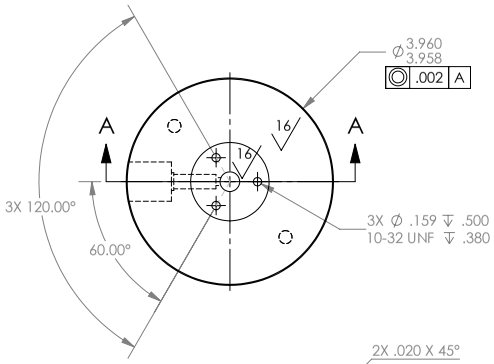

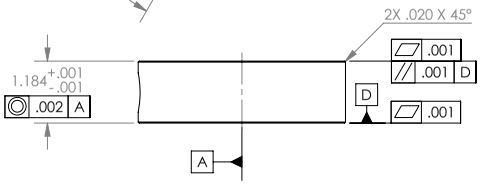

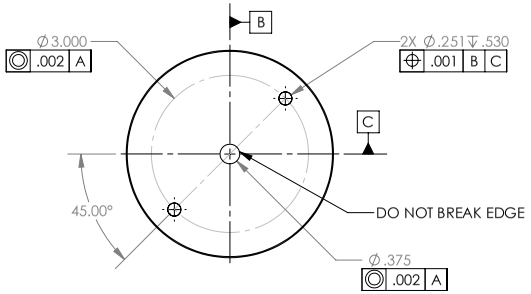

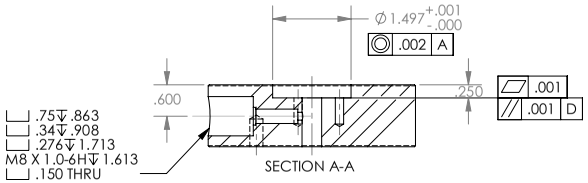

1. DEBURR ALL HOLES
2. BREAK SHARP EDGES

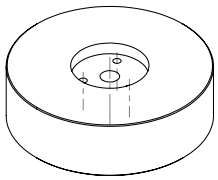

Printed: Monday, March 30, 2015

		NAME	DATE
UNLESS OTHERWISE SPECIFIED:	DRAWN	EBK	3/30/15
DIMENSIONS ARE IN INCHES TOLERANCES: FRACTIONAL ±1/64 ANGULAR: MACH ±1° BEND ±3° TWO PLACE DECIMAL ±.005 THREE PLACE DECIMAL ±.003	CHECKED		
	ENG APPR.		
	MFG APPR.		
INTERPRET GEOMETRIC TOLERANCING PER:	Q.A.		
MATERIAL: INCONEL 600	COMMENTS:		
FINISH			
DO NOT SCALE DRAWING			

IN Space, LLC

TITLE: DVRC-2 INJECTOR OXIDIZER POST

SIZE	DWG. NO.	REV
B	INS-41402-DVRC-1211	

SCALE: 1:2 | WEIGHT: 4.11 | SHEET 1 OF 1

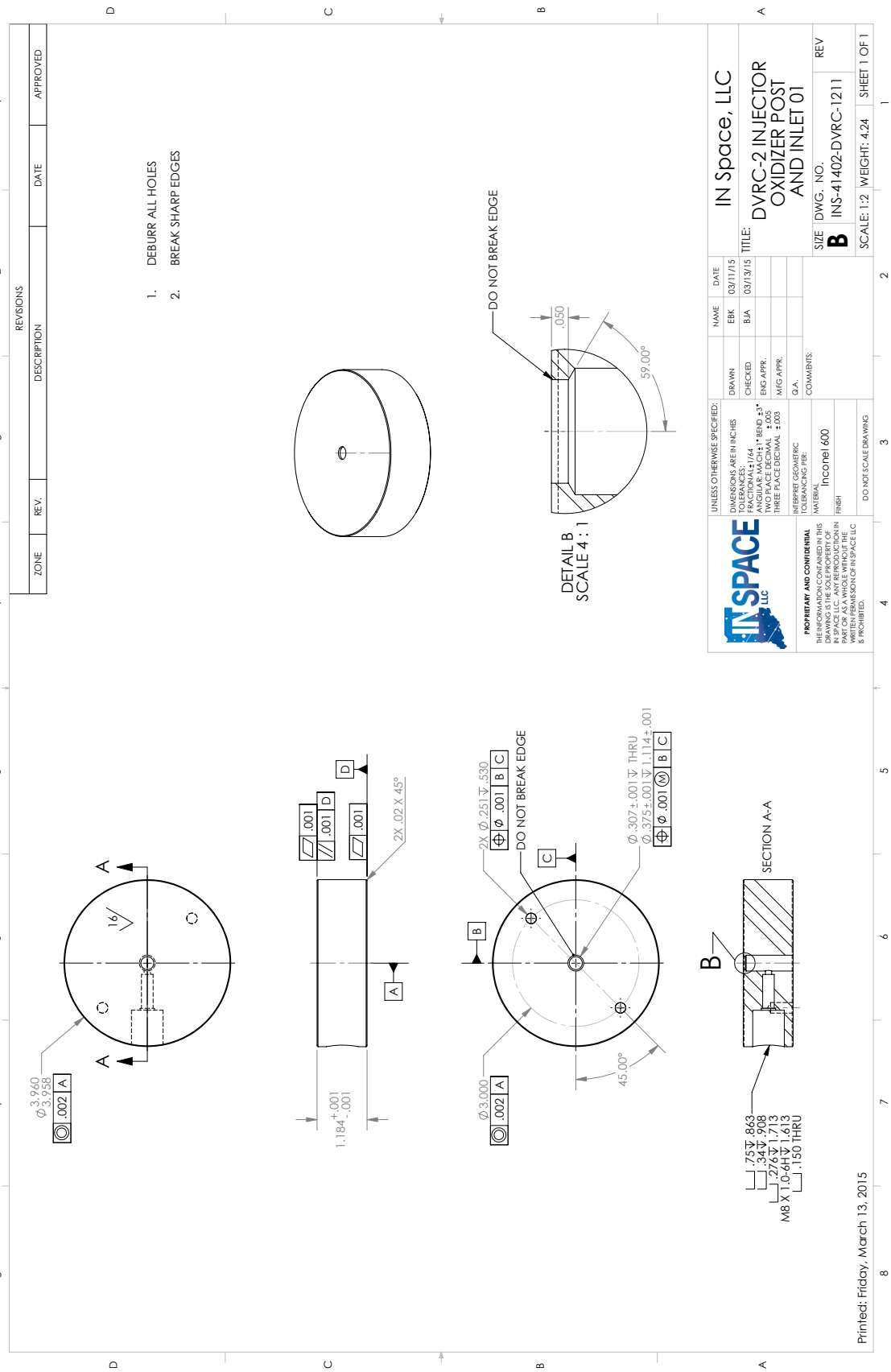
REVISIONS
ZONE
REV.
DESCRIPTION
DATE
APPROVED
1. DEBURR ALL HOLES
2. BREAK SHARP EDGES
DO NOT BREAK EDGE
.050
59.00°
DETAIL B
SCALE 4 : 1
Ø3.960
Ø3.958
.002 A
16
1.184 +.001 -.001
.001
.001 D
2X .02 X 45°
2X Ø.251 ↧ .530
Ø .001 B C
DO NOT BREAK EDGE
Ø3.000
.002 A
45.00°
Ø .307 ± .001 ↧ THRU
Ø .375 ± .001 ↧ 1.114 ± .001
Ø .001 M B C
SECTION A-A
.75 ↧ .863
.34 ↧ .908
.276 ↧ 1.713
M8 X 1.0-6H ↧ 1.613
.150 THRU
UNLESS OTHERWISE SPECIFIED:
DIMENSIONS ARE IN INCHES
TOLERANCES:
FRACTIONAL ± 1/64
ANGULAR: MACH ± 1° BEND ±3°
TWO PLACE DECIMAL ± .005
THREE PLACE DECIMAL ± .003
INTERPRET GEOMETRIC TOLERANCING PER:
MATERIAL
Inconel 600
FINISH
DO NOT SCALE DRAWING
NAME
DATE
DRAWN
EBK
03/11/15
CHECKED
BJA
03/13/15
ENG APPR.
MFG APPR.
Q.A.
COMMENTS:
PROPRIETARY AND CONFIDENTIAL
THE INFORMATION CONTAINED IN THIS DRAWING IS THE SOLE PROPERTY OF IN SPACE LLC. ANY REPRODUCTION IN PART OR AS A WHOLE WITHOUT THE WRITTEN PERMISSION OF IN SPACE LLC IS PROHIBITED.
IN Space, LLC
TITLE:
DVRC-2 INJECTOR OXIDIZER POST AND INLET 01
SIZE
B
DWG. NO.
INS-41402-DVRC-1211
REV
SCALE: 1:2
WEIGHT: 4.24
SHEET 1 OF 1
Printed: Friday, March 13, 2015

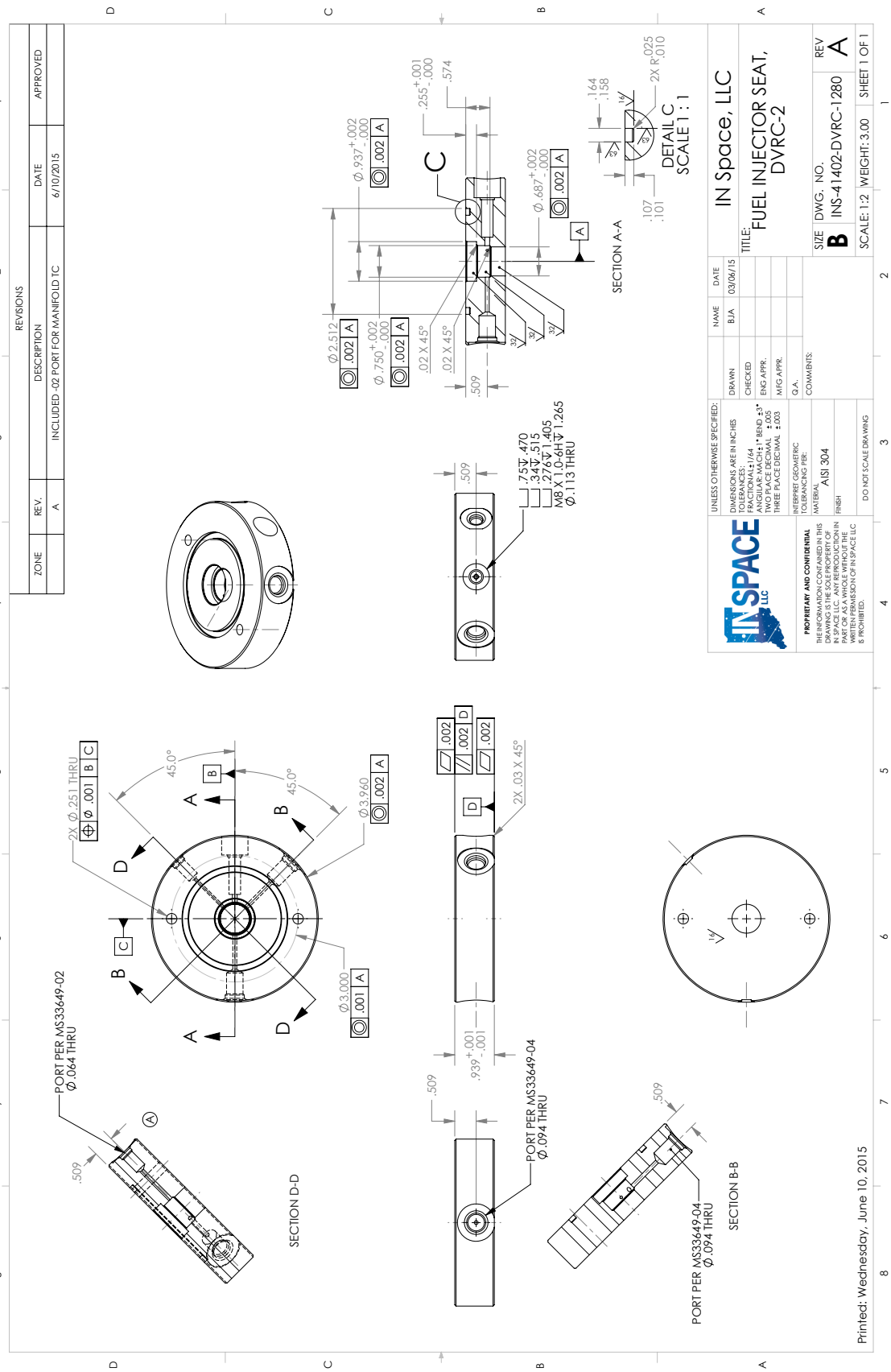
REVISIONS
ZONE | REV. | DESCRIPTION | DATE | APPROVED
A | INCLUDED -02 PORT FOR MANIFOLD TC | 6/10/2015
PORT PER MS33649-02
Ø.064 THRU
SECTION D-D
PORT PER MS33649-04
Ø.094 THRU
SECTION B-B
2X Ø.251 THRU
Ø.001 B C
45.0°
Ø3.960
.002 A
Ø3.000
.001 A
.509
.939+.001 -.001
2X .03 X 45°
.002
.002 D
.002
.75↧.470
.34↧.515
.27↧1.405
M8 X 1.0-6H↧1.265
Ø.113 THRU
Ø2.512
.002 A
Ø.750+.002 -.000
.002 A
Ø.937+.002 -.000
.002 A
.02 X 45°
.02 X 45°
.509
Ø.687+.002 -.000
.002 A
.255+.001 -.000
.574
C
SECTION A-A
.164
.138
.107
.101
2X R.025 .010
DETAIL C
SCALE 1 : 1
UNLESS OTHERWISE SPECIFIED:
DIMENSIONS ARE IN INCHES
TOLERANCES:
FRACTIONAL ± 1/64
ANGULAR: MACH ± 1° BEND ± 3°
TWO PLACE DECIMAL ± .005
THREE PLACE DECIMAL ± .003
INTERPRET GEOMETRIC TOLERANCING PER:
MATERIAL AISI 304
FINISH
DO NOT SCALE DRAWING
DRAWN BJA 03/06/15
CHECKED
ENG APPR.
MFG APPR.
Q.A.
COMMENTS:
PROPRIETARY AND CONFIDENTIAL
THE INFORMATION CONTAINED IN THIS DRAWING IS THE SOLE PROPERTY OF IN SPACE LLC. ANY REPRODUCTION IN PART OR AS A WHOLE WITHOUT THE WRITTEN PERMISSION OF IN SPACE LLC IS PROHIBITED.
IN SPACE LLC
IN Space, LLC
TITLE:
FUEL INJECTOR SEAT, DVRC-2
SIZE B
DWG. NO. INS-41402-DVRC-1280
REV A
SCALE: 1:2 WEIGHT: 3.00 SHEET 1 OF 1
Printed: Wednesday, June 10, 2015

REVISIONS				
ZONE	REV.	DESCRIPTION	DATE	APPROVED

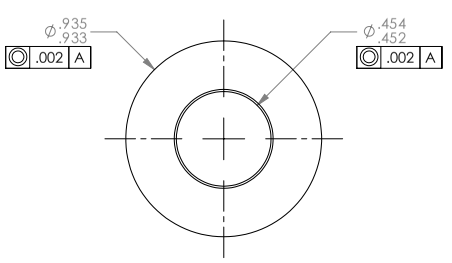

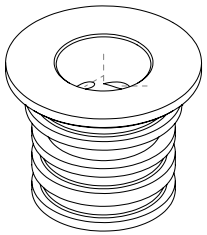

1. DEBURR ALL HOLES
2. BREAK SHARP EDGES

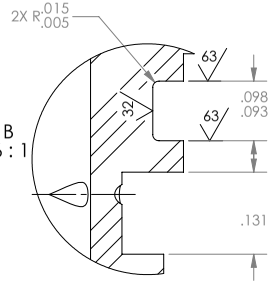

DETAIL B
SCALE 6 : 1

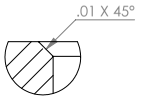

DETAIL D
SCALE 14 : 1

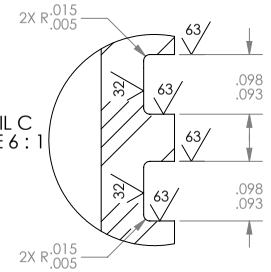

DETAIL C
SCALE 6 : 1

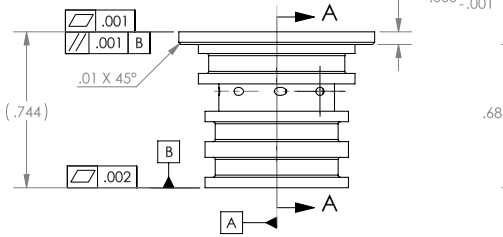

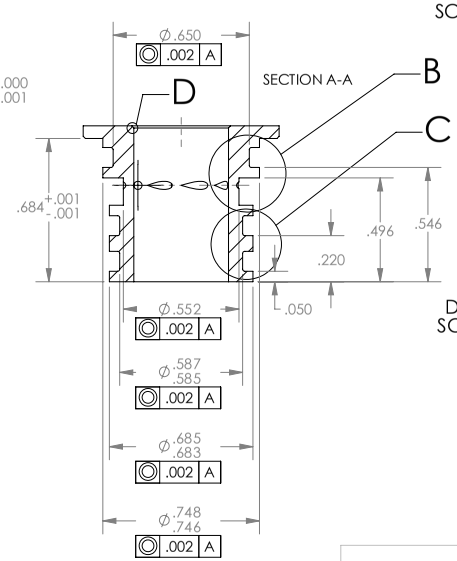

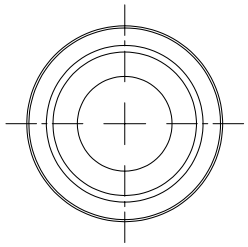

		NAME	DATE
DRAWN		EBK	03/11/15
CHECKED		BJA	03/13/15
ENG APPR.			
M.FG APPR.			
Q.A.			
COMMENTS:			

UNLESS OTHERWISE SPECIFIED:
DIMENSIONS ARE IN INCHES
TOLERANCES:
FRACTIONAL ±1/64
ANGULAR: MACH ±1° BEND ±3°
TWO PLACE DECIMAL ±.005
THREE PLACE DECIMAL ±.003
INTERPRET GEOMETRIC TOLERANCING PER:
MATERIAL: Inconel 600
FINISH:
DO NOT SCALE DRAWING

IN Space, LLC

TITLE:
DVRC-2 INJECTOR,
FUEL INJECTOR 01

SIZE	DWG. NO.	REV
B	INS-41402-DVRC-1261	

SCALE: 2:1 | WEIGHT: 0.04 | SHEET 1 OF 1

Printed: Friday, March 13, 2015

REVISIONS				
ZONE	REV.	DESCRIPTION	DATE	APPROVED

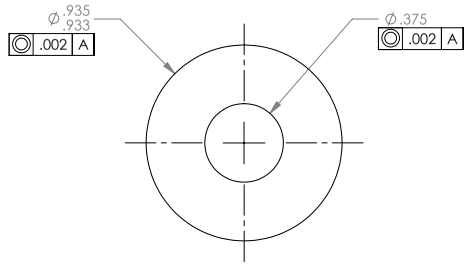

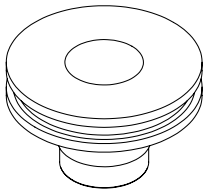

1. DEBURR ALL HOLES
2. BREAK SHARP EDGES

DETAIL B
SCALE 8 : 1

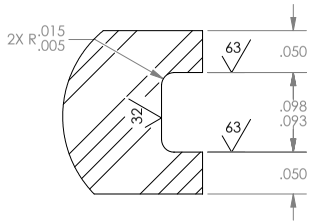

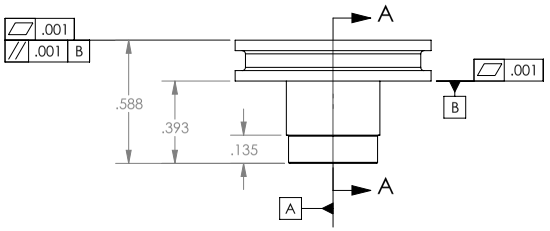

SECTION A-A
SCALE 2 : 1

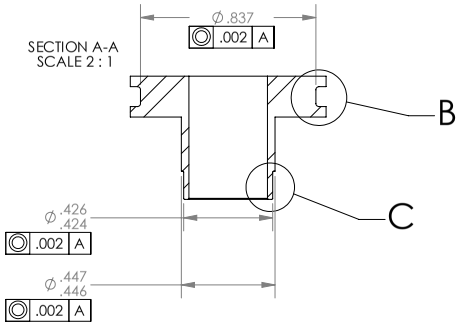

DETAIL C
SCALE 8 : 1

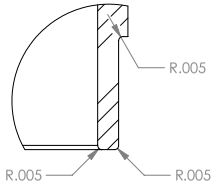

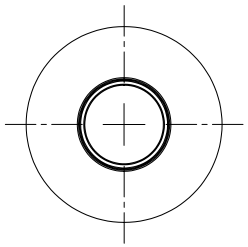

2-

		NAME	DATE
UNLESS OTHERWISE SPECIFIED:	DRAWN	EBK	03/11/15
DIMENSIONS ARE IN INCHES TOLERANCES: FRACTIONAL ±1/64 ANGULAR: MACH ±1° BEND ±3° TWO PLACE DECIMAL ±.005 THREE PLACE DECIMAL ±.003	CHECKED		
	ENG APPR.		
	M.FG APPR.		
INTERPRET GEOMETRIC TOLERANCING PER:	Q.A.		
MATERIAL: Inconel 600	COMMENTS:		
FINISH			
DO NOT SCALE DRAWING			

PROPRIETARY AND CONFIDENTIAL

THE INFORMATION CONTAINED IN THIS DRAWING IS THE SOLE PROPERTY OF IN SPACE LLC. ANY REPRODUCTION IN PART OR AS A WHOLE WITHOUT THE WRITTEN PERMISSION OF IN SPACE LLC IS PROHIBITED.

IN Space, LLC

TITLE: DVRC-2 INJECTOR OXIDIZER POST COLLAR

SIZE	DWG. NO.	REV
B	INS-41402-DVRC-1251	

SCALE: 1:2 | WEIGHT: 0.04 | SHEET 1 OF 1

Printed: Thursday, March 12, 2015

REVISIONS				
ZONE	REV.	DESCRIPTION	DATE	APPROVED

1. DEBURR ALL HOLES
2. BREAK SHARP EDGES

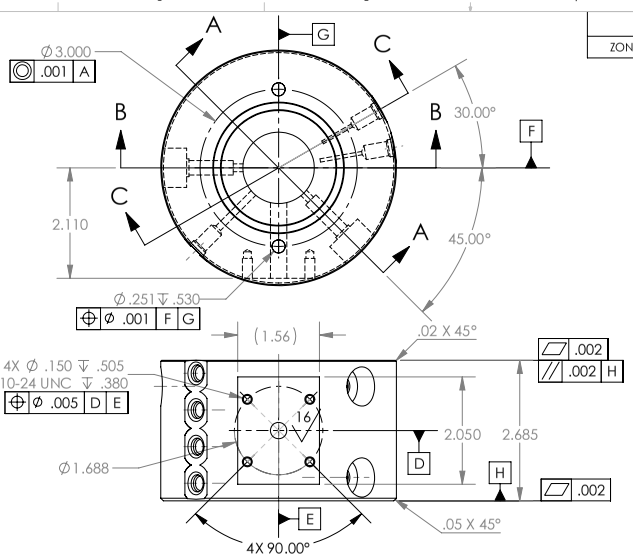

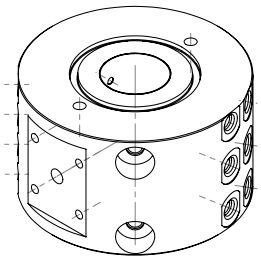

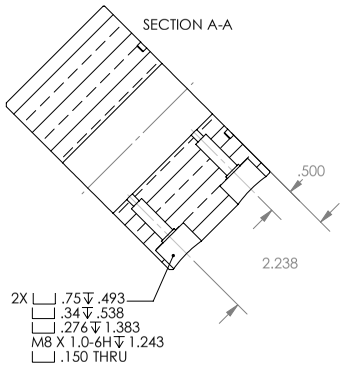

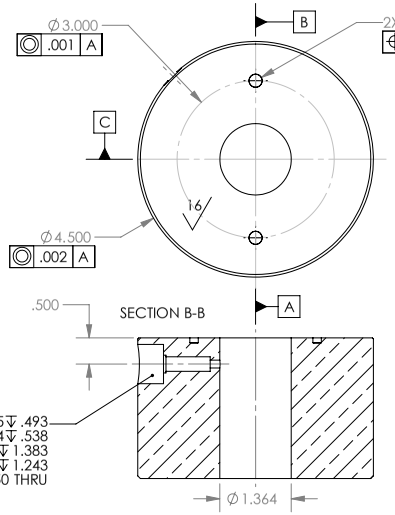

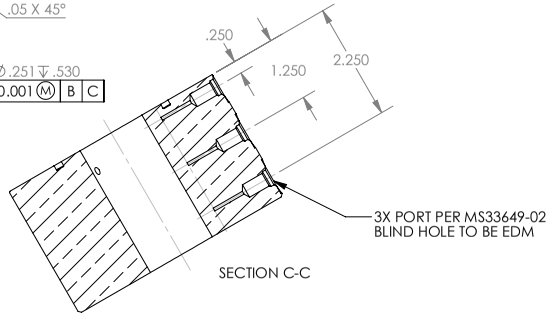

Printed: Tuesday, March 10, 2015

UNLESS OTHERWISE SPECIFIED:
DIMENSIONS ARE IN INCHES
TOLERANCES:
FRACTIONAL ±1/64
ANGULAR: MACH ±1° BEND ±3°
TWO PLACE DECIMAL ±.005
THREE PLACE DECIMAL ±.003
INTERPRET GEOMETRIC TOLERANCING PER:
MATERIAL: COPPER
FINISH
DO NOT SCALE DRAWING

	NAME	DATE
DRAWN	EBK	03/04/15
CHECKED	BJA	03/06/15
ENG APPR.		
M.FG APPR.		
Q.A.		
COMMENTS:		

IN Space, LLC

TITLE: DVCR-2 CHAMBER SPOOL 1, MACHINING

SIZE	DWG. NO.	REV
B	INS-41402-DVRC-1311	

SCALE: 1:2 | WEIGHT: 11.87 | SHEET 1 OF 2

REVISIONS				
ZONE	REV.	DESCRIPTION	DATE	APPROVED

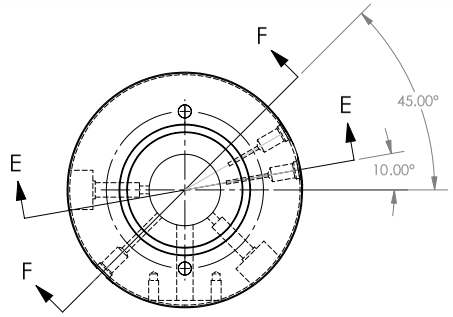

1. DEBURR ALL HOLES
2. BREAK SHARP EDGES

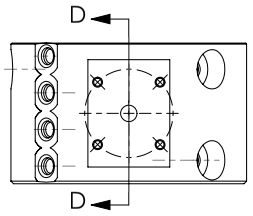

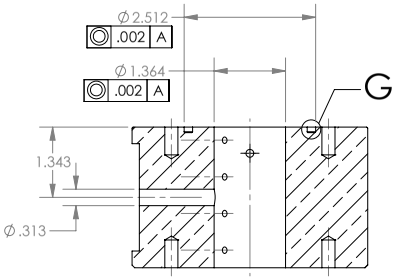

SECTION D-D

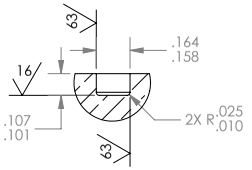

DETAIL G
SCALE 2 : 1

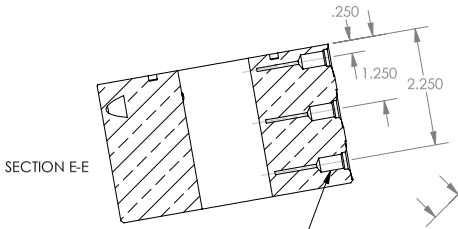

SECTION E-E

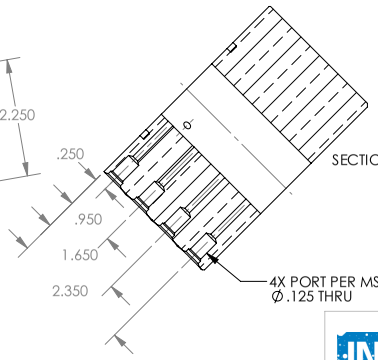

SECTION F-F

4X PORT PER MS33649-02
BLIND HOLES TO BE EDM

		NAME	DATE
DRAWN		EBK	03/05/15
CHECKED		BJA	03/06/15
ENG APPR.			
M.FG APPR.			
Q.A.			
COMMENTS:			

UNLESS OTHERWISE SPECIFIED:
DIMENSIONS ARE IN INCHES
TOLERANCES:
FRACTIONAL ±1/64
ANGULAR: MACH ±1° BEND ±3°
TWO PLACE DECIMAL ±.005
THREE PLACE DECIMAL ±.003
INTERPRET GEOMETRIC TOLERANCING PER:
MATERIAL
COPPER
FINISH
DO NOT SCALE DRAWING

IN Space, LLC

TITLE: DVRC-2 CHAMBER SPOOL 1, MACHINING

SIZE	DWG. NO.	REV
B	INS-41402-DVRC-1311	

SCALE: 1:2 | WEIGHT: 11.87 | SHEET 2 OF 2

Printed: Tuesday, March 10, 2015

REVISIONS				
ZONE	REV.	DESCRIPTION	DATE	APPROVED

1. DEBURR ALL HOLES
2. BREAK SHARP EDGES

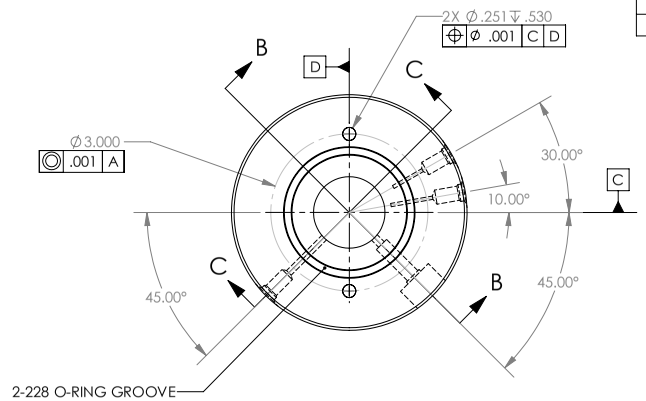

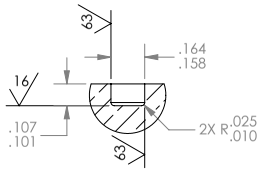

DETAIL F
SCALE 2 : 1

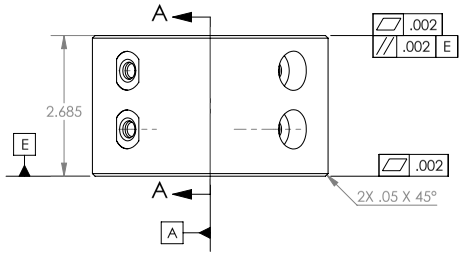

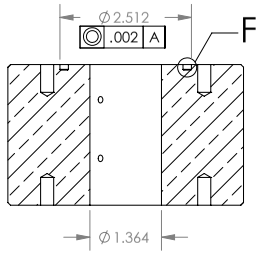

SECTION A-A

SECTION B-B

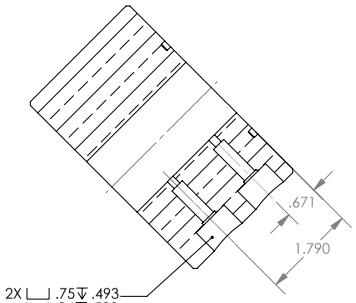

SECTION C-C

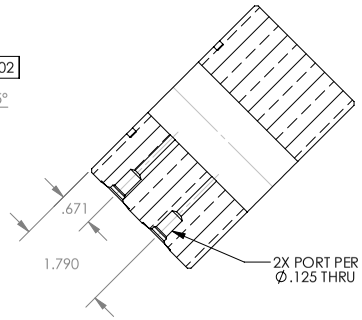

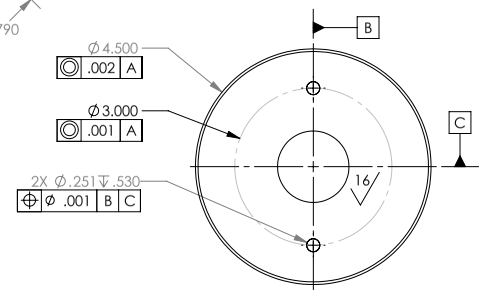

Printed: Thursday, March 12, 2015

UNLESS OTHERWISE SPECIFIED:		NAME	DATE
DIMENSIONS ARE IN INCHES TOLERANCES: FRACTIONAL ±1/64 ANGULAR: MACH ±1° BEND ±3° TWO PLACE DECIMAL ±.005 THREE PLACE DECIMAL ±.003	DRAWN	EBK	03/05/15
	CHECKED	BJA	03/06/15
	ENG APPR.		
	M.FG APPR.		
INTERPRET GEOMETRIC TOLERANCING PER:	Q.A.		
MATERIAL COPPER	COMMENTS:		
FINISH			
DO NOT SCALE DRAWING			

IN Space, LLC

TITLE: DVRC-2 CHAMBER SPOOL 2, MACHINING

SIZE	DWG. NO.	REV
B	INS-41402-DVRC-1312	

SCALE: 1:2 | WEIGHT: 12.20 | SHEET 1 OF 2

REVISIONS				
ZONE	REV.	DESCRIPTION	DATE	APPROVED

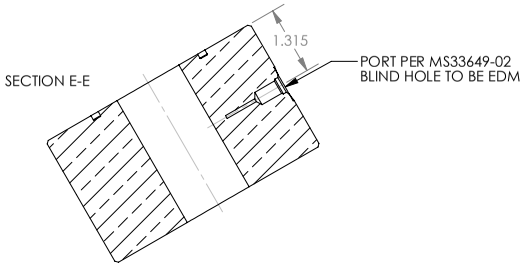

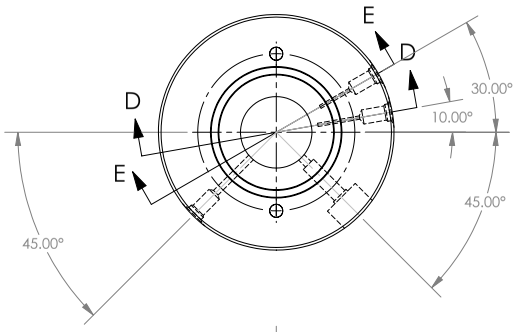

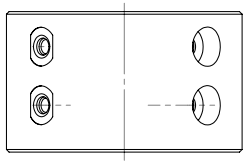

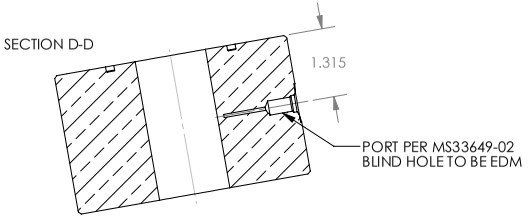

1. DEBURR ALL HOLES
2. BREAK SHARP EDGES

Printed: Thursday, March 12, 2015

UNLESS OTHERWISE SPECIFIED:		NAME	DATE
DIMENSIONS ARE IN INCHES TOLERANCES: FRACTIONAL ±1/64 ANGULAR: MACH ±1° BEND ±3° TWO PLACE DECIMAL ±.005 THREE PLACE DECIMAL ±.003	DRAWN	EBK	03/04/15
	CHECKED	BJA	03/06/15
	ENG APPR.		
	M.FG APPR.		
INTERPRET GEOMETRIC TOLERANCING PER:	Q.A.		
MATERIAL COPPER	COMMENTS:		
FINISH			
DO NOT SCALE DRAWING			

IN Space, LLC

TITLE: DVRC-2 CHAMBER SPOOL 2, MACHINING

SIZE	DWG. NO.	REV
B	INS-41402-DVRC-1312	

SCALE: 1:2 | WEIGHT: 12.20 | SHEET 2 OF 2

REVISIONS				
ZONE	REV.	DESCRIPTION	DATE	APPROVED

1. DEBURR ALL HOLES
2. BREAK SHARP EDGES

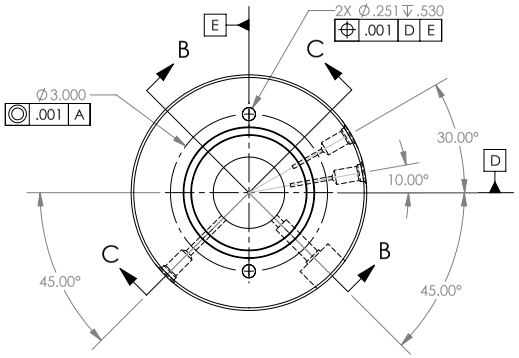

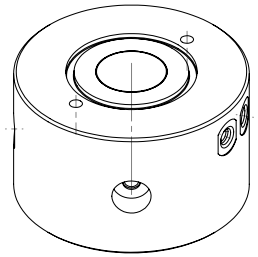

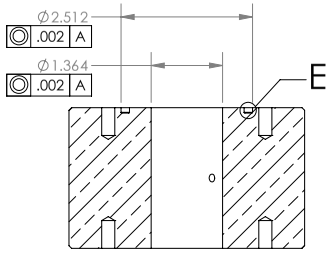

SECTION A-A

SECTION B-B

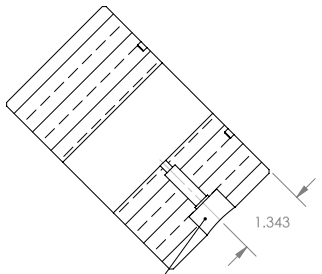

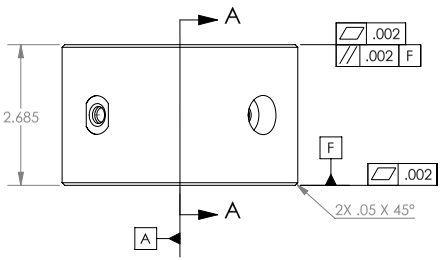

SECTION C-C

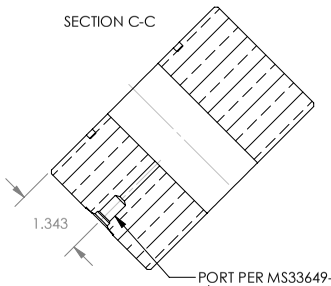

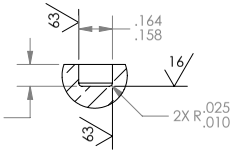

DETAIL E
SCALE 2 : 1

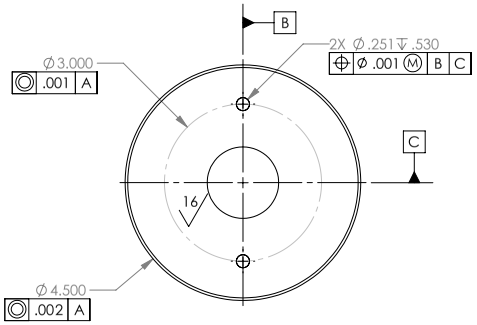

Printed: Thursday, March 12, 2015

UNLESS OTHERWISE SPECIFIED:		NAME	DATE
DIMENSIONS ARE IN INCHES TOLERANCES: FRACTIONAL ±1/64 ANGULAR: MACH ±1° BEND ±3° TWO PLACE DECIMAL ±.005 THREE PLACE DECIMAL ±.003	DRAWN	EBK	03/05/15
	CHECKED	BJA	03/06/15
	ENG APPR.		
	MFG APPR.		
INTERPRET GEOMETRIC TOLERANCING PER:	Q.A.		
MATERIAL COPPER	COMMENTS:		
FINISH			
DO NOT SCALE DRAWING			

IN Space, LLC

TITLE: DVRC-2 CHAMBER SPOOL 3, MACHINING

SIZE	DWG. NO.	REV
B	INS-41402-DVRC-1313	

SCALE: 1:2 | WEIGHT: 12.30 | SHEET 1 OF 2

REVISIONS				
ZONE	REV.	DESCRIPTION	DATE	APPROVED

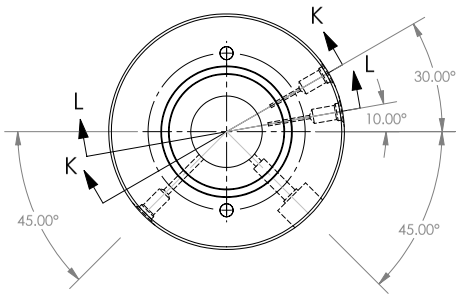

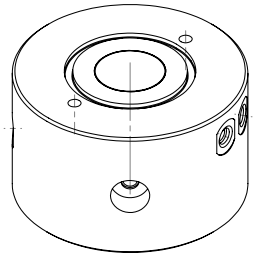

1. DEBURR ALL HOLES
2. BREAK SHARP EDGES

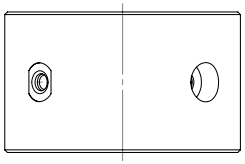

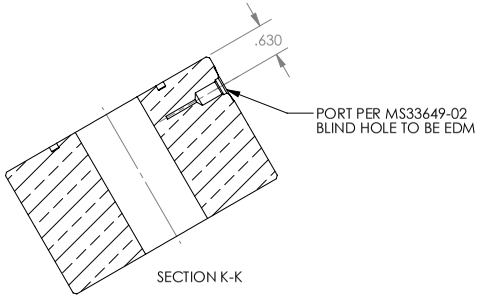

SECTION K-K

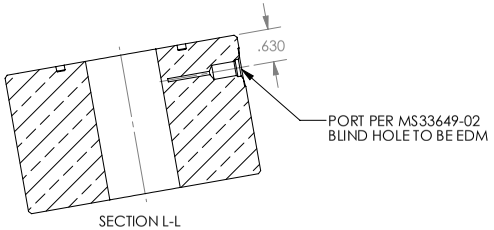

SECTION L-L

Printed: Thursday, March 12, 2015

UNLESS OTHERWISE SPECIFIED:
DIMENSIONS ARE IN INCHES
TOLERANCES:
FRACTIONAL ±1/64
ANGULAR: MACH ±1° BEND ±3°
TWO PLACE DECIMAL ±.005
THREE PLACE DECIMAL ±.003
INTERPRET GEOMETRIC TOLERANCING PER:
MATERIAL: COPPER
FINISH
DO NOT SCALE DRAWING

	NAME	DATE
DRAWN	EBK	03/05/15
CHECKED	BJA	03/06/15
ENG APPR.		
M.FG APPR.		
Q.A.		
COMMENTS:		

IN Space, LLC

TITLE: DVRC-2 CHAMBER SPOOL 3, MACHINING

SIZE	DWG. NO.	REV
B	INS-41402-DVRC-1313	

SCALE: 1:2 | WEIGHT: 12.30 | SHEET 2 OF 2

REVISIONS				
ZONE	REV.	DESCRIPTION	DATE	APPROVED

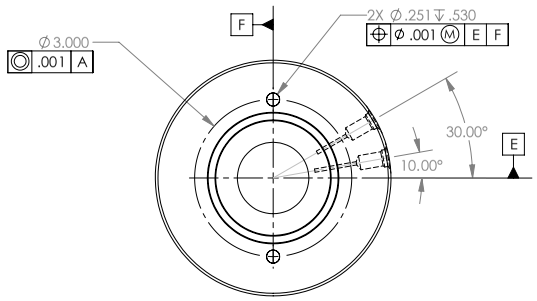

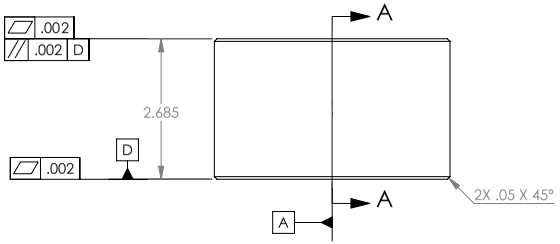

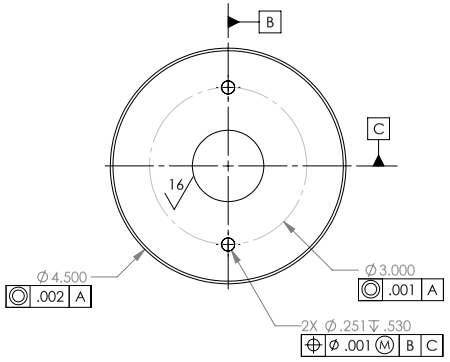

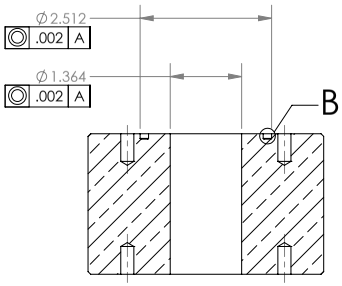

SECTION A-A

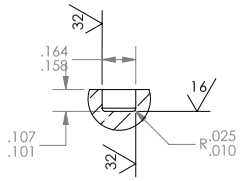

DETAIL B
SCALE 2 : 1

1. DEBURR ALL HOLES
2. BREAK SHARP EDGES

Printed: Tuesday, March 10, 2015

UNLESS OTHERWISE SPECIFIED:		NAME	DATE
DIMENSIONS ARE IN INCHES TOLERANCES: FRACTIONAL ±1/64 ANGULAR: MACH ±1° BEND ±3° TWO PLACE DECIMAL ±.005 THREE PLACE DECIMAL ±.003	DRAWN	EBK	03/05/15
	CHECKED		
	ENG APPR.		
	M.FG APPR.		
	Q.A.		
INTERPRET GEOMETRIC TOLERANCING PER:	COMMENTS:		
MATERIAL COPPER			
FINISH			
DO NOT SCALE DRAWING			

PROPRIETARY AND CONFIDENTIAL

THE INFORMATION CONTAINED IN THIS DRAWING IS THE SOLE PROPERTY OF IN SPACE LLC. ANY REPRODUCTION IN PART OR AS A WHOLE WITHOUT THE WRITTEN PERMISSION OF IN SPACE LLC IS PROHIBITED.

IN Space, LLC

TITLE: DVRC-2 CHAMBER SPOOL 4, MACHINING

SIZE	DWG. NO.	REV
B	INS-41402-DVRC-1314	

SCALE: 1:2 | WEIGHT: 12.38 | SHEET 1 OF 2

REVISIONS				
ZONE	REV.	DESCRIPTION	DATE	APPROVED

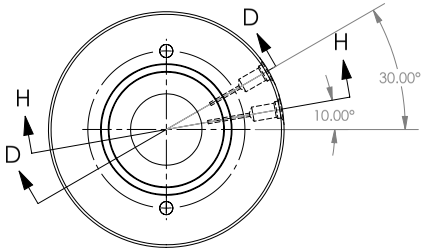

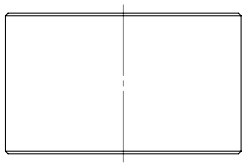

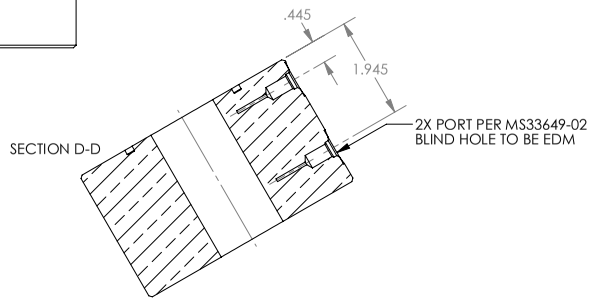

SECTION D-D

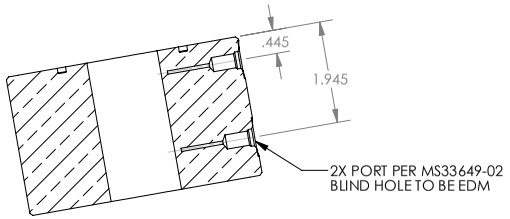

SECTION H-H

1. DEBURR ALL HOLES
2. BREAK SHARP EDGES

Printed: Tuesday, March 10, 2015

		NAME	DATE
UNLESS OTHERWISE SPECIFIED:	DRAWN	EBK	03/05/15
DIMENSIONS ARE IN INCHES TOLERANCES: FRACTIONAL ±1/64 ANGULAR: MACH ±1° BEND ±3° TWO PLACE DECIMAL ±.005 THREE PLACE DECIMAL ±.003	CHECKED		
	ENG APPR.		
	MFG APPR.		
	Q.A.		
INTERPRET GEOMETRIC TOLERANCING PER:	COMMENTS:		
MATERIAL: COPPER			
FINISH			
DO NOT SCALE DRAWING			

IN Space, LLC

TITLE: DVRC-2 CHAMBER SPOOL 4, MACHINING

SIZE	DWG. NO.	REV
B	INS-41402-DVRC-1314	

SCALE: 1:2 | WEIGHT: 12.38 | SHEET 2 OF 2

REVISIONS				
ZONE	REV.	DESCRIPTION	DATE	APPROVED

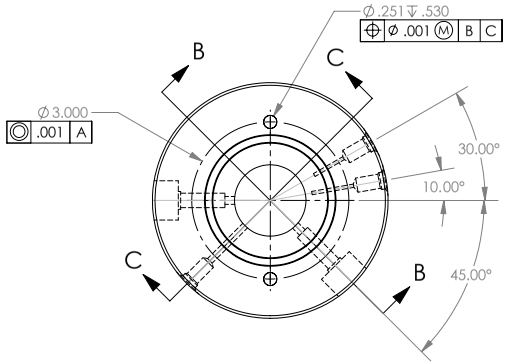

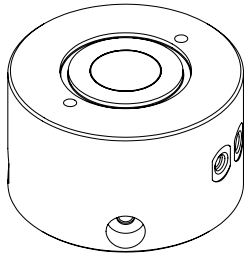

1. DEBURR ALL HOLES
2. BREAK SHARP EDGES

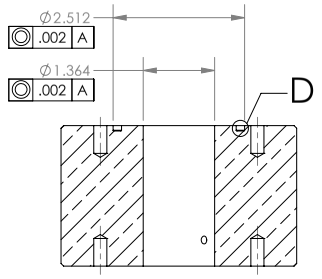

SECTION A-A

SECTION B-B

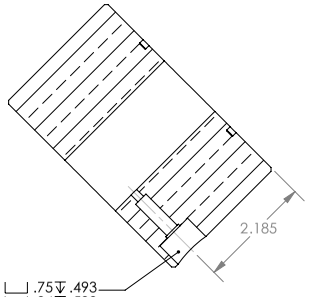

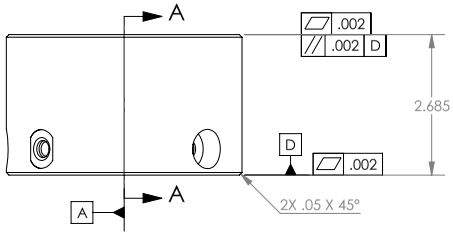

SECTION C-C

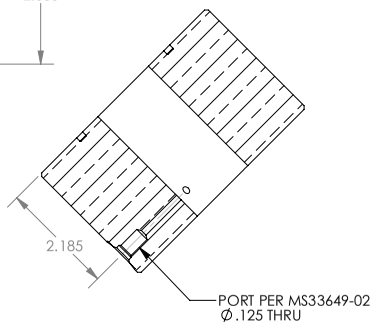

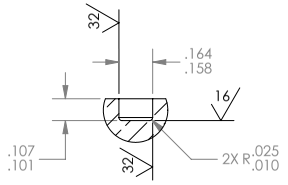

DETAIL D
SCALE 2 : 1

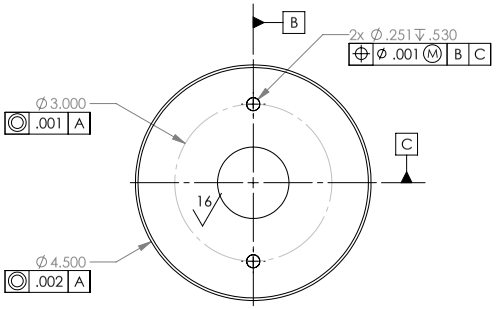

Printed: Thursday, March 12, 2015

UNLESS OTHERWISE SPECIFIED:		NAME	DATE
DIMENSIONS ARE IN INCHES TOLERANCES: FRACTIONAL ±1/64 ANGULAR: MACH ±1° BEND ±3° TWO PLACE DECIMAL ±.005 THREE PLACE DECIMAL ±.003	DRAWN	EBK	03/05/15
	CHECKED	BJA	03/06/15
	ENG APPR.		
	MFG APPR.		
INTERPRET GEOMETRIC TOLERANCING PER:	Q.A.		
MATERIAL: COPPER	COMMENTS:		
FINISH			
DO NOT SCALE DRAWING			

IN Space, LLC

TITLE: DVRC-2 CHAMBER SPOOL 5, MACHINING

SIZE	DWG. NO.	REV
B	INS-41402-DVRC-1315	

SCALE: 1:2 | WEIGHT: 12.22 | SHEET 1 OF 3

REVISIONS				
ZONE	REV.	DESCRIPTION	DATE	APPROVED

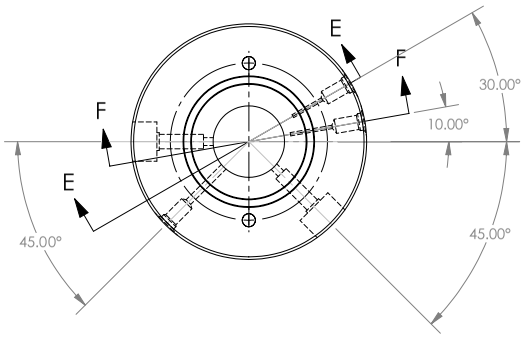

1. DEBURR ALL HOLES
2. BREAK SHARP EDGES

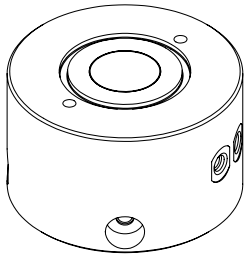

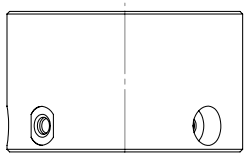

SECTION E-E

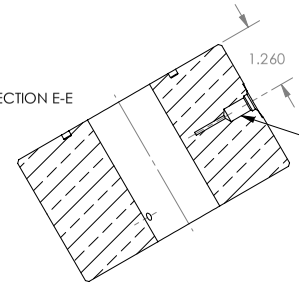

SECTION F-F

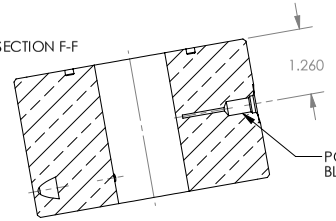

Printed: Thursday, March 12, 2015

IN SPACE LLC

UNLESS OTHERWISE SPECIFIED:
DIMENSIONS ARE IN INCHES
TOLERANCES:
FRACTIONAL ±1/64
ANGULAR: MACH ±1° BEND ±3°
TWO PLACE DECIMAL ±.005
THREE PLACE DECIMAL ±.003
INTERPRET GEOMETRIC TOLERANCING PER:
MATERIAL: COPPER
FINISH
DO NOT SCALE DRAWING

	NAME	DATE
DRAWN	EBK	03/05/15
CHECKED	BJA	03/06/15
ENG APPR.		
M.FG APPR.		
Q.A.		
COMMENTS:		

IN Space, LLC

TITLE: DVRC-2 CHAMBER SPOOL 5, MACHINING

SIZE	DWG. NO.	REV
B	INS-41402-DVRC-1315	

SCALE: 1:2 | WEIGHT: 12.22 | SHEET 2 OF 3

REVISIONS				
ZONE	REV.	DESCRIPTION	DATE	APPROVED

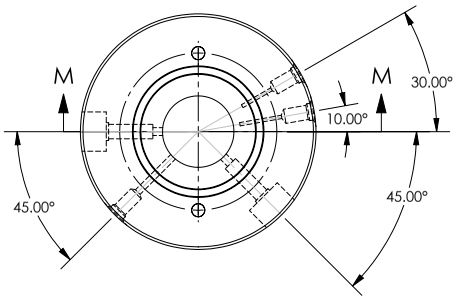

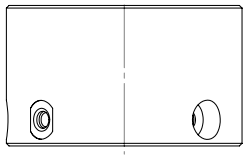

1. DEBURR ALL HOLES
2. BREAK SHARP EDGES

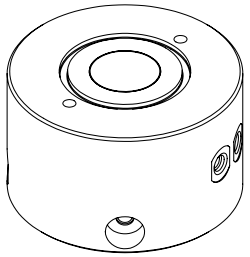

SECTION M-M

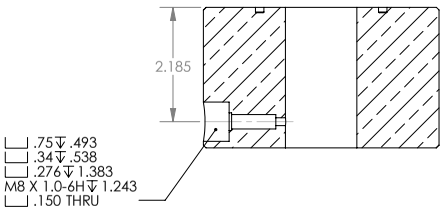

		NAME	DATE
DRAWN		EBK	03/05/15
CHECKED		BJA	03/06/15
ENG APPR.			
M.FG APPR.			
Q.A.			
COMMENTS:			

UNLESS OTHERWISE SPECIFIED:
DIMENSIONS ARE IN INCHES
TOLERANCES:
FRACTIONAL ±1/64
ANGULAR: MACH ±1° BEND ±3°
TWO PLACE DECIMAL ±.005
THREE PLACE DECIMAL ±.003
INTERPRET GEOMETRIC TOLERANCING PER:
MATERIAL: COPPER
FINISH:
DO NOT SCALE DRAWING

IN Space, LLC

TITLE: DVRC-2 CHAMBER SPOOL 5, MACHINING

SIZE	DWG. NO.	REV
B	INS-41402-DVRC-1315	

SCALE: 1:2 | WEIGHT: 12.22 | SHEET 3 OF 3

Printed: Thursday, March 12, 2015

REVISIONS				
ZONE	REV.	DESCRIPTION	DATE	APPROVED

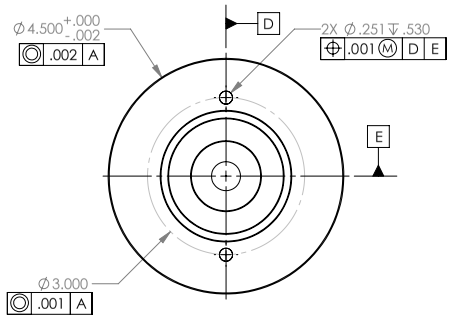

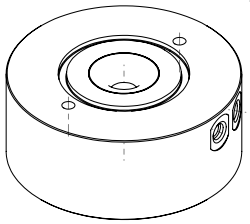

1. DEBURR ALL HOLES
2. BREAK SHARP EDGES
3. APPLY A THIN COAT OF LIGHT OIL TO ALL EXPOSED SURFACES POT MACHINING AND PLACE IN AIR-TIGHT BAG

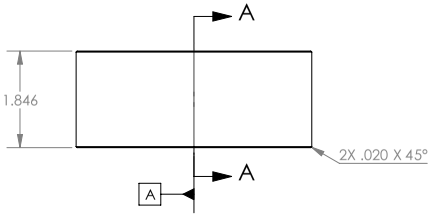

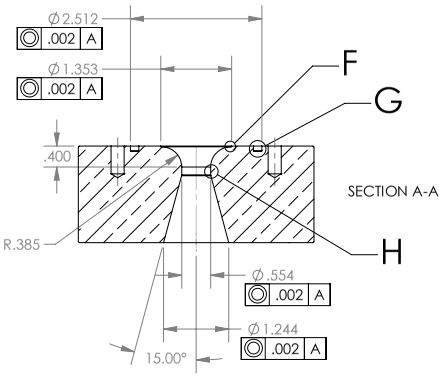

DETAIL F
SCALE 4 : 1

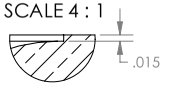

DETAIL G
SCALE 2 : 1

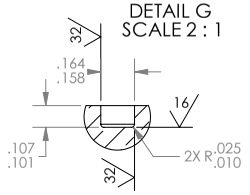

DETAIL H
SCALE 4 : 1

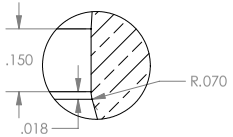

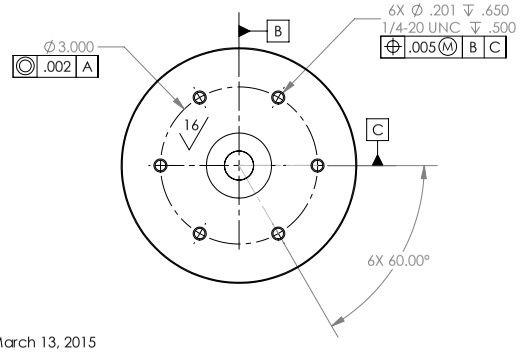

Printed: Friday, March 13, 2015

UNLESS OTHERWISE SPECIFIED:
DIMENSIONS ARE IN INCHES
TOLERANCES:
FRACTIONAL ±1/64
ANGULAR: MACH ±1° BEND ±3°
TWO PLACE DECIMAL ±.005
THREE PLACE DECIMAL ±.003
INTERPRET GEOMETRIC TOLERANCING PER:
MATERIAL: COPPER
FINISH
DO NOT SCALE DRAWING

	NAME	DATE
DRAWN	EBK	03/05/15
CHECKED		
ENG APPR.		
MFG APPR.		
Q.A.		
COMMENTS:		

IN Space, LLC

TITLE:
DVRC-2 CHAMBER THROAT, MACHINING

SIZE	DWG. NO.	REV
B	INS-41402-DVRC-1331	A

SCALE: 1:2 | WEIGHT: 8.97 | SHEET 1 OF 2

REVISIONS				
ZONE	REV.	DESCRIPTION	DATE	APPROVED

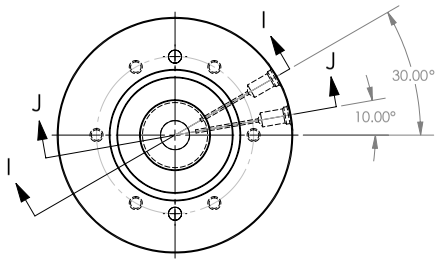

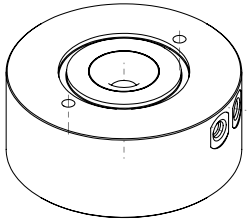

1. DEBURR ALL HOLES
2. BREAK SHARP EDGES
3. APPLY A THIN COAT OF LIGHT OIL TO ALL EXPOSED SURFACES POT MACHINING AND PLACE IN AIR-TIGHT BAG

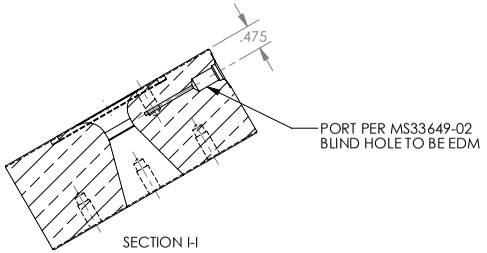

SECTION I-I

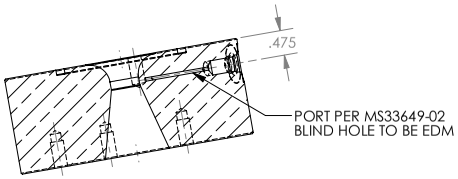

SECTION J-J

UNLESS OTHERWISE SPECIFIED:		NAME	DATE
DIMENSIONS ARE IN INCHES TOLERANCES: FRACTIONAL ±1/64 ANGULAR: MACH ±1° BEND ±3° TWO PLACE DECIMAL ±.005 THREE PLACE DECIMAL ±.003	DRAWN	EBK	03/05/15
	CHECKED		
	ENG APPR.		
	M.FG APPR.		
	Q.A.		
	COMMENTS:		
INTERPRET GEOMETRIC TOLERANCING PER:			
MATERIAL COPPER			
FINISH			
DO NOT SCALE DRAWING			

IN Space, LLC

TITLE:
DVRC-2 CHAMBER THROAT, MACHINING

SIZE	DWG. NO.	REV
B	INS-41402-DVRC-1331	A

SCALE: 1:2	WEIGHT: 8.97	SHEET 2 OF 2

Printed: Friday, March 13, 2015

VITA

VITA

William Zach Hallum was born and raised in Cleveland, Ohio. He attended Case Western Reserve University, where he graduated in 2010 with a Bachelor of Science degree in Aerospace Engineering. He then joined Purdue University in the Fall of 2010, where he completed his Master of Science degree in Aerospace Engineering in the Summer of 2012 under the advisement of Prof. William Anderson. His masters's thesis is entitled "The Use of Proper Orthogonal Decomposition in the Research of Combustion Instability." Following a year of traveling with his wife to support her pursuit of a Doctor of Optometry degree, he returned to Purdue University in Fall of 2013 where he continued his studies in combustion stability under Prof. Anderson. After graduation, William will continue to develop rocket engines at Sierra Nevada Corporation in Madison, Wisconsin.